Wet granular dynamics:

From single particle bouncing to collective motion

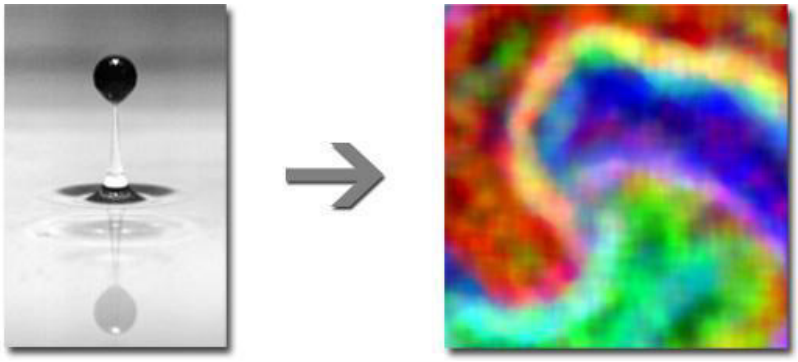

Habilitation thesis

submitted to

Fakultät für Mathematik, Physik und Informatik
Universität Bayreuth

Kai Huang

Bayreuth

October 28, 2014

Wet granular dynamics:

From single particle bouncing to collective motion

Habilitation thesis

submitted to

Fakultät für Mathematik, Physik und Informatik
Universität Bayreuth

Kai Huang

Experimentalphysik V, Universität Bayreuth
95440 Bayreuth, Germany

Bayreuth

October 28, 2014

For *Nian & Jovin*
for the power of love

Preface

Bayreuth, October 28, 2014

Dating back to 1300 B.C., the word 'sand' (沙) had already been used in Chinese bronze inscriptions as one of the earliest words. The desire to communicate on sand at the very beginning of the language evolution demonstrates the ubiquity of granular matter. Since then, the attempts of mankind to describe and understand such a material have never stopped. For example, in the epic poem 'On the nature of things' written in around 55 B.C., Lucretius describes granular flow as the following [Carus & Leonard, 2004]:

" ...To suck the poppy-seeds from palm of hand
Is quite as easy as drinking water down,
And they, once struck, roll like unto the same."

Such daily life experience shows the liquid like behaviour of granular matter. However, a little more strictly speaking, to which extend such a granular liquid behaves like a simple liquid in thermodynamic equilibrium? What can we learn from this similarity? How to classify and define physical quantities of such a 'liquid'? Could it be possible to have a continuum description of its flow? For granular flow, in addition to the 'macroscopic' perspective, it is also feasible to take the 'microscopic' perspective and discuss the collective behaviour from the mobility of individual particles. What can we learn from the connections between both perspectives?

My efforts to address the above questions during the period from 2006 to 2014 are summarized in this cumulative habilitation thesis. In particular, the case with cohesion arising from wetting liquid added to the particles is focused, because of its importance in real life applications. In Chapter 1, a more detailed description of the motivation for the research, from both physical and industrial perspectives, together with a brief review of the advances in this field are given. From a 'microscopic' point of view, Chapter 2 is devoted to the particle-particle interactions with the wetting liquid mediated. The intrinsic time, length and energy scales associated with the impacts and a collisional model are described. From a 'macroscopic' point of view, Chapter 3 contains the collective behaviour of granu2lar matter: From phase transitions to pattern formation. Comparisons between dry and wet granular dynamics, and recent efforts on the dynamics of aspherical particles are also included. Finally in Chapter 4, the connections

between dynamics at both 'microscopic' and 'macroscopic' levels, as well as the links between systems in and out of thermodynamic equilibrium, are summarized, in order to provide a general framework for further studies and to shed light on the widespread applications. In Chapters 6 and 7, detailed descriptions of the work in preprint and published forms are attached. In the thesis, these articles are cited with links to their first pages. All internal links are painted with dark brown, i.e., a color of sand.

Part of the work presented in the thesis is supported by the Deutsche Forschungsgemeinshaft (DFG) through grant number HU1939/2-1.

The research I have been carrying out would not be possible without the support and help from all the colleagues I have been working with. First of all, I would like to take this chance to thank all of them.

I am grateful to Stephan Herminghaus, for giving me the opportunity to continue my academic career in Germany after my Ph.D, and for providing me indispensable support during my stay in the Max Planck Institute for Dynamics and Self-organization in Göttingen. I have enjoyed the enlightening discussions and active collaborations with Matthias Schröter, Martin Brinkmann, Jürgen Vollmer and Ralf Seemann since my stay in Göttingen. I would also like to thank former colleagues Axel Hager-Fingerle, Masound Sohaili, Mario Scheel and Klaus Röller, for helping me both with my research and personal life. I always remembers their warm-hearted help when I tried to settle down in this very much different country 8 years ago.

I would also like to express my deep gratitude to Ingo Rehberg, for providing me the opportunity to continue my career as the leader of the sand group in Experimentalphysik V. His enthusiastic encouragement, helpful hints and critiques are always beneficial. I would also like to extend my acknowledgement to my predecessor Christof Krülle, for his continuous support since I started in Bayreuth, especially for those days he drove more than 600 kilometers to attend the weekly seminar of the sand group. I am also grateful to Reinhard Richter, for his help both as a colleague and as a friend. It is also a pleasure to appreciate all my students during the past 5 years: Frank Gollwitzer, Christopher May, Michael Wild, Lorenz Butzhammer, Laura Meißner, Felix Ott, Philipp Ramming, Simeon Völkel, and Thomas Müller.

Special thanks to the other mentors of the habilitation thesis, Thomas Fischer and Matthias Schmidt, for their helpful hints on my career. I should also extend my acknowledgement to Andrea Fortini and Daniel de las Heras, for the enlightening discussions on our recent collaborations.

Most of all, I would like to thank my wife Nian, for her love over the past 15 years, for caring about me more than I myself do, and for giving birth to our son, Jovin.

Contents

1 Introduction

1.1 A classification

As large agglomerations of macroscopic particles, granular materials are ubiquitous in the universe. From the LCROSS project that found icy water on the moon through exploring the granular jet created by an impact on a crater of the moon in 2009 [Kerr, 2010; Colaprete *et al.*, 2010], to the activities of the latest Mars rover curiosity landing in 2013 [MSL, 2013], our endeavours to explore the universe are becoming more and more closely related to the dynamics of granular matter. No need to mention the Saturn's rings, typical examples of granular gases, which are composed of icy particles spreading hundreds of thousand of kilometers in a rather thin layer with a few tens of meters thick [Cassini, 2014]. Modelling the evolution of such rings and wave propagations inside in response to external perturbations are believed to shed light on the early stage of planet formation [Crida & Charnoz, 2012].

Back to the earth, the dynamics of *wet* granular matter is of more importance, since our blue planet is largely covered with water. Every child knows that something tremendous is happening when a small amount of water is added into sand. It is the magic played by the water added that enables all the fun of playing sand on the beach. Despite of the omnipresence of such experiences, it is not until very recent physicists start to find a clue on the stability of wet sand with the help of X-ray tomography [Scheel *et al.*, 2008]. Generally speaking, the complexity of such kind of problems in static wet granular matter arises from the heterogeneities in both particle packings and liquid distributions.

Concerning the packing of spheres of the same size as a starting point, Kepler's conjecture states that the maximum packing density is the face-centered-cubic (FCC) packing with a packing density $\phi = \pi/\sqrt{18} \approx 0.74$, where ϕ is defined as the volume of the spheres over the total volume that the particles occupy. In 1831, Gauß proved that particles packed in a regular lattice indeed have such a maximum packing density. However, how to prove for the endless irregular packing? In 1951, Tóth showed that this infinite number of configurations can be reduced to a finite but large number. With the help of computer simulations, Hales finally showed a proof of Kepler's conjecture in 2005 [Hales, 2005], which was concluded to be more than 99% complete by the 12 referees from Annuals of Mathematics, after 4 years of reviewing process. Despite of such a success, packing of mono-disperse spheres in reality will not have the energetically favoured FCC packing. Instead, a packing density between the so called random close packing (RCP, with $\phi \approx 0.64$) [Scott, 1960; Scott & Kilgour, 1969] and random loose

packing (RLP, with $\phi \approx 0.56$) [Onoda & Liniger, 1990] will be a more reasonable guess. Moreover, the packing of aspherical particles is a dramatically different story: Turning spheres into ellipsoids can easily lead to an enhanced RCP of $\phi > 0.70$, a trick used by M&M® to pack the candies more efficiently in a jar [Donev *et al.*, 2004]. As to poly-disperse particles, the Arab saying

> "You think your basket is full when you have stuffed it with oranges. In truth, it is full of void, for you can still add nuts, and even chickpeas after that."

actually elucidates the pathway towards a more and more dense packing, correspondingly a more and more rigid structure in terms of granulates used in civil engineering. Additionally, no sand grains are the same in nature, not even look the same. The collection of microscopic photography by Gary Greenberg [Greenberg, 2008] nicely demonstrates such a diversity, and tells us that walking on the beach is actually an experience of travelling along millions of years of biological and geological history.

On the other hand, the cohesion induced by the additional wetting liquid strongly depends on the geometry of the liquid within the voids of packing. This cohesion will most likely change the local packing of particles, triggering a feedback on the distribution of the wetting liquid. Such an interaction will eventually lead to a steady state with an enhanced overall rigidity compared with a dry granular packing. As a consequence, the sand does not have an angle of repose any more, and is ready to be sculptured into almost any shape we want. Without disturbance, a sand sculpture will stay forever, because the thermal energy scale is orders of magnitude smaller than the local potential energy scale required to change the packing. That is the hallmark separating granular from colloidal particles [Duran, 2000]. Typically, the realm of granulates compose of particles with a size range from a few microns such as clay particles to a few thousand kilometers such as large ice floes, covering 12 orders of magnitude.

Figure 1.1 (a) shows an example of wet granular matter in a liquidlike state. The photo was taken in a jumping competition in London Olympic Games 2012. During the impact of the athlete with the wet sand, the kinetic energy transferred to the wet sand drives it into the liquidlike state. In such a situation, wet granular matter acts as an effective damper to protect the player. Compared with sand flowing in an hour glass, or with sand saltating during dune migrations, agitated wet sand behaves differently: The kinetic energy injected doesn't enter the translational and rotational degrees of freedoms of individual particles directly. Instead, the strong cohesion leads to the formation of clusters, the size of which presumably depends on the intrinsic energy scale governed by the formation of capillary bridges inside the wet granular sample. In order to understand the basic principle behind such kind of dynamical behaviour, we start with wet spherical particles in the lab. After a small amount of water is added into the glass beads, a closer view shown in Fig. 1.1 (b) clearly demonstrates the formation of capillary bridges between adjacent particles, which introduces cohesion in the wet granular sample. As an approximation, the cohesive force can be estimated by $F_\mathrm{b} = 2\pi R\sigma$, where R and σ correspond to the radius of the sphere and surface tension of the wetting liquid respectively. For glass beads with $R \approx 200$ μm, comparable to typical sand grains on the beach, the capillary force is two orders of magnitude larger than the gravity of the particle, explaining why simply shaking the hand is not sufficient

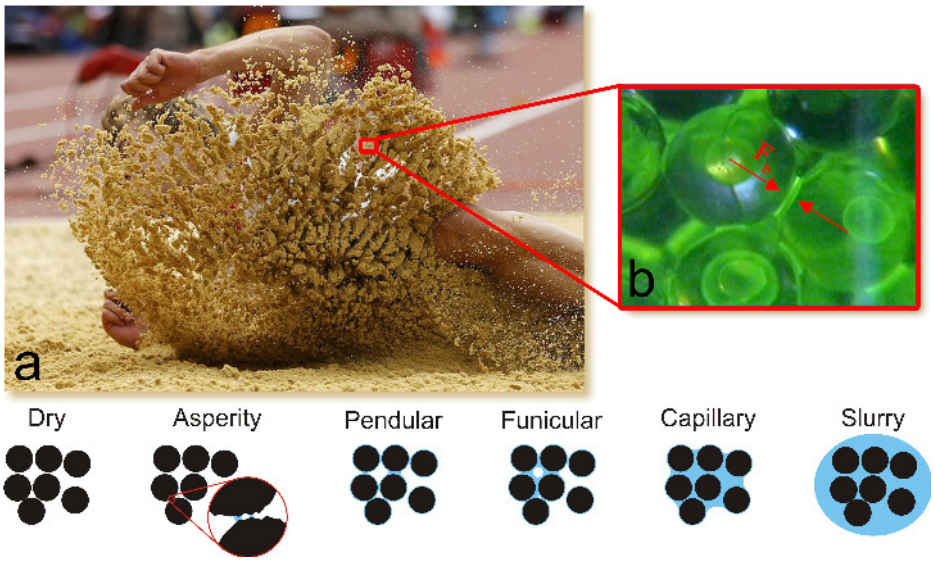

Figure 1.1: Upper panel: A daily life experience (a) of agitated wet granular matter taken during London Olympic Games in 2012 (Image courtesy of Wall Street Journal). The strong tendency for sand grains to form clusters can be attributed to the cohesion introduced by the wetting liquid, as the closer view (b) of water wetting glass beads indicates. Fluorescent dyes are added into the liquid to highlight the capillary bridges. Lower panel: Depending on the amount of wetting liquid added, various states of wet granular matter can be distinguished. See text for a more detailed definition.

to get rid of the sand grains sticking there after playing on the beach. A balance of the capillary force with the gravity suggests that the former dominates for particles with a radius up to 2 mm. Together with the rupture distance of the capillary bridge, the capillary force gives rise to a certain energy scale to overcome, in order for a granular particle to escape the attraction from its neighbours. As continuous energy injections are necessary to compensate such an energy dissipation, agitated wet granular matter can be treated as a non-equilibrium model system. More details of such force and energy scales will be discussed in Chap. 2.

Depending on the amount of wetting liquid added, wet granular matter can be classified into various states, as the lower panel of Fig. 1.1 shows. Dry corresponds to the case where cohesion is negligible, or say the inertia of the particles dominates. The asperity state is the slightly wetting situation where small capillary bridges between the asperities of adjacent particles that are in contact arise. The cohesive force in such a region depends on the length scale associated with the roughness of the sphere surface. The pendular state arises as the small liquid bridges at the asperity level merge into one single bridge. In such a state, the curvature of the spheres starts to play the main role in determining the cohesive force. Further increasing the amount of liquid added leads to the merging of capillary bridges into liquid clusters with voids, which is called a funicular state. As the voids inside are completely filled and the cohesion relies only on the curvature of the wet granular assembly, we speak of a capillary state. Finally, the slurry state means that all particles are immersed in the wetting liquid, and correspondingly no three phase contact lines exist any more. In

such a state, the cohesive force diminishes and the particles interact with each other through hydrodynamic interactions.

Strictly speaking there is no real dry granular matter in our daily life because of the influence from the environment, which may arise from the viscous drag force from the surrounding fluid, from the cohesion induced by the humidity, or from the electrostatic force due to charges. However, as long as the influence from the environment is sufficiently small compared with the inertia of the particles, the collective behaviour can be treated as dry granular phenomena. In order to characterize the relative importance, we can define dimensionless numbers similar to those in fluid mechanics. As an example, reminiscent to the Reynolds number, we define $R_\mathrm{v} = \rho_\mathrm{p} R v/\mu$ for the inertia of particles with respect to the viscous drag force, where ρ_p, v, and μ are density, velocity of the particle, and the viscosity of the fluid correspondingly. For glass beads with a size of 1 mm moving in air, $R_\mathrm{v} \approx 10^4$ suggests a dry granular matter problem. If the same type of particles moving in water, $R_\mathrm{v} \approx 10$ suggests that the interactions with the surrounding liquid have to be taken into account. Similarly, the ratio between the gravity of particles and the cohesive force from the capillary bridges $R_\mathrm{c} \propto \frac{\rho_\mathrm{p} R^2}{\sigma}$ will give us a guide on whether the cohesion should be considered or not. Note that the importance of the inertia of particles grows quadratically with the size of the spheres. Therefore, the smaller the particles, the more the influence from the humid environment should be considered.

Normally the asperity regime [Halsey & Levine, 1998] is not considered in the typical classification [Newitt & Conway-Jones, 1958; Iveson *et al.*, 2001; Mitarai & Nori, 2006] of wet granular matter because of its narrow range in the liquid content W scale. Here W is defined as the volume of the wetting liquid over the total volume that the wet granular sample occupies. Taking glass beads with a diameter of 1 mm as an example, the transition from the asperity to the pendular state occurs at $W \approx 10^{-5}$. Such a small threshold value clearly indicates the prominent role that humidity might play on the mechanical stability of sub-millimeter sized particles. Moreover, despite of the small threshold, enhanced rigidity has already been demonstrated to start well below the threshold for the pendular state to start [Huang *et al.*, 2009a], which will be described in more detail in the following Chap. 2.

The term wet granular matter throughout the following text represents the states with the presence of cohesion arising from wetting liquid added. Special focus will be given to the pendular state where mutual interactions between adjacent particles with a well defined energy scale dominate.

1.2 Motivation

The motivations for understanding the dynamics of wet granular matter are twofold: To shed light on the widespread applications due to its omnipresence, and to use it as a non-equilibrium model system.

Let's start with a discussion on the ubiquity of wet granular matter. In the center of Fig. 1.2, the sculpture mimicking the logo of Beijing Olympic Games 2008 is an example demonstrating the influence from the wetting liquid on the stability of sand. It is the dominating cohesive force present in a wide range of liquid content that makes wet sand a nice sculpturing material that attracts artists all over the world to meet

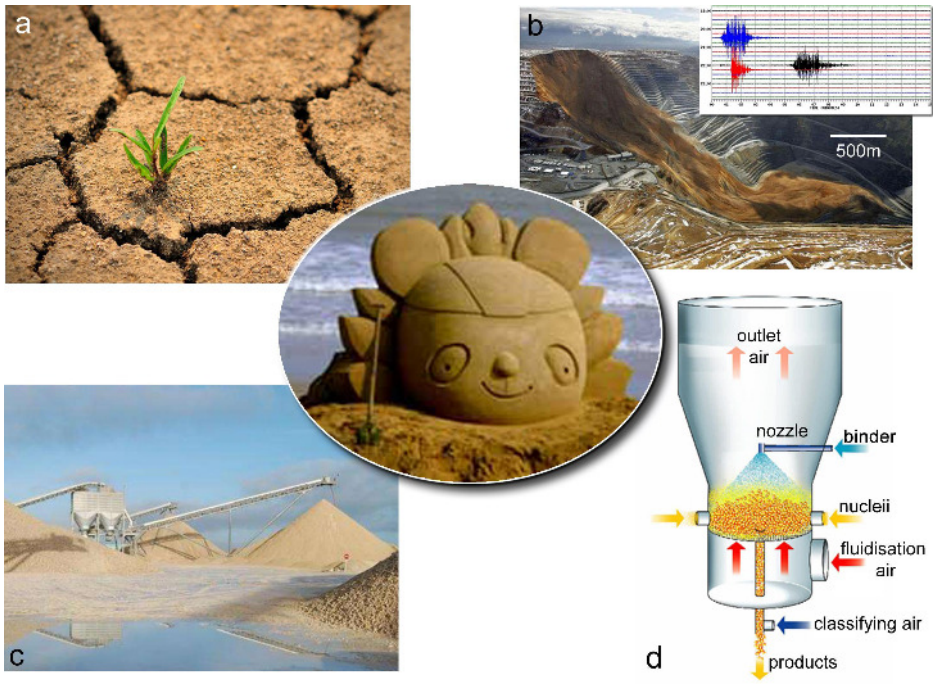

Figure 1.2: Understanding the dynamics of wet granular matter, such as wet sand used to build sand sculptures (center, photo courtesy of dfic.cn), is of importance in a large variety of industries including (a) agriculture, damage control of (b) natural disasters (Bingham Canyon mine landslide in 2013, image courtesy of American Geophysical Union), (c) civil engineering (image courtesy of European Aggregates Association), and (d) chemical engineering (image courtesy of Stefan Heinrich from Technical University of Hamburg Harburg).

regularly for competitions on building sand sculptures [SAND, 2014].

Perhaps examples more close to our daily life are from the kitchen. Preparing espresso as an example: It starts with grinding coffee beans into wet granulates in order to release the taste originally sealed inside, and follows with a filtration process of pumping compressed steam into the wet granulate. The efficiency of the initial grinding process, and the filtration process will influence dramatically the taste of the coffee.

Actually, not only coffee, but also many other foods found in the kitchen are in the form of granular matter. Because granular matter is typically not a good thermal conductor, adding a small amount of liquid, such as water used in cooking rice, or oil used in frying peas, is always necessary for cooking. Therefore, cooking, from a physical point of view, concerns very much on the heat transfer through wet granular matter.

Moreover, think about the plants where our daily foods are originally from. As shown in Fig. 1.2 (a), they are supported by soil, a type of wet granular matter concerned seriously in agriculture. How do the interactions between the roots of a plant with the surrounding soil take place, and in which way the wetting liquid inside helps in the nutrition transportation into the plants? To address those questions, a recent collaboration with Mathias Schröter and Ina Meier from Göttingen has been established to monitor the root growth of plants in an artificial soil, namely wet spherical particles, with the help of three dimensional computer tomography (CT). Because the emerging dynamics there corresponds to a different class, the outcome from this collaboration

is not included in the habilitation thesis.

At a larger length scale, natural disasters, such as avalanches, landslides, debris or mud flows, are also associated with the dynamics of wet granular matter, especially the transition from a solidlike to a fluidlike[1] state. The onset of such a transition, typically an abrupt event, is extremely important since these disasters may cause severe damage to our society. Taking the Bingham Canyon mine landslide (Fig. 1.2 b) occurred last year in Utah, USA, as an example, it is an extreme large event causing serious damages to the mining area. Luckily no one was injured in such a disaster because the deformation of the slope started weeks before and a continuous monitoring of the stress was able to give an alarm before the landslide happens. It is so huge that not only the local seismic recoding station (inset of Fig. 1.2 b), but also the global seismic dataset located over 3000 km away in Columbia University, New York State, had a clear record on it and predicted a mass release of tens of millions of tons [AGU, 2013].

Thinking of the houses we are living in and of the Vitamin tablets we take, wet granular materials are as well widely concerned in the industries. Taking civil engineering as an example: The materials for construction are called aggregates, which are typically of mineral origin such as sand, gravel, and crushed rocks (Fig. 1.2 c). According to the UEPG (Union Européenne des Producteurs de Granulats, Europäischer Gesteinsverband, or European Aggregates Association) annual report in 2013, it is by far the largest non-energy extraction sector. Let the numbers speak: It is a sector processes roughly 3 billion tonnes a year of aggregates, composes of 15,000 companies at 26,000 quarries and pits across Europe, employs 238,000 people directly and indirectly. It is so huge a sector that its growth has a direct correlation to the GDP (Gross domestic product) [UEPG, 2013]. Last but not least, a substantial portion of products from chemical engineering, food and pharmaceutical industries is in the form of granular aggregates. One commonly used way to create such granulates is the so called granulation process. As sketched in Fig. 1.2 (d), liquid binders are used to glue functional powders fluidized by air flow together in such a process. The final size and strength of the granulates formed rely strongly on the balance between the energy scale of the capillary bridge, i.e. the binding energy, and the kinetic energy of particles during impacts. In a simplified view on such an event, considering the effective coefficient of restitution (COR) for wet impacts, binding or breaking corresponds to 0 or a finite COR. A thorough understanding on the impact at a 'microscopic' level, as will be discussed in Chap. 2, is essential in modelling not only the granulation process, but also other industrial processes such as extraction, dredging, crushing, grinding, separation, sifting, washing, desliming, mixing, packing, storage and transport. Again, concerning the impact on our society, let numbers speak: Processing 1 ton of granular materials has an energy cost of about 10 kWh with 10 kg of Carbon Dioxide (CO_2) produced [UEPG, 2013]. In USA, roughly 1.3% of total energy produced across the country is used in grinding granular materials [Duran, 2000].

From a physical point of view, the energy dissipation through the frequent collisions between particles or rupturing of liquid bridges attributes agitated wet granular matter as a model system far from thermodynamic equilibrium. Upon energy injection, such a non-equilibrium system may behave like a solid, a liquid or a gas. As will be dis-

[1] Note that the term fluid is used as a synonym for liquid throughout the thesis, although strictly speaking fluid includes both liquid and gas phases.

cussed in detail in Chap. 3, critical phenomena such as phase transitions and pattern formation found in experiments can be discussed in connection to those observed in equilibrium systems, and compared with large scale molecular dynamics (MD) simulations. This fact gives us a chance of using such a model system to characterize the non-equilibrium steady state (NESS) arising from the balance between the energy injection and dissipation. Such characterizations will not only provide guidelines for the widespread applications of wet granular matter, but also shed light on a continuum description of non-equilibrium systems in general.

1.3 A brief historical review

Due to its ubiquity, granular matter is always acting as one of the essential components in different philosophies and world views across various cultures. As an example, the stamp named 'Erde' shown in Fig. 1.3 uses sand to represent earth, one of the four basic elements that the world is composed of. Again due to its ubiquity, our awareness of granular dynamics started to develop thousands of years ago, probably even earlier than the word to describe such a material was invented. Taking the pictographic Chinese language as an example, the word 'sand' in one of its ancient form, as overlaid in Fig. 1.3, gives us a clue on how ancient people imagine such a material: A composition of small dots that mimic sand grains at a 'microscopic' level, together with curved lines that represent the ripples formed by the 'macroscopic' collective motion of sand grains. It is among the first few hundreds words invented at the early stage of Chinese language evolution roughly 3400 years ago.

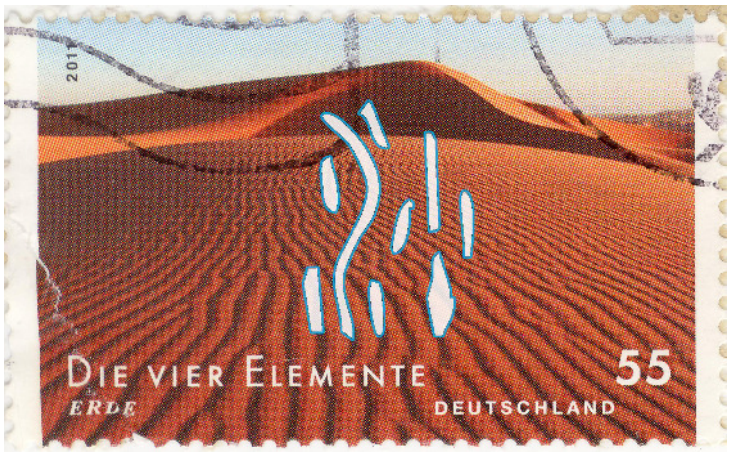

Figure 1.3: In the stamp series 'The four elements', a picture of sand dunes with ripples is used to represent earth (image courtesy of Deutsche Post). The overlaid character is the calligraphy of the word 'sand' in Chinese bronze inscriptions.

Learning is always a refining process, and this is also true for granular matter. The aforementioned awareness of granular materials, as well as the view of flowing poppy seeds from Lucrecius [Carus & Leonard, 2004] sets the starting point of our understanding on such a material. Such an understanding evolves with time, mostly driven

by real life applications. It was the needs to build better forts that Coulomb coined the frictional law [Coulomb, 1773]; it was intrigued by the problem of packing more cannon balls on the decks of warships that Kepler's conjecture was proposed [Hales, 2005]; and it was for visualizing the performance of musical instruments that Chladni figures were discovered [Chladni, 1787]. Those are only few out of many other examples (See e.g. Newton [1687]; Faraday [1831]; Hertz [1882]; Reynolds [1885]; Janssen [1895]) on how granular materials are understood from specific perspectives. In the 20th century, driven by the industrialization process, investigations on granular materials experienced a boost and had consequently been split into various fields, such as earth scientists focusing on dynamics of marine sand, desert sand and dune migrations [Fredsøe & Deigaard, 1992; Pye, 2009; Goudie, 2013], engineers more orientated to the process of such a material [Litster *et al.*, 2004; Rumpf, 1962; Stronge, 2004], civil engineers focusing on soil mechanics [Das, 1997; Schofield & Wroth, 1968].

Despite of the advances on various applications, a unified physical view on the dynamics of granular matter, especially wet granular matter, is still lacking. Proper definitions of various NESS, and the physical quantities to describe them are still under debate. At the current stage, one typical approach driven by applications is to treat granular materials as a continuum medium and use fluid mechanics to describe its dynamical behaviour. This approach will unavoidably encounter the problem when granular matter undergoes phase transitions, e.g. a transition from a liquidlike to a solidlike state. The other approach uses discrete element method (DEM) to calculate the mobilities of individual particles based on certain force laws, in order to predict the large scale collective behaviour with computer simulations. However, describing wet, or even dry impacts at the particle level is typically a complicated story. Assumptions have to be made for large scale simulations of granular matter to be possible [Yu *et al.*, 2013], and contributions to applications with such modelling normally requires a try and trial process. Taking the granulation process as an example, it is not until very recently that useful predictions can be made [Iveson *et al.*, 2001].

In order to have a deeper understanding on granular dynamics, more and more interest has been generated in the past decades from the physical community. In the 1980s, triggered by the discovery of self-organized criticality (SOC) [Bak *et al.*, 1987; Jensen, 1998; Bak, 1999], equipped with the rapidly advancing computer simulation and imaging techniques, a series of investigations have been performed to find the essential ingredients that determine the dynamics of granular materials, such as the avalanches of a sand pile [Jaeger *et al.*, 1989; Held *et al.*, 1990; Frette *et al.*, 1996]. As will be discussed in Chap. 3, it turns out that granular dynamics contains interesting topics itself that are often counter-intuitive and far from understood. Driven by curiosity, physicists tried to find essential components that dominate granular dynamics. After more than one decade's investigations, a few review articles [Guyon *et al.*, 1990; Nagel, 1992; Jaeger *et al.*, 1996; de Gennes, 1999; Goldhirsch, 2003; Aranson & Tsimring, 2006] and introductory books [Duran, 2000; Ristow, 2000; Brilliantov & Pöschel, 2004; Mehta, 2007; Aranson & Tsimring, 2009] were published. In the past decade, more and more interest has been drawn to the physics of wet granular matter. Advances and open questions in such an emerging field have been summarized in recent reviews [Mitarai & Nori, 2006; Herminghaus, 2005, 2013].

As a summary of the knowledge learned from the experimental investigations on wet granular matter, the chapters in the thesis are organized as the following: Chap-

ter 2 is largely devoted to the 'microscopic' particle-particle interactions that determine the intrinsic time, length and energy scales in wet granular matter, including impact mechanics of a spherical particle bouncing on a flat surface covered with a liquid layer, an analysis on the energy dissipation associated with the impact, and a tentative model for simulations. Chapter 3 contains various collective behaviour of wet granular matter, agitated either vertically or horizontally via shaking, swirling or shearing. The focuses will be given to the phase transitions and pattern formation in monolayer as well as multiple-layer systems. Comparisons to dry granular dynamics, as well as the influence from the shape of particles will also be presented briefly. In Chapter 4, possible connections between the 'macroscopic' behaviour and 'microscopic' particle-particle interactions will be drawn as a conclusion. Finally, an outlook with open questions toward a deeper understanding of such a material will be given.

2 'Microscopic' interactions

The universe is viewed as agglomerations of particles. These particles may be point like (0 dimension) as in astrophysics and quantum electromechanics; may be string like (1 dimension) as in string theory [Becker *et al.*, 2006]; may be grains of sand (3 dimensions) that granular matter is composed of.

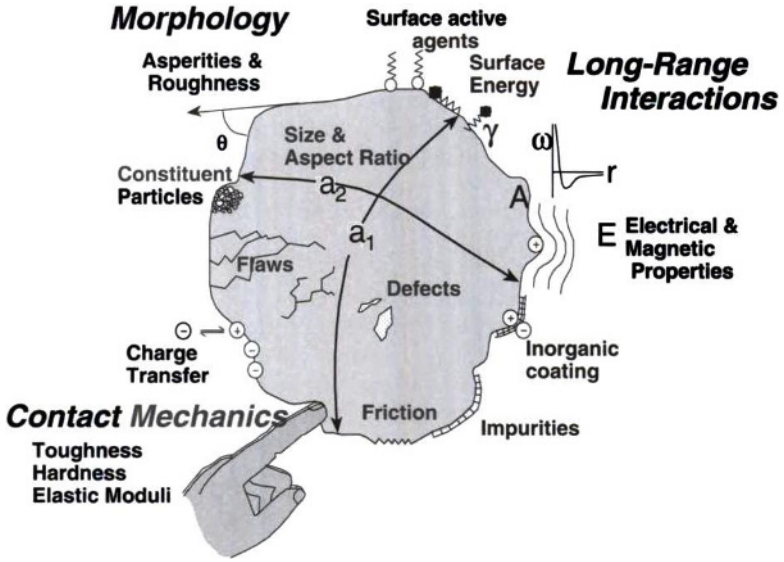

Figure 2.1: A view on a granular particle taken from an engineering text book [Litster *et al.*, 2004], with a list of factors that may influence the dynamics of the particle.

The dynamics of a single granular particle can be described fully by classical mechanics, which seems to be 'simple'. However, a closer view on such a particle reveals its complexity: As the sketch from an engineering textbook shows in Fig. 2.1, there exist a vast number of possible ingredients to be considered, including material properties (e.g. elastic modulus and hardness), geometric aspects (e.g. particle size and shape), surface properties (e.g. roughness, charges, wettability and impurities), as well as internal defects. All those properties will affect the force and energy scales associated with the particle-particle and particle-environment interactions. A proper characterization of those quantities is actually becoming the heart of modern particle processing technologies [Litster *et al.*, 2004], as the treasured advice given by Roland Clift in the 1st international particle processing forum states:

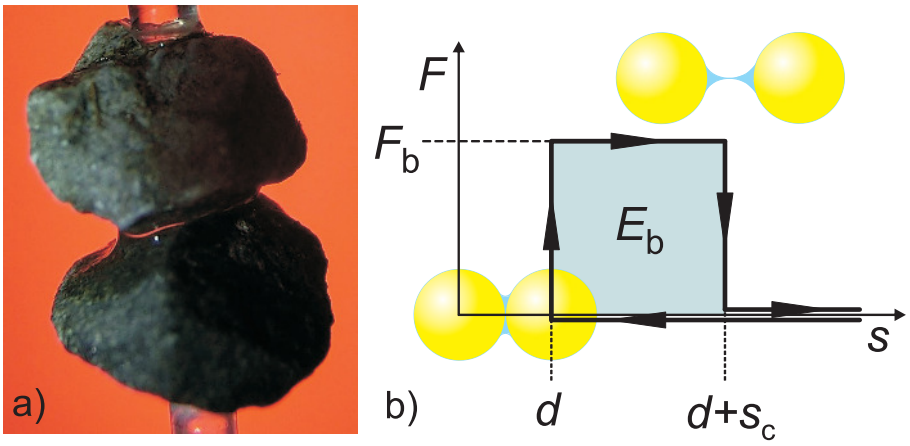

Figure 2.2: a) A snapshot of two grains connected with each other via a capillary bridge, which introduces a cohesive force F_b between them. The scale bar corresponds to 1 mm. b) The minimal capillary model [Fingerle *et al.*, 2008] used to describe the interactions between two wet grains, which considers spherical particles with the same diameter d, constant capillary force F_b, and a rupture distance s_c of the capillary bridge formed. The sketches on the bottom-left and upper-right corners illustrate the configurations of the wet spheres with separation distance $s = 0$ and s_c correspondingly.

"Measure properties, don't perform rituals."

However, even if we have a proper definition for each of those properties and are able to measure them accurately, are we able to predict the 'macroscopic' behaviour, such as when, where, and how strongly a landslide occurs? That is difficult because a general framework that accounts for the collective behaviour of granular matter, in which those measured quantities can be plugged in, is still lacking. As an example, it is not until very recent that a two dimensional continuum model for sheared dense granular flow is proposed [Jop *et al.*, 2006]. And its validity under various conditions is still to be justified. It is more complex for the case of wet granular matter, owing to the additional influence from the wetting liquid. As the snapshot of two wet grains shown Fig. 2.2 (a) indicates, the cohesive force F_b arising from the formation of liquid bridge relies, in addition to the aforementioned particle properties, on the local geometry of the gap as well as liquid properties.

From a physical perspective, it is essential to sort out the key components that dominate the collective behaviour, so as to develop simplified descriptions of granular dynamics for more efficient computer simulations targeting at real life applications. Fig. 2.2 (b) shows one of such simplifications on wet granular matter: It treats grains as spherical particles, and models the mutual interactions between two wet spheres with a hysteresis loop that contains a length s_c and an energy scale E_{cb} that arise from the rupture distance and energy of a capillary bridge. The detailed nature of the binding and the rupture of capillary bridges and interactions between various liquid bridges are ignored. Such kind of *minimal model* can be conveniently implemented into computer simulations, and comparisons to corresponding experiments reveal that it describes phase transitions of agitated wet granular particles qualitatively well [Fin-

gerle *et al.*, 2008]. Moreover, a modification of the force laws applied yields almost identical phase diagrams, suggesting the detailed nature of the rupture event does not play an important role in determining the transition from a liquilike to a gaslike state of vertically agitated wet granular matter, as will be discussed further in Sec. 3.4.3. The essential quantity here is the rupture energy that characterizes the dominating energy dissipation inside the granulates. As a system driven far from thermodynamic equilibrium, it is the balance between such energy dissipation and injection that determines the non-equilibrium steady state.

This chapter is devoted to the characterizations of particle-particle interactions for dry 2.1 and wet 2.2 cases. Special focus will be given to the coefficient of restitution, which quantifies the energy dissipation associated. Finally, preliminary investigations on the contact angle hysteresis will be presented in Section 2.4.

2.1 Dry impact

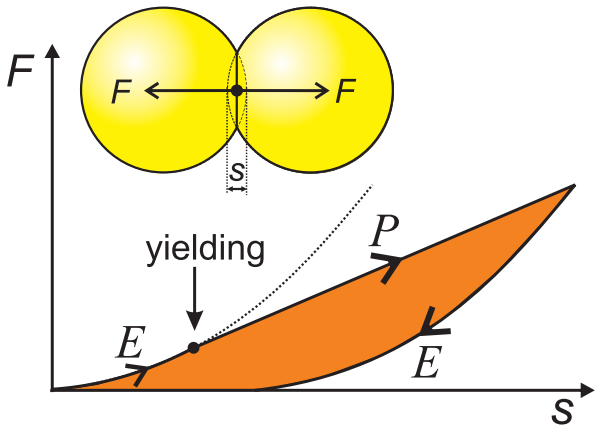

Figure 2.3: Contact force F between two spheres as a function of the penetration depth s. E and P stand for elastic and plastic deformation regions correspondingly. The dash line is an extension of the elastic deformation curve below yielding, following the Hertz contact law. Inset is a sketch of two spheres in contact.

Before we discuss the energy dissipation, let's start with the elastic interaction between two spherical particles, also named as Hertz's problem. In his paper 'On the contact of elastic solids' ('Über die Berührung fester elastischer Körper') published in 1882 [Hertz, 1882], he showed that, within the elastic limit, the contact force between two spheres (inset of Fig. 2.3) is related to the penetration depth s by

$$F_{\mathrm{el}} = k \cdot s^{3/2}, \tag{2.1}$$

where the elastic constant $k \propto Y\sqrt{R}/(1-\nu^2)$ depends on the effective radius R, Young's modulus Y, and Poisson's ratio ν of the particles. Suppose two particles of identical size collide with each other elastically, i.e. no energy dissipation, the above relation can be used to estimate the maximum penetration depth and the duration of the collision. Suppose the mass of the sphere is m and the initial relative velocity is v, energy conservation leads to

$$\frac{1}{2}mv^2 - \frac{1}{2}m(\frac{ds}{dt})^2 = \frac{1}{2}k \cdot s^{5/2}. \tag{2.2}$$

As all the initial kinetic energy is turned into the potential energy, the maximum penetration depth

$$s_{\max} = (\frac{m}{k})^{2/5} \cdot v^{4/5} \tag{2.3}$$

is reached. The duration for the collision can be estimated by [Duran, 2000]

$$\tau = 2\int_0^{s_{\max}} \frac{ds}{\sqrt{v^2 - ks^{5/2}/m}} \approx 2.94 \left(\frac{m^2}{k^2 v}\right)^{1/5}. \tag{2.4}$$

At the end of his paper, Hertz took the collision of two steel balls with a size of the earth as an example:

> For two steel spheres with the size of the earth, a collision with initial velocity of 10 $\frac{\text{mm}}{\text{s}}$ takes about 27 hours.
>
> "Für zwei Stahlkugeln von der Grösse der Erde, die mit einer Anfangsgeschwindigkeit von 10 $\frac{\text{mm}}{\text{s}}$ zusammenträfen, würde die Dauer der Berührung nahe an 27 Stunden betragen."

The extremely long time predicted for this example arises from the large size and small relative velocity. In reality, two 1.5 mm spheres colliding with velocity 5 cm/s will lead to $s_{\max} = 0.2\ \mu m$ and $\tau = 11.7\ \mu s$. In comparison to the sound speed in Aluminium, this duration is sufficient for an elastic wave to travel back and forth inside the sphere for $\approx$20 times.

For pure Aluminium, the yield stress $\sigma_{\text{Y}} \approx 9$ MPa leads to an elastic-plastic transition at a strain of $\sigma_{\text{Y}}/Y \approx 1.30 \cdot 10^{-4}$. Note that this is already slightly smaller than the strain caused by the impact $s_{\max}/2R \approx 1.33 \cdot 10^{-4}$. This comparison suggests that the elastic limit could be easily surpassed in most impacts we are dealing with. In another word, energy dissipation has to be considered in real life applications.

One convenient approach to characterize the energy dissipation is to measure the coefficient of restitution (COR), the ratio between relative rebound and impact velocity of two colliding particles. This definition was introduced by Newton in his famous book 'The mathematical principles of natural philosophy' [Newton, 1687]. There he described an inelastic impact as the following:

> "... In bodies imperfectly elastic the velocity of the return is to be diminished together with the elastic force ... and makes the bodies to return one from the other with a relative velocity, which is in *a given ratio* to that relative velocity with which they met ... "

Using a device with a similar construction to the Newton's pendulum (Fig. 2.4), he performed impact experiments to measure the COR of various types of particles, and used the results to demonstrate the validity of the third law of motion:

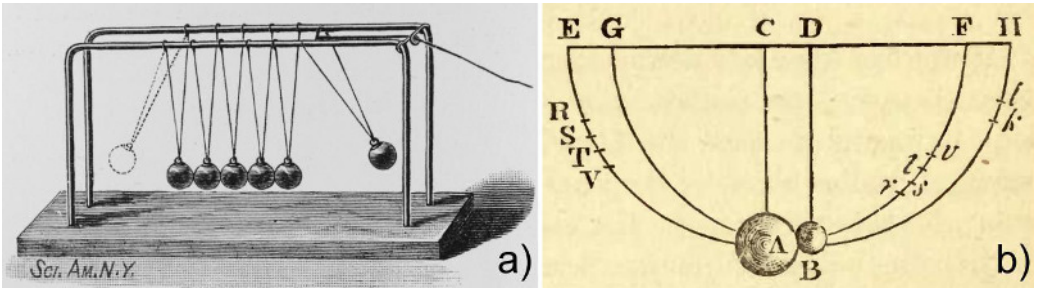

Figure 2.4: A snapshot of Newton's cradle (a) and a sketch of the experimental set-up used to measure the coefficient of restitution (COR) by I. Newton [Newton, 1687].

> " ... This I tried in balls of wool, made up tightly, and strongly compressed. For, first, by letting go the pendulous bodies, and measuring their reflexion, I determined the quantity of their elastic force; and then, according to this force, estimated the reflexions that ought to happen in other cases of congress. And with this computation other experiments made afterwards did accordingly agree; the balls always receding one from the other with a relative velocity, which was to the relative velocity with which they met as about 5 to 9. Balls of steel returned with almost the same velocity: those of cork with a velocity something less; but in balls of glass the proportion was as about 15 to 16. And thus the third Law, so far as it regards percussions and reflexions, is proved by a theory exactly agreeing with experience."

Those measurements are actually quite accurate in comparison to nowadays experiments with high speed photography. Taking the case of glass particles as an example, the error is within 0.03, demonstrating that the COR is indeed a good parameter to characterize binary impacts. However, this assumption that the COR is a material dependent property is known nowadays to be incorrect: More accurate and systematic experiments have demonstrated that the COR depends on the impact velocity, the size, shape, and even the preparation protocol of the particles [Stronge, 2004]. In principle, any factor listed in the above Fig. 2.1 may affect the COR to some extend. Concerning the modelling of granular dynamics, the dependency of COR on the impact velocity v_i is of great importance, since the other properties of agitated particles don't change as much as v_i.

To account for the energy dissipation, we have to speculate possible mechanisms and test their relative importance. Those mechanisms may include plastic or viscoelastic deformations, impact generated body and surface acoustic waves that dissipate into heat through internal frictions, crack formation, capillary interactions with the presence of wetting liquid, sliding frictional forces, etc.

One frequently adopted model for dry impacts is to assume plastic deformation above yielding. Figure 2.3 shows a sketch of the simplest case of a plastic force growing linearly with penetration depth s, in contrast to the Hertz's law $\propto s^{3/2}$ shown as the dash line. Such a combination leads to an offset compared with the unloading process, which is assumed to be elastic. The shaded region indicates the loss of energy through the loading-unloading process, owing to such a plastic deformation [Thornton, 1997].

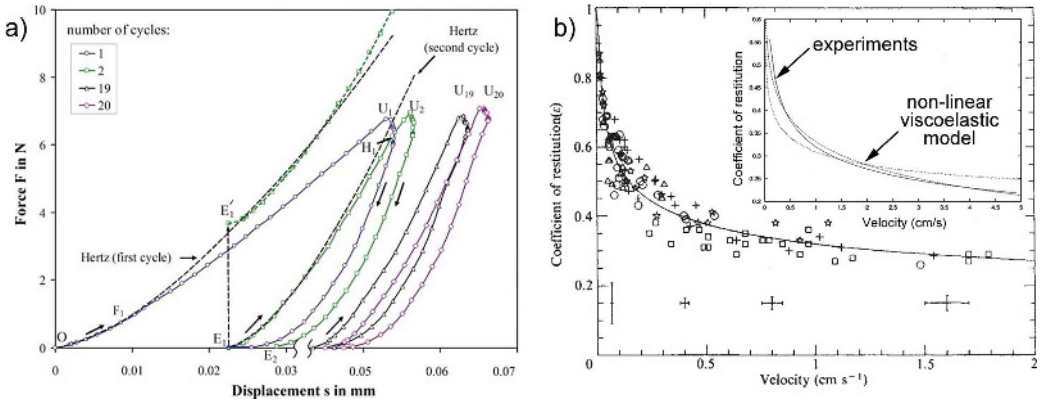

Figure 2.5: a) Force displacement curves of a granular particle under cyclic loading and unloading [Antonyuk *et al.*, 2010] b) Normal coefficient of restitution of ice particles as a function of the impact velocity [Bridges *et al.*, 1984]. Inset shows a comparison between the fitted curve from the data shown in the main panel and a model [Brilliantov *et al.*, 1996].

In the past decades, a substantial amount of work has been devoted to a proper description of the force law governing the impact, leading to a handful of different models. Based on the pathways taken towards energy dissipation, they can be classified into viscoelastic or perfectly plastic cases, linear or nonlinear cases, and combinations in between. For more detailed information of various models, the reader may refer to a recent review [Antonyuk *et al.*, 2010].

As indicated in Fig. 2.3, plastic deformations are not fully recoverable. As a consequence, permanent deformations of the particles arise during each impact, which immediately lead to the question of how reproducible the COR obtained is. Indeed, the amount of energy dissipated has been found to depend on the runs of experiments, or history of the particle under investigations. The force-displacement curves of a spherical particle under cyclic loading-unloading shown in Fig. 2.5 (a) demonstrate such a feature: Deviation from elastic deformation occurs for each loading period, leading to a hysteresis loop that characterizes the energy dissipation associated with the loading-unloading cycle. The loop shifts to higher s value with the cyclic number and with a reduced loop area, indicating that the particles become more and more elastic upon impacts. Despite of the shift with the number of impacts, the area within the loop, i.e. energy dissipated, tends to saturate to a certain value, suggesting that reproducible COR can still be obtained after sufficient number of initial impacts for plastically deforming particles.

Beside plastic deformations, models assuming viscoelastic deformations consider the dissipation of energy through effective viscous damping during impact, which will recover completely after rebound. Therefore no permanent deformation is allowed. It is claimed that such kind of modelling has a better consistency with the assumption of spherical particles in comparison to the plastic model [Brilliantov & Pöschel, 2004]. More specifically, in addition to elastic force proposed by Hertz, such type of models consider a viscous term that determines the energy dissipation:

$$F_v = \frac{3}{2} A k \sqrt{s} \dot{s}, \tag{2.5}$$

where s is the penetration depth and k is the elastic constant (see Eq. 2.1).

$$A = \frac{(3\eta_2 - \eta_1)^2}{3(3\eta_2 + 2\eta 1)} \cdot \frac{(1-\nu^2)(1-2\nu)}{Y\nu^2} \tag{2.6}$$

is a dissipative factor arising from material properties [Brilliantov & Pöschel, 2004; Brilliantov *et al.*, 1996], where η_1 and η_2 are viscous coefficient from the dissipative stress tensor.

Taking F_{el} and F_{v} as the only forces acting on the sphere, one can write the equation of motion and derive the coefficient of restitution for a normal impact [Brilliantov & Pöschel, 2004]:

$$e_{\mathrm{n}} = 1 - C_1 A\kappa^{2/5} v_{\mathrm{i}}^{1/5} + C_2 A^2 \kappa^{4/5} v_{\mathrm{i}}^{2/5} \mp \ldots, \tag{2.7}$$

where $\kappa = k/m_{\mathrm{eff}}$ with m_{eff} the effective mass of the particle, and C_1, C_2, ... are pure numbers. Taking a first order approximation, it predicts a decay of the COR with v_{i}. This is reasonable considering the scaling of the damping term with v_{i}: A larger initial velocity leads to a larger energy dissipation from viscosity, i.e. a smaller COR. Such a model has been successfully used to explain the v_{i} dependence of the COR for ice particles, in order to shed light on the formation of the Saturn's rings from a 'microscopic' perspective, as shown in Fig. 2.5 (b) [Bridges *et al.*, 1984; Brilliantov *et al.*, 1996].

In a more recent work [Weir & Tallon, 2005], the energy loss due to elastic wave generation is also found to play an important role in determining the COR. Within such type of energy loss, roughly 67% turned into the surface acoustic (Rayleigh) waves, 7% into pressure (P) waves and 26% into shear (S) waves. Moreover, a dimensionless number, v_{i}/c with c the speed of sound, is argued to be a key parameter determining such types of energy loss.

To summarize: Despite of the advances over past centuries, impacts between particles, even without considering the influence from the environment, are still not completely understood. A proper classification of the associated energy dissipation mechanisms, and a search for the essential parameters dominating the process still have a long way to go. Nevertheless, motivated by the vast number of applications in various industries, as described in Chap. 1, a consideration of the humid environment is essential and has been a topic of interest over the past decades. Thus we focus on the impacts of wet particles in the following section.

2.2 Wet impact

As the experience of playing basketball in the rain tells, wet impacts cost more energy than the dry ones, owing to the additional energy taken from the wetting liquid covering the ground. A closer look at this process, shown in Fig. 2.6, reveals rich dynamical behaviour of the wetting liquid during the impact, such as the formation of liquid bridges, surface waves, cavitation, singularity upon the rupture of liquid bridges [Eggers, 1997], as well as satellite droplets formation. Those droplets may bounce or coalesce partially with the liquid film, leading to a cascade of daughter droplets [Thoroddsen & Takehara, 2000; Thoroddsen, 2006]. First reported by Rayleigh [1899], the dynamics of the bouncing droplets can be attributed to the interplay between the time scale for the impact

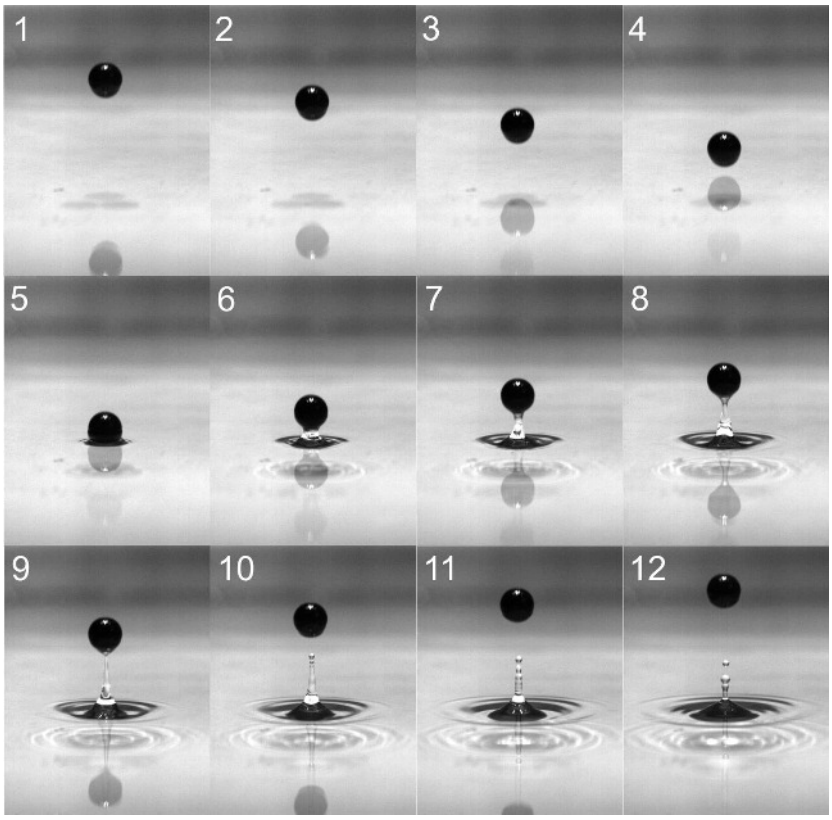

Figure 2.6: A series of snapshots showing a wet spherical glass bead bouncing on a glass plate covered with a 1 mm thick water film. [R4: Gollwitzer *et al.*, 2012]

and that for the air to flow out of the gap, leading to the possibility to avoid coalescence completely by introducing oscillations to the bulk liquid [Couder *et al.*, 2005].

Since the energy required for such rich dynamics of the droplets arises from the kinetic energy of the bouncing particle, it is counted as the energy loss that influences the COR. Moreover, direct inspections indicate that the influence from surface tension could also play a role, owing to the formation and rupture of liquid bridges. No need to mention the viscous effect, which can be extremely large as the liquid film is compressed during the impact. According to the lubrication theory, the viscous drag force diverges as the liquid film is sufficiently thin. Depending on the time scale of impact and that for the liquid to be squeezed out, recent investigations predict that glass transition of the liquid has to be considered in modelling the impact of wet particles [Donahue *et al.*, 2010*b*, 2012].

Before go to the details of various energy dissipation mechanisms, it is helpful to have an overview of the main components and a characterization of their relative importance. As shown in Fig. 2.7, inertia, surface tension and viscosity are considered to be the main energy dissipation sources. Depending on the liquid and particle properties, one or another factor will dominate. In order to judge the relative importance of the three factors, capillary number $\mathrm{Ca} \equiv \mu v/\sigma$, Reynolds number $\mathrm{Re} \equiv \rho_\mathrm{l} v R/\mu$, and bond number $\mathrm{Bo} \equiv \mathrm{Re} \cdot \mathrm{Ca} = \rho_\mathrm{l} v^2 R/\sigma$ are used, where ρ_l represents the density of the

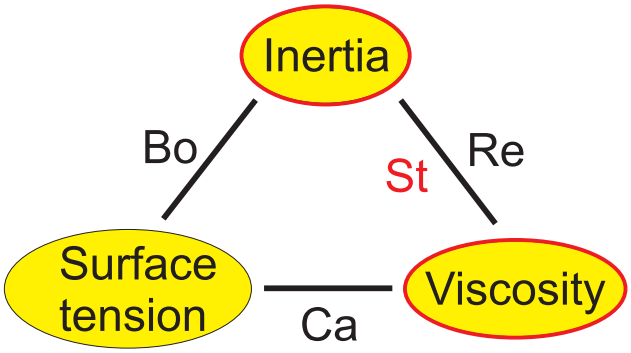

Figure 2.7: Possible liquid properties that influence the energy loss of a wet impact. The associated dimensionless numbers can be used to distinguish the dominating factors.

liquid. On the limit of viscosity dominating, the elastohydrodynamic theory developed by Davis *et al.* [1986] have been successfully employed to describe the COR [Barnocky & Davis, 1988; Davis *et al.*, 2002; Donahue *et al.*, 2010*a*] for normal as well as oblique impacts. It considers the coupling between the elastic deformation of spheres and the hydrodynamics of the liquid film in the low Reynolds number (Re) regime where lubrication theory applies. It turns out that the impact dynamics can be characterized with the dimensionless Stokes number that measures the inertia of the particles with respect to the viscous force:

$$\mathrm{St} \equiv \frac{mv}{6\pi\mu R^2} = \frac{2\rho_\mathrm{p} R v}{9\mu}, \tag{2.8}$$

where m and ρ_p represent the mass and density of the sphere.

In most daily life experiences or industrial applications, such as the one shown in Fig. 2.6, the precondition for the elastohydrodynamic theory is violated. This is due to the strong inertia effect, as judged by the relatively high Re. Therefore, it is essential to figure out the important factors, and search for additional dimensionless numbers to be considered, and eventually discuss the scalings of the COR with those parameters. In short, the central task is to have a simplified model that is capable of capturing the essential physical mechanisms, and adaptable to large scale computer simulations. As a first step toward such a goal, we analyse the three possible factors shown in Fig. 2.7 in the following subsections.

2.2.1 Influence from surface tension

Due to surface tension, a liquid surface has the tendency to minimize its area. For example, emulsion droplets will have a spherical shape. For a more complicated geometry such as at the pore level of a porous media, or between grains in a granular medium, a determination of the shape of the embedded liquid is not so straightforward. Taking the simplest geometry of a gap between two equally sized spheres as a starting point, the liquid bridge formed there can be approximated to have a toroidal shape, which gives rise to two curvatures: The radius of curvature of the bridge profile in the meridional plane r_1 and the neck radius r_2 (see the inset of Fig. 2.8 for a sketch).

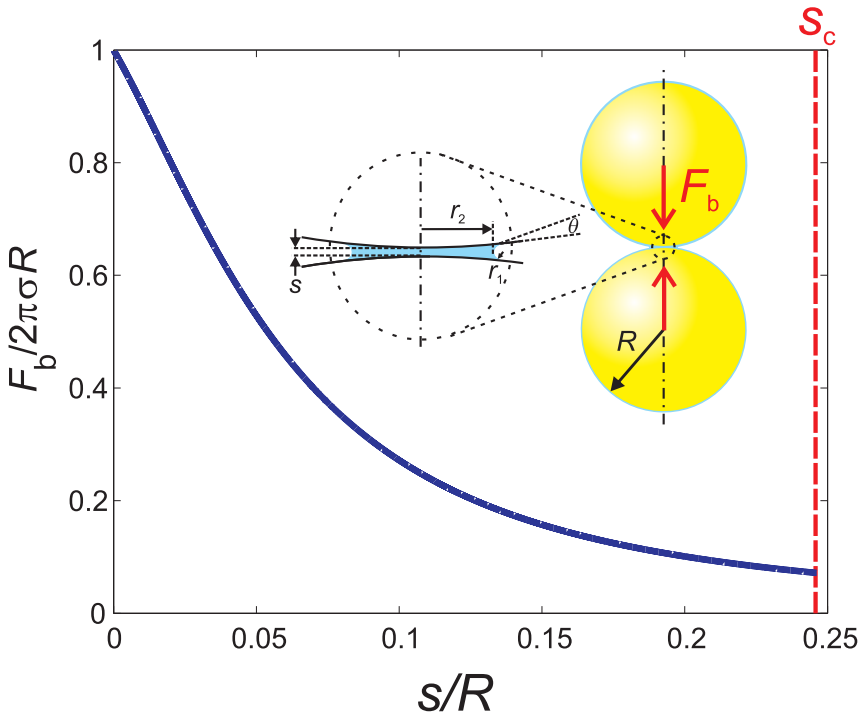

Figure 2.8: Capillary force induced by the liquid bridge formed between two spheres, as sketched in the inset, as a function of the separation distance, see text for details.

Hence, the pressure difference across the air-liquid interface, i.e. the Laplace pressure, can be estimated with the Young-Laplace equation,

$$\Delta p = \sigma \left(\frac{1}{r_1} + \frac{1}{r_2} \right). \tag{2.9}$$

Further assuming that the cohesive force is determined by the curvatures at the neck, and ignoring the influence from gravity, i.e. considering the size of bridges smaller than the capillary length $l_c = \sqrt{\sigma/\rho_l g}$ with g the gravitational acceleration, the capillary force between two spherical particles can be estimated with

$$F_b = 2\pi r_2 \sigma - \pi r_2^2 \Delta p, \tag{2.10}$$

where the first term corresponds to the line tension acting on the perimeter of the neck, and second term, typically dominating, arises from the pressure difference on the cross section of the neck. Such assumptions can be extended to liquid bridges between various shaped surfaces, such as sphere-plane, plane-cone, or cone-cone surfaces (see e.g. Butt & Kappl [2009] for a recent review).

On the limit of bridge volume $V_b \to 0$, i.e. $r_1 \ll r_2 \ll R$, and for the case of close contact $s = 0$, Eq. 2.10 can be further simplified [Herminghaus, 2005] into [1]

[1] For such a limiting case, the second term in Eq. 2.10 dominates, and the Pythagorean theory $R^2 + (r_1 + r_2)^2 = (R + r_1)^2$ leads to the relation $r_2^2 \approx 2Rr_1$.

$$F_{\mathrm{b}} = 2\pi r_2 \sigma - \pi r_2^2 \Delta p \approx 2\pi R\sigma \cos\theta \tag{2.11}$$

with θ the contact angle. Note that the particle size is the only length scale left in this simplification, thus it provides a convenient estimation on the cohesive force.

As the distance between the spheres varies, a numerical solution for F_{b} as a function of s with fixed Δp shows a monotonic decay of F_{b} until the capillary bridge ruptures. This agrees well with experiments done on the quasi-static limit [Willett *et al.*, 2000]. Based on such an agreement, a close form relation was introduced to estimate the capillary force between two equal sized spheres

$$F_{\mathrm{b}} = \frac{2\pi\sigma R\cos\theta}{1 + 2.1 s_{\mathrm{r}} + 10.0 s_{\mathrm{r}}^2}, \tag{2.12}$$

where $s_{\mathrm{r}} \equiv \frac{s}{2} \cdot \sqrt{R/V_{\mathrm{b}}}$ is the rescaled half-separation distance with V_{b} the volume of the capillary bridge. Additionally, the rescaled rupture distance can be estimated analytically with

$$s_{\mathrm{c}} = (1 + \frac{\theta}{2}) \cdot (\frac{V_{\mathrm{b}}^{\frac{1}{3}}}{R} + \frac{V_{\mathrm{b}}^{\frac{2}{3}}}{10R^2}). \tag{2.13}$$

It suggests that, as a first order approximation, one can estimate the rupture distance simply from the cubic root of the bridge volume $V_{\mathrm{b}}^{\frac{1}{3}}$ for the case of complete wetting.

Figure 2.8 presents an estimation of the capillary force, rescaled to its maximum value (Eq. 2.11), as a function of the rescaled separation distance s/R. It corresponds to the case of a water bridge between two equal sized glass spheres with a radius of 1 mm, and a liquid content $W = 1\%$. The liquid content is related to the bridge volume through $V_{\mathrm{b}} = \frac{8\pi W}{3\phi N} \cdot R^3$ with N the coordination number and ϕ the packing fraction. The capillary force decays monotonically with the separation distance until the rescaled rupture distance s_{c} is reached.

Careful comparisons to the experiments [Willett *et al.*, 2000] reveal that the error for such an estimation grows with V_{b}. For a rescaled volume $V_{\mathrm{b}}^{\frac{1}{3}}/R \approx 0.001$, or correspondingly a half opening angle of $\beta \approx 10°$ (see Fig. 2.9 a for a definition), the above estimation is accurate within 4%. A more accurate analytical estimation for $V_{\mathrm{b}}^{\frac{1}{3}}/R$ up to 0.1, covering almost the whole pendular state, is also provided in the same reference as an appendix.

In Eq. 2.10, the two dominating curvatures, r_1 and r_2, are not independent from each other and also not easily accessible in experiments. Thus, we try to represent the Laplace pressure with respect to the separation distance s and the half opening angle β of the liquid bridge (see the sketch in Fig. 2.9 a). Based on geometry, we can write Δp as a function of β and s with $r_1 = \frac{R(1-\cos\beta)+s/2}{\cos(\beta+\theta)}$, and $r_2 = R\sin\beta - r_1(1 - \sin(\theta+\beta))$. As the example with $s = 0.02R$ shown in Fig. 2.9 demonstrates, there exists a critical $\beta_{\mathrm{c}} \approx 0.055$ at which Δp exhibits a valley, suggesting a minimum of the Laplace pressure. Because of the pressure difference in various liquid bridges, liquid transport is expected to occur through either the thin film covering the particles or through the vapor phase. For $\beta < \beta_{\mathrm{c}}$, liquid transports from small to large liquid bridges since larger ones have relatively small pressure in the liquid phase. On the contrary, liquid transports from large to small bridges for the case of $\beta > \beta_{\mathrm{c}}$. Thus, the

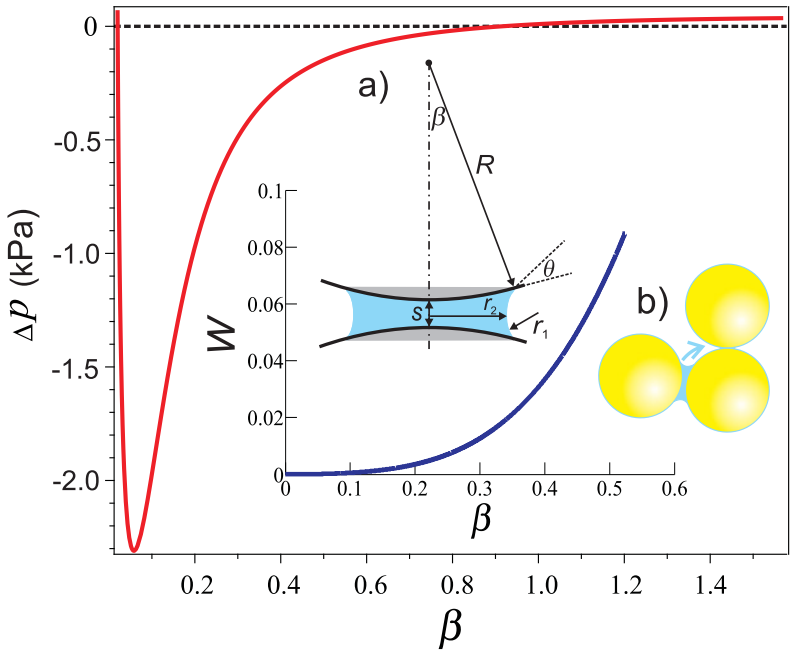

[h]

Figure 2.9: Laplace pressure of capillary bridges with the half opening angle β of the liquid bridge. Inset figure shows the liquid content W as a function of β. Sketch a) illustrates liquid transport from one capillary bridge to the other. Sketch b) shows a capillary bridge with definitions of various variables (see text for details).

critical angle β_c acts as an attractor for equilibration of the volume of liquid bridges (see Fig. 2.9 b for a sketch). Such kind of equilibration is indeed found in computer tomography measurements of wet glass beads after shaking [Scheel *et al.*, 2008]. Note that the positive Δp at $\beta > 0.9$, suggesting the sign change of the curvature of the liquid bridge, is not realistic because merging of liquid bridges starts already at $\beta = \pi/6$ for the ideal case of a triangular configuration.

Experimentally, the half opening angle is not a well accessible parameter. Since the change of β arises predominately from change of bridge volume, we can use bridge volume V_b, or liquid content W associated as control parameters. Simplified estimation of $V_b = \pi s R^2 \sin^2 \beta$ considering the bridge as a cylinders is typically used in literature (see e.g. Willett *et al.* [2000]). Taking one step further, we remove the volume from the spherical caps (regions shielded with gray in Fig. 2.9 a) and estimate the bridge volume with

$$V_b = \pi R^2 \sin^2 \beta (s + 2h) - \frac{2}{3}\pi h^2 (3R - h), \tag{2.14}$$

with the height of the spherical cap $h = R(1 - \cos \beta)$. According to such an estimation (shown in the inset of Fig. 2.9), the valley of Laplace pressure occurs at relatively small liquid content, $W \approx 0.15\%$. Although the actual flow of wetting liquid relies on the local vapor pressure, which related to the local curvature by the Kelvin equation, the qualitative trend for the capillary bridges to exchange their volumes toward an equilibrium state should be justified.

From the capillary force-distance relation shown in Fig. 2.8, we integrate for the rupture energy required for the breaking of a capillary bridge. Ignoring the higher order term in Eq. 2.13 and assuming relatively small V_b, we have

$$E_{cb} \approx 5.2\sigma\sqrt{V_b R}\cos\theta. \tag{2.15}$$

Note that it is independent on the velocity of impact and thus acts as an offset to the energy dissipation associated with the wet impact.

2.2.2 Influence from viscosity

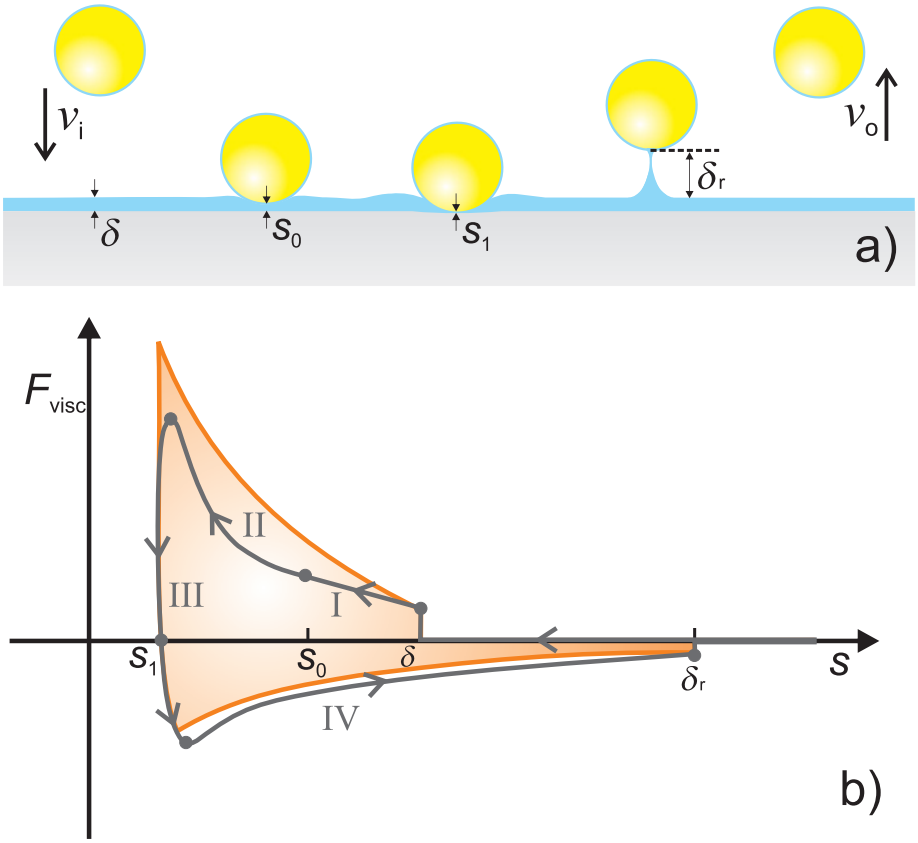

Figure 2.10: a) A sketch of a wet impact, where v_i and v_o correspond to the impact and rebound velocities, δ and δ_r are the liquid film thickness and the rupture distance, s_0 is the distance between the particle and the plate as lubrication theory starts to apply, and s_1 is the shortest distance.

As illustrated in Fig. 2.10, the influence from viscous force differs at various stages of the impact. In stage I, from separation distance $s = \delta$ to the critical distance for the lubrication theory to be valid $s = s_0$, we assume Stokes's law for the sake of simplicity,

$$F_{visc} = 6\pi\mu R\dot{s}, \tag{2.16}$$

with $\dot{s}$ the velocity of the particle at impact. Note that this is a crude assumption since the coalescence between the liquid film covering the particle and that covering the plate may occur at $s < \delta$, owing to the air film in between. As described above, it's also possible that those liquid surfaces never touch, provided that the time scale of bouncing is shorter than that for the air to escape from the gap. Thus the assumption taken here is expected to be an overestimation. Nevertheless, for liquid with low surface energy that favours coalescence, such an assumption is appropriate.

Stage II starts from $s = s_0$ to the shortest distance between the particle and the plate s_1. The starting position s_0 and the corresponding velocity v_0 are used in former literature as free parameters [Davis *et al.*, 1986]. Sometimes s_0 is also chosen as a fixed fraction of the film thickness $2\delta/3$ [Barnocky & Davis, 1988; Davis *et al.*, 2002], and consequently the velocity v_0 can be derived assuming Eq. 2.16 to be the only dissipative force. In this region, the lubrication theory predicts an enhanced viscous damping force as the two surfaces are close enough to each other

$$F_{\text{visc}} = 6\pi\mu R\dot{s} \cdot \lambda. \tag{2.17}$$

Various empirical forms of the factor λ had been used in literature [Mazzone *et al.*, 1987], such as R/s, $1 + 2R/s$ or $(1 - \cos(2\beta))/2$. In comparison to the Stokes' law (Eq. 2.16), the additional factor states that the viscous damping force diverges as the two surfaces are infinitely close to each other. Thus the viscous force reaches its maximum at $s = s_1$. For the sake of simplicity, we take $\lambda = R/s$ for the calculations below. In reality, the two surfaces cannot be infinitely close to each other due to the surface roughness, which endows the other integration limit for an estimation of the energy loss in this region.

In stage III, F_{visc} decays until a negative peak value is reached, where the velocity and the viscous force change the sign. Suppose the change of s in this region is small, the valley corresponds to the largest rebound velocity during the impact.

In stage IV, the lubrication theory is still considered to be valid, thus the same force law as in Eq. 2.17 applies. Additionally, F_{b} starts to play a role in this region since a capillary bridge is developing.

With the viscous force-distance relations described above, one could proceed to estimate the total viscous damping during the whole impact. The four stages described above are illustrated in Fig. 2.10 as the closed solid curve, the area of which corresponds to the energy dissipated. For relatively thin films, the factor R/δ is sufficiently large so that the viscous damping from stage I much less than II, thus we can ignore stage I and consider stage II to start at $s = \delta$. Moreover, for relatively hard impacts, the velocity turnover takes place in a rather narrow region roughly two orders of magnitude smaller than the film thickness [Marston *et al.*, 2010], thus we can skip the energy dissipation in region III. Based on the above assumptions, the solid curve could be further simplified into the orange one considering only the lubrication forces. Consequently, the energy dissipation during the whole impact from viscosity can be estimated with the integrations of Eq. 2.17 for both approaching and rebounding phases,

$$\Delta E_{\text{visc}} = 6\pi\mu R^2 v_{\text{i}} \left(\ln \frac{\delta}{\epsilon} + e_{\text{n}} \ln \frac{\delta_{\text{r}}}{\epsilon} \right), \tag{2.18}$$

with the roughness of the sphere ϵ taken as the integration limit. Note that constant velocities are assumed through the impact and rebound regions. For relatively hard im-

pact, e.g., the glass beads used here, this assumption is appropriate, since the measurements by Marston *et al.* [2010] show that velocity change takes place predominately in a rather narrow region, roughly two orders of magnitude smaller than the film thickness .

2.2.3 Influence from inertia

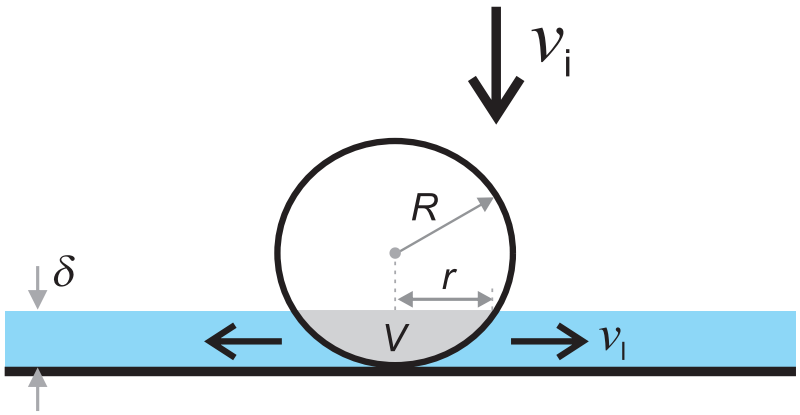

Figure 2.11: A simplified view on the momentum transfer from the particle to the liquid being pushed aside, based on which a model (see text for details) is derived to account for the energy dissipation from the inertia effect.

As described at the beginning of this section, hydrodynamics of the liquid film induced by the bouncing sphere, particularly in association with the air film trapped in between, can be complex. As a starting point, we skip all those complex influences and discuss only the energy loss due to the repelled volume from the sphere penetrating into the liquid film (sketched in Fig. 2.11). In such a case, the time scale required for the sphere to travel from the surface of liquid film to the glass plate can be estimated with $t = \delta/v_\mathrm{i}$, assuming v_i to be constant during the penetration period. In the quasi-static limit, the volume of the liquid being pushed aside equals to the spherical cap volume $V = \pi\delta(3r^2 + \delta^2)/6$. Here it is assumed that the film thickness is constant, and $r = \sqrt{\delta(2R - \delta)}$ is the radius of the base of the spherical cap, which can be treated as the length scale for the squeezed liquid to travel. Combining the length and time scales gives rise to a velocity $v_\mathrm{l} = l/t$, which could be approximately considered as the average velocity of the liquid being squeezed aside. Therefore, the kinetic energy taken by the liquid can be estimated with

$$\Delta E_\mathrm{int} = \frac{1}{2}\rho_\mathrm{l} V v_\mathrm{l}^2 = 3\tilde{\rho}\left(\tilde{\delta} - \frac{5}{3}\tilde{\delta}^2 + \frac{2}{3}\tilde{\delta}^3\right) E_\mathrm{i}, \tag{2.19}$$

where $\tilde{\delta} = \delta/2R$ and $\tilde{\rho} = \rho_\mathrm{l}/\rho_\mathrm{p}$ are defined as the dimensionless film thickness and liquid density.

Note that this part of energy dissipation scales linearly with the kinetic energy at impact E_i, different from the viscous and the capillary effects discussed above.

2.3 Scaling

Based on the above analysis on various energy dissipation mechanisms, we proceed in this section to estimate the COR for wet impacts. Based on the definition of the COR, we have

$$e_{\mathrm{n}} = \sqrt{1 - \Delta E_{\mathrm{diss}}/E_{\mathrm{i}}} \tag{2.20}$$

with E_{diss} the total energy dissipation. Note that it is not the energy dissipated into heat, but the energy loss of the particle during the impact here. Such a total energy dissipation could be attributed to the inelastic deformation of the particles as in the case of dry impact, as well as the inertia, viscous and capillary forces arising from the presence of the wetting liquid. Suppose the effect from the inelastic deformation of the solid phase is independent from the other mechanisms associated with the wetting liquid, we have $\Delta E_{\mathrm{diss}} = \Delta E_{\mathrm{dry}} + \Delta E_{\mathrm{wet}}$. Further assuming that the energy dissipation from such inelastic deformation is identical to the impact without the wetting liquid, i.e., $e_{\mathrm{dry}} = \sqrt{1 - \Delta E_{\mathrm{dry}}/E_{\mathrm{i}}}$, and taking into account the three possible mechanisms discussed above, we have

$$e_{\mathrm{n}} = \sqrt{e_{\mathrm{dry}}^2 - \frac{\Delta E_{\mathrm{int}}}{E_{\mathrm{i}}} - \frac{\Delta E_{\mathrm{visc}}}{E_{\mathrm{i}}} - \frac{\Delta E_{\mathrm{cb}}}{E_{\mathrm{i}}}}. \tag{2.21}$$

Before start to discuss the analytical solution of e_{n}, we first analyze the scaling of the wet COR with the impact velocity. Based on Equations (2.15), (2.18) and (2.19), we find that the inertia term leads to a constant offset to the COR with respect to e_{dry}, the viscous effect leads to a term $\propto 1/v_{\mathrm{i}}$, and the influence from capillary forces gives rise to a term $\propto 1/v_{\mathrm{i}}^2$. Thus, Eq. 2.21 predicts a monotonic growth of e_{n} with v_{i}. Moreover, it also predicts that no real COR value for v_{i} below a critical value v_{c}, since a negative value in the square root is not realistic. Experimentally, v_{c} corresponds to the case of no rebound, i.e. the kinetic energy completely damped in the one impact. This is in contrast to the case of dry impact (Eq. 2.7), where the COR decays as impact velocity grows. A comparison between the predicted dry and wet impacts is illustrated in the upper panel of Fig. 2.12. Finally, Eq. 2.21 suggests that the wet COR saturates as $v_{\mathrm{i}} \to \infty$, and this limiting value e_{inf} is smaller than the corresponding dry COR, owing to the inertia effect. Analytically, it can be estimated with

$$e_{\mathrm{inf}} = \sqrt{e_{\mathrm{dry}}^2 - 3\tilde{\rho}\left(\tilde{\delta} - \frac{5}{3}\tilde{\delta}^2 + \frac{2}{3}\tilde{\delta}^3\right)}. \tag{2.22}$$

The above relation suggests the important role that two dimensionless numbers, $\tilde{\delta}$ and $\tilde{\rho}$, play: Relatively larger density or thicker liquid film with respect to the particle size leads to more energy taken by the inertia effect, and hence smaller e_{inf}.

Accordingly, we may rewrite Eq. 2.21 in terms of impact velocity v_{i} as

$$e_{\mathrm{n}} = \sqrt{e_{\mathrm{inf}}^2 - \frac{\alpha}{v_{\mathrm{i}}} - \frac{\beta}{v_{\mathrm{i}}^2}}, \tag{2.23}$$

where factors α and β arise from the influence from viscous and capillary forces.

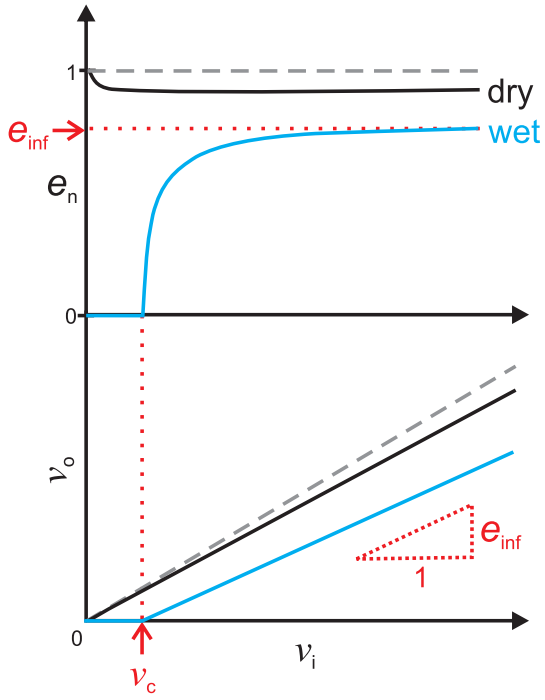

Figure 2.12: Normal coefficient of restitution (upper panel) and the rebound velocity v_r (lower panel) as a function of the impact velocity v_i for both dry and wet impacts. e_{inf} and v_c correspond to the wet COR at infinitely large v_i and the threshold impact velocity below which no rebound occurs.

The lower panel of Fig. 2.12 shows that the growth of e_n with v_i can be characterized, in the plane of v_r and v_i, with a linear fit. The critical impact velocity v_c and the saturated coefficient of restitution e_{inf}, correspond to the offset and the slope of the fit. Such a simplification is based on a recent experimental investigation [R4: Gollwitzer *et al.*, 2012]. In the following part of this subsection, we will discuss in detail how such a linear fit is justified, and the dominating factors determining v_c.

As the experimental results show in Fig. 2.13 (a), the COR for wet impacts grows monotonically with v_i, which is suggested qualitatively by Eq. 2.21. Moreover, the growth rate of e_n relies on the viscosity of the wetting liquid μ and the liquid film thickness δ, which manifest the influence from E_{visc}. Plotting in the plane of rebound v_r as a function of impact velocity v_i, it is found that the data fall into lines with various slopes and offsets. From v_c, one could estimate the critical energy scale $E_c = mv_c^2/2$ for a rebound to occur, where m is the mass of the sphere. Note that rebound here is not defined as the turnover of the particle velocity, but as the detachment of the sphere from the wetting liquid, i.e. the rupture of the capillary bridge. The demonstrated possibility to use only two parameters E_c and e_{inf} to describe the impact velocity dependency of the wet COR provides a convenient way to model particle-particle interactions. However, such an approach has to be justified from the perspective of the above prediction (Eq. 2.23).

Assuming the linear fit is a first order approximation of Eq. 2.23, we can ignore higher order term of $1/v_i$, i.e., the influence from the capillary force E_{cb}/E_i, and expand

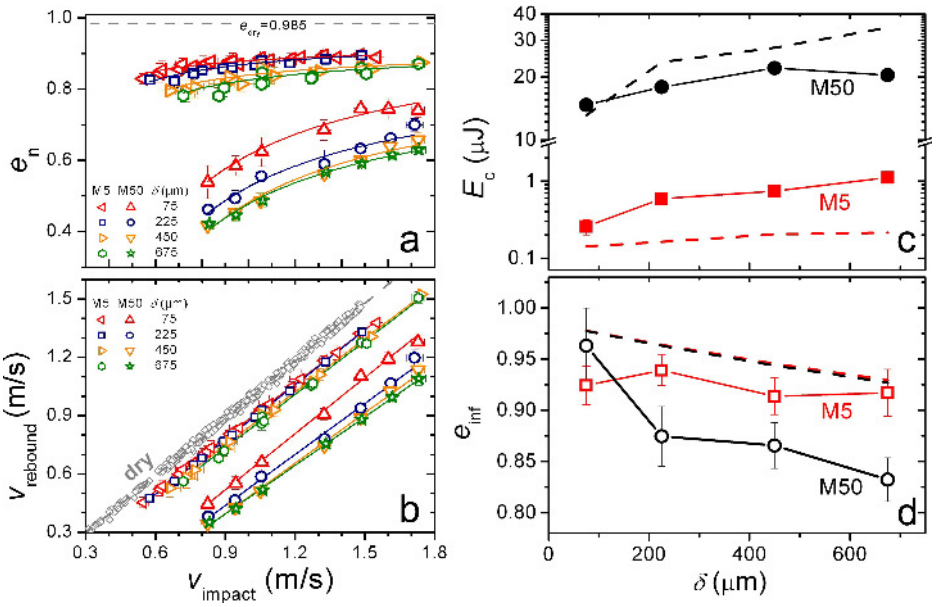

Figure 2.13: Normal coefficient of restitution (a) and the rebound velocity v_o (b) as a function of the impact velocity v_i obtained experimentally from various liquid film thickness δ and two different liquids. The threshold kinetic energy for a wet particle to rebound E_c and the limiting wet COR e_{inf}, both obtained through linear fits of the v_o vs v_i data, as a function of the liquid film thickness. Dash lines are predictions from the model described in the text.

e_n into Taylor series in the limit of $v_i \to \infty$,

$$e_n = e_{inf}\left(1 + \frac{\alpha'}{2v_i} - \frac{\beta'}{8v_i^2} + \ldots\right) \approx e_{inf}\left(1 + \frac{\alpha'}{2v_i}\right), \tag{2.24}$$

where $\alpha' \equiv \alpha/e_{inf}^2$ with

$$\alpha = \frac{-9\mu(\ln\frac{\delta}{\epsilon} + \ln\frac{\delta_r}{\epsilon})}{\rho_p R} \tag{2.25}$$

arises from the viscous damping term. Because the factor δ/ϵ for the spheres used in the experiments is large owing to the smooth surface, the influence from the factor e_n in Eq. 2.18 is presumably small. For the sake of simplicity, it is ignored in the estimation of α. From a comparison of the first order approximation of Eq. 2.24 to the linear fits used in characterizing the experimental data, we can estimate the critical energy scale,

$$E_c = \left(\frac{\frac{3}{2}\mu(\ln\frac{\delta}{\epsilon} + \ln\frac{\delta_r}{\epsilon})}{e_{inf}^2}\right)^2 \frac{6\pi R}{\rho_p}, \tag{2.26}$$

which relies mainly on the viscous damping. At first glance, it might be surprising to see that the rupture energy of the liquid bridges does not play a role since the snapshots shown in Fig. 2.6 demonstrate such a rupture event. However, an estimation of the rupture energy yields $E_{cb} \approx 0.7\mu J$, which is far less than the kinetic energy of the impacting particles. Note that the various scaling of $E_{int} \propto R^3$ and $E_{cb} \propto \sqrt{R}$, the rupture energy will take effect as the particle size and impact velocity are small enough.

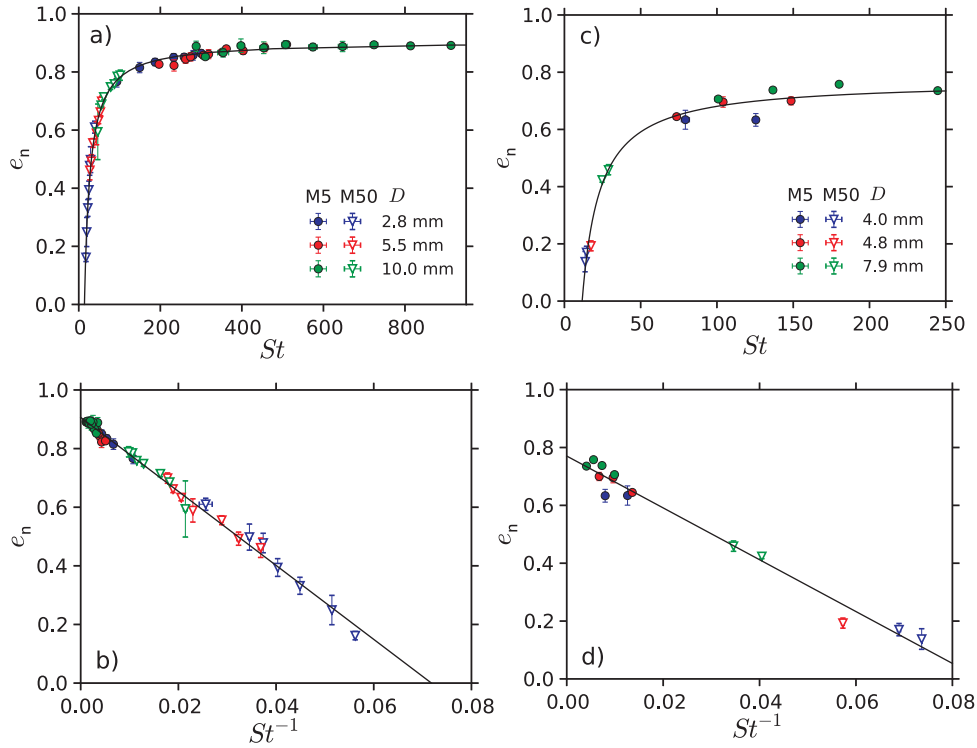

Figure 2.14: Scaling of the wet COR with the Stokes number with fixed dimensionless film thickness $\tilde{\delta} \approx 0.04$ for both glass (a) and PE (b) particles. Figures (a) and (b) adapted from [R4: Gollwitzer *et al.*, 2012] and [R2: Mueller *et al.*, 2013] correspondingly.

Based on the above linear approximation, a comparison of the predicted E_c and e_{inf} to experiments are shown in Fig. 2.13 (c) and (d). Qualitatively, the trend of E_c and e_{inf} are well predicted by the model. Quantitatively, the model gives overestimated e_{inf} values in comparison to the experiments. It strongly suggests that a refined model with a proper consideration of the hydrodynamics is needed, because Eq. 2.22 shows that e_{inf} relies on the energy dissipation due to the inertia of the liquid. For the comparison of E_c, a better agreement is found for more viscous M50 wetting case than the order of magnitude less viscous M5 case, suggesting the prediction of E_{visc} is more appropriate for more viscous wetting liquid. Considering the simplification applied to the model, such comparison results provide evidence for the approach used here. Further investigations with more detailed description of the inertia part of the energy dissipation will presumably yield better predictions of the fit parameters, thus facilitate a better analytical prediction of the wet COR.

Moreover, after inserting the factor α' into the above Eq. 2.24, one finds that the approximated e_n can be written in terms of the Stokes number defined above in Eq. 2.8,

$$e_n = e_{inf}\left(1 - \frac{\ln\frac{\delta}{\epsilon} + \ln\frac{\delta_r}{\epsilon}}{e_{inf}^2} \cdot \frac{1}{St}\right). \tag{2.27}$$

It demonstrates that the dependency of e_n on the density and size of particles, viscos-

ity of the wetting liquid, and the impact velocity can be replaced by the dimensionless Stokes number that characterizes the inertia of the particle over the viscous force of the wetting liquid. Rescaling of the wet COR with St has been discussed by several authors (see e.g. Davis *et al.* [1986, 2002]) for the case of highly viscous liquids, i.e. low Re. For the case of Reynolds number $\mathrm{Re} \gg 1$ focused here, inertia effect associated with e_{inf} has to be considered in addition, which suggests scaling with the two additional dimensionless numbers: relative density $\tilde{\rho}$ and dimensionless film thickness $\tilde{\delta}$ (see Eq. 2.22).

Experimentally, wet COR for various liquid and particle properties have been measured systematically for glass and polyethelyne (PE) particles. As shown in Fig. 2.14, the collapse of data demonstrate that the scaling of e_{n} with St is justified provided that $\tilde{\delta}$ is fixed [R4: Gollwitzer *et al.*, 2012; R2: Mueller *et al.*, 2013]. Further experiments on various density ratio $\tilde{\rho}$ are being carried out in order to refine the theory described here for wet COR and figure out how the COR scales with the two additional parameters: $\tilde{\rho}$ and $\tilde{\delta}$.

2.4 Wetting

While characterizing the capillary force and the associated energy scale between spherical particles, one typically assumes a constant contact angle θ, which is small for typical combinations of wetting liquids and particles used in the lab, such as water or silicone oil on glass. However, in real life applications, the contact angle, which arises from the balance of surface energy at the three phase contact line, will be influenced by a number of factors including surface roughness and chemical impurities of the substance [de Gennes, 1985]. As a consequence, the measured contact angle is typically within a certain range between the advancing θ_{adv} and receding θ_{rec} contact angles. Thus, experimentally measured values scatter and the exact contact angle is typically hard to predict. Moreover, the equilibrium condition (i.e. the Young condition) assumed in many literature is rarely achieved for agitated wet granular matter. Before the system relax to its equilibrium state, another event causing a morphological change of the liquid structure will most likely to occur, leading to a dynamic contact angle. For example, a perfectly wetting liquid evaporating on a perfectly smooth solid substance such as mica may lead to a finite contact angle [Elbaum & Lipson, 1994].

Moreover, contaminations in forms of small dirt particles inside the droplet are found to form rings along the rim of the droplet, i.e. the coffee stain effect [Deegan *et al.*, 1997]. Such a robust effect influences substantially the product quality in various industries, such as printing and coating. Due to the ubiquity of such a non-equilibrium process, the 'coffee stain effect' has been a topic of intensive investigations in the past decades, including a characterization of patterns formed by the dirt particles after drying [Deegan, 2000], various methods to reduce such an effect [Eral *et al.*, 2011; Yunker *et al.*, 2011], as well as possible applications on the self-organization of particles [Marín *et al.*, 2012]. For a recent review, the reader may refer to Bonn *et al.* [2009].

For agitated wet granular matter focused here, wetting and non-wetting play an important role as well. Liquid transport inside a wet pile of sand, due to the structure change or inhomogeneous distribution of the wetting liquid, will presumably lead to a distribution of the contact angle between θ_{adv} and θ_{rec}. Therefore, measuring the static contact angle by one set of experiments is not sufficient. Recently, an intjet

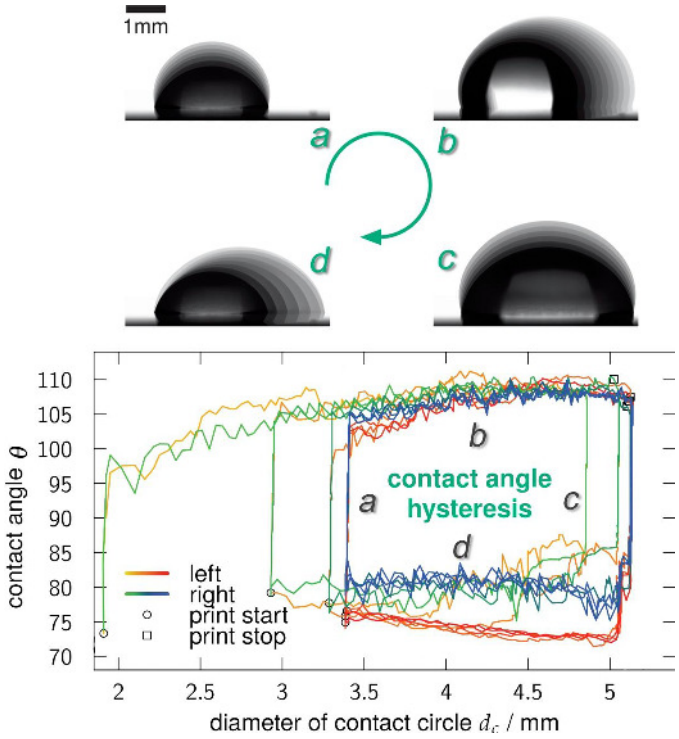

Figure 2.15: Contact angle hysteresis represented by a water droplet on a polytetrafluoroethylene (PTFE) surface. Upper panel shows overlaid snapshots of the droplets in the following 4 stages: a. increasing volume with pinned interface, b. advancing after de-pinning, c. decreasing volume with pinned interface, d. receding after de-pinning. The volume increase is controlled with an intjet printing setup [Völkel, 2014], and the volume decrease is caused by evaporation. Lower panel presents the contact angle for both sides of the droplet as a function of the mean diameter of the contact line. The color coding of the curves represents time evolution of the angles. Figure adapted from Völkel [2014].

printing device for the measurement the contact angle hysteresis has been built up [Völkel, 2014], which employs a intjet printer head to add liquid into the droplet in a well controlled and accurate manner. Thanks to the tiny size of its nozzles, such a device provides droplets with a size down to $\approx$ 33 pL.

Figure 2.15 shows the contact angle hysteresis of a water droplet on a polytetrafluoroethylene (PTFE) substance. It contains four phases: From the initial growth of the droplet while printing (a, b), to the following shrinking of the droplet during evaporation (c, d). As the contact line is pinned, the droplet may have any contact angle in between the limiting θ_{adv} and θ_{rec}. As de-pinning starts as the limiting contact angles are achieved. From the overlaid snapshots shown in the upper panel, it is obvious that such a process may not be homogeneous: De-pinning may occur at one edge of the rim, a manifestation of the surface inhomogeneity. In total, 6 runs of printing-evaporating cycles are performed. Printing starts initially on a small droplet of $\approx$1.8 mm, leading to a symmetrically growing contact angle, as shown in overlaid snapshot Fig. 2.15 (a). As θ_{adv} is achieved, contact line de-pins and the contact angle grows slightly as well. After a certain amount of water is printed, the shrinking of the droplet starts due to

evaporation. Contact angle reduces until θ_{rec} is reached. In stage d, the droplet shrinks at the receding angle $\approx \theta_{\text{rec}}$ until the given evaporating time is reached.

Continuous 6 experimental runs yield a similar behaviour. After 2 cycles, the sizes of the droplets in region a and c start to be fixed, demonstrating the reproducibility of the experiment. In region d, the contact angle from either side differs, which can be attributed to the surface inhomogeneity arising from the 'coffee stain effect'. Indeed, ring patterns are observed in the region of the evaporating droplet at the end of the experiment. This preliminary experiment indicates the existence of a 'limiting cycle' for the contact angle hysteresis, within which both advancing and receding contact angles could be determined accurately. Further experiments on how the contact angle depends on the experimental details such as the droplet printing rate, or the time for printing and evaporation will help to check the robustness of the measured contact angles.

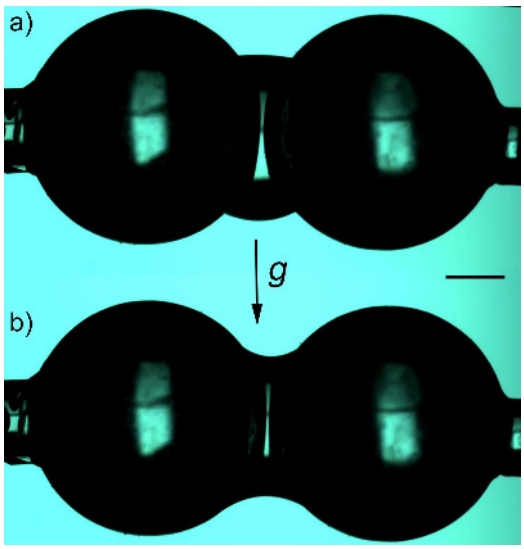

Figure 2.16: Snapshots showing the dynamics of a capillary bridge between two glass spheres with a diameter of 4 mm during advancing (a) and receding (b) stages. The scale bar corresponds to 1 mm.

Within the geometry of a liquid bridge between two equal-sized spheres, as shown in Fig. 2.16, the contact angle hysteresis will presumably be influenced by other factors such as gravity. Further experiments on such a geometry, aiming at finding the 'limiting cycle' for the measurements of θ_{adv} and θ_{rec} in such a geometry will be a topic of further investigations. From the snapshot shown here, one could clearly see the influence from pinning as well as gravity on the contact angle: During the printing period, advancing contact angle can be as large as 71° for the case of water wetting on glass. Such a large contact angle will presumably lead to a weakened cohesive force in such a period. Thus, the contact angle hysteresis can be an essential factor to be considered for the investigations of wet granular dynamics.

3

Collective behaviour

In Chapter 2, the dissipative nature of granular particle interactions, especially with wetting liquid mediated, is demonstrated. It is because of this nature that the collective behaviour of agitated granular particles is characterized as far from thermodynamic equilibrium. In such non-equilibrium systems, many counter-intuitive phenomena have been discovered, such as clustering of granular gases [Goldhirsch & Zanetti, 1993; Olafsen & Urbach, 1998] that is claimed to be associated with the formation of planetary rings [Spahn & Schmidt, 2006], high energy tail of the velocity distributions [Brey *et al.*, 1999; Brilliantov & Pöschel, 2004], shock wave propagation [Losert *et al.*, 1999; Bougie *et al.*, 2002; Huang *et al.*, 2006], heap formation, transport and associated migration of sand dunes in nature [Faraday, 1831; Bagnold, 1941; Clément *et al.*, 1992; Falcon *et al.*, 1999; Miao *et al.*, 2006], an analogue of Maxwell's Demon [Eggers, 1999; Reimann, 2002; Eshuis *et al.*, 2010], Reynolds dilatancy [Reynolds, 1885; Onoda & Liniger, 1990; Schröter *et al.*, 2007; Métayer *et al.*, 2011], size (Brazil nut effect) or density segregations [Rosato *et al.*, 1987; Hong *et al.*, 2001; Reis & Mullin, 2002; Burtally *et al.*, 2002; Breu *et al.*, 2003; Schnautz *et al.*, 2005; Schröter *et al.*, 2006], as well as localized excitations [Umbanhowar *et al.*, 1996]. In comparison to the states of matter in thermodynamic equilibrium, granular matter may also behave like a solid, a liquid or a gas [Jaeger *et al.*, 1996], depending on the balance between the energy injection and the dissipation. Thus, a straightforward question is: How well can we extend existing knowledge on equilibrium systems to such a non-equilibrium model system, and how well can such extensions shed light on our understanding of the omnipresent non-equilibrium systems in nature, from active particles such as bacteria colonies [Zhang *et al.*, 2010], or actin filaments [Schaller *et al.*, 2010] to animal groups [Buhl, 2006; Couzin *et al.*, 2005; Liu *et al.*, 2013].

To address these questions, collective behaviour of agitated wet granular matter, which can be treated as a non-equilibrium model system, will be discussed in this chapter. In Section 3.1, I will demonstrate with a 'quantum paste', i.e. granular particles wetted by liquid helium, that a few atomic layers of liquid coverage are sufficient to influence the rigidity of the sample. After a brief review on the dynamics of dry granular matter in Section 3.2, the collective behaviour of wet granular matter under vertical (Section 3.4) and horizontal (Section 3.3) agitations will be presented, including phase transitions, pattern formation and clustering. Finally in Section 3.5, recent progresses on the influence from shape on the ordering transitions of granular particles will be summarized in short.

3.1 How wet is wet?

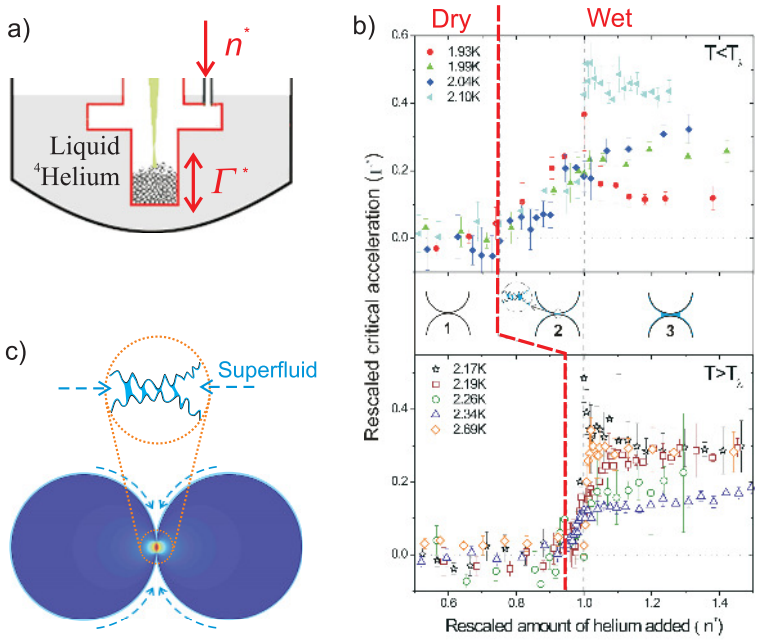

Figure 3.1: The liquid ^{4}Helium wetting experiment to probe the threshold between dry and wet granular matter. a) A sketch of the sample cell with the control and order parameters illustrated. Here the control parameter n^* is the rescaled amount of helium added, and the order parameter Γ^* is the rescaled critical acceleration for the granular sample to fluidize. b) The rigidity enhancement represented by Γ^*, as a function of n^* at temperature below (upper panel) and above (lower panel) the T_λ, the transition temperature between normal and superfluid helium. Various wetting regimes are sketched in the middle panel, where 1, 2 and 3 correspond to dry, asperity wetting and completely wetting regimes. c) An illustration on the energy dissipation induced enhancement of the capillary bridges formed at the asperity level for superfluid wetting. The colors represent local temperature gradient close to the contact point (warmer color corresponds to higher temperature). Figures adapted from R8: Huang *et al.*, [2009a].

As shown in Section 1.1, wet granular matter can be classified with the amount of wetting liquid added. In contrast to the boundary between the asperity and complete wetting regimes that can be estimated from the roughness ϵ and size of the particles (more specifically from $\sqrt{\epsilon^2 R}$) [Halsey & Levine, 1998], the threshold for the cohesion to start, i.e. the boundary between dry and the asperity wetting regime, is still unclear. This is a non-trivial question to be addressed experimentally since wetting is typically not considered as homogeneous in a granular packing, as discussed in Section 2.4. Moreover, the amount of wetting liquid added can not be precisely controlled and distributed homogeneously. In a recent work [R8: Huang *et al.*, 2009a], liquid ^{4}Helium has been used as wetting liquid to address this question. The use of such a special liquid has the following advantages: (i) A low surface energy that facilitates wetting of

almost all surfaces; (ii) A well controllable volume down to an atomic level owing to the well calibrated isotherms; (iii) A superfluid phase without the influence from viscosity.

As sketched in Fig. 3.1 (a), the amount of liquid helium is controlled by the amount of helium gas added. Above the saturated vapor pressure, all the amount of gas added is expected to condense on the sample. Below the saturated vapor pressure, the liquid film thickness can be estimated from the vapor pressure measured in the sample cell. For a better comparison of the results from various temperatures, the amount of wetting liquid added n^* is rescaled by the amount of helium for the saturated vapor pressure to be reached. To check the rigidity enhancement due to wetting, vertically sinusoidal vibrations are applied to the sample. The order parameter is chosen to be $\Gamma^* = \Gamma_{\rm wet}/\Gamma_{\rm dry} - 1$, where $\Gamma_{\rm wet}$ corresponds to the critical peak acceleration for the particles on the top layers to move, and $\Gamma_{\rm dry}$ is the corresponding critical value obtained without any helium added. To visualize the mobility of particles, a green laser beam is used to illuminate the sample, and a sensitive camera is employed to visualize the variations of the speckle patterns reflected from the sample. As demonstrated in Fig. 3.1 (b), the transition from dry to asperity wetting regimes may start well below the saturated vapor pressure is reached at $n^* = 1$. Based on the isotherms measured for ^{4}He at various temperature [Bower, 1953], this transition corresponds to ≈ 5 atomic layers of liquid helium coverage.

Moreover, a comparison between temperature below and above T_λ suggests enhanced rigidity starts at a smaller n^* for superfluid than for normal fluid wetting. This can be attributed to the 'fountain effect': As illustrated in Fig. 3.1 (c), collisions between particles generate local heat gradient in the vicinity of the contact point, owing to the energy dissipated. Such a heat gradient effectively drives the flow of superfluid helium toward the contact point, which facilitates the formation of capillary bridges at a 'microscopic' level as well as the enhanced rigidity of the sample at a 'macroscopic' level.

In a former experiment [Hornbaker *et al.*, 1997] using the angle of repose of oil wetting polystyrene beads to address this question, a threshold liquid film thickness was found to be ≈ 20 nm. Here we demonstrate that this threshold can be as low as a few atomic layers, suggesting that the influence from humidity is ubiquitous and hence needs to be considered carefully in real life applications.

3.2 Dry granular dynamics: A brief review

After the threshold between dry and wet granular matter is distinguished, let's start with a brief review on the dynamics of dry granular matter, particularly the transition from a solidlike to a liquidlike state and the collective behaviour associated. It serves as a basis for further comparisons to the dynamics of wet granular matter.

In the helium wetting experiment, the fluidization threshold of vertically agitated granular matter is used as the order parameter. More specifically, it corresponds to the critical acceleration, or force, applied to mobilize particles on the top layers. The melting process of dry granular matter, due to its wide applications in the industries, has been a topic of interest over the past two decades. The important questions are the thresholds for the melting to start and to complete, and the key control parameters or scaling associated. More specifically for agitated monolayer systems, the question of whether the two stage melting scenario predicted by the KTHNY theory [Halperin &

Nelson, 1978; Strandburg, 1988] applies for such a non-equilibrium system or not arises. For a monolayer of particles both confined and agitated in the direction parallel to the gravitational acceleration $\vec{g}$, such a two stage continuous melting scenario predicted by KTHNY theory for equilibrium systems applies [Olafsen & Urbach, 2005]. However, for a monolayer of particles confined in the direction perpendicular but driven parallel to $\vec{g}$, a layer by layer granular meltdown, as well as discontinuous transitions are found [Götzendorfer *et al.*, 2006]. The peak vibration velocity was found to be the critical parameter determining the fully fluidized state, suggesting an energy driven phase transition. This is in contrast to former investigations on the start of melting in a similar system, where Γ was used to characterize the transition threshold, and a typical threshold $\Gamma \approx 1.2$ was found [Clement & Rajchenbach, 1991].

Dating back to the investigations on the heap formation by M. Faraday [Faraday, 1831], the convection in agitated granular layers has been found to be an ubiquitous phenomenon, which may arise from interstitial air [Laroche *et al.*, 1989] or container walls [Clément *et al.*, 1992; Knight *et al.*, 1993]. Moreover, at a larger agitation strength, more pairs of convection rolls, typically with particles close to the wall flowing upwards, were detected [Aoki *et al.*, 1996]. This behaviour is drastically different from the wall induced convection where typically two convection rolls with downward particle motions close to the walls are present [Clément *et al.*, 1992; Knight *et al.*, 1993]. In a recent work [Eshuis *et al.*, 2007], a phase diagram of agitated dry granular matter is presented, where the convection pattern is found to be a robust behaviour covering a wide parameter range. Indeed it is found to be a ubiquitous phenomenon widely existing in various industries, and triggering undesired mixing and segregation effects [Rosato *et al.*, 1987; Duran *et al.*, 1993, 1994; Shinbrot & Muzzio, 1998; Hong *et al.*, 2001; Reis & Mullin, 2002; Burtally *et al.*, 2002; Breu *et al.*, 2003; Schnautz *et al.*, 2005; Khan & Morris, 2005; Schröter *et al.*, 2006]. More recently, single convection roll has also been found in a slowly rotating quasi-two-dimensional sand box on the rim of jamming, suggesting that temporal and local heterogeneous motion of particles is sufficient to generate convective motion [Rietz, 2013]. Despite of the long history of investigations and wide applications in the industries, the emerging counter-intuitive behaviour of convective motions in agitated granular matter indicate that a comprehensive understanding on the origin of convection has not yet been accomplished.

Utilizing experiments and molecular dynamics (MD) simulations, we have recently addressed the question of how defects play the role in triggering the convective motion [P1: Fortini & Huang, 2014]. Fig. 3.2 shows a sequence of snapshots taken from the experiments. As the displacements of the tracer particles marked with blue suggest, mobilized particles in a very narrow region (2 columns in this case) close to the wall, where defects are most likely to be generated, are sufficient to induce the convective motion. While in the bulk region, the particles stay in a crystalline phase and move upward collectively step by step (see tracer particles marked in red). In some occasions, the regions close to the wall are not symmetric, owing to the configurations of the initial defects. Consequently, the downward flow velocity differs from the left to the right sides. In extreme cases, single convection roll can also be detected. Thus, we conclude that the onset of convection is associated with the generation of defects upon agitations. Therefore, strong dependency on the initial configurations of the defects should be expected.

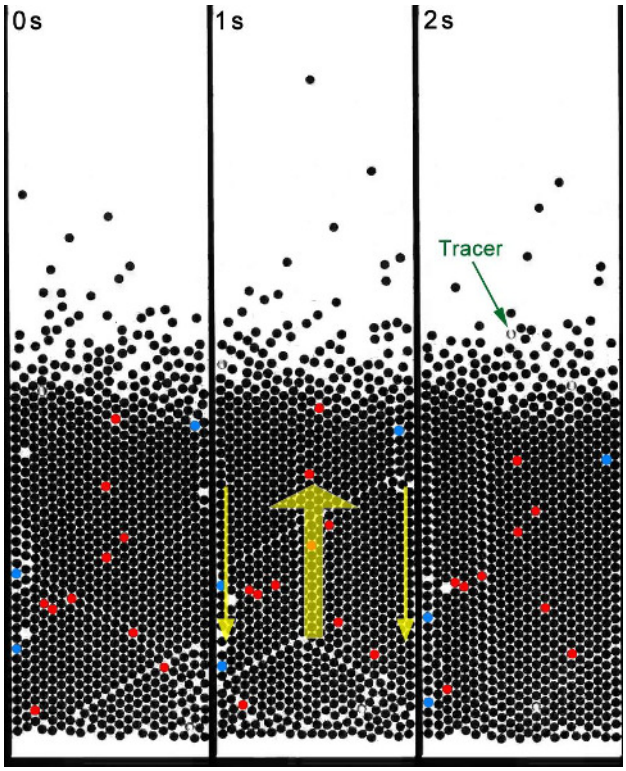

Figure 3.2: Sequence of snapshots showing the convection in a monolayer of glass spheres under sinusoidal agitations against gravity. The vibration frequency f =10 Hz and the dimensionless acceleration Γ =4.53. Red and blue dots mark the tracer particles that are moving up and down correspondingly, as illustrated with the yellow arrow overlaid on the middle snapshot. Note that the download motion occurs in a very narrow region (2 columns) next to the walls, while the upward motion is manifested by the collective motion of hexagonally packed particles in the bulk.

Good agreements between experiments and MD simulations with defects initiated are found for the onset of convection. MD simulations for a crystal initialized without defects predict a larger agitation strength for the onset of convection, because defects have to be generated first. As the agitation strength increases, one can distinguish three regimes: A bouncing bed regime with all particles move collectively, a defects generating regime where sharp growth of the slip probability[1] can be detected, and a convective regime.

Moreover, the slip probability p_{s} is found to follow Arrhenius type law $p_{\mathrm{s}} \propto e^{-\frac{E_{\mathrm{b}}}{K_{\mathrm{m}}}}$, which suggests the existence of activation events, where E_{b} and K_{m} correspond to the activation and injected energy scale. Thus, we reach to the conclusion that sufficient energy injection to overcome the activation energy for a particle to move out of its cage determines whether a convection starts or not.

Beside vertical agitations against gravity that have been frequently employed to investigate granular dynamics, horizontal agitations or a combination between horizon-

[1] A slip event is defined as a displacement of a particle with respect to two nearest neighbours greater than $0.4\,R$ after one oscillation.

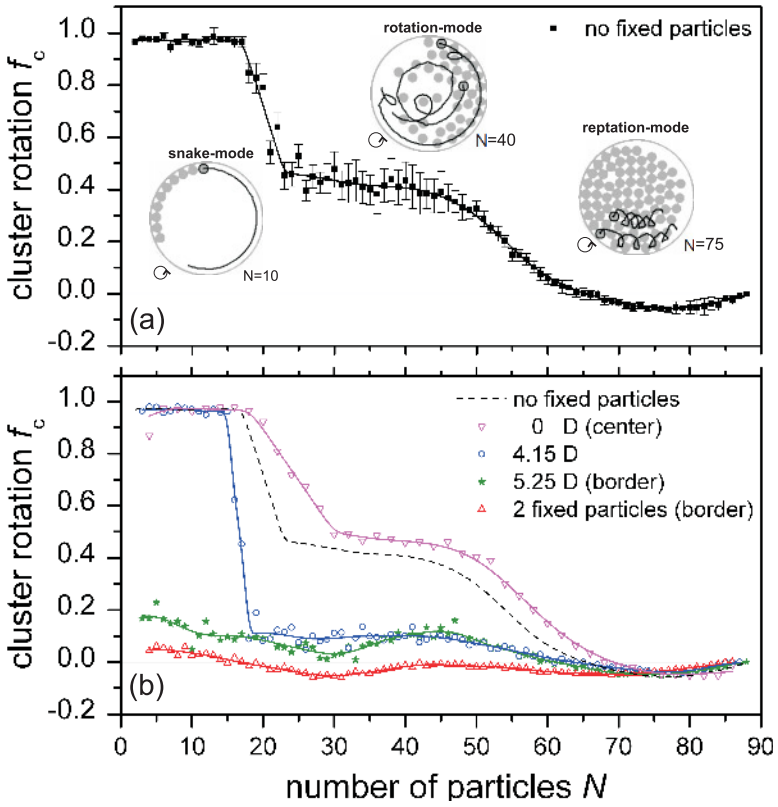

Figure 3.3: Rescaled rotation frequency of a dry granular cluster under horizontal swirling motion f_c as a function of number of particles added without (a) and with (b) intruders at various distances to the center of the container. Three modes, namely snake-mode ($f_c = 1$), rotation-mode ($f_c>0$) and reptation-mode ($f_c<0$) can be distinguished. Insets are snapshots from various modes with the trajectories of tracer particles presented as solid lines.

tal and vertical agitations have also been used to check the universality of the phase behaviour of agitated granular matter (see e.g. R7: Huang *et al.*, [2010] for a review). With agitations perpendicular to the gravitational force, the influence from gravity can be minimized. Alternatively, the rolling friction of spheres on the plate [Kondic, 1999] is found to play an important role [Ristow *et al.*, 1997; Tennakoon *et al.*, 1999; Straßburger & Rehberg, 2000; Aumaître *et al.*, 2003].

By combining two horizontal vibrations that are perpendicular with each other, one generates a swirling motion for energy injection. This type of driving is isotropic, since all the points of the container perform the same type of orbit motion and the energy injection through collisions between particles and the container wall is independent on the phase when impacts occur. In Fig. 3.3 (a), collective behaviour of cohesionless particles in such an apparatus is presented [R10: Feltrup *et al.*, 2009]. As shown in the insets, three modes can be distinguished: (i) A snake-mode with all particles line up at the boundary layer and move collectively with the same direction and collectively rotational frequency f_c as the swirling container. (ii) A rotation-mode with randomness generated through particle-particle collisions and a reduced but still positive f_c. (iii) A reptation mode with a negative f_c. The rotation-reptation transition suggests a

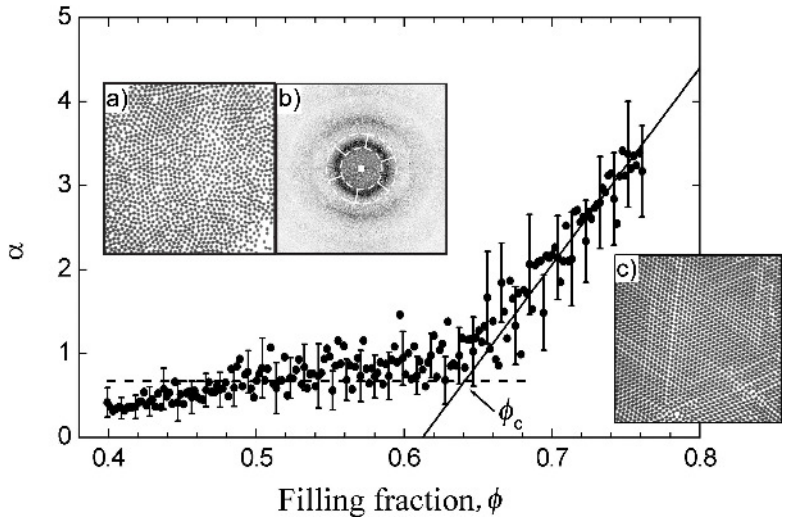

Figure 3.4: Ordering transition of spherical particles under horizontal swirling motion. a) and c) are snapshots of a liquidlike (area fraction ϕ=0.46) and a crystalline (ϕ=0.76) state correspondingly. b) 2D power spectrum of snapshot a). The order parameter α is chosen as the normalized intensity variation in azimuth direction in the power spectrum. The critical area fraction ϕ_c is found to be 0.64 ± 0.01. Adapted from Aumaître *et al.* [2003].

threshold area fraction where the cluster does not rotate. Such a change of the rotation direction may cause problems in applications such as the vibrational mills for grinding feed materials [Yokoyama *et al.*, 1994; Inoue & Okaya, 1994].

To shed light on possible ways to control or to avoid such a transition, intruders are placed inside the swirling table to disturb the dynamics of the cluster. As shown in Fig. 3.3 (b), the rotation frequency can actually be enhanced with the presence of the intruder in the middle of the container. A broken symmetry with the intruder placed away from the center leads to a suppressed rotation, demonstrating the possibility to control the cluster rotation through intruders added inside. Such an effect may have potential applications in the industries to improve mixing or transport processes. Moreover, it is demonstrate that f_c is directly linked to the number of particles staying at the border of the container, indicating that the rotation and reptation motion is mainly driven by the wall [R10: Feltrup *et al.*, 2009].

Beside the collective motion of the clusters, there exists as well a transition from a liquidlike to a solidlike state, as revealed by the snapshots shown in Fig. 3.4 (a) and (c). Such a transition has been investigated in details by several authors [Scherer *et al.*, 2000; Aumaître *et al.*, 2003]. Using an order parameter derived from the two dimensional Fourier transformation of the snapshots taken with various filling fractions, the transition threshold if found to be $\phi_c = 0.64 \pm 0.01$ (Fig. 3.4).

3.3 Wet granular dynamics under horizontal agitations

In contrast to the critical area fraction of ≈ 0.64 for dry granular monolayers shown above (Section 3.2), a dramatically different behaviour arises if the particles are slightly wet.

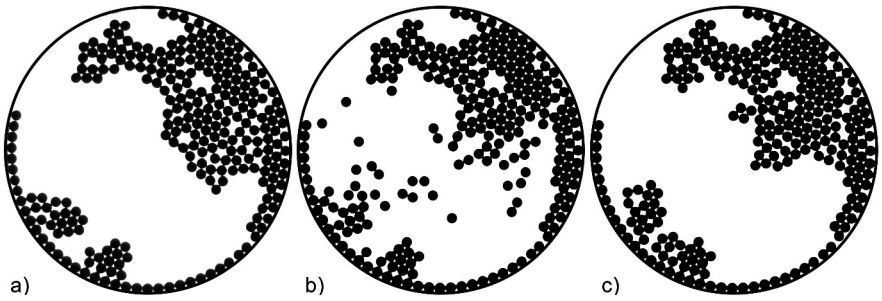

Figure 3.5: Sequential snapshots showing an intermittent sublimation event of wet spheres with a liquid content $W = 1\%$ under horizontal swirling motion with f =1.67 Hz and a =1.59 cm. a), b) and c) are taken before, during and after the event correspondingly. The swirling motion is in the clockwise direction. Note that wet particles self-assemble themselves into a crystalline state already at the area fraction of 28%, owing to the strong cohesive force. Images adapted from [R7: Huang *et al.*, 2010].

As shown in Fig. 3.5, hexagonal lattice readily appears at a global area fraction of 28% under a similar driving condition to the dry case shown in Fig. 3.4, owing to the cohesive force stemming from the capillary bridges formed between adjacent particles. Moreover, the clusters formed are driven to the boundary of the container by the inertial force and tend to be attached there. Such a condensed state can be stable over many periods of swirling motions, with occasional sublimation processes. As shown in Fig. 3.5 (b), the 'gasified' particles during the sublimation process effectively reshape the resting solidlike phase via impacts. This behaviour differs from the corresponding dry granular matter, where energy injection through collisions with the container walls is comparably well distributed and dissipated through collisions everywhere in the sample. Here, the energy injected is much more localized to a few particles capable of overcoming the energy scale set by the capillary bridges.

3.3.1 Surface melting under swirling motion

In this section, I will show that a different dynamical behaviour, namely surface melting, arises if the cohesion from the container wall is suppressed. Technically, this is done by replacing the glass container with PTFE. Because the contact angle of water on PTFE is larger than 90° (see Section 2.4), the cohesive force between the particles and the container wall is dramatically reduced. Consequently, the formation of free standing wet granular crystals is favoured.

As demonstrated in Fig. 3.6, wet spheres tend to organize themselves into a crystalline state with a perfectly hexagonal packing. Depending on the ramping rate of the agitation strength, states with defects may also arise. There are two time scales associated with such a 'crystallization' process: In a rather short time scale (few seconds), initially isolated particles merge with each other into small assemblies. The percent-

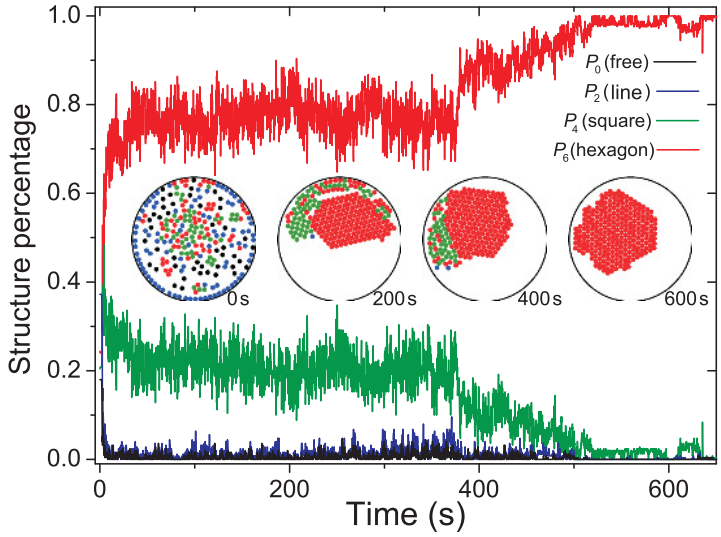

Figure 3.6: Initialization process of a wet granular crystal, represented by the time evolution of the percentage for a particle to be free (P_0), or in a hexagonal (P_6), square (P_4), line (P_2) structure. Insets are sample images with particles color coded according to their local structures: Free particles with black; Line, square, hexagonal structures with blue, olive and red correspondingly.

age of particles being free or in a line structure drops dramatically to 0, indicating a strong tendency of clustering. As a consequence, the percentage of particles falling into a hexagonal structure (P_6) grows substantially to more than 60%. Here the local structures of the particles are characterized with bond orientational order parameters (see R1: May *et al.*, [2013] and references therein for details). In a relatively longer time scale (hundreds of seconds), those assemblies merge into a single cluster deforming continuously under swirling, accompanied with large fluctuations of various structure factors. The final crystalline state (see snapshot taken at 600 s) formed is considered to be a steady state in such a non-equilibrium system, as further collisions with the container do not lead to structure changes.

Melting of such a wet granular 'crystal' (Fig. 3.7) with the growth of f demonstrates an abrupt transition from an amorphous to a surface melting state with a *premelted* 'liquid' film covering the 'crystalline' core [R1: May *et al.*, 2013]. Such a striking similarity to surface melting observed frequently in equilibrium systems such as the melting of ice [Dash *et al.*, 2006] triggers again the question of how well can our knowledge on equilibrium systems be extended to the widespread non-equilibrium systems. Moreover, the threshold is found to be insensitive to the step size (down to $6.2{\cdot}10^{-4}$ Hz) and the waiting time (down to 1 minute) of the control parameter f variations, thus one can speculate that the steady state of such a dissipative system is independent on the time scale imposed by the way of driving.

Four states, including the abrupt transition into the surface melting state, can be identified in the melting process [R1: May *et al.*, 2013]: (i) A state with a perfectly hexagonal structure at low agitation strength. Note that the 'crystal' moves around collectively in the co-moving frame with its internal structure kept stable. (ii) An amorphous state with 'cracks' or voids formed inside, leading to reduced area fraction

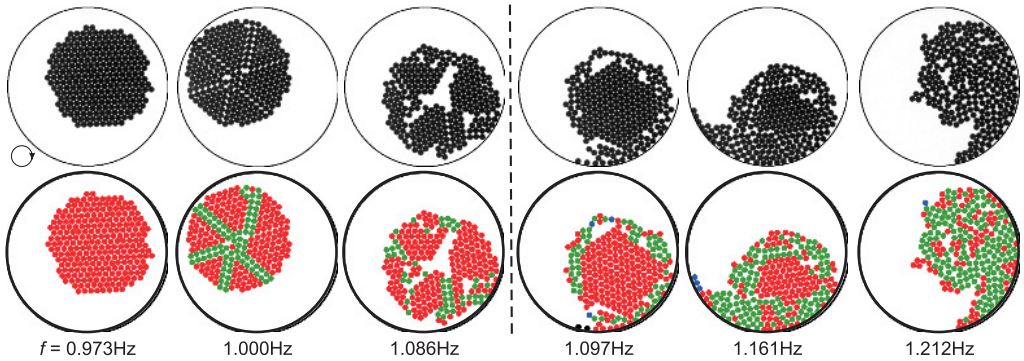

Figure 3.7: Melting process of a wet granular crystal as the swirling frequency increases, represented by the snapshots (upper panel) and local structures (lower panel). The particles in the lower panel are color coded according to their local structures as in Fig. 3.6. The gray dash line corresponds to the start of surface melting. The container swirls in the clockwise direction. Figure adapted from [R1: May *et al.*, 2013].

and associated plastic deformation upon impacts with the container wall. Note that the enhanced energy dissipation at those defects effectively increases the susceptibility for the cluster to deform under normal stress applied by the container. Meanwhile, the shear stress drives the rotation of the cluster along the swirling direction. (iii) A surface melting state with a perfectly hexagonal core surrounded by few liquidlike layers, after the collapse of all voids inside the cluster at a threshold f_{th}. Further increase of the agitation strength leads to an increase of molten layers, reminiscent to the melting of an ice crystal upon the growth of temperature. An interesting feature associated is the circular shape, which suggests a tendency to reduce its surface energy, i.e., a signature for the existence of an interfacial tension. (iv) A completely molten state where no stable crystalline structure can be found. The cluster evolves into a comma shaped 'droplet' moving along the rim of the container in the co-moving frame, evocative of a glass of wine being swirled.

Utilizing bond orientational order parameters, the deviation of the local structure of edge particles can be characterized. It serves as the order parameter to determine the melting transitions. A comparison between increasing and decreasing f reveals small hysteresis for such a transition, which has been discussed in [R1: May *et al.*, 2013]. Systematic investigations reveal that the surface melting threshold f_{th} depends on the agitation amplitude a and the liquid content W, which can be understood quantitatively with a model based on the balance between the energy injection E_{inj} and dissipation E_{cb} at a single particle level.

The energy injection is considered to be a two step process: Colliding with the container wall provides 'macroscopic' collective motion of the cluster, followed by a transfer into the 'microscopic' thermal energy through particle-particle interactions inside. As illustrated in Fig. 3.8 (a), a particle on the edge of a cluster has more freedom to roll compared with those in the bulk, due to less restrictions from its neighbours. This difference provides the 'thermal' energy for the edge particle $m(2\pi fak)^2/2$, with m its mass and $k = 1 - v_{\mathrm{s}}/v_{\mathrm{b}}$ the relative velocity difference. The latter is 5/7 for the case that only edge particles roll, and roll without sliding and rolling frictions [Kondic, 1999]. As the second step only occurs without interruptions from the wall, we introduce

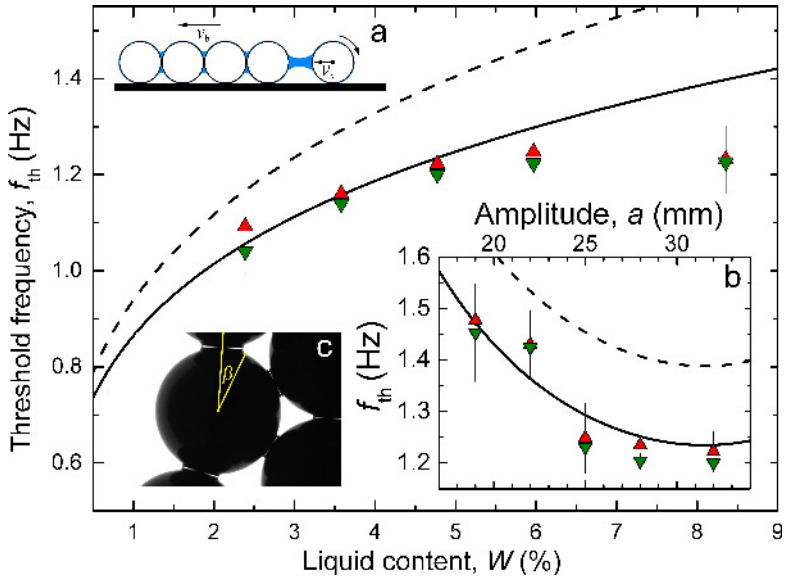

Figure 3.8: Dependency of the threshold frequency on the liquid content and the swirling amplitude (inset b). f_{th} is measured with the bond orientational order parameter of edge particles. The upper and lower triangles correspond to increasing and decreasing f. a and W are fixed at 31.8 mm and at $W = 4.77\%$ in the main panel and in b, correspondingly. The dash and solid lines are estimations from the model. Inset a: A sketch illustrating an edge particle rolling away from the bulk. v_{s} and v_{b} are the velocity of edge, and of the bulk particles in the lab frame. Inset c: A close view of the edge of a crystal with $W = 2.39\%$, captured with a microscope. β denotes the half opening angle of a capillary bridge. Figure taken from R1: May *et al.*, [2013].

an additional factor $\alpha = (D_{\mathrm{c}} - 2a)/(D_{\mathrm{c}} + 2a)$, the length scale for a particle to move without disturbance from the wall over that for the swirling table (diameter of the container D_{c}) to reach. Thus, the energy injection can be estimated with

$$E_{\mathrm{i}} = \frac{\alpha m}{2}(2\pi f a k)^2. \tag{3.1}$$

On the other hand, the energy dissipation can be estimated with the rupture energy of a capillary bridge E_{cb} (see Eq. 2.15 in Section 2.2.1). Since the relative velocity of the edge particles rolling away from the bulk is relatively small, the viscous damping term can be neglected here. A balance of the two energy scales gives rise to an analytical form for the melting threshold

$$f_{\mathrm{th}} = \frac{0.60}{ka}\left(\frac{\sigma\cos\theta}{2\rho_{\mathrm{p}}R}\cdot\frac{D+2a}{D-2a}\right)^{1/2}\left(\frac{W}{N}\right)^{1/4}, \tag{3.2}$$

where N is the mean coordination number of the particles.

Predictions from this formula are shown as dash lines in Fig. 3.8, with parameters measured experimentally. It demonstrates qualitatively the trend of f_{th} and quantitatively the correct order of magnitude. Quantitative disagreement to the experimental data is not surprising, because, as discussed in Section 2.2.1, Eq. 2.15 is an approximation that has an error growing with W. A more accurate estimation of E_{cb} from

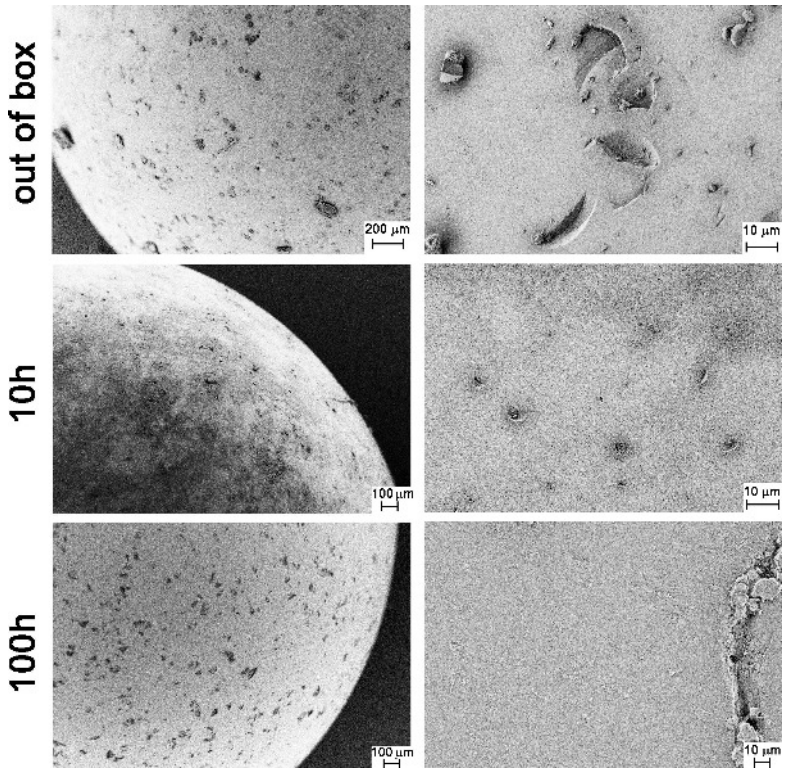

Figure 3.9: Scanning electron microscope (Leo 1530) images of a glass bead (Sili beads, type P) used in the experiment. Upper, middle and lower panels correspond to beads directly out of the box, and after 10 or 100 hours of continuous swirling. Left and right columns are from different resolution.

a numerical integration of a more exact force law (appendix of Willett *et al.* [2000]), which is accurate within 3% for W up to 6.58%, yields a much better comparison to the experimental results, as the solid curves demonstrate. The limit for such a more accurate estimation corresponds to the merge of capillary bridges at $\beta = \pi/6$. Thus, without any fit parameter, the model proposed here can describe fairly well the melting threshold, provided that the system is in a pendular state [R1: May *et al.*, 2013].

Such a success in characterizing the melting threshold demonstrates that a detailed knowledge on the interactions between particles at a 'microscopic' level is essential. Actually not only the wetting liquid, but also the surface properties of the particles will influence the collective behaviour. As the scanning electron microscope (SEM) images show in Fig. 3.9, particles become more and more smooth after swirling, owing to the frequent polishing between adjacent particles that are closely bound with each other on the merits of capillary bridges formed. Such a smoothing process is found to influence the melting threshold: It decays systematically with experimental runs and becomes stable only after at least 80 hours of continuous swirling. Moreover, the condensation of liquid on the container lid has to be minimized in order to obtain reproducible results, because it influences the liquid content W. This is achieved through keeping the container lid slightly warmer than the rest part of the container [Wild, 2013]. These examples on the care one has to take for the investigations of granular matter manifest

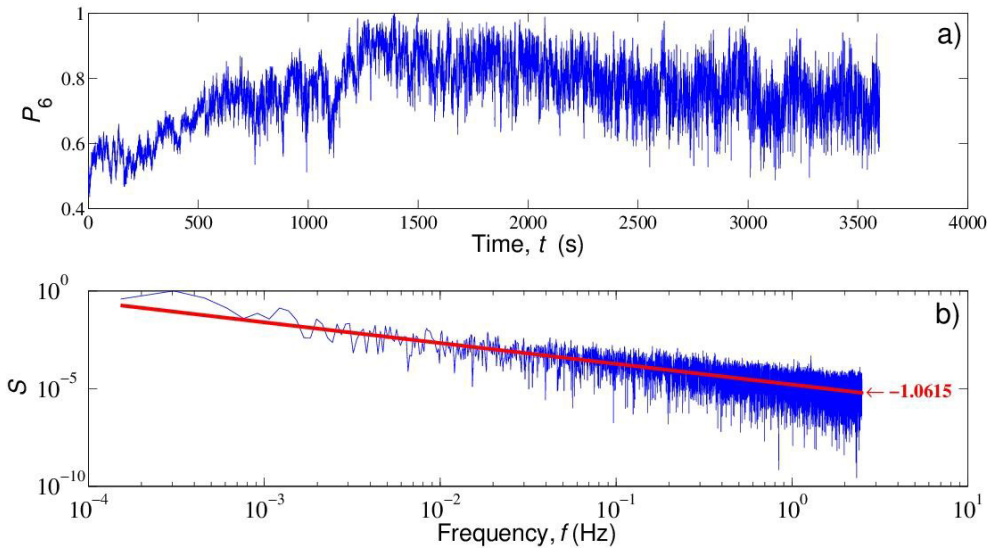

Figure 3.10: a) Fluctuations of P_6 at a frequency close to f_{th}, where switching between the amorphous and surface melting states can be observed. b) A representation of such fluctuations demonstrate a $1/f$ noise, a characteristic feature of systems with self-organized criticality [Bak, 1999].

what P. G. deGennes, a pioneer of soft matter physics, mentioned [Duran, 2000],

> "The physics of granulars may not require costly hardware,
> but it demands enormous care."

As melting starts, strong fluctuations of the structure factor P_6 are observed (Fig. 3.10). Such a behaviour corresponds to a frequent switching between a more 'fragile' state with loose accumulation of small rigid clusters, and the surface melting state. This strong fluctuations presumably arise from the non-equilibrium nature of the system: The balance between the energy injection and dissipation, which determines its steady state, is not homogeneous in both time and space. An interesting feature, namely a $1/f$ decay, arises if the fluctuation is viewed from the frequency domain. Such a $1/f$ noise is a robust and still mysterious phenomenon widely existing in nature, ranging from the blinking of stars to the occurrence of earthquakes as well as avalanches of a pile of sand at a much smaller length scale [Bak, 1999; Mandelbrot, 2002; Milotti, 2002]. In 1987, Bak *et al.* proposed that such a noise can be explained with self-organized criticality: A critical state that a system naturally evolves into without detailed specifications of the initial condition, and such a critical state (attractor) is very susceptible to small perturbations, i.e. small events may trigger large events. Consider a pile of sand: It has a certain angle of repose that the particles will evolve into, and small rearrangements of particles or even force connections in between may trigger larger events, i.e. avalanches. From this perspective, the onset of avalanches for a pile of sand has been extensively investigated in the past [Bak *et al.*, 1987, 1988; Jaeger *et al.*, 1989; Held *et al.*, 1990; Nagel, 1992; Frette *et al.*, 1996; Buchholtz & Poeschel, 1996]. The observation here for the structure fluctuations of a wet granular 'crystal' demonstrates again such a

ubiquity. More preliminary experimental runs suggest that this type of noise starts to occur already in the 'crack' forming region at a relatively weak agitation strength. It indicates that large events such as avalanches or voids collapse associated with the melting transitions may originate from critical states at a more 'microscopic' level, such as the local density or structure changes. Further investigations on the scaling laws and possible mechanisms behind are being carried out presently.

3.3.2 Clustering under steady shear flow

Figure 3.11: Dark polyethylene (PE) spheres at the air-water interface to reduce the level of bromate in Ivanhoe clean water reservoir. Image taken from [Ivanhoe, 2011].

With a different type of driving, namely a steady shear flow, I will demonstrate again in this section that the collective behaviour of a two dimensional wet granular cluster can be traced down to the particle-particle interactions at a 'microscopic' level.

Agglomerations of particles or foams trapped at an air-liquid interface are ubiquitous phenomena frequently observed in our daily lives, e.g. cornflakes floating on milk, mosquito eggs floating on a pond or in a glass of champagne, and in various industries such as mining or waste water treatment [Whitesides & Grzybowski, 2002; Wills, 1997]. As an example, Figure 3.11 shows how a layer of dark particles is used to avoid the formation of bromate, a carcinogen that forms when bromide and chlorine react with sunlight, in Ivanhoe reservoir that serves over half a million inhabitants in Los Angles Ivanhoe [2011].

For colloidal particles at the interface, interactions with each other through van der Waals interactions and surface charges in the presence of electrolytes in the bulk liquid will dominate [Robinson & Earnshaw, 1992; Pieranski, 1980; Nikolaides *et al.*, 2002; Manoharan *et al.*, 2003; Lu *et al.*, 2006]. For particles with a diameter larger than tens of microns, i.e. within the granular realm, the capillary force induced by the distorted air-liquid interface starts to take effect [Stamou *et al.*, 2000; Hoekstra *et al.*, 2003; Vassileva

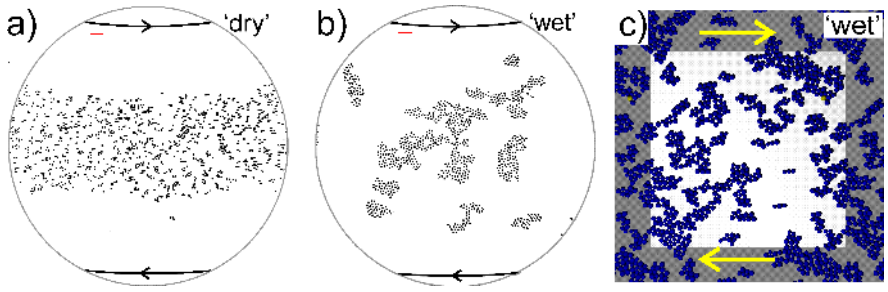

Figure 3.12: A comparison between particles trapped at the air-glycerol interface without (a) and with (b) the additional oil phase, i.e., a comparison between 'dry' and 'wet' granular clusters. The dark curves correspond to the inner and outer cells of the Couette device, and arrows denote the rotation direction. Scale bar length is 1 mm. (c) A snapshot taken from discrete element method (DEM) simulations for wet particles (see text for a short description of the model, image courtesy of M. Brinkmann). Experimental snapshots are adapted from R5: Huang *et al.*, [2012].

et al., 2005]. As an example, particles with a diameter around 100 μm will experience an attractive force of this type on the level of nN, sufficient to drive aggregations.

Here, I will show that the strength of capillary interactions can drastically be enhanced by adding a second immiscible liquid to the particles [R5: Huang *et al.*, 2012], which is believed to be an analogue of the gelation described for pickering emulsions by Koos & Willenbacher [2011], and to shed light on the stability mechanism of bicontinuous interfacially jammed emulsion gels (bijels) [Stratford *et al.*, 2005; Cates & Clegg, 2008].

To prepare wet granular clusters at an air-liquid interface, glass beads employed are treated initially to allow their centers of mass slightly above the air-liquid interface. This will consequently facilitate the formation of capillary bridges. In order to create a monolayer of 'wet' particles, a solution of silicone oil in hexane is then applied to the interface. Initially particles rearrange themselves into a monolayer owing to the lubrication of the additional oil phase. Driven by the evaporation front of hexane, a compact 'wet' granular cluster is formed. By control the amount of oil added, one can assemble compact 'wet' granular crystals with particles interact mutually through the formation of capillary bridges (see R5: Huang *et al.*, [2012] for more details).

Due to the high viscosity of the subphase, thermal energy will not influence the dynamics of the clusters. Instead, steady shear flow is employed to drive the wet granular clusters. As the snapshots in Fig. 3.12 indicate, dramatically different behaviour is found for 'wet' particles in comparison to the 'dry' ones. Starting from the evaporation driven compact state, 'dry' particles interact with each other through hard core repulsions, leading to a slight dilation from the central region where the initial 'crystalline' structures are formed. After that stage, the particles will follow the steady shear profile and no more interactions could be observed within the observation period. For the 'wet' case, large, persisting clusters are formed under continuous shear flow, which rotate around their center of mass, collide, merge, deform or break into several parts. Such a difference calls a detailed understanding on how cohesion plays the role here.

To explore the essential role that cohesion takes, the dynamics of 'wet' particles in a linear shear profile was also numerically simulated applying a two dimensional

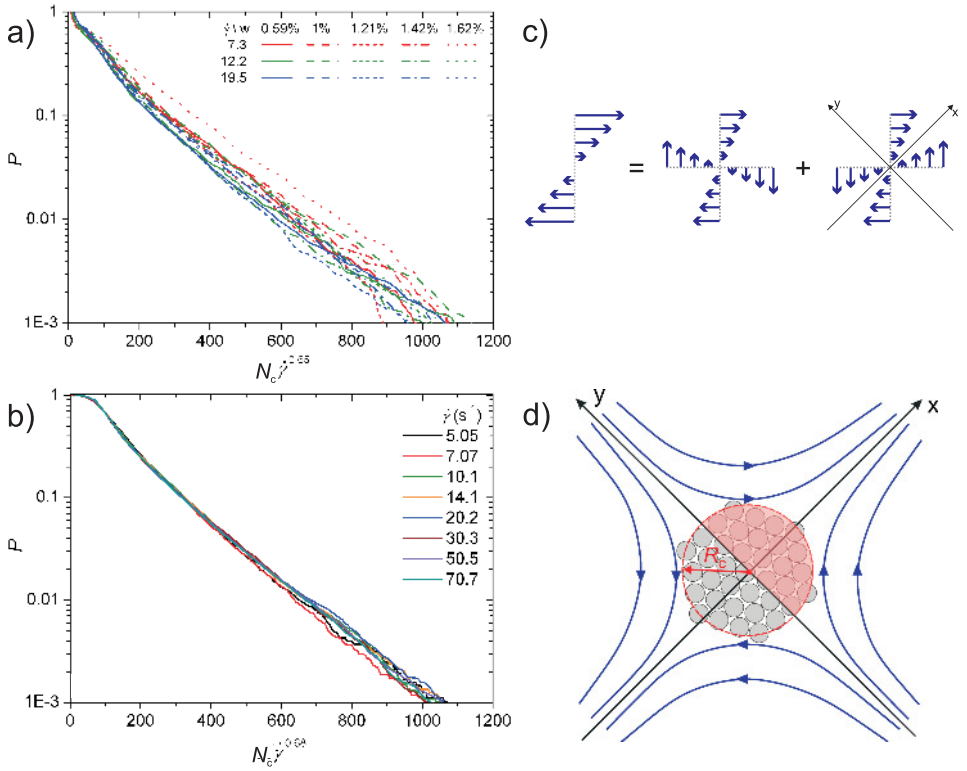

Figure 3.13: Cumulative cluster size distribution P, the probability to find a cluster out of N_c or more particles, as a function of the rescaled cluster size $N\dot{\gamma}^j$ from experiments (a) and DEM simulations (b). The exponent j arises from the scaling of the characteristic size of the cluster N_c with the shear rate $\dot{\gamma}$. (c) shows that any linear shear profile can be decomposed into a rotating and a hyperbolic straining flow field. (d) illustrates the model used to describe the critical exponent j (see text for more details). The hyperbolic stream lines tend to compress the cluster with an effective radius R_c along the y axis and stretch it along the x axis. Figures taken from R5: Huang *et al.*, [2012].

discrete-element model (DEM) [R5: Huang *et al.*, 2012]. The model considers three forces acting on the particle: Elastically repulsive force, capillary and viscous drag forces. After solve the Newton's equation of motion, the mobility of the particles can be obtained. As shown in Fig. 3.12 (c), such a simplified model leads to the clustering of particles reminiscent to the experiments. As the cluster size distributions shown in Fig. 3.13 (a) and (b) suggest, such a model is capable of reproducing the cumulative cluster size distribution: It decays exponentially with the rescaled cluster size $N_c\dot{\gamma}^j$. Such a scaling suggests that the larger the shear rate, the faster the decay rate. This could be understood since the viscous drag force grows with the shear rate. Step further, I will show that the balance between the viscous drag force and the capillary force determines the scaling exponent j.

As shown in Fig. 3.13 (c), any linear shear profile can be decomposed into a hyperbolic strain flow and a rotation. It is the stretching component from the former part contribute to the break of the cluster, as sketched in Fig. 3.13 (d). For such a

cluster shape, integrating the Stokes' drag force acting on each particles in the region shaded with red, one could obtain the total drag force $F^{(\mathrm{d})}$ exerted on the cluster along the central cutting line $x = 0$:

$$F^{(\mathrm{d})} \propto \mu\,\phi\,\dot{\gamma}\,R_{\mathrm{g}}^3/R, \tag{3.3}$$

where $\phi \equiv N_{\mathrm{c}}\,R^2/R_{\mathrm{g}}^2 \propto N_{\mathrm{c}}^{1-2/D_{\mathrm{f}}}$ is the area fraction of particles in the cluster, and R_{g} corresponds to the gyration radius of the cluster. Here D_{f} is the fractal dimension of the cluster.

On the other hand, the total capillary force $F^{(\mathrm{c})}$ acting along a cut $x = 0$ into the direction of the x axis can be estimated, as a first approximation 2.11 with

$$F^{(\mathrm{c})} \propto n\,\sigma\,R, \tag{3.4}$$

where n is the number of capillary bridges in a cut along the line $x = 0$. There are two limiting cases for the breaking of clusters: (i) A compact disk like cluster as illustrated in Fig. 3.13 (d), with a corresponding $n \propto \phi R_{\mathrm{g}}\,R$, (ii) A more fractal structure built with a hierarchy of rigid sub-clusters with a characteristic size, i.e. constant n. Consequently, the scaling of the cumulative cluster size with the shear rate is expected to be

$$\frac{D_{\mathrm{f}}}{1+D_{\mathrm{f}}} \leq j \leq \frac{D_{\mathrm{f}}}{2}\ , \tag{3.5}$$

.

where the fractal dimension of the cluster D_{f} is found to be ≈ 1.6 for both experiments and DEM simulations [R5: Huang *et al.*, 2012]. Therefore, we can predict the exponent to be $0.6 \leq j \leq 0.8$, which captures the measured value from both experiments 0.65 ± 0.06 and DEM simulations 0.68 ± 0.02. Moreover, it is remarkable that the values of both experiments and the DEM simulations lie closer to the lower bound that corresponds to the hierarchical structure, which agrees with the qualitative analysis based on the snapshot shown in Fig. 3.12 (b). Note that the model for cluster size distribution is based on the force balance, which differs from the melting transition shown in the above Section 3.3.1, this could be attribute to the fact that both viscous drag force and the capillary force are acting at the same time during the rupture event.

At a larger area fraction $\phi = 23\%$, Fig. 3.14 demonstrates the percolation of the clusters after a quench of the shear rate. Such a tendency for the particle network to percolate, i.e. 'gelation', with the presence of the secondary wetting liquid is a robust phenomena found in vast number of liquid-particle systems [Koos & Willenbacher,

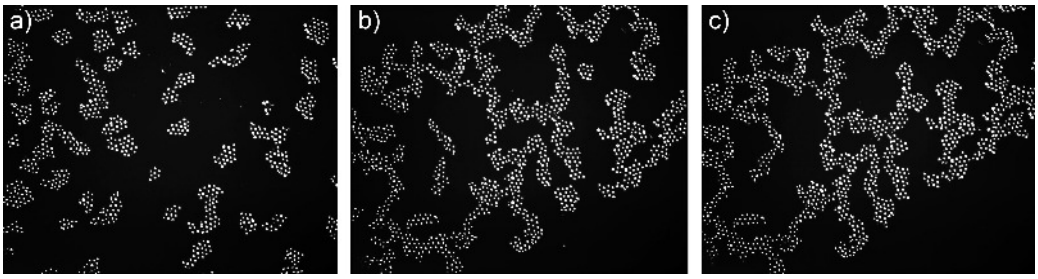

Figure 3.14: Time sequence (t=0, 20, 40 min) of the aggregation of clusters after switching off the shear rate from $\dot{\gamma} = 48.8\ \mathrm{s}^{-1}$. The global area fraction is $\phi = 23\%$.

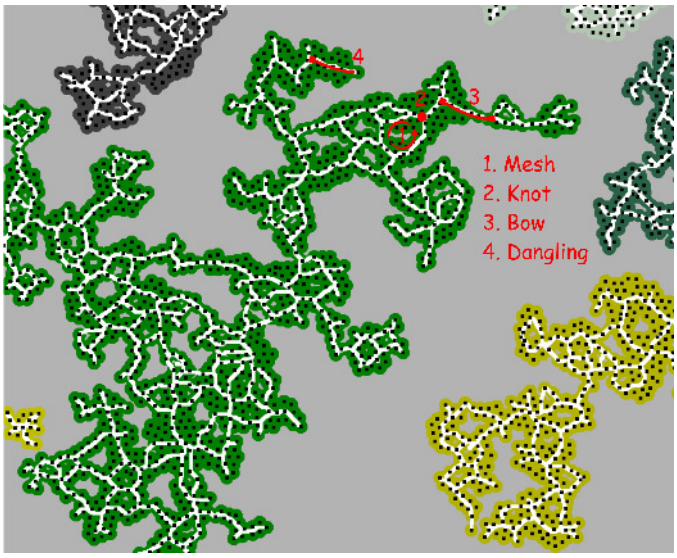

Figure 3.15: Network representative of shearing 'wet' granular clusters at an area fraction close to percolation transition. Based on the positions of particles detected (black dots), the network structure of the clusters formed (white lines) can be obtained. Various clusters are coded with different colors. How does the collective behaviour of the clusters close to the percolation transition depend on the dynamics of the network morphology is a question to be addressed in such a 'wet' granular model system.

2011]. The two dimensional system focusing here has the advantage that not only the bulk properties such as percolation transition threshold, or rheological behaviour [Edwards & Brenner, 1991], can be measured quantitatively, but also the dynamics of the 'microscopic' structure can be characterized in real time with the positions of particles found. More importantly, as the above analysis of the clustering of particles has already demonstrated, the connections between 'macro-' and 'microscopic' worlds will help to elucidate crucial properties that dominate the rheological behaviour. Therefore, further investigations on such a system will focus on the percolation transition, rheology of two dimensional 'wet' granular gels, and the dynamics of network structure close to the percolation transition.

Figure 3.15 corresponds to one possible way to characterize the structures formed by 'wet' particles at the interface: By a 'thinning' process, the rigid backbone of the clusters can be distinguished as the white lines. As the clusters deform under the shear flow, a frequent change of the network structure is expected. One important question we can address with such a characterization is: From a statistical point of view, what type of bonds dominates the rigidity of the 'gels' formed? The rigidity of such cohesive network structure could be a counterpart for the force chains network in a dry pile of sand that determines when and where avalanches happen [Vanel *et al.*, 1999; Howell *et al.*, 1999; Geng *et al.*, 2001; Bi *et al.*, 2011], thus shed light on the jamming phase diagram proposed to unify thermal and athermal systems [Liu & Nagel, 1998].

3.4 Wet granular dynamics under vertical agitations

As the most direct way to overcome gravity, vertical agitations are frequently used to drive granular matter (see e.g. Iveson *et al.* [2001]). In this section, we focus on the dynamical behaviour of wet granular matter under vertical agitations. Due to the additional cohesive force arising from the formation of capillary bridges, typically being orders of magnitude larger than the gravity of particles (see Chap. 1), strong agitations with a dimensionless acceleration Γ up to 80 are necessary to effectively 'thermalize' multiple layers of wet granular matter into a gaslike state. In this section, phase behaviour as well as the associated scaling laws in such a quasi-two-dimensional system will be presented. In particular, I will demonstrate again how 'microscopic' time, length and energy scales influence the collective behaviour of agitated wet granular matter.

3.4.1 Melting

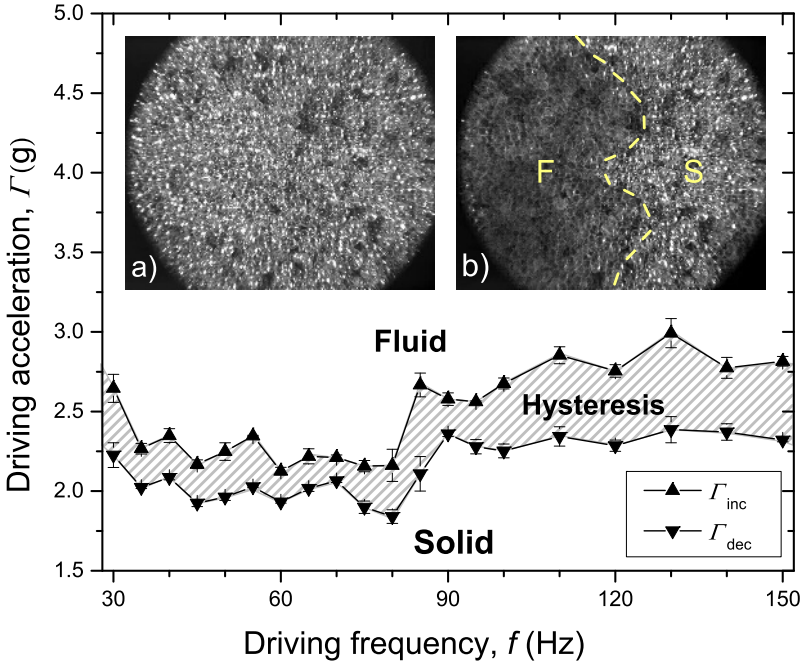

Figure 3.16: Melting transition for $3\sim4$ layers of wet transparent glass beads under vertical agitations measured through visual inspections on the mobility of particles on the top layers. Insets are obtained through a minimization of consequent 500 synchronized snapshots below a) and above b) the melting threshold, where the bright spots correspond to the reflections of the illuminating light by the glass beads. Note that the fluidized region (F) in b) is darker and blurrier in comparison to the solidlike (S) region, because of the particle movements.

As learned from monolayer systems, agitated wet granular 'crystals' tend to melt from the surface layers, therefore we can determine the melting threshold via visual inspections on the mobility of particles on the top layers as the agitation strength varies experimentally. A closer view of such a transition, as shown in the insets (a) and (b) of Fig. 3.16, suggests that melting in the top layers is heterogeneous, with

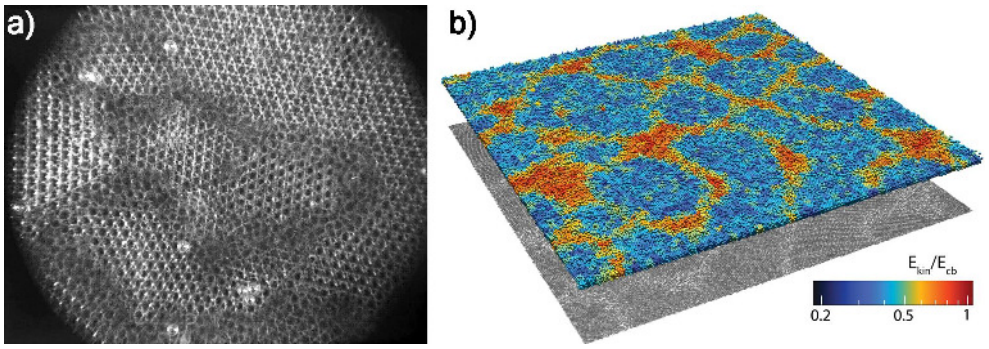

Figure 3.17: a) Melting of 3∼4 layers of slightly wet glass beads of diameter 1.2 mm under vertical agitations with f =150 Hz and Γ =7.42. The image is obtained by minimizing continuous 50 snapshots taken at a fixed phase of each vibration cycle, thus particles mobilized are blurred. b) A snapshot from MD simulations [Roeller, 2010] for a comparable configurations, with particles color coded by their kinetic energy E_{kin} rescaled by the rupture energy of a single capillary bridge E_{cb}, the intensity of the shadow indicates the local density of particles. Simulation performed by K. Röller.

the possibility of having part of the layer in a molten state while the other part still being rigid. Moreover, visual inspections also show that the mobility of particles in the molten region can be dramatically different: (i) A few particles, which have only single bonds with the solidlike phase below, may swing around the contact points with their neighbours rapidly. (ii) The threshold detected exhibits hysteresis for all frequencies used, a manifestation of the influence from the hysteretic nature of a single bridge forming and rupturing. (iii) The threshold Γ value exhibits a jump of $\approx$ 0.5 as a threshold frequency $f_{\mathrm{c}} \approx 80$ Hz is reached.

At a vibration frequency larger than f_{c}, a different melting scenario arises: Melting tends to be initiated at the 'grain' boundaries, stemming from the formation of 'crystalline' structures in this frequency region. The molten regimes coexist with blocks of particles with 'crystalline' structures. This observation suggests that the jump of the melting threshold could be due to additional force needed to create defects in a crystal for the system to melt, reminiscent to the convection threshold in the dry system discussed above in Section 3.2. Furthermore, one could understand why the threshold frequency occurs at $\approx$ 80 Hz: It corresponds to a match between the peak-peak agitation amplitude ($a_{\mathrm{p-p}} = 2\Gamma\, g/(2\pi f_{\mathrm{c}}^2) \approx 213\ \mu m$) and the rupture distance of a capillary bridge ($s_{\mathrm{c}} \cdot R \approx V_{\mathrm{b}}^{1/3} \approx 210\ \mu m$). Such an explanation indicates that smaller enough agitation amplitude will lead to an ordering transition. This type of melting is also found to be in agreement with MD simulations (Fig. 3.17 b). From the energy level of particles provided by the simulations, one clearly distinguishes a different kinetic temperature level between crystalline and molten regions. The kinetic energy level for most particles, even for those in the molten region, is smaller than the rupture energy of single capillary bridge, suggesting that a rupture of capillary bridge is not a precondition for melting.

For such a 3D system, it is helpful to explore the melting process along the agitation direction. Here we use ruby fluorescence to have a qualitative view on the mobility of particles below the top layers. As illustrated in Fig. 3.18, ruby tracers are placed initially at the bottom layer. After shined with green Light-emitting diode (LED) light source, they emit red light, reminiscent to a ruby laser. By putting a proper filter

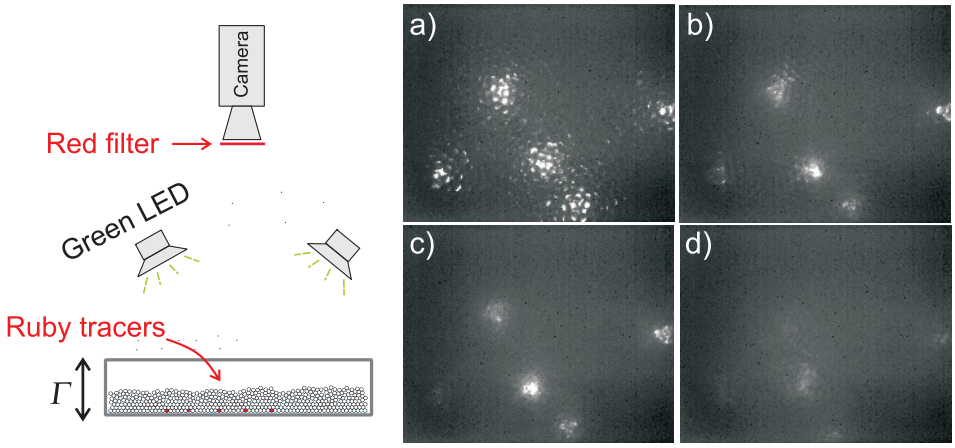

Figure 3.18: Surface melting demonstrated by ruby fluorescence. The sketch illustrates the experimental set-up that enables a qualitative characterization of particle mobility below the top layer. Images a) - d) are obtained through the same minimization process as used for Fig. 3.16in order to identify various molten levels. Corresponding accelerations are $\Gamma = 2.91$, 3.56, 4.08 and 4.87. Here only 10 frames are used for each Γ due to the frequent fluctuations of the patterns.

in front of the camera, one obtains only the light emitted from the tracer particles. In another word, those tracers serve as lamps embedded in the granular layer. As a consequence, patterns such as the ones shown in Fig. 3.18 (a) can be detected, which show the positions of the ruby tracers as well as the organizations of particles on top. Qualitatively the mobility of particles above the tracer can be detected from the local variations of the pattern, while that of the tracer can be determined from the collective movement of the pattern.

By varying the driving acceleration step by step and observe the patterns observed, we can qualitatively demonstrate that melting in such a 3D system also starts from the free surface. Utilizing the same minimization process, the mobility of particles at various layers can be distinguished. At $\Gamma = 2.91$, particles on top layers are only weakly fludized, as the sharpness of the minimized image shown in Fig. 3.18 (a) indicates. As Γ increases further to 3.56 (Fig. 3.18 b), particles on the top layers move locally, leading to a slightly blurry top layers. However, the overall position of each pattern is not changing, suggesting that particles at the bottom layers are still immobile. Such a process continues as Γ increases to 4.08 (Fig. 3.18 c), where the particles in the top layers become more mobile. Until finally at $\Gamma = 4.87$, the whole image is dark and blurry. Visual inspections on the consequent snapshots taken indicate the patterns are mobile, which indicate that the system melts completely. Such a surface melting scenario has also been confirmed with numerical simulations [Roeller & Herminghaus, 2011]. Moreover, the transition into the completely molten state measured by ruby fluorescence is found to grow linearly with the driving frequency, indicating a threshold agitation velocity and a certain energy scale associated. This agrees with the melting scenario found for agitated dry granular matter discussed in the above Sec. 3.2.

3.4.2 Granular 'gas bubbles'

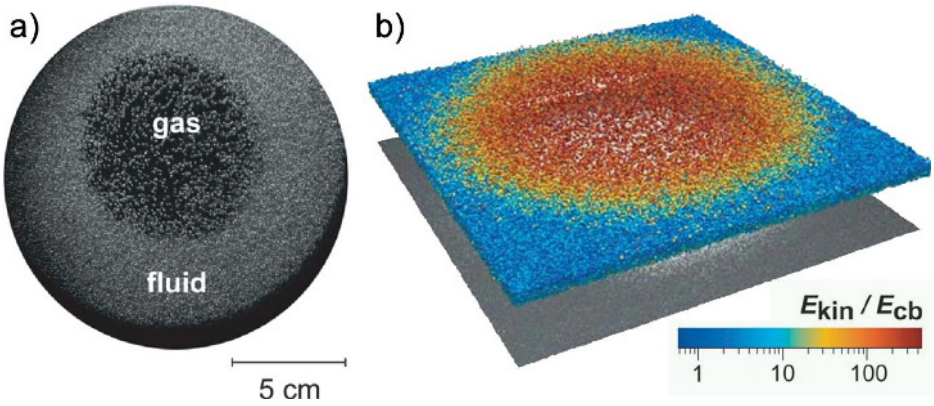

Figure 3.19: Snapshots of a wet granular 'gas bubble' surrounded by a liquidlike phase from both experiments (a) and MD simulations (b). Such a phase separation is observed in a thin wet granular layer (3∼4 layers) under vertical agitations against gravity. In (a), bright spots arise from the light reflected from the glass beads. In (b), the particles are logarithmically color coded by their kinetic energy E_{kin} rescaled by the rupture energy of a single capillary bridge E_{cb}. It demonstrates the sharp temperature gradient across the phase boundary. Images from R11: Fingerle *et al.*, [2008].

The melting process described above shows the possibility of having lateral inhomogeneities. Such a behaviour is as well true if the acceleration increases further: Wet granular 'gas bubbles' tend to nucleate from the surrounding liquid phase, i.e., a phase separation into a coexistence of a liquidlike and a gaslike phases [R11: Fingerle *et al.*, 2008]. Fig. 3.19 shows such an example with a single 'gas bubble': The number density of particles in the gaslike region is much less dilute than that in the liquidlike region. Moreover, MD simulations reveal that the kinetic temperature in the gaslike phase is orders of magnitude larger than that in the liquid phase, demonstrating that this system is driven far from thermodynamic equilibrium. Note that MD simulations consider only the energy dissipation from the rupture of capillary bridges (inelastic collisions between particles are ignored). That means only the rupture energy and the rupture distance are parameters controlling the particle-particle interactions. This striking similarity between experiments and the MD simulations based on such a simplified model suggests that the rupture of single capillary bridges plays an important role in the phase separation. For thermally driven molecular or colloidal systems, phase separations in the metastable region of the phase diagram have been extensively discussed in terms of spinodal decompositions (see e.g. Cahn [1965]; Zaccarelli [2007]. In agitated dry granular matter, phase separation has also been found and discussed in detail from a similar perspective [Roeller *et al.*, 2011; Clewett *et al.*, 2012]. Such a similarity across thermal and athermal systems again triggers the question of how well can existing knowledge on thermal system be extended to athermal systems.

Figure 3.20 shows the nucleation and merging dynamics of wet granular 'gas bubbles'. As a certain threshold acceleration Γ_{fc} is reached, a 'gas bubble' may nucleate from the center or the boundary region of the container. It is found that the former case has a slightly larger threshold than the latter case. After nucleation, it grows with

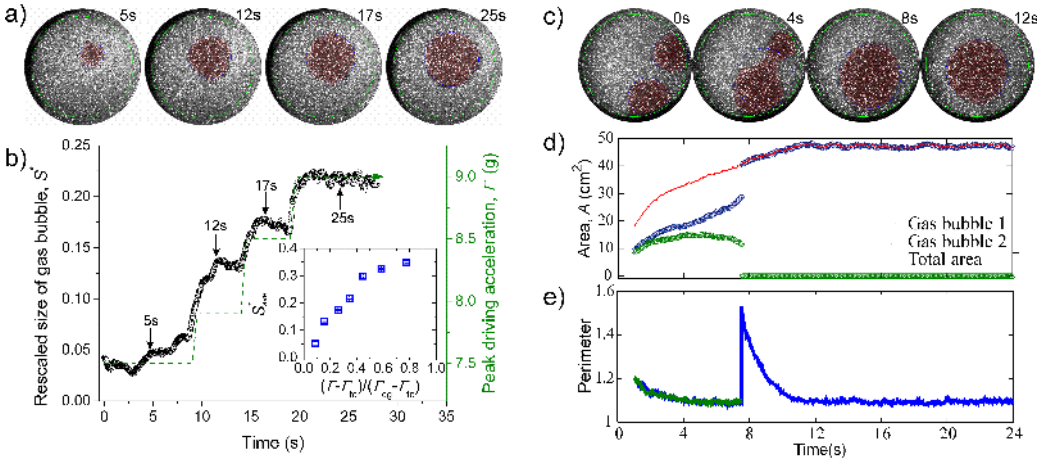

Figure 3.20: Left panels: Nucleation of a wet granular 'gas bubble' in a thin wet granular layer driven vertically with fixed f and peak vibration acceleration Γ increasing step by step (dash line in b). a) Images taken at various Γ to demonstrate the growth of the 'gas bubble' (highlighted in red). b) The size of the 'gas bubble', rescaled by the total area of the container, as a function of time. Inset of b) shows the averaged size s^*_{ave} of the 'gas bubble' as a function of Γ. The size of a gas bubble S^* is rescaled by the total area of the container. Γ_{fc} and Γ_{cg} are the critical accelerations for the transitions from a fluidlike to the fluid-gas coexistence, and from the fluid-gas coexistence to a gaslike phase correspondingly. Right panels: Merging of two 'gas bubbles' at fixed f =50 Hz and Γ =9.45. d) and e) correspond to the evolution of the areas and perimeters of the gas bubbles with time. To illustrate the deformation of the phase boundary from a circular shape, the perimeter in e) is rescaled by that of a circle with the same area as the 'gas bubble' region found.

fluctuations to a certain size. As Γ increases step by step, the size of the 'gas bubble' follows with fluctuations until a saturated s^* is reached (see inset of Fig. 3.20 b). This is mainly due to the enhanced resistance from the thickening of surrounding fluid phase as 'gas bubble' grows. In the limiting case of the layer thickness reaches the top of the container, s^* saturates. From the snapshots taken at various Γ, the 'gas bubble' always tends to have a circular shape, despite of the fluctuations of its size. This behaviour suggests the existence of an interfacial tension, a feature already demonstrated by the surface molten state of a wet granular crystal in 2D (Section 3.3.1). Such a feature is also demonstrated from the merging of two 'gas bubbles' (Fig. 3.20 c).

Interestingly, the size evolutions of 'gas bubbles' during the merging process also suggest a transport of particles from the smaller to the bigger 'gas bubbles' as they are approaching each other. Considering an effective surface tension at the interface, smaller 'gas bubbles' will presumably have larger effective 'Laplace pressure', which suggests a higher pressure in the small 'gas bubble' assuming the same pressure in the liquilike phase. Thus, as two 'gas bubbles' with different sizes are closer enough, transfer of particles from the smaller to the larger 'gas bubble' is expected occur. Such a transport arises from the frequent exchange of particles between the gaslike and surrounding liquidlike phases. The effective interfacial tension is as well demonstrated by the rescaled perimeter shown in Fig. 3.20 (e): Merged 'gas bubble' tends to relax into a circular shape in a few seconds.

A natural question following the existence of an effective interface tension is wet-

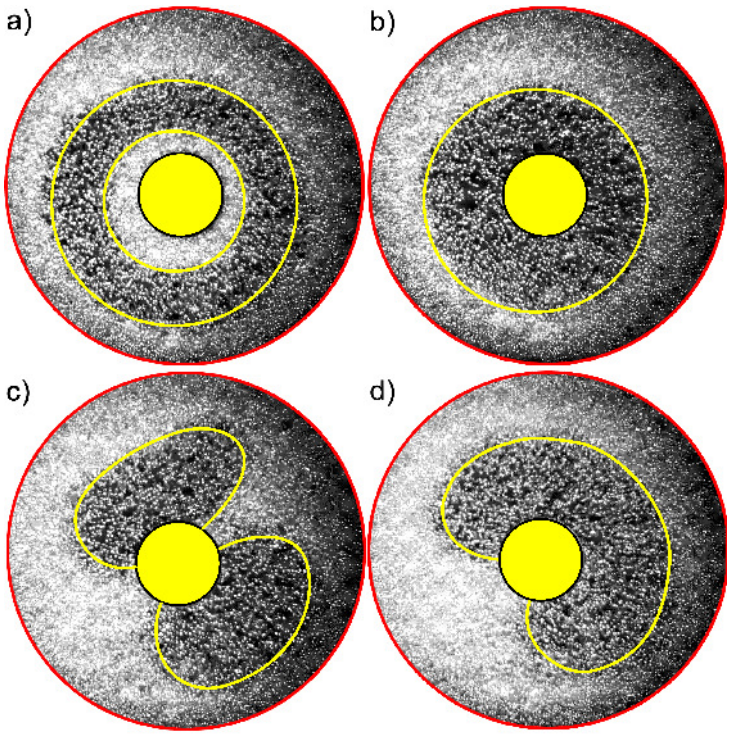

Figure 3.21: Interactions between a 'gas bubble' and a cylindrical intruder (area covered with yellow) with a diameter of 3 cm placed in the center of the container, which demonstrate an effective 'contact angle' for wet granular fluid. Upper panels: A 'gas bubble' formed by a quench from a gaslike phase into the phase separation region with f =50 Hz and Γ =12.5. a) and b) correspond to snapshots taken at 80 and 220 vibration cycles after the quench. Lower panels: 'Gas bubbles' formed by a jump of Γ from a liquidlike phase to the coexistence phase Γ =11.6. c) and d) correspond to 90 and 160 vibration cycles after the jump. The yellow curves, which highlight the phase boundaries, are guide to the eyes.

tability. With a cylindrical intruder added into the container, the effective wetting properties are explored. The question of whether a wet granular liquid wets or not the intruder turns out to be not trivial and strongly relies on the initial states of the experiments: A quench from a gaslike state into the coexistence phase leads to the shrinking of an initially large 'gas bubble' to a steady state with the intruder embedded (Fig. 3.21 b). In the initial stage, a liquidlike region tends to 'wet' the intruder (Fig. 3.21 a). However, it vaporizes away in the steady state (Fig. 3.21 b). According to the Kelvin equation, such a behaviour can be understood from the vapor pressure gradient in the intermediate gaslike region along the radial direction [Herminghaus, 2013]. On the contrary, a jump from a liquidlike into a coexistence state leads to the nucleation of multiple 'gas bubbles' (Fig. 3.21 c), preferably close to the intruder. They will eventually merge into a single one attached to the intruder with a contact angle close to 90° (Fig. 3.21 d).

Figure 3.22 (a) shows the change of the gas bubble size with Γ. In contrast to the sudden jump of s^* as Γ goes beyond Γ_{fc}, a continuous decrease of the 'gas bubble' size is found as Γ decreases. Such a hysteretic behaviour can be treated as a magnification of the hysteresis from the rupture of single capillary bridges. Thus the fact that the

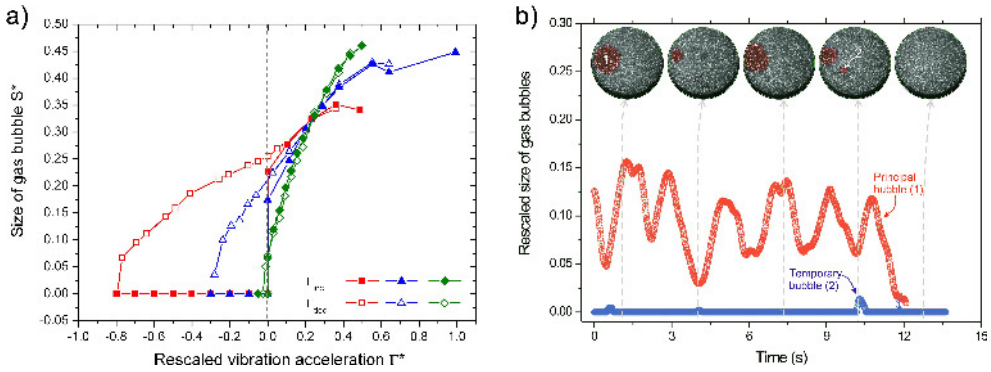

Figure 3.22: a) Hysteresis of the size of 'gas bubbles' across the transition from a fluidlike to a fluid-gas coexistence region. The size of the 'gas bubble' S^* and Γ^* are defined the same as in Fig. 3.20 with $\Gamma_{\rm fc}$ and $\Gamma_{\rm cg}$ measured by increasing Γ step by step. Data obtained by increasing and decreasing Γ are shown by solid and open symbols separately. Square, upper triangle and diamond correspond to d =1 mm, f =50 Hz; d =1.2 mm, f =100 Hz and d =1.5 mm, f =100 Hz. b) Size fluctuation of a 'gas bubble' with f =85 Hz and Γ = 24.1, which is close to Γ_{fc} = 27 above which a stable 'gas bubble' is observed. As time evolves, size of the principle 'gas bubble 1' decreases with strong fluctuations until vanishes. Sometimes temporary 'gas bubble 2' nucleates as the size of the principal 'gas bubble' fluctuates to its minimum.

hysteresis region being larger for small particles could be attributed to the enhanced total rupture energy for the nucleation of the 'gas bubble'. Note that although the rupture energy decreases with particle radius ($\propto \sqrt{R}$), the total number of bridges to break for the nucleation of a 'gas bubble' ($\propto R^{-3}$) increases as R decreases.

In the hysteretic regime of 1 mm particles and $f > 85$ Hz, the size of 'gas bubble' fluctuates strongly. Fig. 3.22 (b) shows such fluctuations for transient 'gas bubbles' observed in the hysteresis region, together with snapshots taken at various time. The principle 'gas bubble' fluctuates at an amplitude of around half of its mean value and a frequency of about 0.5 Hz. The shrinking of the principle 'gas bubble' is normally accompanied with nucleation of one or more small temporary 'gas bubbles' at other locations in the surrounding granular fluid. The competition between newly nucleated 'gas bubbles' and the principle 'gas bubble' leads to the strong fluctuations. The fluctuation region is not in a steady state, because normally after tens of seconds, all the 'gas bubbles' vanish and the system enters a complete liquidlike state. Such fluctuations are found to be much stronger for small particles in comparison to larger ones, which can be speculated from the level of energy barrier generated after phase separation. The nucleation of a 'gas bubble' can be considered as a symmetry breaking process [R11: Fingerle *et al.*, 2008]. In the metastable region, the net power injection has two stable zero points: Either strongly dissipated through the rapid collisions (high $E_{\rm diss}$) in the dilute gaslike phase, or weakly dissipated through particle-particle interactions without frequent rupture of capillary bridges. One can speculate that the barrier in between determines the level of fluctuations, i.e. smaller particles with larger number of layers give rise to stronger fluctuations.

3.4.3 Phase diagram and scaling laws

In order to have an overview of the phase behaviour of agitated wet granular matter, transitions between the solidlike, liquidlike and gaslike states of agitated wet spheres are measured systematically through a variation of the agitation acceleration at fixed frequencies [R9: Huang *et al.*, 2009b].

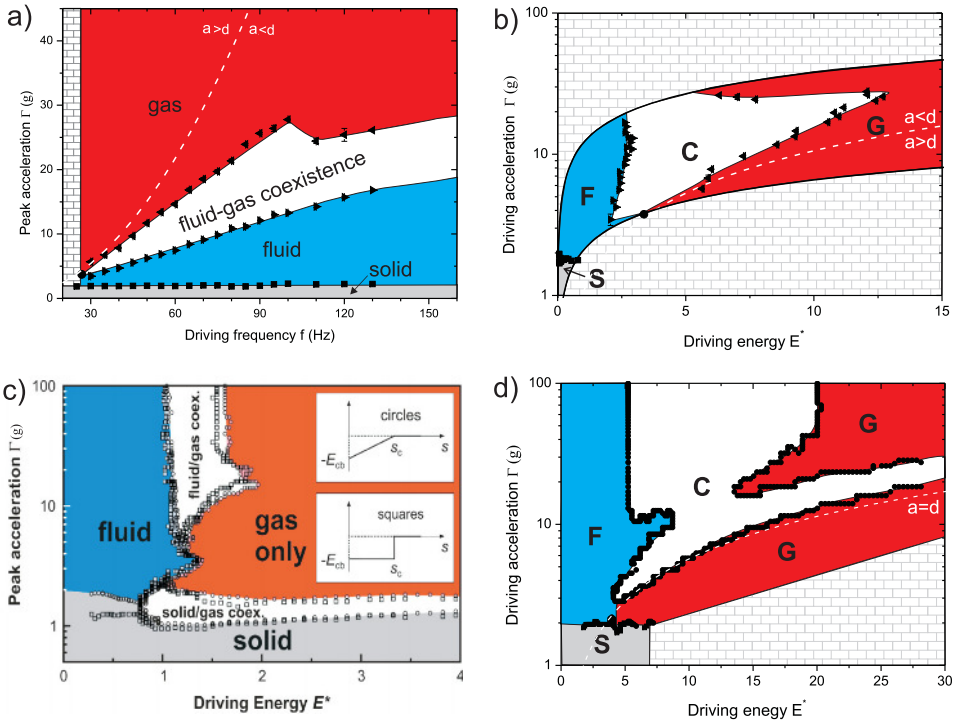

Figure 3.23: Phase diagrams of water wetting glass spheres with diameter d =1.5 mm and liquid content $W = 1\%$ in Γ - f (a) and Γ - E^* (b) planes, where $E^* = mv_p^2/(2E_{cb})$ corresponds to the maximum kinetic energy a particle with mass m can obtain from the vibration plate (v_p being the peak vibration velocity) rescaled by the rupture energy of a single capillary bridge E_{cb}. The regions covered with brick patterns are unexplored due to the limitation of the apparatus. The solid black dot corresponds to the converging point of the F-C and C-G transition lines. Dash line indicates $a = d = 1.5$ mm, where a is the vibration amplitude. c) and d) correspond to phase diagrams from MD simulations with 1200 particles in two dimensions for the elastic and inelastic cases, respectively. The restitution coefficient is fixed at $e_{pp} = 0.8$ for particle-particle collisions, and $e_{pw} = 1$ for particle-wall collisions. Insets of c) show the hysteretic interaction potentials chosen (dotted: approach and solid: retract). Regions color coded with gray, blue, white and red correspond to solidlik (S), fluidlik (F), fluid-gas coexistence (C) and gaslike (G) phases. Figures a), b), d) adapted from R9: Huang *et al.*, [2009b], and c) from R11: Fingerle *et al.*, [2008]).

As the phase diagram presented in Fig. 3.23 (a) shows, the transition from a solidlike (S) phase to a fluidlike (F) phase occurs at a constant $\Gamma \approx 2$, slightly larger than the typical value 1.2 found for dry granular matter (see Section 3.2), demonstrating the influence from the capillary force [Scheel *et al.*, 2004]. Because Γ determines the mean

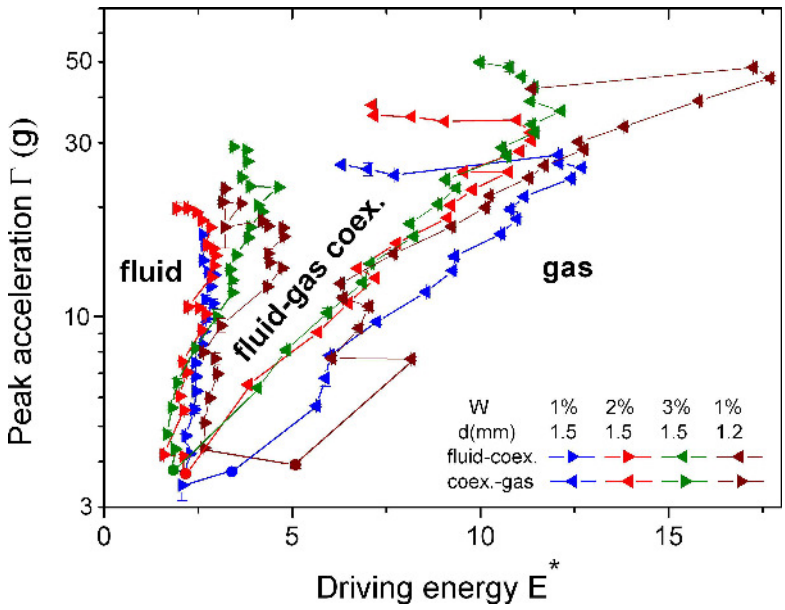

Figure 3.24: Phase diagram for water wetting glass spheres at different liquid content W and particle diameters d in the Γ - E^* plane. Figure from [R9: Huang *et al.*, 2009b].

driving force acting on the granular layer, a constant Γ for such a transition suggests that this transition is force driven. Here, only the threshold value for decreasing Γ is shown in the phase diagram because starting from a fluidlike phase lead to a more reproducible result. According to the above analysis on the hysteretic nature of this transition (see Sec. 3.4.1), the threshold for surface melting will be slightly larger.

A different behaviour is found for the transition from a fluidlike to a fluid-gas coexistence region: The transition line grows linearly with f, suggesting that the agitation velocity ($v_\mathrm{p} \propto \Gamma/a$), plays the dominating role. Here, Γ_fc is determined by the nucleation of 'gas bubbles', which is conveniently accessible in the experiments. Former discussions on the hysteretic nature of such a transition suggest a smaller Γ_fc for the vanishing of 'gas bubbles', but the difference for $d = 1.5\,\mathrm{mm}$ particles used here is negligible. The dependency of F-C transition on the driving velocity suggests a certain energy scale to overcome for a 'gas bubble' to nucleate. This is indeed the case since the phase diagram measured by MD simulations of a 2D system (Fig. 3.23 c) clearly shows that F-C transition corresponds to a vertical line ($E^* \approx 1$ in the Γ - E^* plane, i.e. rupture energy of a single capillary bridge. A rescale of experimental data with the rupture energy scale estimated with Eq. 2.15 demonstrates as well the presence of such an energy scale, despite of being $E^* \approx 2.5$. Such a difference arises from the additional energy dissipation from the inelasticity of particles. This is confirmed with an implementation of a constant normal COR in the MD simulations, which leads to a shift of E^* to ≈ 5 (Fig. 3.23 d). Moreover, MD simulations also suggest that the detailed nature of how energy dissipated plays a minor role in phase transitions, since a change of the force laws (insets of Fig. 3.23 c) for the rupture of a capillary bridge leads to almost the same transition threshold (Fig. 3.23 c).

As shown in both experiments Fig. 3.23 (b) and MD simulations Fig. 3.23 (d), the transition from the coexistence (C) phase to the gaslike phase (G) doesn't rely on the

energy injection E^*. Instead, it shows a tendency to follow the curve of $a = d$, which indicates the influence from the geometry of the system.

In Fig. 3.24, scaling of the F-C transition line with the rupture energy is further demonstrated through a variation of liquid content and particle diameter. The collapse of data in the $\Gamma - E^*$ plane demonstrates the universal aspect of such a transition: For a 'gas bubble' to nucleate, sufficient energy to overcome locally the energy dissipation from inelastic collisions as well as the rupture energy of single capillary bridges is needed. Thus, we can again conclude that understanding the 'microscopic' energy dissipation is the key to elucidate 'macroscopically' collective behaviour.

Moreover, there are non-universal aspects in the phase diagram, as the C-G transition line and the kink close to the F-C-G 'tri-critical' point (Fig. 3.23 c and d) indicate. Those features are found to be related to the geometrical parameters including the height of the granular layer h, container height H as well as particle diameter d. For more extensive discussions on the universal and non-universal aspects of the phase diagram, the reader may refer to R11: Fingerle *et al.*, [2008] and R9: Huang *et al.*, [2009b].

3.4.4 Pattern formation

"Why is the universe not boring?"

An answer to the above question raised by Cross and Greenside in their book on pattern formation [Cross & Greenside, 2009] is far from trivial. However, as they suggested, one should consider the universe as an evolving non-equilibrium system as a staring point. As an equilibrium system is perturbed, or driven out of equilibrium, one ubiquitous feature is the formation of patterns, which may range from the atomic scale magnetic ordering [Ferriani *et al.*, 2008] to the growing surface of a single cell [Wada, 1966], from stirring milk on the coffee to the galaxy formation (e.g. Messier 74 is named as a perfect spiral galaxy [Messier, 2014]). One peculiar example of pattern formation is solitary waves through which energy can be kept and transferred to a long distance without dissipation. It was discovered by J. S. Russell in the 19th century [Russell, 1844] and further elaborated by mathematicians to be a balance between the nonlinearity and dispersion (see e.g. Craik [2004]). Such a localized pattern finds

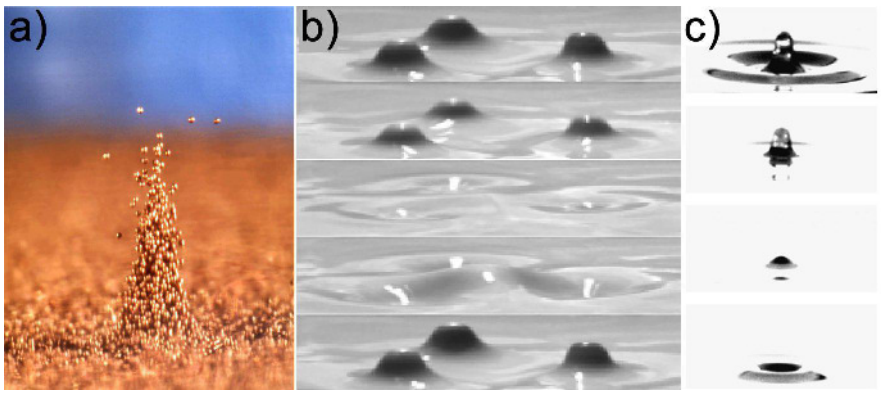

Figure 3.25: Localized excitations observed in (a) agitated granular media [Umbanhowar *et al.*, 1996], (b) clay suspensions [Lioubashevski *et al.*, 1999] and (c) Newtonian fluid [Arbell & Fineberg, 2000].

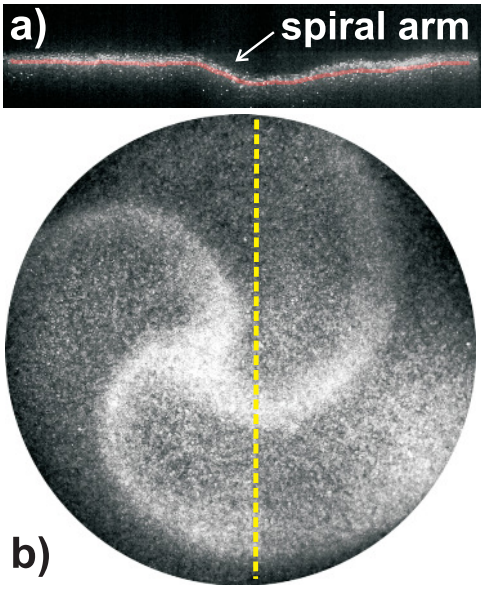

Figure 3.26: Snapshots of a typical 3-armed spiral pattern observed in vertically agitated thin wet granular layers: (a) is captured with the laser sheet illumination. The red half transparent line is a surface profile determined by an image processing procedure. The spiral arm corresponds to a kink between regions with different heights. (b) is obtained from the top view of the pattern (averaged over three synchronized images to enhance the contrast). The yellow line marks the region shined by the laser sheet. Images adapted from R6: Huang & Rehberg, [2011].

applications, for example, in optics [Chen *et al.*, 2012; Renninger & Wise, 2013] to transport information efficiently.

More recently, localized excitations, named as 'oscillons', in dissipative granular systems under vertical vibrations have been discovered in the vicinity of period doubling bifurcation [Umbanhowar *et al.*, 1996]. Figure 3.25 (a) shows a closer view of an oscillon composed of bronze particles. It is a subharmonic pattern with the peak turning into a crater in the next vibration cycle. Although oscillons arise from the highly dissipative granular systems, they persist for a long time under continuous vibrations. They can also interact with each other and form pairs, or even lattices. Later on, similar patterns are discovered in vertical agitated clay suspensions and temporarily in Newtonian fluid (Fig. 3.25 b and c), suggesting the ubiquity of such type of localized patterns.

For vertically agitated wet granular matter, a dramatically different pattern formation scenario has been found [R6: Huang & Rehberg, 2011]: 3-armed rotating spirals, as shown in Fig. 3.26 (b), are the dominating pattern. Such a pattern arises from a peculiar period tripling bifurcation that leads to the spatiotemporal chirality. With the help of laser profilometry, it is found that the spiral arms, which appear brighter in Fig. 3.26 (b), correspond to kinks separating regions with different height (Fig. 3.26 a). The existence of kinks actually indicates as well energy localization, since most of the injected energy is dissipated in the kink region where interactions between particles most frequently occur. Due to the strong cohesion from the formation of capillary bridges, the wet granular layer tends to move collectively upon agitations. At a certain

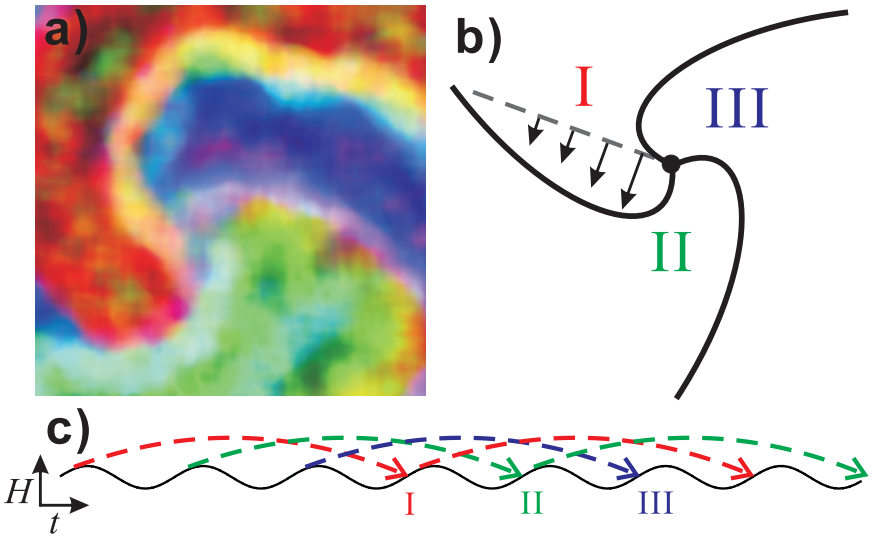

Figure 3.27: (a) Spatially resolved covariance between two subsequent images taken as the collision with the container occurs. They are color coded by various regions (red for I, green for II, and blue for III) separated by the spiral arms. The brightness of each color corresponds to the mobility of particles. Sketches (b) and (c) indicate the spatiotemporal chirality of the pattern (see text for detailed explanations). The black line in (c) indicates the positions of the vibrating bottom, the dash lines correspond to the center of mass in regions I, II and III. H denotes the height. Images adapted from [R6: Huang & Rehberg, 2011].

point, the energy dissipation through particle-particle interactions within the granular fluid [2] is not sufficient to balance the energy injection. Consequently, new forms of energy dissipation must take place: One possibility is the nucleation of 'gas bubbles' as discussed in Section 3.4.2, and the other possibility is the kink waves shown here.

As discussed in detail elsewhere [R6: Huang & Rehberg, 2011], period tripling actually leads to three possible phases for the agitated granular layer to choose (illustrated with various colors in Fig. 3.27). From the time evolution of the spatially resolved covariance (representing the mobility of particles) in various regions, one can find a clue for the rotation mechanism. As interpreted in Fig. 3.27 (b) and (c), the collision of region I with the container leads to a higher mobility of particles (granular temperature) there in comparison to the other two regions. Suppose energy is injected through collisions with the container bottom and dissipated through the free flying period, the kinetic temperature will have a gradient $T_{\mathrm{I}} > T_{\mathrm{III}} > T_{\mathrm{II}}$ at the moment region I collides with the container. Such a gradient effectively drives the expansion of region I into region III, i.e., along the highest temperature gradient. Such an expansion will typically lead to a propagating front. However, the presence of the other two kink waves, i.e. the other two spiral arms, gives rise to a central region (spiral core) within which the mobility of particles is dramatically reduced. Consequently, it is plausible to guess that the pinned spiral core region leads to a distortion of the front initially formed in a way that the particles closest to the core region obtain the highest rotation

[2] Note that such interactions won't necessarily include a frequent breaking of capillary bridges, since particles within the liquidlike layer are still bound with each other via capillary bridges.

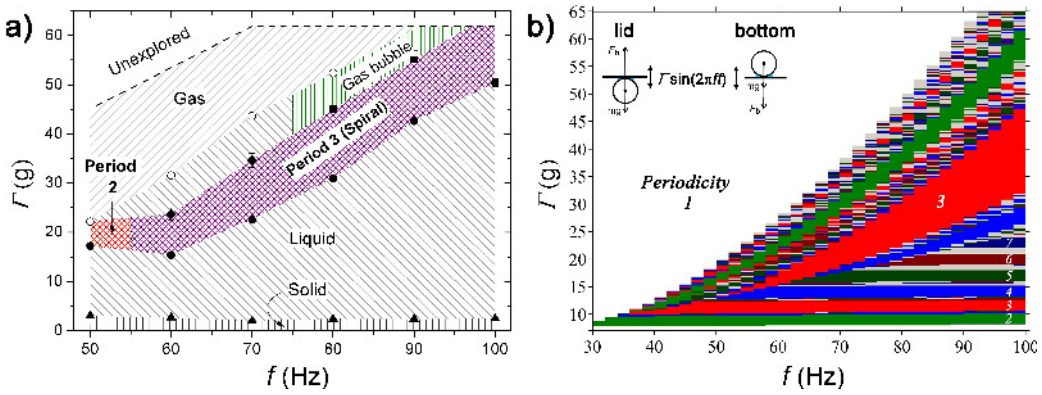

Figure 3.28: a) Phase diagram for 113 g (corresponding to $4\sim5$ particle layers) water wetting glass beads (d≈780±70 μm) with W =1.6% under vertical agitations [Butzhammer, 2012]. It demonstrates the dominating period tripling pattern, i.e. three armed rotating spirals. In a narrow region at $f \approx 50$ Hz, period doubling pattern can also be observed. See Fig. 3.29 below for sample snapshots. b) Periodicity diagram from a simple model considering the whole granular layer as a single particle colliding completely inelastic with the container. Inset shows interacting forces between the granular layer and the lid or the container bottom considered in the model. As indicated by the periodicity number overlaid on the diagram, periodicity is represented with colors. Regions painted with gray correspond to a periodicity ≥ 7.

speed (see sketch in Fig. 3.27 a), and hence spiral shaped fronts are formed.

Figure 3.28 (a) shows a phase diagram for the pattern formation of agitated wet granular layers. It demonstrates that period tripling spiral is the preferred pattern, covering a wide range of f and Γ. Transition lines shown here correspond to an average of thresholds measured for both increasing and decreasing Γ, since no hysteresis is observed for the pattern to appear. As Γ grows above the threshold, spiral patterns spontaneously appear with a certain rotation speed and an Archimedean shape, which grows linearly with Γ in the pattern forming region [R3: Huang *et al.*, 2013]. It is still unclear what determines the emerging the time, length scales as well as their dependency on Γ. Moreover, a 'gas bubble' region is also found in the phase diagram, which triggers the question of why one or the other dissipation mechanisms appear in the system. A comparison of phase diagrams measured with various combinations of granular layer thickness h and container height H indicates that the filling fraction h/H is the dominating factor [Butzhammer, 2012]: 'Gas bubbles' are more favoured for small h/H, while spiral/kink patterns are more favoured for larger h/H.

In a former work [R6: Huang & Rehberg, 2011], a simplified model was introduced to explain the favoured period tripling behaviour in the system for one certain frequency. It considers the granular layer as a single particle bouncing with COR $= 0$ in the container. After colliding with the container wall, the particle may detach immediately or move together with the container, depending on the whether the driving force is sufficiently large to overcome the sum of the capillary and gravitational forces (see the sketch in Fig. 3.28 b). Here in Fig. 3.28 (b), a diagram of periodicity from such a model for the specific experimental condition used in Fig. 3.28 (a) is presented. Qualitatively, the model predicts a dominating period tripling region (red) with its boundaries growing with f. Quantitatively, the starting $f \approx 55$ Hz and the boundaries for f up to 80 Hz agree with the rotating spiral region formed in the experiments. For

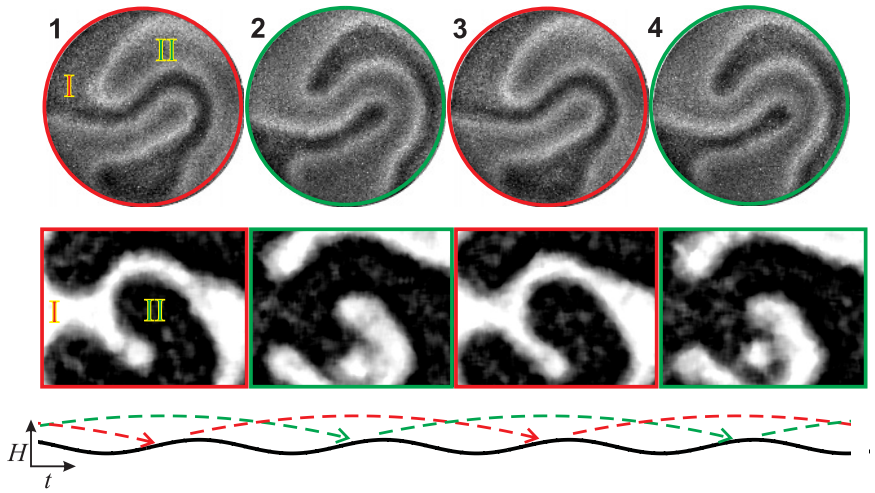

Figure 3.29: Upper row: Snapshots of the period doubling pattern taken at a fixed phase of 4 consequent vibration cycles. Middle row: Corresponding spatially resolved covariance at the colliding phase in the center region of the container, where the mobility of the particles are represented by the brightness of the image. Lower row: Height of the center of mass of the two anti-phase regions (marked with I and II) as a function of time. The snapshots used in the upper rows correspond to the time when region I (cycle 1 and 3, red border) or II (cycle 2 and 4, green border) collide with the vibrating bottom (black line). Collisions with the lid of the container are found to be less prominent for the period doubling pattern.

higher frequencies, the threshold for spiral pattern is underestimated by the model. This can be attributed to the enhanced energy transfer into the local vibrational degrees of freedom, i.e. the effective 'thermal' energy, which weakens the single particle assumption. In addition, the diagram exhibits horizontal strips with periodicity growing with Γ. Those regions correspond to the situation that only collisions with the container bottom occur. In those regions, we speculate that the energy injection can be well dissipated through the particle-particle interactions in the liquidlike phase, thus no additional energy dissipation mechanisms, e.g. patterns or 'gas bubbles', are needed.

In short, despite of the simplicity of the model, it can to some extent quantitatively predict the dominating periodicity of the pattern. More specifically, it indicates that the collisions with the lid, or to say the distance $H - h$ for the granular layer to travel play an important role. Thus the system could in principle generate patterns with a controlled number of periodicity, e.g., four-phase patterns [Elphick *et al.*, 1998; Lin *et al.*, 2000; Meron, 1999; Marts *et al.*, 2004].

Period doubling pattern is also observed in a relatively small frequency region of the phase diagram shown in Fig. 3.28 (a). It corresponds as well to kink waves, but non-propagating. As the sequence of snapshots in Fig. 3.29 shows, the kink fronts swing back and forth as one (I) or the other (II) region collides with the container. This fact can be clearly illustrated in the same manner as the rotation of spiral arms. As the spatially resolved covariance images shown in the middle panel indicate, collisions of region I with the container bottom lead to a granular temperature gradient towards region II, thus push the kink front along the same direction. As region II collides with the container in the next vibration cycle, a reversed temperature gradient leads

to a counter-flow. Note that the curved kink fronts shown here are not the steady state, they will slowly evolve into a target pattern. Further investigations are necessary to characterize such a relaxation process, in order to shed light on the emerging line tension in such a non-equilibrium model system.

3.5 How does shape matter?

Most of the investigations on the dynamics of granular matter, including the ones described above, use spherical particles or circular disks as granular particles for the sake of simplicity. Despite of such simplicity, I have demonstrated above that the collective behaviour of dry as well as wet granular matter driven far from thermodynamic equilibrium is far from trivial and deserves deeper understandings. However, as shown in Fig. 2.2 (a), grains picking up arbitrarily from the world outside of the lab will have a certain shape. Moreover, as demonstrated by Fig. 3.9 in Section 3.3.1, spherical particles typically used in the lab, despite of how well being polished during the manufacturing process, will exhibit time evolving surface morphologies that influence the collective behaviour such as phase transitions. Therefore, one has to bear in mind that *shape matters* while dealing with real life applications such as predictions of landslides or debris flows.

Stepping further, we can ask the follow-up question: How does shape matter? Due to the large variety of possibilities, including changes into regular or irregular shapes as well as changes at a surface or a global level, it is logic to consider the key factors that a variation of shape will deliver. One of the factors is the aspect ratio of ellipsoidal particles: It determines, as discussed in Section 1.1, how many candies can be fit into a jar. Another factor is considered to be the coordination number, i.e. how many neighbours a particle can have. It is an essential parameter accompanying with any ordered state of any particle systems, despite of being thermally or athermally driven. It is also closely related to the mechanical properties of such order states. Preliminary investigations for both parameters are presented below with dry granular rods (Subsection 3.5.1) [P2: Mueller *et al.*, 2014] and wet granular hexagons (Subsection 3.5.2) as model systems.

3.5.1 Granular rods

Beside the well known example of molecules with a rod-like shape organizing into various liquid crystalline phases [Gennes & Prost, 1995], the self-organization of rod-like particles into ordered states is a universal phenomenon appearing widely in nature. Examples range from thermally driven molecules, colloids or polymers [Stephen & Straley, 1974; Onsager, 1949; Vroege & Lekkerkerker, 1992] to granular particles such as a pile of rice [Frette *et al.*, 1996] and active particles such as bacteria colonies [Zhang *et al.*, 2010], actin filaments [Schaller *et al.*, 2010], as well as animal groups [Buhl, 2006; Couzin *et al.*, 2005; Liu *et al.*, 2013]. Theoretically, considering purely hard rods with excluded volume interactions is found to be sufficient to drive the transition from an isotropic to an uniaxial nematic state [Vroege & Lekkerkerker, 1992; de las Heras *et al.*, 2013], thus triggering, again, the question of how well can those theories be applied to non-equilibrium systems.

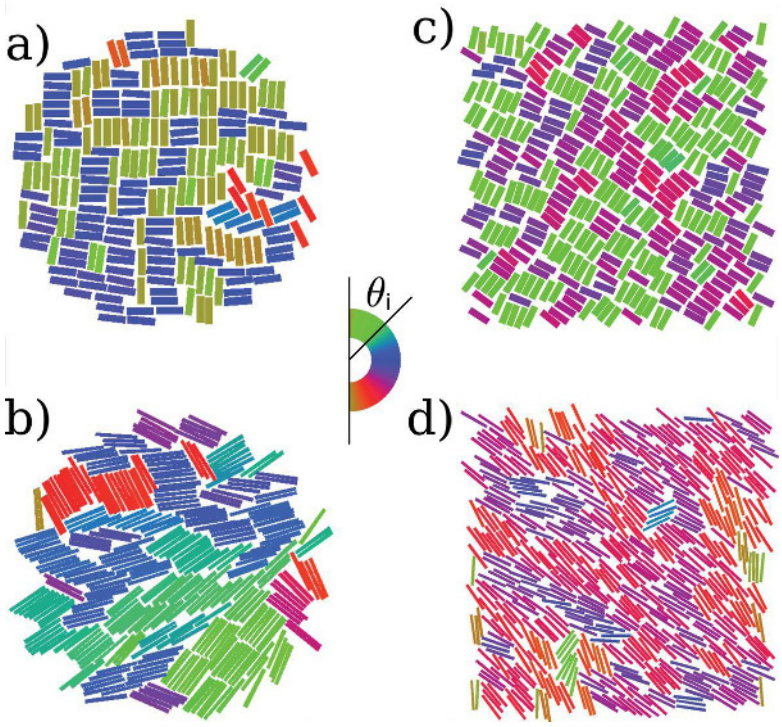

Figure 3.30: Typical snapshots of tetratic (upper row, aspect ratio $l/d = 3.3$) and uniaxial nematic (lower row, $l/d = 10.0$) ordering in the bulk. a) and b) are reconstructed from the positions and orientations of particles detected experimentally in the center region of the container. c) and d) are from Monte Carlo (MC) simulations with periodical boundary conditions. The rods are painted with various colors according to their orientations. Images adapted from P2: Mueller *et al.*, [2014].

With vertically agitated rod-shaped particles in a quasi-two-dimensional configurations as a model system, it is demonstrated that the aspect ratio and area fraction ϕ are the key parameters determining the ordering transitions [P2: Mueller *et al.*, 2014]. Moreover, as presented in Fig. 3.30, the ordered states (tetratic and uniaxial nematic) from both experiments and MC simulations exhibit certain similarities. Such a striking similarity across the two dramatically different systems reveals the universality of such a transition: As long as particles are sufficiently mobilized, confinement will lead to the transition into a tetratic at low aspect ratios or a uniaxial nematic state at large aspect ratios. This finding suggests that the exact way of energy injection is not essential for the transitions, which is confirmed with a variation of Γ in the experiments. Quantitatively, both experiments and MC simulations suggest the same critical aspect ratio $\approx 8.3 \pm 1.7$ separating tetratic and uniaxial nematic states. The critical area fractions measured experimentally for the ordering transitions to occur are slightly larger than those from MC simulations. Such a difference can be attributed to the fact that granular rods continuously collect energy from the vibrating plate, which may generate temporal disorder to a system that could in principle relax into an ordered state. Further experiments are being carried out presently to distinguish further universal and non-universal factors dominating the transitions.

3.5.2 Hexagonal disks and more

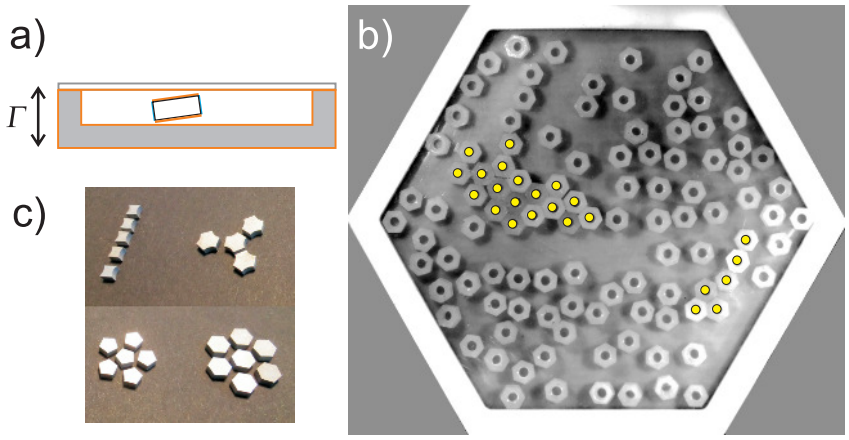

Figure 3.31: Clustering of wet hexagonal disks under vertical agitations. a) A sketch of the experimetal set-up. The disks are treated in a way that only their side walls are hydrophilic (blue), all other surfaces are hydrophobic (orange). b) Top view of clusters formed (marked with yellow dots) by hexagonal disks in a hexagonal confinement. c) A systematic tuning of the particle shape is planned to investigate the influence from the maximum coordination number N_{COR} on the collective behaviour. Sample disks with shape designed: Upper and lower rows correspond to N_{COR} =2, 3 and 5, 6.

For thermal systems, Damasceno *et al.* [2012] has analysed systematically the ordering transition of 145 various types of polyhedra . Particularly, they showed that the coordination number and the isoperimetric quotient, which measures how close to a spherical shape a particle is, are the key parameters dominating the ordered state. For particles close to spheres and with coordination number close to 12, FCC packings are preferred. While for strongly anisotropic rod-like or disk-like particles with coordination number ≈ 2, as suggested in the above Section 3.5.1, liquid crystalline phases arise. Thus, the task for our athermal model system is to find out whether such a diagram applies as well to non-equilibrium systems or not.

As a starting point, hexagonal disks are used because they have the same coordination number as spherical particles confined in a quasi-two-dimensional conditions. Due to the possibility of having a much larger contact area, clusters formed by the wet disks are expected to have much stronger rigidity. To avoid such kind of rigidity enhancement at other surfaces of the disks, special efforts have been taken to allow hydrophilic surfaces only at the side walls of the disks (Fig. 3.31 a). Figure 3.31 (b) demonstrates the collective behaviour of such a model system: Different from isolated disks that move vigorously upon agitation, the rigid blocks formed by the disks (marked with yellow dots) are much less mobile: They tend to stay on the bottom of the container without any movements. In addition to the currently ongoing investigations on the comparisons between spheres and hexagonal disks, it is also planned in the future to measure the collective behaviour as well as associated 'microscopic' particle-particle interactions for disks with designed shapes. As shown in Fig. 3.31 (c), such a shape tuning will effectively influence the maximum number of neighbours of the particles, thus

allow a systematic investigations on the influence from the other key factor, namely the maximum coordination number in the non-equilibrium model system.

4 Concluding remarks

From the dissipative interactions of granular particles at a 'microscopic' level, to their collective behaviour at a 'macroscopic' level, the studies presented in the thesis are devoted to a better understanding of the following two questions:

- How well are 'macroscopic' and 'microscopic' worlds connected through the emerging time, length and energy scales?
- How well can existing knowledges on thermal systems be extended to systems driven far from thermodynamic equilibrium?

These questions are addressed with agitated granular matter, particularly with cohesive particles, as a non-equilibrium model system. In Chapter 2, a characterization of possible energy dissipation mechanisms, particularly for the case with wetting liquid mediated, provides the critical time, length and energy scales associated with 'microscopic' particle-particle interactions. In Chapter 3, I have shown that those critical scales, particularly the dissipative energy scale, indeed play an important role in determining collective behaviour in the 'macroscopic' world, ranging from surface melting (Sec.s sections 3.3.1 and 3.4.1) to clustering (Sec. 3.3.2), from phase transitions (Sec. 3.4.3) to pattern formation (Sec. 3.4.4), despite of the direction of driving and the dimensionality. Moreover, signatures of surface melting, emerging inter-facial tension, phase separations (Sec. 3.4.2), as well as ordering transitions of rod-like particles (Sec. 3.5.1) all find their counter-parts in equilibrium systems, suggesting the essential role such a model system can take for a better understanding of non-equilibrium systems in general. Such an understanding is important since the whole universe is an evolving non-equilibrium system [Cross & Greenside, 2009].

More specifically to the physics of granular matter, careful characterizations of their dynamical behaviour are essential in a large variety of industrial applications as well as in geologically disastrous events, as introduced in Chap. 1. The characterizations of wet COR at the 'microscopic' level in Chapter 2 provide appropriate models for large scale simulations aiming at real life applications [Yu *et al.*, 2013]. The characterizations of collective behaviour presented in Chap. 3 demonstrate the key role that 'microscopic' properties can play. More importantly, possible links between the those 'microscopic' energy scales and 'macroscopic' behaviour found in various experimental investigations call for a continuum description independent on the detailed nature of energy injection and dissipation. At this point, I would like to add the following statement to the one given by Roland Clift quoted at the beginning of Chap. 2:

> "Before measure properties, understand their connections."

Concerning the road ahead, I would like to continue with the following steps toward a deeper understanding of the two general questions raised above:

1. At a 'microscopic' level: Develop a refined model for wet impacts considering higher order approximations and contact line dynamics, based on further characterizations on the capillary bridge forming and rupturing dynamics.

2. At a 'macroscopic' level: Explore possible definitions for the properties of wet granular liquid, such as the interfacial tension, and discuss the possibility to generalize those definitions to non-equilibrium systems.

3. Bridging 'macroscopic' and 'microscopic' perspectives: Represent wet granular agglomerates with the connection network of particles, and develop algorithms to characterize the topology of such networks at various simplification levels, in order to explore essential control parameters at a 'microscopic' level that determines the mechanical properties of wet granular matter at a 'macroscopic' level.

4. Addressing further the influence from shapes: Adjust systematically the maximum coordination number via tuning the shape of particles, in order to discuss the universal role that this control parameter plays in the ordering transitions of particles, across both thermal and athermal systems.

5 Bibliography

AGU 2013 Bingham canyon mine landslide. URL http://blogs.agu.org/landslideblog/2013/04/12/.

Antonyuk, S., Heinrich, S., Tomas, J., Deen, N. G., Buijtenen, M. S. & Kuipers, J. A. M. 2010 Energy absorption during compression and impact of dry elastic-plastic spherical granules. *Granular Matter* **12** (1), 15–47.

Aoki, K. M., Akiyama, T., Maki, Y. & Watanabe, T. 1996 Convective roll patterns in vertically vibrated beds of granules. *Phys. Rev. E* **54** (1), 874–883.

Aranson, I. S. & Tsimring, L. S. 2006 Patterns and collective behavior in granular media: Theoretical concepts. *Reviews of Modern Physics* **78** (2), 641.

Aranson, I. S. & Tsimring, L. S. 2009 *Granular Patterns*. Oxford University Press.

Arbell, H. & Fineberg, J. 2000 Temporally harmonic oscillons in newtonian fluids. *Phys. Rev. Lett.* **85** (4), 756–759.

Aumaître, S., Schnautz, T., Kruelle, C. A. & Rehberg, I. 2003 Granular phase transition as a precondition for segregation. *Phys. Rev. Lett.* **90** (11), 114302.

Bagnold, R. A. 1941 *The physics of blown sand and desert dunes*. Mineola, N.Y.: Methuen, London.

Bak, P. 1999 *How Nature Works: the science of self-organized criticality*, 1 edition. New York, NY, USA: Copernicus.

Bak, P., Tang, C. & Wiesenfeld, K. 1987 Self-organized criticality: An explanation of the 1/f noise. *Phys. Rev. Lett.* **59** (4), 381–384.

Bak, P., Tang, C. & Wiesenfeld, K. 1988 Self-organized criticality. *Phys. Rev. A* **38** (1), 364–374.

Barnocky, G. & Davis, R. H. 1988 Elastohydrodynamic collision and rebound of spheres: Experimental verification. *Phys. Fluids* **31** (6), 1324.

Becker, K., Becker, M. & Schwarz, J. H. 2006 *String Theory and M-Theory: A Modern Introduction*. Cambridge University Press.

Bi, D., Zhang, J., Chakraborty, B. & Behringer, R. P. 2011 Jamming by shear. *Nature* **480** (7377), 355–358.

Bonn, D., Eggers, J., Indekeu, J., Meunier, J. & Rolley, E. 2009 Wetting and spreading. *Rev. Mod. Phys.* **81** (2), 739–805.

Bougie, J., Moon, S. J., Swift, J. B. & Swinney, H. L. 2002 Shocks in vertically oscillated granular layers. *Phys. Rev. E* **66** (5), 051301.

Bower, R. 1953 The adsorption of gases at high saturations II: The thickness of the unsaturated helium film **44**, 485.

Breu, A. P. J., Ensner, H.-M., Kruelle, C. A. & Rehberg, I. 2003 Reversing the brazil-nut effect: Competition between percolation and condensation. *Phys. Rev. Lett.* **90** (1), 014302.

Brey, J. J., Cubero, D. & Ruiz-Montero, M. J. 1999 High energy tail in the velocity distribution of a granular gas. *Phys. Rev. E* **59** (1), 1256–1258.

Bridges, F. G., Hatzes, A. & Lin, D. N. C. 1984 Structure, stability and evolution of saturn's rings. *Nature* **309**, 333.

Brilliantov, N. & Pöschel, T. 2004 *Kinetic theory of granular gases*. Oxford; New York: Oxford University Press.

Brilliantov, N. V., Spahn, F., Hertzsch, J.-M. & Pöschel, T. 1996 Model for collisions in granular gases. *Phys. Rev. E* **53** (5), 5382–5392.

Buchholtz, V. & Poeschel, T. 1996 Avalanche statistics of sand heaps. *J. Stat. Phys.* **84**, 1373, vol.84, 1373 (1996).

Buhl, J. 2006 From disorder to order in marching locusts. *Science* **312** (5778), 1402–1406.

Burtally, N., King, P. J. & Swift, M. R. 2002 Spontaneous air-driven separation in vertically vibrated fine granular mixtures. *Science* **295** (5561), 1877–1879.

Butt, H. J. & Kappl, M. 2009 Normal capillary forces. *Advances in Colloid and Interface Science* **146** (1-2), 48–60.

Butzhammer, L. 2012 Musterbildung in kohäsivem granulat. B. S. thesis, Universität Bayreuth.

Cahn, J. W. 1965 Phase separation by spinodal decomposition in isotropic systems. *The Journal of Chemical Physics* **42** (1), 93–99.

Carus, T. L. & Leonard, W. E. 2004 *On the Nature of Things*. Mineola, N.Y: Dover Publications.

Cassini 2014 About saturn & its moons. URL http://saturn.jpl.nasa.gov/science/index.cfm?SciencePageID=55.

Cates, M. E. & Clegg, P. S. 2008 Bijels: a new class of soft materials. *Soft Matter* **4** (11), 2132.

Chen, Z., Segev, M. & Christodoulides, D. N. 2012 Optical spatial solitons: historical overview and recent advances. *Rep. Prog. Phys.* **75** (8), 086401.

Chladni, E. F. F. 1787 *Entdeckungen über die Theorie des Klanges*. Leipzig: Weizmanns Erben und Reih.

Clement, E. & Rajchenbach, J. 1991 Fluidization of a bidimensional powder. *Europhysics Letters* **16** (2), 133–138.

Clewett, J. P. D., Roeller, K., Bowley, R. M., Herminghaus, S. & Swift, M. R. 2012 Emergent surface tension in vibrated, noncohesive granular media. *Phys. Rev. Lett.* **109** (22), 228002.

Clément, E., Duran, J. & Rajchenbach, J. 1992 Experimental study of heaping in a two-dimensional "sand pile". *Phys. Rev. Lett.* **69** (8), 1189–1192.

Colaprete, A., Schultz, P., Heldmann, J., Wooden, D., Shirley, M., Ennico, K., Hermalyn, B., Marshall, W., Ricco, A., Elphic, R. C., Goldstein, D., Summy, D., Bart, G. D., Asphaug, E., Korycansky, D., Landis, D. & Sollitt, L. 2010 Detection of water in the LCROSS ejecta plume. *Science* **330** (6003), 463–468.

Couder, Y., Fort, E., Gautier, C.-H. & Boudaoud, A. 2005 From bouncing to floating: Noncoalescence of drops on a fluid bath. *Phys. Rev. Lett.* **94** (17), 177801.

Coulomb, C. A. 1773 Essay on the rules of maximis and minimis applied to some problems of equilibrium related to architechture **7**, 343.

Couzin, I. D., Krause, J., Franks, N. R. & Levin, S. A. 2005 Effective leadership and decision-making in animal groups on the move. *Nature* **433** (7025), 513–516.

Craik, A. D. 2004 The origins of water wave theory. *Annual Review of Fluid Mechanics* **36** (1), 1–28.

Crida, A. & Charnoz, S. 2012 Formation of regular satellites from ancient massive rings in the solar system. *Science* **338** (6111), 1196–1199.

Cross, M. & Greenside, H. 2009 *Pattern Formation and Dynamics in Nonequilibrium Systems*. Cambridge University Press.

Damasceno, P. F., Engel, M. & Glotzer, S. C. 2012 Predictive self-assembly of polyhedra into complex structures. *Science* **337** (6093), 453–457.

Das, B. M. 1997 *Advanced Soil Mechanics*. Washington: Taylor & Francis.

Dash, J. G., Rempel, A. W. & Wettlaufer, J. S. 2006 The physics of premelted ice and its geophysical consequences. *Rev. Mod. Phys.* **78** (3), 695.

Davis, R., Serayssol, J. M. & Hinch, E. J. 1986 The elastohydrodynamic collision of two spheres. *J. Fluid Mech.* **163**, 479.

Davis, R. H., Rager, D. A. & Good, B. T. 2002 Elastohydrodynamic rebound of spheres from coated surfaces. *J. Fluid Mech.* **468**, 107.

Deegan, R. D. 2000 Pattern formation in drying drops. *Phys. Rev. E* **61** (1), 475–485.

Deegan, R. D., Bakajin, O., Dupont, T. F., Huber, G., Nagel, S. R. & Witten, T. A. 1997 Capillary flow as the cause of ring stains from dried liquid drops. *Nature* **389** (6653), 827–829.

Donahue, C. M., Davis, R. H., Kantak, A. A. & Hrenya, C. M. 2012 Mechanisms for agglomeration and deagglomeration following oblique collisions of wet particles. *Physical Review E* **86** (2).

Donahue, C. M., Hrenya, C. M. & Davis, R. H. 2010*a* Stokes's cradle: Newton's cradle with liquid coating. *Phys. Rev. Lett.* **105** (3), 034501.

Donahue, C. M., Hrenya, C. M., Davis, R. H., Nakagawa, K. J., Zelinskaya, A. P. & Joseph, G. G. 2010*b* Stokes' cradle: normal three-body collisions between wetted particles. *Journal of Fluid Mechanics* **650**, 479–504.

Donev, A., Cisse, I., Sachs, D., Variano, E. A., Stillinger, F. H., Connelly, R., Torquato, S. & Chaikin, P. M. 2004 Improving the density of jammed disordered packings using ellipsoids. *Science* **303** (5660), 990–993.

Duran, J. 2000 *Sands, Powders and Grains (An Introduction to the Physics of Granular Materials)*, New York: Springer-Verlag.

Duran, J., Mazozi, T., Clément, E. & Rajchenbach, J. 1994 Size segregation in a two-dimensional sandpile: Convection and arching effects. *Phys. Rev. E* **50** (6), 5138–5141.

Duran, J., Rajchenbach, J. & Clément, E. 1993 Arching effect model for particle size segregation. *Phys. Rev. Lett.* **70** (16), 2431–2434.

Edwards, D. & Brenner, H. 1991 *Interfacial Transport Processes and Rheology*. Butterworth-Heinemann.

Eggers, J. 1997 Nonlinear dynamics and breakup of free-surface flows. *Rev. Mod. Phys.* **69** (3), 865–930.

Eggers, J. 1999 Sand as Maxwell's demon. *Phys. Rev. Lett.* **83** (25), 5322–5325.

Elbaum, M. & Lipson, S. G. 1994 How does a thin wetted film dry up? *Phys. Rev. Lett.* **72** (22), 3562–3565.

Elphick, C., Hagberg, A. & Meron, E. 1998 Phase front instability in periodically forced oscillatory systems. *Phys. Rev. Lett.* **80** (22), 5007–5010.

Eral, H. B., Augustine, D. M., Duits, M. H. G. & Mugele, F. 2011 Suppressing the coffee stain effect: how to control colloidal self-assembly in evaporating drops using electrowetting. *Soft Matter* **7** (10), 4954–4958.

Eshuis, P., van der Weele, K., Lohse, D. & van der Meer, D. 2010 Experimental realization of a rotational ratchet in a granular gas. *Phys. Rev. Lett.* **104** (24), 248001.

Eshuis, P., van der Weele, K., van der Meer, D., Bos, R. & Lohse, D. 2007 Phase diagram of vertically shaken granular matter. *Phys. Fluids* **19** (12), 123301.

Falcon, r., Kumar, K., Bajaj, K. M. S. & Bhattacharjee, J. K. 1999 Heap corrugation and hexagon formation of powder under vertical vibrations. *Phys. Rev. E* **59** (5), 5716–5720.

Faraday, M. 1831 On a peculiar class of acoustical figures; and on certain forms assumed by a group of particles upon vibrating elastic surfaces. *Philosophical Transactions of the Royal Society* **121**, 299–318.

Ferriani, P., von Bergmann, K., Vedmedenko, E. Y., Heinze, S., Bode, M., Heide, M., Bihlmayer, G., Blügel, S. & Wiesendanger, R. 2008 Atomic-scale spin spiral with a unique rotational sense: Mn monolayer on W(001). *Physical Review Letters* **101** (2), 027201.

Fingerle, A., Roeller, K., Huang, K. & Herminghaus, S. 2008 Phase transitions far from equilibrium in wet granular matter. *New J. Phys.* **10** (5), 053020.

Fredsøe, J. & Deigaard, R. 1992 *Mechanics of Coastal Sediment Transport*. World Scientific.

Frette, V., Christensen, K., Malthe-Sørenssen, A., Feder, J., Jøssang, T. & Meakin, P. 1996 Avalanche dynamics in a pile of rice. *Nature* **379** (6560), 49–52.

Geng, J., Howell, D., Longhi, E., Behringer, R. P., Reydellet, G., Vanel, L., Clément, E. & Luding, S. 2001 Footprints in sand: The response of a granular material to local perturbations. *Phys. Rev. Lett.* **87** (3), 035506.

de Gennes, P. G. 1985 Wetting: statics and dynamics. *Rev. Mod. Phys.* **57** (3), 827–863.

de Gennes, P. G. 1999 Granular matter: a tentative view. *Rev. Mod. Phys.* **71** (2), S374.

Gennes, P. G. d. & Prost, J. 1995 *The Physics of Liquid Crystals*. Clarendon Press.

Goldhirsch, I. 2003 Rapid granular flows. *Annu. Rev. Fluid Mech.* **35**, 267.

Goldhirsch, I. & Zanetti, G. 1993 Clustering instability in dissipative gases. *Phys. Rev. Lett.* **70** (11), 1619–1622.

Goudie, A. S. 2013 *Arid And Semi Arid Geomorphology*. Cambridge University Press.

Greenberg, G. 2008 *A grain of sand : nature's secret wonder*. St. Paul, MN: Voyageur Press.

Götzendorfer, A., Tai, C.-H., Kruelle, C. A., Rehberg, I. & Hsiau, S.-S. 2006 Fluidization of a vertically vibrated two-dimensional hard sphere packing: A granular meltdown. *Phys. Rev. E* **74** (1), 011304.

Guyon, E., Roux, S., Hansen, A., Bideau, D., Troadec, J.-P. & Crapo, H. 1990 Non-local and non-linear problems in the mechanics of disordered systems: application to granular media and rigidity problems. *Rep. Prog. Phys.* **53** (4), 373.

Hales, T. 2005 A proof of the kepler conjecture. *Annals of Mathematics* **162** (3), 1065–1185.

Halperin, B. I. & Nelson, D. R. 1978 Theory of two-dimensional melting. *Phys. Rev. Lett.* **41** (2), 121.

Halsey, T. & Levine, A. 1998 How sandcastles fall. *Phys. Rev. Lett.* **80** (14), 3141–3144.

Held, G. A., Solina, D. H., Solina, H., Keane, D. T., Haag, W. J., Horn, P. M. & Grinstein, G. 1990 Experimental study of critical-mass fluctuations in an evolving sandpile. *Phys. Rev. Lett.* **65** (9), 1120–1123.

de las Heras, D., Martínez-Ratón, Y., Mederos, L. & Velasco, E. 2013 Two-dimensional nematics in bulk and confined geometries. *Journal of Molecular Liquids* **185**, 13–19.

Herminghaus, S. 2005 Dynamics of wet granular matter. *Adv. Phys.* **54** (3), 221–261.

Herminghaus, S. 2013 *Wet Granular Matter: A Truly Complex Fluid*, *Series in Soft Condensed Matter*, vol. 6. World Scientific.

Hertz, H. 1882 Über die Berührung fester elastischer Körper. *J. reine und angewandte Mathematik* **92**, 156.

Hoekstra, H., Vermant, J., Mewis, J. & Fuller, G. G. 2003 Flow-induced anisotropy and reversible aggregation in two-dimensional suspensions. *Langmuir* **19** (22), 9134–9141.

Hong, D. C., Quinn, P. V. & Luding, S. 2001 Reverse brazil nut problem: Competition between percolation and condensation. *Phys. Rev. Lett.* **86** (15), 3423–3426.

Hornbaker, D. J., Albert, R., Albert, I., Barabasi, A. L. & Schiffer, P. 1997 What keeps sandcastles standing? *Nature* **387** (6635), 765.

Howell, D., Behringer, R. P. & Veje, C. 1999 Stress fluctuations in a 2D granular couette experiment: A continuous transition. *Phys. Rev. Lett.* **82** (26), 5241–5244.

Huang, K., Röller, K. & Herminghaus, S. 2009 Universal and non-universal aspects of wet granular matter under vertical vibrations. *Eur. Phys. J. Spec. Top.* **179** (1), 25–32.

Huang, K., Zhang, P., Miao, G. & Wei, R. 2006 Dynamic behaviors of supersonic granular media under vertical vibration. *Ultrasonics* **44**, e1487–e1489.

Inoue, T. & Okaya, K. 1994 In *Proceedings of the Eighth European Symposium on Comminution* (ed. E. Forssberg), pp. 425–437.

Ivanhoe 2011 Ivanhoe reservoir covered with 400,000 black plastic balls. URL http://www.amusingplanet.com/2011/11/ivanhoe-reservoir-covered-with-400000.html.

Iveson, S. M., Litster, J. D., Hapgood, K. & Ennis, B. J. 2001 Nucleation, growth and breakage phenomena in agitated wet granulation processes: a review. *Powder Technology* **117** (1-2), 3–39.

Jaeger, H. M., Liu, C.-h. & Nagel, S. R. 1989 Relaxation at the angle of repose. *Phys. Rev. Lett.* **62** (1), 40–43.

Jaeger, H. M., Nagel, S. R. & Behringer, R. P. 1996 Granular solids, liquids, and gases. *Rev. Mod. Phys.* **68** (4), 1259.

Janssen, H. A. 1895 Versuche über getreidedruck in silozellen. *Zeitschrift des Vereines deutscher Ingenieure* **39** (35), 1045–1049.

Jensen, P. H. J. 1998 *Self-Organized Criticality: Emergent Complex Behavior in Physical and Biological Systems*. Cambridge; New York: Cambridge University Press.

Jop, P., Forterre, Y. & Pouliquen, O. 2006 A constitutive law for dense granular flows. *Nature* **441** (7094), 727–730.

Kerr, R. A. 2010 How wet the moon? Just damp enough to be interesting. *Science* **330** (6003), 434–434.

Khan, Z. S. & Morris, S. W. 2005 Subdiffusive axial transport of granular materials in a long drum mixer. *Phys. Rev. Lett.* **94** (4), 048002.

Knight, J. B., Jaeger, H. M. & Nagel, S. R. 1993 Vibration-induced size separation in granular media: The convection connection. *Phys. Rev. Lett.* **70** (24), 3728–3731.

Kondic, L. 1999 Dynamics of spherical particles on a surface: Collision-induced sliding and other effects. *Phys. Rev. E* **60** (1), 751.

Koos, E. & Willenbacher, N. 2011 Capillary forces in suspension rheology. *Science* **331** (6019), 897 –900.

Laroche, C., Douady, S. & Fauve, S. 1989 Convective flow of granular masses under vertical vibrations. *J. Phys. France* **50** (7), 699–706.

Lin, A. L., Hagberg, A., Ardelea, A., Bertram, M., Swinney, H. L. & Meron, E. 2000 Four-phase patterns in forced oscillatory systems. *Phys. Rev. E* **62** (3), 3790–3798.

Lioubashevski, O., Hamiel, Y., Agnon, A., Reches, Z. & Fineberg, J. 1999 Oscillons and propagating solitary waves in a vertically vibrated colloidal suspension. *Phys. Rev. Lett.* **83** (16), 3190–3193.

Litster, J., Ennis, B. & Lian, L. 2004 *The Science and Engineering of Granulation Processes*. Springer.

Liu, A. J. & Nagel, S. R. 1998 Nonlinear dynamics: Jamming is not just cool any more. *Nature* **396** (6706), 21–22.

Liu, Q.-X., Doelman, A., Rottschäfer, V., Jager, M. d., Herman, P. M. J., Rietkerk, M. & Koppel, J. v. d. 2013 Phase separation explains a new class of self-organized spatial patterns in ecological systems. *Proc. Natl. Acad. Sci.* **110** (29), 11905–11910.

Losert, W., Cooper, D. G. W. & Gollub, J. P. 1999 Propagating front in an excited granular layer. *Phys. Rev. E* **59** (5), 5855–5861.

Lu, P. J., Conrad, J. C., Wyss, H. M., Schofield, A. B. & Weitz, D. A. 2006 Fluids of clusters in attractive colloids. *Phys. Rev. Lett.* **96** (2), 028306.

Mandelbrot, B. 2002 *Gaussian Self-Affinity and Fractals: Globality, The Earth, 1/f Noise, and R/S*. Springer.

Manoharan, V. N., Elsesser, M. T. & Pine, D. J. 2003 Dense packing and symmetry in small clusters of microspheres. *Science* **301** (5632), 483 –487.

Marín, l. G., Gelderblom, H., Susarrey-Arce, A., Houselt, A. v., Lefferts, L., Gardeniers, J. G. E., Lohse, D. & Snoeijer, J. H. 2012 Building microscopic soccer balls with evaporating colloidal fakir drops. *Proc. Natl. Acad. Sci.* .

Marston, J., Yong, W., Ng, W., Tan, R. & Thoroddsen, S. 2010 Cavitation structures formed during the rebound of a sphere from a wetted surface. *Experiments in fluids* p. 1–18.

Marts, B., Hagberg, A., Meron, E. & Lin, A. 2004 Bloch-front turbulence in a periodically forced belousov-zhabotinsky reaction. *Physical Review Letters* **93** (10).

Mazzone, D., Tardos, G. & Pfeffer, R. 1987 The behavior of liquid bridges between two relatively moving particles. *Powder technology* **51** (1), 71–83.

Mehta, A. 2007 *Granular Physics*. Cambridge University Press.

Meron, E. 1999 Phase front and synchronization patterns in forced oscillatory systems .

Messier 2014 URL http://en.wikipedia.org/Messier_74 2014-07-02.

Miao, G. Q., Huang, K., Yun, Y., Zhang, P., Chen, W. Z. & Wei, R. J. 2006 Formation and transport of a sand heap in an inclined and vertically vibrated container. *Phys. Rev. E* **74** (2), 021304.

Milotti, E. 2002 1/f noise: a pedagogical review. *Preprint* arXiv: physics/0204033.

Mitarai, N. & Nori, F. 2006 Wet granular materials. *Advances in Physics* **55** (1-2), 1–45.

MSL 2013 Mars science laboratory. URL http://mars.jpl.nasa.gov:80/msl/mission.

Métayer, J.-F., Iii, D. J. S., Radin, C., Swinney, H. L. & Schröter, M. 2011 Shearing of frictional sphere packings. *Eur. Phys. L* **93** (6), 64003.

Nagel, S. R. 1992 Instabilities in a sandpile. *Rev. Mod. Phys.* **64** (1), 321–325.

Newitt, D. & Conway-Jones, J. M. 1958 Tensile strength and capillary pressure of moist agglomerates **36**, 422.

Newton, S. I. 1687 *Mathematical Principles of Natural Philosophy*.

Nikolaides, M. G., Bausch, A. R., Hsu, M. F., Dinsmore, A. D., Brenner, M. P., Gay, C. & Weitz, D. A. 2002 Electric-field-induced capillary attraction between like-charged particles at liquid interfaces. *Nature* **420**, 299.

Olafsen, J. S. & Urbach, J. S. 1998 Clustering, order, and collapse in a driven granular monolayer. *Phys. Rev. Lett.* **81** (20), 4369–4372.

Olafsen, J. S. & Urbach, J. S. 2005 Two-dimensional melting far from equilibrium in a granular monolayer. *Phys. Rev. Lett.* **95** (9), 098002.

Onoda, G. Y. & Liniger, E. G. 1990 Random loose packings of uniform spheres and the dilatancy onset. *Phys. Rev. Lett.* **64** (22), 2727–2730.

Onsager, L. 1949 The effects of shape on the interaction of colloidal particles. *Annals of the New York Academy of Sciences* **51** (4), 627–659.

Pieranski, P. 1980 Two-dimensional interfacial colloidal crystals. *Phys. Rev. Lett.* **45** (7), 569.

Pye, K. 2009 *Aeolian sand and sand dunes*. Berlin: Springer.

Rayleigh, F. R. S. 1899 XXXVI. investigations in capillarity:—the size of drops.—the liberation of gas from supersaturated solutions.—colliding jets.—the tension of contaminated water-surfaces. *Philosophical Magazine Series 5* **48** (293), 321–337.

Reimann, P. 2002 Brownian motors: noisy transport far from equilibrium. *Physics Reports* **361** (2–4), 57–265.

Reis, P. M. & Mullin, T. 2002 Granular segregation as a critical phenomenon. *Phys. Rev. Lett.* **89** (24), 244301.

Renninger, W. H. & Wise, F. W. 2013 Optical solitons in graded-index multimode fibres. *Nat. Commun.* **4**, 1719.

Reynolds, O. 1885 On the dilatancy of media composed of rigid particles in contact, with experimental illustrations. *Philosophical Magazine* **20**, 469—481.

Rietz, F. 2013 Convection and segregation of beads in a flat rotating box. PhD thesis, Otto-von-Guericke-Universität Magdeburg.

Ristow, G. H. 2000 *Pattern Formation in Granular Materials*. Springer.

Ristow, G. H., Strassburger, G. & Rehberg, I. 1997 Phase diagram and scaling of granular materials under horizontal vibrations. *Phys. Rev. Lett.* **79** (5), 833–836.

Robinson, D. J. & Earnshaw, J. C. 1992 Experimental study of colloidal aggregation in two dimensions. i. structural aspects. *Phys. Rev. A* **46** (4), 2045.

Röller, K. 2010 Numerical simuations of wet granular matter. PhD thesis, Georg-August-Universität Göttingen.

Roeller, K., Clewett, J. P. D., Bowley, R. M., Herminghaus, S. & Swift, M. R. 2011 Liquid-gas phase separation in confined vibrated dry granular matter. *Phys. Rev. Lett.* **107** (4), 048002.

Roeller, K. & Herminghaus, S. 2011 Solid-fluid transition and surface melting in wet granular matter. *Eur. Phys. Lett.* **96** (2), 26003.

Rosato, A., Strandburg, K. J., Prinz, F. & Swendsen, R. H. 1987 Why the brazil nuts are on top: Size segregation of particulate matter by shaking. *Phys. Rev. Lett.* **58** (10), 1038–1040.

Rumpf, H. 1962 *Agglomeration*. New York: AIME, Interscience.

Russell, J. S. 1844 Report on waves. *Report of the 14th Meeting of the British Association for the Advancement of Science* pp. 311–390.

SAND 2014 Sand festival. URL http://en.wikipedia.org/wiki/Sand_festival 2014-05-27.

Schaller, V., Weber, C., Semmrich, C., Frey, E. & Bausch, A. R. 2010 Polar patterns of driven filaments. *Nature* **467** (7311), 73–77.

Scheel, M., Geromichalos, D. & Herminghaus, S. 2004 Wet granular matter under vertical agitation. *J. Phys.: Condens. Matter* **16** (38), S4213–S4218.

Scheel, M., Seemann, R., Brinkmann, M., Di Michiel, M., Sheppard, A., Breidenbach, B. & Herminghaus, S. 2008 Morphological clues to wet granular pile stability. *Nat. Mater.* **7** (3), 189–193.

Scherer, M. A., Kötter, K., Markus, M., Goles, E. & Rehberg, I. 2000 Swirling granular solidlike clusters. *Phys. Rev. E* **61** (4), 4069–4077.

Schnautz, T., Brito, R., Kruelle, C. A. & Rehberg, I. 2005 A horizontal brazil-nut effect and its reverse. *Phys. Rev. Lett.* **95** (2), 028001.

Schofield, A. & Wroth, P. 1968 *Critical State Soil Mechanics*.

Schröter, M., Nägle, S., Radin, C. & Swinney, H. L. 2007 Phase transition in a static granular system. *Eur. Phys. Lett.* **78** (4), 44004.

Schröter, M., Ulrich, S., Kreft, J., Swift, J. B. & Swinney, H. L. 2006 Mechanisms in the size segregation of a binary granular mixture. *Phys. Rev. E* **74** (1), 011307.

Scott, G. D. 1960 Packing of spheres: Packing of equal spheres. *Nature* **188** (4754), 908–909.

Scott, G. D. & Kilgour, D. M. 1969 The density of random close packing of spheres. *Journal of Physics D: Applied Physics* **2** (6), 863–866.

Shinbrot, T. & Muzzio, F. J. 1998 Reverse buoyancy in shaken granular beds. *Phys. Rev. Lett.* **81** (20), 4365–4368.

Spahn, F. & Schmidt, J. 2006 Hydrodynamic description of planetrary rings. *GAMM-Mitt.* **29**, 115.

Stamou, D., Duschl, C. & Johannsmann, D. 2000 Long-range attraction between colloidal spheres at the air-water interface: The consequence of an irregular meniscus. *Phys. Rev. E* **62** (4), 5263–5272.

Stephen, M. J. & Straley, J. P. 1974 Physics of liquid crystals. *Rev. Mod. Phys.* **46** (4), 617–704.

Strassburger, G. & Rehberg, I. 2000 Crystallization in a horizontally vibrated monolayer of spheres. *Phys. Rev. E* **62** (2), 2517–2520.

Strandburg, K. J. 1988 Two-dimensional melting. *Rev. Mod. Phys.* **60** (1), 161–207.

Stratford, K., Adhikari, R., Pagonabarraga, I., Desplat, J. C. & Cates, M. E. 2005 Colloidal jamming at interfaces: A route to fluid-bicontinuous gels. *Science* **309** (5744), 2198–2201.

Stronge, W. J. 2004 *Impact Mechanics*. Cambridge University Press.

Tennakoon, S. G. K., Kondic, L. & Behringer, R. P. 1999 Onset of flow in a horizontally vibrated granular bed: Convection by horizontal shearing. *Europhysics Letters* **45** (4), 470–475.

Thornton, C. 1997 Coefficient of restitution for collinear collisions of elastic-perfectly plastic spheres. *J. Appl. Mech.* **64** (2), 383–386.

Thoroddsen, S. T. 2006 Fluid dynamics: Droplet genealogy. *Nat. Phys.* **2** (4), 223–224.

Thoroddsen, S. T. & Takehara, K. 2000 The coalescence cascade of a drop. *Physics of Fluids* **12** (6), 1265–1267.

UEPG 2013 European aggregates association: Annual review 2012-2013. URL http://www.uepg.eu/.

Umbanhowar, P. B., Melo, F. & Swinney, H. L. 1996 Localized excitations in a vertically vibrated granular layer. *Nature* **382** (6594), 793–796.

Vanel, L., Howell, D., Clark, D., Behringer, R. P. & Clément, E. 1999 Memories in sand: Experimental tests of construction history on stress distributions under sandpiles. *Phys. Rev. E* **60** (5), R5040–R5043.

Vassileva, N. D., van den Ende, D., Mugele, F. & Mellema, J. 2005 Capillary forces between spherical particles floating at a liquid-liquid interface. *Langmuir* **21** (24), 11190–11200.

Völkel, S. 2014 Messung der Kontaktwinkelhysterese von Wassertropfen auf einer horizontalen Teflonoberfläche. B. S. thesis, Universität Bayreuth.

Vroege, G. J. & Lekkerkerker, H. N. W. 1992 Phase transitions in lyotropic colloidal and polymer liquid crystals. *Rep. Prog. Phys.* **55** (8), 1241.

Wada, K. 1966 Spiral growth of nacre. *Nature* **211** (5056), 1427–1427.

Weir, G. & Tallon, S. 2005 The coefficient of restitution for normal incident, low velocity particle impacts. *Chemical Engineering Science* **60** (13), 3637.

Whitesides, G. M. & Grzybowski, B. 2002 Self-assembly at all scales. *Science* **295** (5564), 2418 –2421.

Wild, M. 2013 Oberächenschmelzen granularer Materie. Diploma thesis, Universität Bayreuth.

Willett, C. D., Adams, M. J., Johnson, S. A. & Seville, J. P. K. 2000 Capillary bridges between two spherical bodies. *Langmuir* **16** (24), 9396–9405.

Wills, B. A. 1997 *Mineral processing technology*, 6. Oxford, U. K.: Butterworth-Heinemann.

Yokoyama, T., Tamura, H., Usui, H. & Jimbo, G. 1994 In *Proceedings of the Eighth European Symposium on Comminution* (ed. E. Forssberg), pp. 413–425.

Yu, A., Dong, K., Yang, R. & Stefan, L. (eds.) 2013 *Powders and grains 2013: proceedings of the 7th International Conference on Micromechanics of Granular Media*, vol. 1542. Melville, New York: American Institute of Physics.

Yunker, P. J., Still, T., Lohr, M. A. & Yodh, A. G. 2011 Suppression of the coffee-ring effect by shape-dependent capillary interactions. *Nature* **476** (7360), 308–311.

Zaccarelli, E. 2007 Colloidal gels: equilibrium and non-equilibrium routes. *J. Phys.-Condes. Matter* **19** (32).

Zhang, H. P., Be'er, A., Florin, E.-L. & Swinney, H. L. 2010 Collective motion and density fluctuations in bacterial colonies. *Proc. Natl. Acad. Sci.* **107** (31), 13626–13630.

6

Preprint Articles

Role of defects in the onset of wall-induced granular convection

Andrea Fortini*
Theoretische Physik II, Physikalisches Institut, Universität Bayreuth, Universitätsstraße 30, D-95447 Bayreuth, Germany and Department of Physics, University of Surrey, Guildford GU2 7XH, United Kingdom

Kai Huang
Experimentalphysik V, Physikalisches Institut, Universität Bayreuth, Universitätsstraße 30, D-95447 Bayreuth, Germany

We investigate the onset of the wall-induced convection in vertically vibrated granular matter by means of experiments and two-dimensional computer simulations. In both simulations and experiments we find that the wall-induced convection occurs inside the *bouncing bed* region of the parameter space in which the granular bed behaves like a bouncing ball. A good agreement between experiments and simulations is found for the peak vibration acceleration at which convection starts. By comparing the results of simulations initialised with and without defects, we find that the onset of convection occurs at lower vibration strengths in the presence of defects. Furthermore, we find that the convection of granular particles initialised in a perfect hexagonal lattice is related to the nucleation of defects and the process is described by an Arrhenius law.

PACS numbers: 45.70.-n, 61.72.Bb, 47.55.P-

I. INTRODUCTION

Mixing and demixing of vibrated granular matter [1, 2] are of importance in nature [3] as well as in many industrial processes. For example, they are used in the pharmaceutical, construction [4] or waste reprocessing [5] industries. The term Brazil Nut Effect (BNE) [6], which originally referred to the rise of a large particle to the top of a container filled with smaller grains, is now used to indicate the more general demixing of differently sized particles under vertical oscillations. Schröter *et al.* [7] reviewed and identified seven possible mechanisms that lead to the BNE and to the Reverse Brazil Nut Effect (RBNE) [8]. Convective cells induced by the walls of the container were found to be a major contributing mechanism to the occurrence of the BNE [9–13].

The complexity of the BNE characterisation is in part due to an underlying dynamical behaviour which even for one component systems is very rich. At driving accelerations smaller than the gravitational acceleration, the granular bed comoves with the bottom wall. Upon increasing the acceleration the granular bed behaves like a bouncing ball [14], and above this bouncing bed region collective undulations (also known as arches) appear [15–18]. At still higher accelerations the granular *Leidenfrost* effect occurs, in which a dense granular fluid hovers over a granular gas. Recently, Eshuis *et al.* [19] systematically drew phase diagrams for all these phenomena, and found at very high accelerations a convective regime in which the sample is completely fluidized [18, 19].

However, this convection regime is distinct from the wall-induced convection which occurs at low accelerations and is one of the driving mechanisms for the BNE. The wall-induced convection is caused by the shear forces between particles and walls. During the upward acceleration the mixture gets compacted and shear forces induced by the side walls propagate efficiently through the whole sample. During the downward motion the mixture is more expanded and consequentially those particles adjacent to the walls experience stronger downward shear forces than those in the centre of the container. The combination of the two type of motions gives rise to convection [7]. This cycle of expansion and compression of the granular bed was studied by Sun *et al.* [20] and found to be strongly dependent on wall friction. Even though their study was done in relation to BNE no connection to the convective motion is made. The onset of convection has been studied extensively in both experiments [21, 22] and with numerical simulations [23–26].

In this article, we study with both computer simulations and experiments the dynamical phase diagram of two-dimensional vertically oscillated granular matter and analyse the mechanism behind the onset of the wall-induced convection to clarify the role of topological defects.

II. METHODS

For the theoretical investigation we carry out Molecular Dynamic(MD) [27] simulations of a two-dimensional system in a box of size $L_x \times L_z$ delimited by flat hard walls and gravity $\boldsymbol{g} = -g\boldsymbol{e}_z$ pointing in the negative z direction. The particles have two translational degrees of freedom in the $x-$ and $z-$ directions and one rotational degree of freedom about the perpendicular y-axes. The granular beads are described as soft disks of diameter σ, mass m, and moment of inertia $I = m\sigma^2/8$, which interact via a linear contact model with viscoelastic damping

* andrea.fortini@uni-bayreuth.de

between the disks and via static friction [28]. This model and its parameter values (See Tab. I) have been chosen because they reproduce the contact properties [29] of granular beads, and give results for the dynamics of an intruder in a vertically oscillated granular bed, which are in good agreement with experiments [20].

The simulation box is driven sinusoidally, i.e., the bottom of the container is moved in time according to

$$z_b = -\frac{1}{2}L_z + A\sin(\omega t) \ , \tag{1}$$

where z_b is the height coordinate of the bottom of the container, A is the amplitude of the oscillation, ω is the frequency and t is the time.

We traced the dynamical phase diagram for a fixed oscillation frequency $\omega = 1.0t_0^{-1}$ and lateral wall separation $L_x/\sigma = 20$. Reduced units are used throughout the article: the particle mass m, the particle diameter σ and the gravitational acceleration g are our fundamental units. Consequently, the derived units are the time $t_0 = \sqrt{\sigma/g}$, velocity $v_0 = \sqrt{g\sigma}$, force $f_0 = mg$, elastic constant $k_0 = mg/\sigma$ and damping coefficient $\gamma_0 = \sqrt{g/\sigma}$. Further details of the model are given in appendix A.

The external driving force is characterised by a dimensionless acceleration $\Gamma = A\omega^2/g$, corresponding to the maximum acceleration due to Eq. (1) divided by the gravitational acceleration g. Alternatively, we use the dimensionless energy parameter [30] $K_m = \frac{A^2\omega^2}{\sigma g}$, i.e., the maximum kinetic energy per particle 'injected' in the system every period of oscillation [31].

The experiment is conducted with a monolayer of spherical polished opaque glass beads (SiLiBeads P) with a diameter of 2 ± 0.02 mm. A rectangular cell made up of two glass plates 40 mm width by 200 mm height separated by a distance of 2.3 mm is used to create a quasi-two-dimensional configuration. The cell is mounted on an electromagnetic shaker (Tira TV50350) with the sinusoidal frequency and amplitude controlled by a function generator (Agilent FG33220). The acceleration is obtained by an accelerometer (Dyson 3035B2). In order to avoid the influence from electrostatic forces, the side walls of the container are made of aluminium. With a backlight illumination, the mobility of the particles are captured with a high speed camera (IDT MotionScope M3) mounted in front of the cell. The camera is externally triggered so as to take images at fixed phases of each vibration cycle. The snapshots captured are subjected to an image processing procedure to locate all spheres based on a Hough transformation [32]. Tracer particles are used to determine the convection threshold (see appendix B for details).

In order to compare the results of the simulations with the experiments, we produced results for fixed numbers of particles, namely $N = 200, 400, 800, 1200, 1600$. The different sets are identified via the linear density $N_l = N/L_x$. This number gives an approximate value for the number of particle layers and hence, the height of the granular bed. In reality the height depends on the local structure of the granular bed, namely, the orientation of the hexagonally-ordered particles, and the type and amount of defects.

III. INITIALISATION

In the experiment the system is initialised with a strong agitation to create a completely fluidized state, followed by a slow ramping down of the vertical acceleration. In the simulation the initial configuration is prepared with two distinct procedures. In the crystal initialisation, the particles are placed in a perfect hexagonal lattice resting at the bottom of the container. In the random initialisation, the particles are placed randomly in the box. Via molecular dynamics we evolve the system until all particles have fallen under gravity and have reached a rest position.

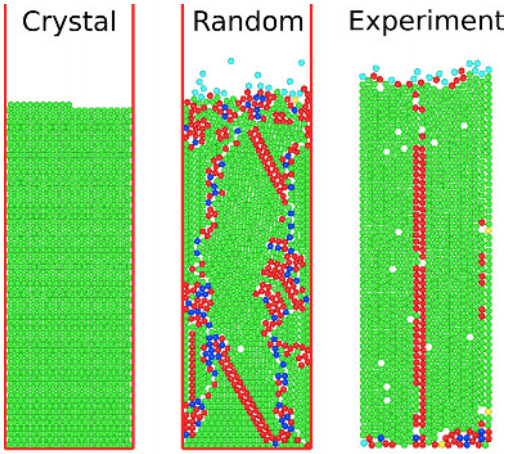

Figure 1. (colour online) Simulation snapshots of the typical initial configurations for $N_l = 60$. The colour indicate the local order of the particles according to an analysis with the q_6 order parameter [33]. Green (light grey) indicates hexagonal order, red (dark grey) indicates a square local order while other colours indicate a disordered configuration. From left to right: the crystalline and random initialisations of the simulation, and the experimental initial configuration.

The resulting configurations are shown in Fig. 1. We note that in both simulations initialised randomly and the experiments a large amount of particles have local hexagonal order with many topological defects, such as dislocations and grain boundaries. For a two dimensional system there are two favoured orientations of the hexagonal lattice, when in contact with a flat wall. In Fig. 2a) the Orientation A with the [111] direction parallel to the wall is shown. In Fig. 2b) the orientation B has the [010] direction parallel to the wall. In the crystalline initialisation we chose to place the particles according to orientation A. After the random initialisation processes, we find

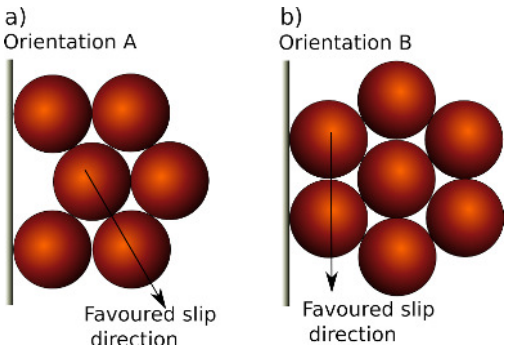

Figure 2. (colour online) Sketch of the possible orientations of the hexagonal crystal in contact with the lateral wall of the container box.

that in the experiment almost all particles have orientation B, while in simulation the orientation A seems to be favoured, but grain boundaries between the different orientations are visible. Figure 1 shows the configurations obtained in the three cases.

IV. DYNAMICAL PHASES

We have systematically investigated the onset of convection at different dimensionless accelerations/energies and heights of the granular bed. Figure 3 shows the location of the dynamical phases as a function of the dimensionless acceleration Γ and the energy parameter K_m for different values of the linear density N_l. The parameter $N_l\sigma$ is also a measure of the number of layers in the granular bed, and therefore of its height.

The transition from the comoving to bouncing bed phase occurs, as expected, at $\Gamma \simeq 1$ with the critical value of the acceleration increasing slightly with increasing number of layers. We find good agreement between simulations started with defects (green triangles) and experiments (connected squares). On the other hand, for simulations without initial defects we find a stronger dependence on the number of layers (blue circles). Inside the bouncing bed regime, we observe a transition from a bouncing bed phase without convection to a bouncing bed phase with convection. For the number of layers $N_l\sigma \geq 40$, we find reasonable agreement between experiments and the simulations initialised randomly. On the other hand, for $N_l\sigma$=10 and 20 the model overestimates the amount of energy necessary for the convection to start. At small heights of the granular bed, the effective force that drives the onset of convection, i.e., the frictional force between particles and walls, reduces because the normal stress to the side walls reduces. This is reminiscent of the Janssen's law for the static case [34, 35]. As a consequence, one expects a higher agitation strength for the onset of convection for small number of layers. On the other hand, the experimental box is not exactly two-dimensional and the presence of a front and a back wall effectively increases the amount of wall surface available with respect to the simulations. We believe this is the reason behind the lack of the increase in the critical acceleration for $N_l\sigma$=10, and 20. For simulations that start without topological defects we consistently detect the onset of convection (blue circles) at higher values of the acceleration with respect to the experiments and to the simulations started with defects. The enhancement of the convection due to the presence of defects explains the observation of Pöschel and Herrmann [11] that an intruder can initiate convection. The presence of an intruder induces topological defects [36] that initiate the convection and segregation.

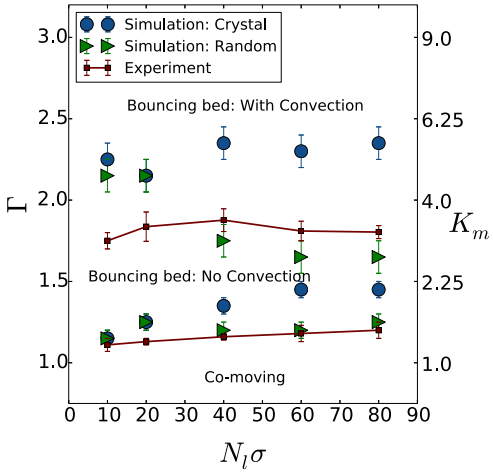

Figure 3. (colour online) Dynamical phases at different accelerations Γ and linear density/number of layers $N_l\sigma$. On the right y-axis the energy parameter K_m is also reported. Symbols are for simulation results for either the system initialised randomly (triangles) or in a crystalline configuration (circles). The connected squares are the experimental results.

V. ONSET OF CONVECTION

In crystalline materials collective particle movements occur via crystalline plane slips [10]. The same occurs in our granular systems, but we noted some differences in slip behaviour between simulation and experiments. In simulation the slip occur primarily along the oblique directions, while in the experiment it occurs mainly along the vertical direction. The difference can be explained by the different orientation of the hexagonal crystal in the two cases. The granular particles experience a shear stress due to the wall of the container along the vertical direction. In the experiments the particles are oriented

like in Fig. 2b), and slips occur preferentially in the vertical direction. On the other hand, in simulations we find more particles with an orientation like in Fig. 2a) and the pyramidal slip planes will be activated first. As long as plane slips are concerned, the worst case scenario is represented by a perfect crystal with orientation A. Since no defects are initially present, slips along the pyramidal planes can only occur if defects are nucleated first. Another difference is that in experiments we often observe single convective rolls similar to the observation in a two-dimensional rotating cell [37]. This type of convective motion is not detected in simulation and the reason for the discrepancy is likely due to a small tilt of the side walls [9].

In order to clarify the role of defects in the onset of convection, we analyse in computer simulations the granular temperature T_g in relation to the average input energy K_m The granular temperature is defined as

$$T_g = \frac{m}{N}\langle\sum_{i=1}^{N}\frac{1}{2}(\boldsymbol{v}_i(t) - \boldsymbol{v}_{\rm cm}(t))^2\rangle \qquad (2)$$

where $\boldsymbol{v}_{\rm cm}$ is the centre of mass velocity and $\boldsymbol{v}_i(t)$ is the velocity of particle i at time t and $\langle\rangle$ indicates a time average. Figures 4a-b show the behaviour of the reduced granular temperature $T_g^* = T_g/(mg\sigma)$ as a function of the dimensionless energy parameter K_m for systems initialised with and without defects, respectively. In both cases the temperature increases monotonically over many orders of magnitude. The curve gives an indication of how much input energy K_m is converted into the kinetic energy of the granular particles.

We divide the energy K_m parameter space in regions with different slopes of the temperature curves. For the random initialisation (Fig. 4a) we find two regions: A and B. The transition occurs at $K_m \simeq 3.3$ as signalled by a change in slope of the temperature curve. Comparing the energy value for this transition with the diagram of Fig. 3, we note that it corresponds to the energy value at the onset of convection.

On the other hand, for the case initialised without defects (Fig. 4b) we can distinguish three regions. Following the naming convention used in Fig. 4a, we indicate with B the region where convection is detected. The region A, without convection, is now divided in two subregions A_1 and A_2.

In order to clarify the origin of the different regions of temperature behaviour, we investigate the slip probability of a particle in the bulk of the granular bed, i.e. away from the top free interface [38]. The slip of a particle is detected if a displacement larger than 0.2 σ is measured for at least two nearest neighbours after one oscillation. We define the slip probability p_s as the fraction of particles which undergo a slip in one oscillation period. The value of p_s is averaged over 200 periods of oscillation. The slip probability as a function of $1/K_m$ is shown in Figs. 5a-b for the random and crystal initialisation, respectively. For the random case we do not observe a change in the slip behaviour between regions A and B. On the other hand a quite dramatic change of behaviour is observed for the crystal case. In particular, in region A_1 the number of detected slip is exactly zero, while region A_2 is characterised by a quite steep increase of slip events, which slows down considerably upon onset of convection (region B).

In all cases the curves can be fitted to an Arrhenius law, $p_s \propto \exp(-E_b/K_m)$, indicating the presence of activating mechanisms. The energy parameter E_b is a measure of the barrier height and the dimensionless energy K_m assumes the role of a reservoir temperature. For the random case just a single curve can be fitted to the entire range of inverse energies. From the fit we find an average dimensionless barrier height $E_b = 7 \pm 1$. For the case initialised with the crystal, we find a barrier $E_b = 130 \pm 20$ in region A_2, and a barrier $E_b = 7 \pm 1$ in region B.

Since the barrier height is the same for the system with initial defects, independent of the presence of convection, we can speculate that the activation mechanism indicated by the Arrhenius equation is the activation of slip events in a crystal with topological defects. Interestingly, the same barrier is measured for the system without initial defects in region B, suggesting the same activation mechanism. But in order for this to occur defects must first nucleate inside a perfect crystal, and we speculate that the very high barrier in region A_2 is due to the nucleation of defects in a perfect hexagonal crystal.

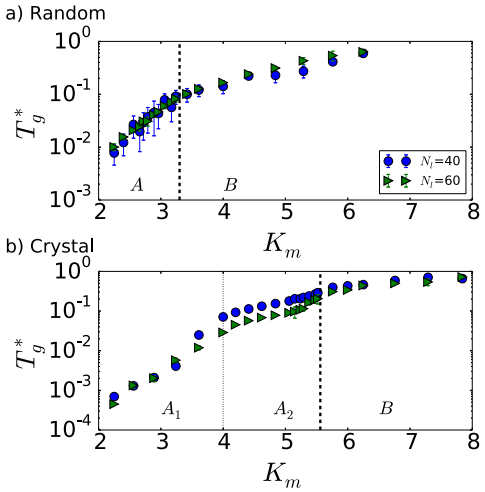

Figure 4. (colour online) Granular temperature T_g versus dimensionless energy parameter K_m. The dashed lines separate regions with different slopes of the temperature curves. a) For the system initialised randomly, i.e. with defects. b) For the system initialised in a perfect hexagonal lattice, i.e. without initial defects.

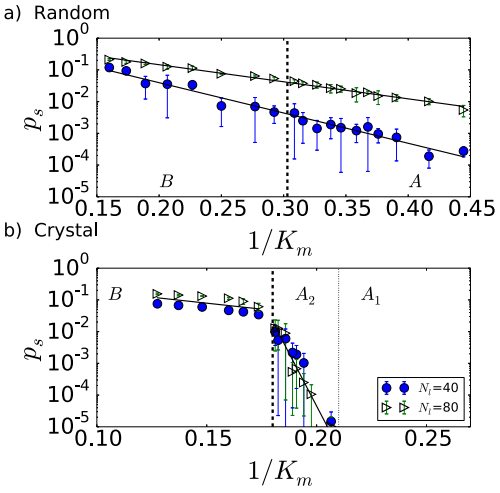

Figure 5. (colour online) Slip probability p_s versus the inverse dimensionless energy parameter $1/K_m$. The continuos lines represent exponential fit functions. The dashed lines separate the regions defined in Fig. 4. a) For the system initialised randomly, i.e. with defects. b) For the system initialised in a perfect hexagonal lattice, i.e. without initial defects.

VI. CONCLUSIONS

In conclusion, using two-dimensional computer simulations and experiments we locate the wall-induced convection in the bouncing bed region in the dynamical phase diagram of vertically vibrated granular matter.

For the onset of convection, we find an overall good agreement between the experimental results and those from simulations initialised with defects, for a linear density/number of layers of $N_l\sigma \geq 40$. On the other hand, for $N_l\sigma$=10, and 20 the model overestimates the amount of energy necessary for the convection to start. We believe the reason behind the discrepancy is the presence of a front and a back wall in the experimental box, which effectively increase the amount of wall friction "available" for convection to start. Other phenomenological differences between simulations and experiments are observed for the favoured crystal orientation and slip events. We think that this differences are due to a small tilt of the experimental box and small variations of the experimental box width L_x.

For a system initialised in a perfect crystal, i.e., without initial defects, we consistently observe the wall-induced convective motion to occur at higher values of the dimensionless energy parameter (shaking strength) with respect to the system initialised randomly. From the analysis of the granular temperature we distinguish different regions based on the slope of the temperature as a function of the dimensionless energy K_m. For systems initialised randomly, i.e. with many initial defects, we distinguish two regions (A and B) of temperature. The transition between the two regions occurs at the onset of convection, but we do not observe any change in the slip probability in the transition between regions A and B.

On the other hand, for systems initialised with a perfect hexagonal lattice, i.e. without initial defects, we distinguish three regions in the temperature curve. Moreover, in this case the slip probability has very different behaviour in the three regions. In particular, in region A_1 the number of detected slips is exactly zero, while region A_2 is characterised by a quite steep increase of slip events with the input energy, which slows down considerably upon onset of convection (region B).

The slip probability follows an Arrhenius law, indicating the presence of an activating mechanisms. The very high barrier in the region A_2 of the system without defects is due to the nucleation of defects in the perfect hexagonal crystal. We noted that the barrier in region B is the same for the system initialised with and without initial defects. In this region the behaviour of the slip probability is related to the activation of slip events.

The results of our work provide an explanation for the onset of the convective regime in vertically oscillated granular systems and clarify the role of defects. The question we want to answer in the future is how the size polydispersity of the granular particles changes the onset of the wall-induced convection as well as what is the influence of the box size on the dynamical behaviour. Furthermore we would like to explore the effect of shock waves [39] on the dynamical behaviour of the system.

Appendix A: Details of the Model

We carry out Molecular Dynamics simulations at fixed time step dt, for two translational degrees of freedom and one rotational degree of freedom for a system of soft disks. An illustration of the model is shown in Fig. 6. Two particles at positions $\boldsymbol{r}_i$ and $\boldsymbol{r}_j$ with velocities $\boldsymbol{v}_i$ and $\boldsymbol{v}_j$ and angular velocities $\boldsymbol{\omega}_i$ and $\boldsymbol{\omega}_j$ define a system with an effective mass $m_{\text{eff}} = m_i m_j/(m_i+m_j)$ and a normal unit vector $\boldsymbol{n}_{ij} = \frac{\boldsymbol{r}_i-\boldsymbol{r}_j}{|\boldsymbol{r}_i-\boldsymbol{r}_j|}$. The tangential direction is defined as $\boldsymbol{t}_{ij} = \frac{\boldsymbol{v}_{t_{ij}}}{|\boldsymbol{v}_{t_{ij}}|}$ where

$$\boldsymbol{v}_{t_{ij}} = \boldsymbol{v}_{ij} - \boldsymbol{v}_{n_{ij}} - \frac{1}{2}(\sigma_i\boldsymbol{\omega}_i + \sigma_j\boldsymbol{\omega}_j) \times \boldsymbol{n}_{ij} \ , \qquad \text{(A1)}$$

with $\boldsymbol{v}_{n_{ij}} = (\boldsymbol{v}_{ij} \cdot \boldsymbol{n}_{ij})\boldsymbol{n}_{ij}$.

We define the displacement in the two directions $\delta_{n_{ij}} = d - |\boldsymbol{r}_i - \boldsymbol{r}_j|$, with $d = 1/2(\sigma_i + \sigma_j)$, and $\delta_{t_{ij}}\boldsymbol{t}_{ij} = \boldsymbol{v}_{t_{ij}}dt$. For the disk-disk interactions we use a linear model with forces

$$\boldsymbol{F}_{n_{ij}} = (\kappa_n\delta_{n_{ij}}\boldsymbol{n}_{ij} - \gamma_n m_{eff}\boldsymbol{v}_{n_{ij}}) \qquad \text{(A2)}$$
$$\boldsymbol{F}_{t_{ij}} = (-\kappa_t\delta_{t_{ij}}\boldsymbol{t}_{ij} - \gamma_t m_{eff}\boldsymbol{v}_{t_{ij}}) \ , \qquad \text{(A3)}$$

in the normal and shear tangential directions, respectively. The parameters κ_n and κ_t are the stiffness co-

efficients in the normal and tangential direction, respectively. The energy dissipated during the contact is regulated by the damping coefficients γ_n and γ_t. In addition we model the static friction by keeping track of the elastic shear displacement $\delta_{t_{ij}}$ over the contact lifetime and truncate it such that the Coulomb condition $|F_{t_{ij}}| < |\mu F_{n_{ij}}|$ is satisfied, where μ is the static friction coefficient. The same kind of interaction is used between

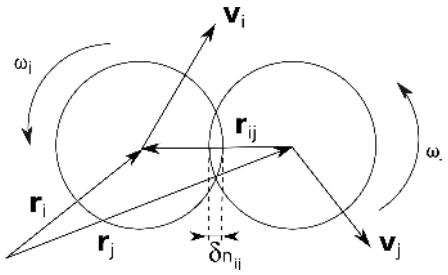

Figure 6. Illustration of the contact model of two granular disks at distance $\boldsymbol{r}_{ij} = \boldsymbol{r}_i - \boldsymbol{r}_j$ and relative velocity $\boldsymbol{v}_{ij} = \boldsymbol{v}_i - \boldsymbol{v}_j$, which overlap by a distance $\delta_{n_{ij}}$.

the particles and the container wall. We also consider the gravitational force $\boldsymbol{g} = -g\boldsymbol{e_z}$, where $\boldsymbol{e_z}$ is the unit vector pointing in z direction.

Once the forces on all particles are known the total force and torque τ_i on a particle i is determined by

$$\boldsymbol{F}_i = m\boldsymbol{g} + \sum_j (\boldsymbol{F}_{n_{ij}} + \boldsymbol{F}_{t_{ij}}) \qquad \text{(A4)}$$

$$\boldsymbol{\tau}_i = -\frac{1}{2}\sum_j \sigma_j \boldsymbol{n}_{ij} \times \boldsymbol{F}_{t_{ij}} \ .$$

Coefficient		Particle-Particle	Wall-Particle
Normal stiffness	k_n	10^6 (k_0)	10^6 (k_0)
Tangential stiffness	k_t	10^4 (k_0)	10^4 (k_0)
Static friction	μ	0.6	0.6
Normal damping	γ_n	100 (γ_0)	100 (γ_0)
Tangential damping	γ_t	100 (γ_0)	100 (γ_0)

Table I. Numerical values of the simulation parameters.

The typical numerical values of simulation parameters are shown in Table I. In this linear model it is possible to calculate the contact duration [40]

$$t_c = \pi \left(\frac{k_n}{m_{eff}} - \frac{\gamma_n^2}{4} \right)^{-0.5} \ . \qquad \text{(A5)}$$

In order to obtain an accurate integration of the equation of motion during contact, the time step of the simulation is chosen to be $\delta t \approx t_c/50$ [41].

Appendix B: Detection of the dynamical phases

The detection of the bouncing bed dynamical phase is performed visually, in both computer simulations and experiments. In the experiments the distance between the granular bed and the bottom of the container depends on the phase lag between the camera and the shaker, which can be adjusted to inspect the collective motion of the granular bed over the whole vibration cycle.

The detection of the convective motion is done in simulation by colouring the particles according to their initial height as shown in Fig. 7. After few oscillation cycles we determine visually the presence, or not, of the typical structures of the convective rolls.

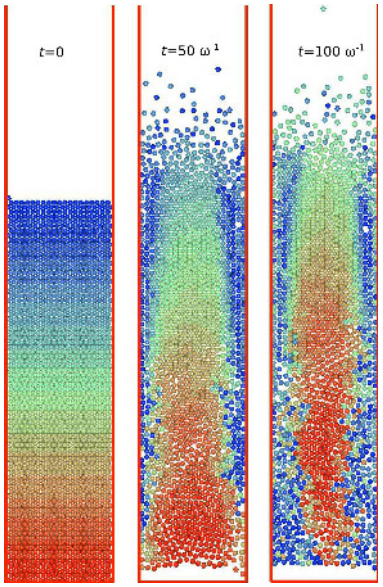

Figure 7. (colour online) Sequence of simulation snapshots. The particles color/grey scale is based on the height at t=0. In this example the formation of the convection rolls is evident at $t\omega = 50, 100$.

In the experiments, convection is detected with the help of tracer particles. From the occurrences of slip events for tracer particles at the side walls within a period of 1000 vibration cycles, we determine the convection threshold. An example is shown in Fig. 8.

ACKNOWLEDGMENTS

The authors thank Ingo Rehberg and Matthias Schmidt for discussions and acknowledge Philipp Ramming for the help in image processing. Maximilian von Teuffenbach, Andreas Fischer and Philip Krinninger are acknowledged for helping with the initial development of

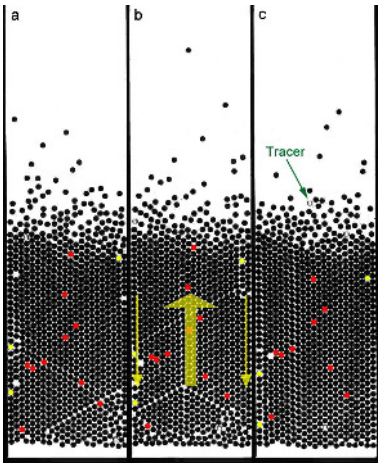

Figure 8. (colour online) A sequence of experimental snapshots showing convection of the granular particles (black spheres) under sinusoidal vibrations with an agitation frequency f =10 Hz and Γ =4.53. Red (dark grey) and yellow (light grey) spheres mark the tracer particles that are moving up and down, respectively. a) At t=0. b) t=1 s. c) t=2 s.

the granular simulation code as a part of their final bachelor projects. K.H. is supported by the DFG through Grant No. HU1939/2-1.

[1] H. M. Jaeger, S. R. Nagel, and R. P. Behringer, Rev. Mod. Phys. **68**, 1259 (1996).
[2] S. Luding, Nonlinearity **22**, R101 (2009).
[3] H. Miyamoto, H. Yano, D. J. Scheeres, S. Abe, O. Barnouin-Jha, A. F. Cheng, H. Demura, R. W. Gaskell, N. Hirata, M. Ishiguro, T. Michikami, A. M. Nakamura, R. Nakamura, J. Saito, and S. Sasaki, Science **316**, 1011 (2007).
[4] J. Duran., *Sands, powders, and grains: An introduction to the physics of granular materials.* (Springer Verlag, 2000).
[5] N. Mohabuth and N. Miles, Resources, Conservation and Recycling **45**, 60 (2005).
[6] A. Rosato, K. Strandburg, F. Prinz, and R. Swendsen, Phys. Rev. Lett. **58**, 1038 (1987).
[7] M. Schröter, S. Ulrich, J. Kreft, J. Swift, and H. Swinney, Phys. Rev. E **74**, 011307 (2006).
[8] D. Hong, P. Quinn, and S. Luding, Phys. Rev. Lett. **86**, 3423 (2001).
[9] J. Knight, H. Jaeger, and S. Nagel, Phys. Rev. Lett. **70**, 3728 (1993).
[10] W. Cooke, S. Warr, J. Huntley, and R. Ball, Phys. Rev. E **53**, 2812 (1996).
[11] T. Pöschel and H. J. Herrmann, Europhysics Letters **29**, 123 (1995).
[12] A. Kudrolli, Rep. Prog. Phys. **67**, 209 (2004).
[13] M. Majid and P. Walzel, Powder Technology **192**, 311 (2009).
[14] A. Mehta and J. Luck, Phys. Rev. Lett. **65**, 393 (1990).
[15] S. Douady, S. Fauve, and C. Laroche, Europhysics Letters **8**, 621 (1989).
[16] A. Ugawa and O. Sano, Journal of the Physical Society of Japan **72**, 1390 (2003).
[17] O. Sano, Phys. Rev. E **72**, 051302 (2005).
[18] P. Eshuis, R. Bos, D. Lohse, D. Van der Meer, and K. Van der Weele, Phys. of Fluid **19**, 123301 (2007).
[19] P. Eshuis, D. van der Meer, M. Alam, H. J. van Gerner, K. van der Weele, and D. Lohse, Phys. Rev. Lett. **104**, 038001 (2010).
[20] J. Sun, F. Battaglia, and S. Subramaniam, Phys. Rev. E **74**, 061307 (2006).
[21] E. Clément, J. Duran, and J. Rajchenbach, Phys. Rev. Lett. **69**, 1189 (1992).
[22] J. B. Knight, E. E. Ehrichs, V. Y. Kuperman, J. K. Flint, H. M. Jaeger, and S. R. Nagel, Phys. Rev. E **54**, 5726 (1996).
[23] Y.-h. Taguchi, Phys. Rev. Lett. **69**, 1367 (1992).
[24] S. Luding, E. Clément, A. Blumen, J. Rajchenbach, and J. Duran, Phys. Rev. E **50**, R1762 (1994).
[25] M. Bourzutschky and J. Miller, Phys. Rev. Lett. **74**, 2216 (1995).
[26] D. Risso, R. Soto, S. Godoy, and P. Cordero, Phys. Rev. E **72**, 011305 (2005).
[27] D. Frenkel and B. Smit, *Understanding Molecular Simulation* (Academic Press, London, 2002).
[28] P. A. Cundall and O. D. L. Strack, Géotechnique **29**, 47 (1979).
[29] J. Schafer, S. Dippel, and D. Wolf, Journal De Physique I **6**, 5 (1996).
[30] H. Pak and R. Behringer, Physical Review Letters **71**, 1832 (1993).
[31] This parameter is also called dimensionless shaking strength [18].
[32] C. Kimme, D. H. Ballard, and J. Sklansky, Comm. As-

soc. Comp. Mach. **18**, 120 (1975).
[33] P. Steinhardt, D. Nelson, and M. Ronchetti, Phys. Rev. B **28**, 784 (1983).
[34] H. A. Janssen, Z. Ver. Dt. Ing. **39**, 1045 (1895).
[35] U. M. B. Marconi, A. Petri, and A. Vulpiani, Physica A **280**, 279 (2000).
[36] V. W. de Villeneuve, R. P. Dullens, D. G. Aarts, E. Groeneveld, J. H. Scherff, W. K. Kegel, and H. N. Lekkerkerker, Science **309**, 1231 (2005).
[37] F. Rietz and R. Stannarius, Phys. Rev. Lett. **108**, 118001 (2012).
[38] We have chosen to exclude particles closer than 10 σ to the free interface.
[39] K. Huang, G. Miao, P. Zhang, Y. Yun, and R. Wei, Phys. Rev. E **73** (2006).
[40] J. Schaefer, S. Dippel, and D. Wolf, J. Phys. I France **6**, 5 (1996).
[41] J. Lee, J. Phys. A **27**, L257 (1994).

Ordering of Granular Rod Monolayers Driven Far from Thermodynamic Equilibrium

Thomas Müller,[1] Daniel de las Heras,[2] Ingo Rehberg,[1] and Kai Huang[1,*]

[1] *Experimentalphysik V, Universität Bayreuth, D-95440 Bayreuth, Germany*
[2] *Theoretische Physik II, Universität Bayreuth, D-95440 Bayreuth, Germany*

(Dated: October 22, 2014)

The orientational order of vertically agitated granular rod monolayers is investigated experimentally and compared with equilibrium Monte Carlo simulations and density functional theory. At sufficiently high density, short rods form a tetratic state and long rods form a uniaxial nematic state. The length-to-width ratio at which the order changes from tetratic to uniaxial is around 7.3 in both experiments and simulations. Such a comparison illustrates the universal aspects of the self-organization of rod-shaped particles across thermal and athermal systems.

PACS numbers: 45.70.-n, 05.70.Ln, 64.70.M-

The self-organization of anisotropic particles into ordered states is a universal phenomenon appearing widely in nature, ranging from thermally driven molecules or colloids [1–4] to active particles such as bacteria colonies [5], actin filaments [6, 7], animal groups [8–10], and living liquid crystals [11]. In equilibrium lyotropic systems, such as hard rods interacting only through excluded volume interactions, the transition of sufficiently anisotropic particles into various ordered states is entropy driven. The loss in rotational degrees of freedom in the ordered state is compensated by the gain in the translational ones [3, 4, 12]. For example, in a two dimensional system of hard rectangles a tetratic state with fourfold rotational symmetry has recently been discovered in Monte Carlo (MC) simulations [13, 14], and studied theoretically with density functional theory (DFT) [15, 16]. Given the ubiquity of ordering transitions in nature, it is important to ask how well primary tools for the investigation of equilibrium (thermal) systems, such as MC and DFT, can be used to describe nonequilibrium (athermal) systems.

Due to the dissipative interactions between particles, agitated granular matter has been frequently used as a nonequilibrium model system for phase transitions [17–23]. Rich and often counterintuitive dynamical behaviors [24] have been discovered for granular rods, including vortex patterns [25], collective swirling motions [26], giant number fluctuations [27, 28], violation of the equipartition theorem [29], and an enhanced ordering transition in an effective 'thermal' bath of spherical particles [30]. Particularly, ordering transitions into either uniaxial nematic [31, 32] or tetratic states [32, 33] have been reported in agitated granular rods. The shape of the rods [32] and that of the container [31, 33] play important roles in determining the ordered state. In this Letter, we investigate experimentally the orientational ordering of granular rod monolayers driven far from thermodynamic equilibrium, and compare the results to the analogous equilibrium system. We show that the aspect ratio and the density of rods are the key parameters determining the state diagram in both systems. Such a comparison illustrates the universal aspects of the self-organization of rod-shaped particles in both nonequilibrium and equilibrium systems.

A sketch of the experimental set-up is shown in Fig. 1. Monodisperse polyvinyl chloride (PVC) rods of diameter D and length L, cut from welding wires of $D = 3\,\mathrm{mm}$ (aspect ratio $L/D \leq 5$) or $1.5\,\mathrm{mm}$ ($L/D \geq 5$), are confined in a cylindrical container of height H and radius $R = 10\,\mathrm{cm}$. The ratio $H/D = 4/3$ is kept constant for both diameters to ensure a monolayer of particles; that is, no rods can cross or jump over each other. The inner surface of the container is covered with antistatic spray (Kontakt Chemie, Antistatik 100) to minimize electrostatic forces. An electromagnetic shaker (Tira TV50350) is employed to drive the sample sinusoidally against gravity with frequency $f = 50\,\mathrm{Hz}$ and peak acceleration $\Gamma = 4\pi^2 f^2 z_0/g$, where z_0 is the peak vibrational amplitude and g is the gravitational acceleration. The acceleration is monitored with an accelerometer (Dytran 3035B2). We capture high contrast images of the rods using backlight LED illumination and a camera (IDT MotionScope M3) mounted above the container. The camera is synchronized with the shaker so as to capture images at a fixed phase of each vibration cycle. The images are subjected to an analysis algorithm that deter-

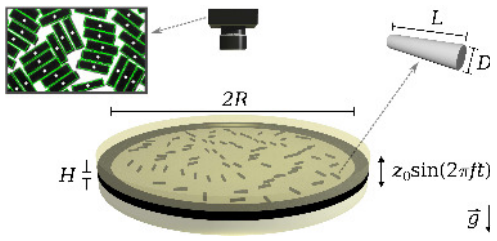

FIG. 1. (Color online) Sketch of the experimental set-up. The closed cylindrical container of height H and radius R is driven sinusoidally against gravity with an electromagnetic shaker. The rods have a length L and a diameter D. The embedded image shows a close view of the detected particles.

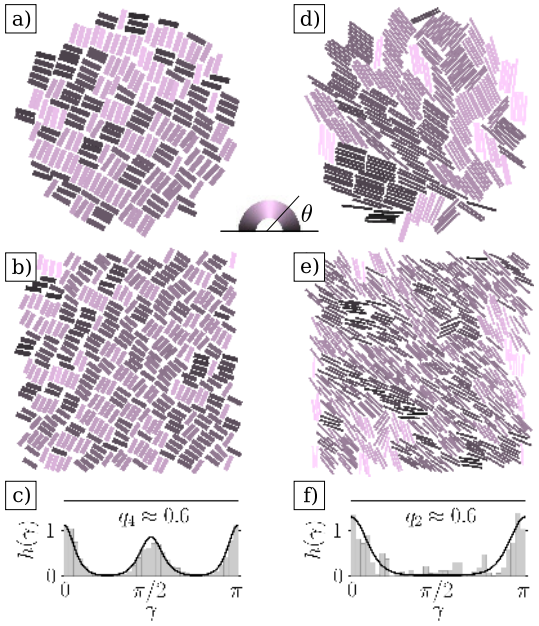

FIG. 2. (Color online) Typical snapshots of tetratic (left column, $L/D = 3.3$) and uniaxial nematic (right column, $L/D = 10.0$) states. a) and d) are reconstructed from the positions and orientations of the particles detected in the center region of the container. b) and e) are from MC simulations with periodic boundary conditions. The rods are color (grayscale) coded according to their orientations. The lower panels show the orientational distribution functions $h(\gamma)$ of the rods in experiments (gray bars) and simulations (solid line). γ is the angle with respect to the director.

mines the center of mass $P_i = (x_i, y_i)$ and the orientation $\theta_i \in [0, \pi[$ of the i-rod with $i \in [1, N]$. θ_i is the angle of the main rod axis with respect to a fixed laboratory axis, and N is the total number of rods in the container. The detection rate is 100 % for $D = 3$ mm and 95 % for $D = 1.5$ mm.

Correspondingly, the rods are modelled as two-dimensional hard rectangles with the same aspect ratio as in the experiments. We consider only excluded volume interactions between the particles. We use standard MC simulations in the canonical ensemble and an Onsager-like DFT to study the equilibrium bulk phase behavior. See the supplemental material [34] for details about the implementation of MC and DFT.

Figure 2 shows a comparison of typical ordered states in the center region of the agitated granular rods to the MC simulations with periodic boundary conditions. The comparison reveals qualitative agreement between nonequilibrium and equilibrium systems. Short rods (left column) form a tetratic state with orientational order

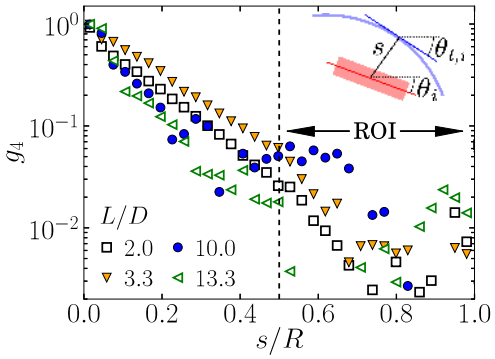

FIG. 3. (Color online) Wall-rod angular correlation function g_4 as a function of the rescaled distance s/R to the wall for various L/D. A sketch with various definitions is shown in the inset. Error bars are comparable to the data scattering.

along two perpendicular axis. The orientational distribution function $h(\gamma)$, where γ is the angle with respect to the director, has two peaks at $\gamma = 0$ and $\gamma = \pi/2$ (c). In contrast, long rods (right column) form a uniaxial nematic state in which the rods are oriented on average along the director (f). To quantify the orientational order we measure

$$q_k = \int_0^\pi \mathrm{d}\gamma h(\gamma) \cos(k\gamma), \quad k = \{2, 4\}, \tag{1}$$

where q_2 and q_4 are the uniaxial and tetratic order parameters, respectively. In an isotropic state (no orientational order) q_2 and q_4 vanish. In a uniaxial nematic state $q_2 > 0$ and $q_4 > 0$. Finally in a tetratic state $q_2 = 0$ and $q_4 > 0$. The states in Fig. 2 are selected such that q_2 and q_4 are comparable in both experiments and MC simulations.

To systematically study the behavior of the system, we vary the global area fraction $\Phi_g = \frac{NLD}{\pi R^2}$ between ~ 0.3 and ~ 0.9, and the aspect ratio L/D between 2.0 and 13.3. For each Φ_g and L/D, we vary the peak acceleration Γ with a step of 1 from 2 to 20 and back. The waiting time between each step is fixed at ~ 1.5 minutes. We repeat the whole cycle at least 3 times.

As we are interested in the bulk behavior, we first need to characterize the influence of the wall. Former experiments [31, 35, 36] and MC simulations [37] show that the container induces a preferential alignment of particles close to the wall. Following the ideas in [31], we calculate the wall-rod angular correlation function $g_4(s) = \langle \cos[4(\theta_{t,i} - \theta_i(s))] \rangle$, where s is the shortest distance from the rod center to the container wall, $\theta_{t,i}$ is the tangential direction of the corresponding point on the wall (see inset in Fig. 3), and $\langle ... \rangle$ denotes an average over all the particles with a distance s. Either planar (parallel) or homeotropic (perpendicular) alignment of

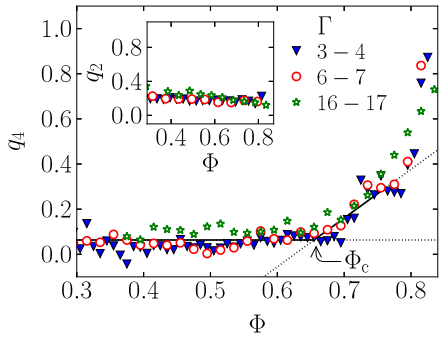

FIG. 4. (Color online) Tetratic q_4 and uniaxial q_2 order parameters in the ROI as a function of the area fraction Φ, for rods with aspect ratio $L/D = 3.3$ for three ranges of peak acceleration Γ. The threshold Φ_c is obtained through linear fits to the data averaged over all Γ (see text for details). The order parameters are not exactly zero in the isotropic state due to the finite size of the system [38].

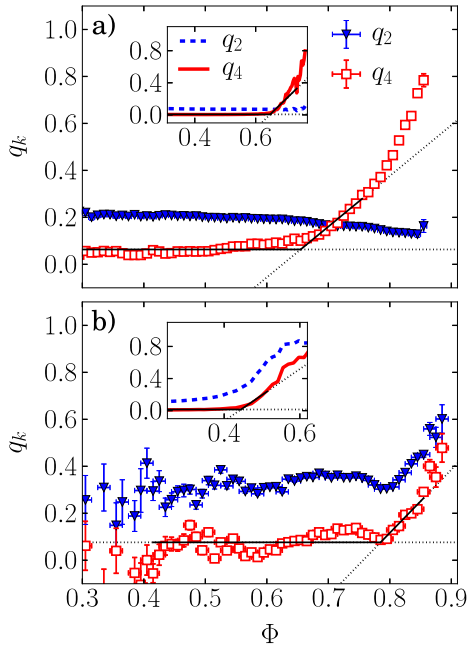

FIG. 5. (Color online) Tetratic and uniaxial order parameters q_k as a function of the area fraction Φ for a) $L/D = 3.3$ and b) $L/D = 10.0$. The insets show the corresponding results from MC simulations. The experimental data is an average over all Γ. Straight lines are linear fits to determine the threshold Φ_c.

the particles with respect to the wall results in $g_4 \sim 1$. In Fig. 3, g_4 is presented as a function of the rescaled distance to the wall s/R, binned over a width of $0.03R$, and averaged over all experimental runs. For all aspect ratios investigated, g_4 decays exponentially from ≈ 1.0 to ≈ 0.1, a value comparable to the data scattering, within a distance $s/R \approx 0.5$. To minimize the influence of the wall, we consider only those particles with $s > 0.5R$ to be in the region of interest (ROI). We characterize the state of the system by measuring the area fraction Φ and $h(\gamma)$ in circular regions with radius $3L$ inscribed in the ROI. Subsequently, we calculate q_k from $h(\gamma)$ accumulated over all the regions that share the same Φ.

Figure 4 shows the order parameters as a function of Φ for $L/D = 3.3$ and various Γ. It indicates an area fraction Φ_c above which the tetratic order parameter q_4 grows from its initial low value, while the uniaxial order parameter q_2 remains low. To obtain Φ_c, we fit q_4 with a constant value in the isotropic region and with a straight line in the ordered state. Φ_c corresponds to the intersection point that minimizes the standard error. Only data with sufficient statistics (i.e. error bar < 0.02) and $q_4 < 0.3$ are chosen for the fits. The combination of q_2 and q_4 shown in Fig. 4 suggests a gradual isotropic-tetratic transition at $\Phi \approx \Phi_c$. The behavior of q_2 and q_4 does not depend on the peak vibration acceleration. This is further confirmed through a comparison among data obtained for all Γ in the range of $2 \leq \Gamma \leq 20$ and also for all aspect ratios investigated. Moreover, for $L/D = 3.3$ we have varied the vibration frequency f from 35 Hz to 80 Hz and found quantitatively the same behavior of $q_k(\Phi)$. Hence we conclude that the details of how the rods are 'thermalized' in our nonequilibrium system are not essential in determining the ordering transitions. Accordingly, we average the data over all Γ for a more accurate characterization of the transition threshold.

The order parameters averaged over all experimental runs are shown in Fig. 5 for rods with $L/D = 3.3$ (a) and $L/D = 10$ (b). As discussed above, tetratic ordering occurs in the system of short rods (a). In contrast, the system of long rods (b) exhibits a different behavior. Both order parameters start to grow gradually above a certain area fraction, suggesting an isotropic-uniaxial nematic transition. This is qualitatively in agreement with the corresponding equilibrium MC simulations, see the insets of Fig. 5. Such comparisons across thermal and athermal systems indicate that the ordering of granular rods is governed by the geometric constrain of non-overlapping rods, which is the only interaction considered in the simulations.

As L/D and Φ are found to be the key parameters determining the state of the system, we compare the experimental (nonequilibrium) results with MC (equilibrium) simulations in a state diagram shown in Fig. 6. In both systems short rods form a tetratic state and long rods an uniaxial state at sufficiently high area fractions. The aspect ratio at which the ordered state changes

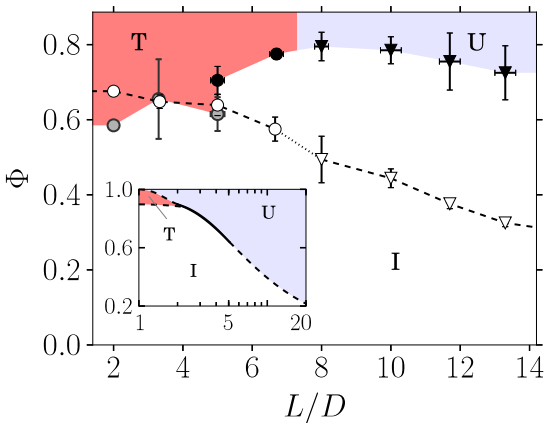

FIG. 6. (Color online) State diagram in the plane of aspect ratio L/D, and area fraction Φ obtained via experiments of agitated granular rods (filled symbols) and MC simulations of thermally driven hard rectangles (empty symbols). The labels denote the states: isotropic (I), uniaxial nematic (U), and tetratic (T). They are colored (grayscaled) according to the experimental data. The diameter of the rods used in the experiments is $D = 1.5$ mm (black symbols) or 3.0 mm (light gray symbols). Circles and triangles indicate the I-T and I-U transitions, respectively. The inset shows the state diagram of equilibrium hard rods according to DFT. Dashed lines are continuous transitions and solid lines denote first order transitions (see a full-size figure in the supplemental material [34]).

from tetratic to uniaxial nematic is in both systems $(L/D)_{\mathrm{T-U}} = 7.3 \pm 0.7$ [39]. Such an agreement between systems driven in and out of thermodynamic equilibrium illustrates the universal aspect of the self-organization of rod-shaped particles. In the inset of Fig. 6 we show the state diagram according to DFT. It is similar to the one predicted by the scaled particle theory [40]. DFT also predicts a tetratic state for small L/D and a uniaxial state for large L/D. However, the tetratic state is stable only for $L/D \lesssim 2.2$, most likely because only two-body correlations are considered in the theory [15, 41]. The deviations in Φ_c between MC and DFT are due to the mean field character of the theory.

On the other hand, the threshold Φ_c for agitated rods differs from that in equilibrium MC simulations, indicating the non-universal aspects of the ordering transitions. First, the experimentally determined Φ_c exhibit a peak around $(L/D)_{\mathrm{T-U}}$. However, both MC simulations and DFT show a monotonic decay with L/D. Second, there exists a systematic deviation of Φ_c in experiments compared to MC simulations as L/D grows. For the largest aspect ratio investigated, $L/D = 13.3$, roughly 30% higher area fraction is required for the uniaxial state to develop. This difference might be attributed to: (i) The steady states formed by the granular rods are far from thermodynamic equilibrium. The strong fluctuations in these states will lead to temporal disorder in a system that could in principle relax into an ordered state. (ii) The stronger clustering of granular rods in comparison to MC, especially for large L/D (compare panels (d) and (e) of Fig. 2). (iii) Finally, the container might frustrate the orientational order of the agitated rods. Further characterizations on the mobility of rods at a 'microscopic' level and experiments using containers with different sizes and shapes might shed light on such a discrepancy. Moreover, experimental results with rods of the same aspect ratio $L/D = 5.0$ but different D agree with each other within the error bar, suggesting that the mass of the rods does not play a dominating role in the ordering transition. The limit of very high area fractions has not been investigated due to the limitations in experiments and MC simulations. In this limit, new states with positional order will presumably be stable and a transition between tetratic and uniaxial states, as predicted by DFT, might occur in systems with $L/D < (L/D)_{\mathrm{T-U}}$.

To summarize, the self-organization of agitated monodisperse granular rod monolayers is found to be determined predominately by the aspect ratio of the rods and the area fraction, while the agitation strength is irrelevant. It suggests that the detailed nature of energy injection into such a nonequilibrium system is not important, analogous to the role that temperature plays in equilibrium hard rod models. Depending on whether the aspect ratio is smaller or larger than ≈ 7.3, a gradual isotropic-tetratic or isotropic-uniaxial nematic transition is observed as the area fraction grows. This agrees with the predictions from equilibrium MC simulations considering only excluded volume interactions. Such an agreement suggests the universality of the self-organization of rods, and thus paves the way for a general understanding of self-organization across equilibrium and nonequilibrium systems. Further investigations will focus on the characterization of the density and velocity fluctuations of the system, in order to find an effective 'thermal' energy scale for such an 'athermal' system.

The authors would like to thank Wilhelm August for the preliminary work on the experimental set-up. Inspiring discussions with M. Schmidt, D. van der Meer, and C. Krülle are greatly acknowledged. TM and KH acknowledge the support from the DFG through Grant No. HU1939/2-1.

* kai.huang@uni-bayreuth.de

[1] M. J. Stephen and J. P. Straley, Rev. Mod. Phys. **46**, 617 (1974).
[2] P. G. d. Gennes and J. Prost, *The Physics of Liquid Crystals* (Clarendon Press, 1995).
[3] L. Onsager, Ann. N. Y. Acad. Sci. **51**, 627 (1949).
[4] G. J. Vroege and H. N. W. Lekkerkerker, Rep. Prog.

Phys. **55**, 1241 (1992).
[5] H. P. Zhang, A. Beer, E.-L. Florin, and H. L. Swinney, PNAS **107**, 13626 (2010).
[6] V. Schaller, C. Weber, C. Semmrich, E. Frey, and A. R. Bausch, Nature **467**, 73 (2010).
[7] T. Sanchez, D. T. N. Chen, S. J. DeCamp, M. Heymann, and Z. Dogic, Nature **491**, 431 (2012).
[8] J. Buhl, Science **312**, 1402 (2006).
[9] I. D. Couzin, J. Krause, N. R. Franks, and S. A. Levin, Nature **433**, 513 (2005).
[10] Q.-X. Liu, A. Doelman, V. Rottschäfer, M. d. Jager, P. M. J. Herman, M. Rietkerk, and J. v. d. Koppel, PNAS **110**, 11905 (2013).
[11] S. Zhou, A. Sokolov, O. D. Lavrentovich, and I. S. Aranson, PNAS **111**, 1265 (2014).
[12] D. Frenkel, Physica A **263**, 26 (1999).
[13] K. W. Wojciechowski and D. Frenkel, Comput. Methods Sci. Technol. **10**, 235 (2004).
[14] A. Donev, J. Burton, F. H. Stillinger, and S. Torquato, Phys. Rev. B **73** (2006).
[15] Y. Martínez-Ratón and E. Velasco, Phys. Rev. E **79**, 011711 (2009).
[16] J. Geng and J. Selinger, Phys. Rev. E **80**, 011707 (2009).
[17] H. M. Jaeger, S. R. Nagel, and R. P. Behringer, Rev. Mod. Phys. **68**, 1259 (1996).
[18] G. H. Ristow, G. Straßburger, and I. Rehberg, Phys. Rev. Lett. **79**, 833 (1997).
[19] A. Götzendorfer, C.-H. Tai, C. A. Kruelle, I. Rehberg, and S.-S. Hsiau, Phys. Rev. E **74**, 011304 (2006).
[20] P. Eshuis, K. van der Weele, D. van der Meer, R. Bos, and D. Lohse, Phys. Fluids **19**, 123301 (2007).
[21] A. Fingerle, K. Roeller, K. Huang, and S. Herminghaus, New J. Phys. **10**, 053020 (2008).
[22] K. Huang, C. Krülle, and I. Rehberg, Zeit. Angew. Math. Mech. **90**, 911 (2010).
[23] C. May, M. Wild, I. Rehberg, and K. Huang, Phys. Rev. E **88**, 062201 (2013).
[24] T. Börzsönyi and R. Stannarius, Soft Matter **9**, 7401 (2013).
[25] D. Blair, T. Neicu, and A. Kudrolli, Phys. Rev. E **67** (2003).
[26] I. S. Aranson, D. Volfson, and L. S. Tsimring, Phys. Rev. E **75**, 051301 (2007).
[27] V. Narayan, S. Ramaswamy, and N. Menon, Science **317**, 105 (2007).
[28] I. S. Aranson, A. Snezhko, J. S. Olafsen, and J. S. Urbach, Science **320**, 612 (2008).
[29] K. Harth, U. Kornek, T. Trittel, U. Strachauer, S. Höme, K. Will, and R. Stannarius, Phys. Rev. Lett. **110**, 144102 (2013).
[30] N. Kumar, H. Soni, S. Ramaswamy, and A. K. Sood, Nat. Commun. **5**, 4688 (2014).
[31] J. Galanis, D. Harries, D. Sackett, W. Losert, and R. Nossal, Phys. Rev. Lett. **96** (2006).
[32] V. Narayan, N. Menon, and S. Ramaswamy, J. Stat. Mech. **2006**, P01005 (2006).
[33] R. Sánchez and A. Huerta, Rev. Mex. Fis. **60**, 119 (2014).
[34] See supplemental material.
[35] J. Galanis, R. Nossal, W. Losert, and D. Harries, Phys. Rev. Lett. **105**, 168001 (2010).
[36] A. Kudrolli, G. Lumay, D. Volfson, and L. S. Tsimring, Phys. Rev. Lett. **100**, 058001 (2008).
[37] D. de las Heras and E. Velasco, Soft Matter **10**, 1758 (2014).
[38] J. A. Cuesta and D. Frenkel, Phys. Rev. A **42**, 2126 (1990).
[39] This value represents the average between $L/D = 6.6$ (tetratic) and $L/D = 8$ (uniaxial).
[40] Y. Martínez-Ratón, E. Velasco, and L. Mederos, J. Chem. Phys. **122**, 064903 (2005).
[41] Y. Martínez-Ratón, E. Velasco, and L. Mederos, J. Chem. Phys. **125**, 014501 (2006).

Supplemental Material: Ordering of Granular Rod Monolayers Driven Far from Thermodynamic Equilibrium

Thomas Müller,[1] Daniel de las Heras,[2] Ingo Rehberg,[1] and Kai Huang[1]
[1] *Experimentalphysik V, Universität Bayreuth, D-95440 Bayreuth, Germany*
[2] *Theoretische Physik II, Universität Bayreuth, D-95440 Bayreuth, Germany*

DENSITY FUNCTIONAL THEORY

We use an Onsager-like density functional theory (DFT) with Parsons-Lee rescaling. A similar DFT was previously used to analyze the state diagram of two dimensional rods confined in a circular cavity [1]. We are interested in the behavior of fluid states in which the density is spatially homogeneous. Hence we can write, without loss of generality, the one body density distribution as

$$\rho(\vec{r},\gamma) = \rho h(\gamma), \tag{1}$$

where ρ is the number density and $h(\gamma)$ is the orientational distribution function. Here γ is the angle with respect to the director. $h(\gamma)$ is normalized such that

$$\int_0^\pi \mathrm{d}\gamma h(\gamma) = 1. \tag{2}$$

We split the free energy into two parts

$$F[\rho] = F_{\mathrm{id}}[\rho] + F_{\mathrm{ex}}[\rho], \tag{3}$$

where F_{id} is the ideal gas part and F_{ex} is the excess part accounting for the excluded volume interactions. The ideal free energy per unit of area A is given exactly by

$$\frac{\beta F_{\mathrm{id}}[\rho]}{A} = \int_0^\pi \mathrm{d}\gamma \rho h(\gamma) \ln(\Lambda \rho h(\gamma) - 1), \tag{4}$$

where $\beta = 1/k_{\mathrm{B}}T$ with k_{B} the Boltzmann's constant and T the absolute temperature. Λ is the (irrelevant) thermal volume that we set to one. The excess part is approximated by

$$\frac{F_{\mathrm{ex}}[\rho]}{A} = \frac{\psi_{\mathrm{ex}}(\phi)}{4LD}\rho \int_0^\pi \mathrm{d}\gamma_1 \int_0^\pi \mathrm{d}\gamma_2 h(\gamma_1) h(\gamma_2) v_{\mathrm{exc}}(\gamma_{12}). \tag{5}$$

$v_{\mathrm{exc}}(\gamma_{12})$ is the excluded area between two rectangles with length L, width D and relative orientation γ_{12}:

$$v_{\mathrm{exc}}(\gamma_{12}) = (L^2 + D^2)|\sin\gamma_{12}| + 2LD(1 + |\cos\gamma_{12}|), \tag{6}$$

and $\psi_{\mathrm{ex}}(\phi)$ is the excess free energy per particle of a reference system of hard disks at the same area fraction $\phi = \rho LD$ as our system of hard rectangles. The diameter of the disks is selected such that both disks and rectangles have the same area. Following Baus and Colot [2] we approximate ψ_{ex} by:

$$\beta\psi_{\mathrm{ex}}(\phi) = (c_2 + 1)\frac{\phi}{1-\phi} + (c_2 - 1)\ln(1-\phi), \tag{7}$$

with $c_2 = 7/3 - 4\sqrt{3}/\pi \approx 0.1280$. Eq. (5) recovers the Onsager approximation in the low density limit.

Finally, the grand potential is given by

$$\Omega[\rho]/A = F[\rho]/A - \mu\rho, \tag{8}$$

with μ the chemical potential. We minimize Ω with respect to ρ and $h(\gamma)$ in order to find the equilibrium states. We use a standard conjugated gradient method to minimize the functional. We use a truncated Fourier expansion to describe $h(\gamma)$. We truncate the expansion such that the absolute value of the last coefficient in the expansion is smaller than 10^{-7}.

MONTE CARLO SIMULATIONS

We model the particles as two dimensional hard rectangles of length L and width D that interact through excluded volume interactions. N of such particles are placed in a box with dimensions L_x and L_y along the x- and y-axes, respectively. We use periodic boundary conditions in both axes. We study the equilibrium bulk configurations by means of standard Monte Carlo (MC) simulations in the canonical ensemble. That is, we fix the number of particles N and the system area $A = L_x L_y$ (the temperature is irrelevant in hard models). The number of particles is similar to that in the experiments, $N \sim 10^3$. We use simulation boxes with rectangular and square shapes. No difference has been found between both geometries.

The simulation method is as follows. In order to equilibrate the system we start at very high area fractions, $\phi \approx 0.95$, placing the particles, with their main axes pointing in the same direction, in a rectangular lattice. Next we run 10^7 Monte Carlo steps (MCSs). Each MCS is an attempt to move and rotate all the particles in the system. The maximum displacement $\Delta r_{\max}$ and maximum rotation $\Delta\theta_{\max}$ that each particle is allowed to perform in a MCS is fixed such that the acceptance probability is 0.2. Then we remove a few particles randomly chosen, recalculate $\Delta r_{\max}$ and $\Delta\theta_{\max}$, and start a new simulation. The number of removed particles is such that the change in area fraction is $\Delta\phi \lesssim 0.01$. In order to rule out metastable configurations related to the preparation of the initial state, we discard simulations with $\phi \gtrsim 0.8$. When the area fraction is below that limit we start the proper simulation. For each simulation we

first run 10^6 MCSs to equilibrate the system and then accumulate data over 10^7 MCSs. For selected L/D we have also simulated the system by increasing the number of particles, i.e. by adding particles instead of removing them. We have found no differences between both methods.

The state of the system is characterized by the area fraction, the uniaxial order parameter q_2 and the tetratic order parameter q_4.

COMPARISON BETWEEN DFT AND MC

A comparison between DFT and MC results is given in Fig. 1, where we represent the state diagram in the plane of area fraction and aspect ratio of the particles. The theory predicts a tetratic state at low aspect ratios and a uniaxial state for high aspect ratios, in agreement with MC results. The agreement is qualitative for $L/D \gtrsim 8$. The theory overestimates the transition density for low aspect ratios and underestimates the aspect ratio at which the ordered state changes from tetratic to uniaxial nematic. Another discrepancy between DFT and MC is the order of the transitions. DFT predicts a first order transition for $2 \lesssim L/D \lesssim 6$. The discrepancies between DFT and MC are most likely related to the mean field character of the theory.

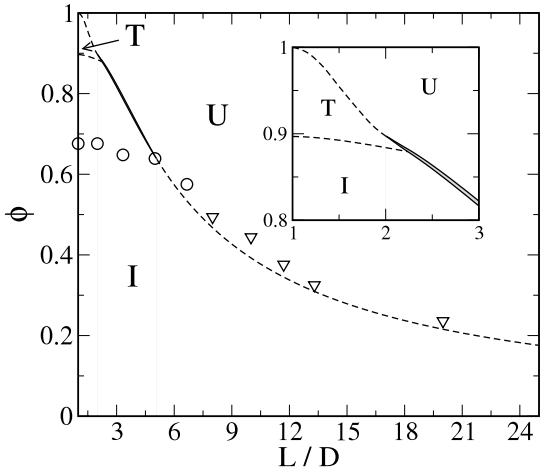

FIG. 1. State diagram of a system of hard rectangles in the plane of area fraction ϕ and aspect ratio L/D according to our DFT. The states are isotropic (I), uniaxial nematic (U), and tetratic (T). The gray area is a two phase region. Dashed lines indicate continuous transitions and solid lines are binodals. The inset is a zoom of the region in which the tetratic state is stable. Open symbols are Monte Carlo data: circles indicate the I-T transition and triangles denote the I-U transition.

[1] D. de las Heras, E. Velasco, and L. Mederos, Phys. Rev. E **79**, 061703 (2009).
[2] M. Baus and J. L. Colot, Phys. Rev. A **36**, 3912 (1987).

7

Recent Articles

Analog of surface melting in a macroscopic nonequilibrium system

Christopher May, Michael Wild, Ingo Rehberg, and Kai Huang*
Experimentalphysik V, Universität Bayreuth, 95440 Bayreuth, Germany
(Received 23 January 2013; revised manuscript received 5 October 2013; published 5 December 2013)

Agitated wet granular matter can be considered as a nonequilibrium model system for phase transitions, where the macroscopic particles replace the molecules and the capillary bridges replace molecular bonds. It is demonstrated experimentally that a two-dimensional wet granular crystal driven far from thermal equilibrium melts from its free surface, preceded by an amorphous state. The transition into the surface melting state, as revealed by the bond orientational order parameters, behaves like a first order phase transition, with a threshold being traceable to the rupture energy of a single capillary bridge. The observation of such a transition in the macroscopic nonequilibrium system triggers the question of the universality of surface melting.

DOI: 10.1103/PhysRevE.88.062201 PACS number(s): 45.70.−n, 05.70.Ln, 64.70.D−

Surface melting has been a topic of interest since Michael Faraday's observations on regelation, the welding of two blocks of ice after contact below 0 °C [1]. After more than a century of investigations, it becomes clear that melting is a continuous process that tends to start from the free surface [2–4]. The qualitative idea initiated by Frenkel [5] is the reduction of surface energy due to the weaker binding of molecules at the surface compared with that within the bulk. Quantitative experiments pioneered by Frenken and colleagues [6,7] have revealed that many solids melt by forming a premelted film, an intermediate state between a solid and a liquid, below the bulk melting temperature [4]. From a microscopic perspective, the kinetics of melting transition have also been explored in detail by means of molecular dynamics simulations [8–10] and experiments [11–15] with colloidal suspensions as model systems, in order to test existing models [16]. Despite that the term "surface melting" was originally introduced for equilibrium systems and most investigations are performed with thermodynamic equilibrium as a precondition, there exists evidence showing surface melting persists as a crystal is driven away from thermal equilibrium [2,17]. An interesting follow-up question is: Can our current microscopic view on melting be extended to the wide spreading nonequilibrium systems in nature?

Here, we try to address this question with a wet granular model system. Granular matter, besides its ubiquity in nature [18,19], has been frequently used as a model system for phase transitions far from thermal equilibrium [20–29], due to the strongly dissipative particle-particle interactions. Here, we use a monolayer of wet particles as a model system, because the cohesion arising from the formation of capillary bridges, which mimics molecular bonds, effectively leads to a crystalline structure with a free surface. The melting of such a wet granular crystal is found to be a two-step process: a plastic deformation into an amorphous state, followed by melting from the surface. The abrupt transition into the surface melting regime is reminiscent of a first order phase transition. The transition threshold can be rationalized by a balance between the effective energy injection and the rupture energy of a single capillary bridge.

*kai.huang@uni-bayreuth.de

The wet granular sample is prepared by adding a certain volume of purified water V_l into a monolayer of $N = 250$ cleaned black glass spheres (SiliBeads P) with a density $\rho_p = 2.58$ g/cm^3 and a diameter $d = 4 \pm 0.02$ mm. The liquid content is defined as $W = V_l/V_s$, with V_s the total volume of the spheres. The cylindrical container made of polytetrafluoroethylene (PTFE) has an inner diameter of $D = 102$ mm, a height of 6 mm, and a glass lid sealed with indium to avoid evaporation. The glass lid is heated slightly during the experiments to minimize the liquid condensation. The container is fixed on a swirling table leveled within 5.7×10^{-3} degrees to avoid the influence from gravity. The swirling table (see [30] for a sketch) provides a horizontal circular motion with a frequency f and amplitude a as control parameters. These two combined horizontal vibrations provide an isotropic energy injection, since the amplitude of the agitation velocity is independent of the phase. The computer-controlled swirling frequency can be varied with an accuracy of 6.2×10^{-4} Hz. The dynamics of the spheres are captured by a camera (Lumenera LU125M) mounted on the comoving frame of the swirling table. f is obtained via tracing a fixed point on the swirling table with a second camera (Lumenera LU075M). The snapshots captured are subjected to an image-processing procedure to locate all spheres based on a Hough transformation [31].

From the positions found, the connectivity of two neighboring particles is determined through a comparison of their distance to the critical bond length $r_b = 1.25\,d$, which is estimated from the rupture distance of a capillary bridge [32]. Local symmetries of particle configurations are characterized with the bond orientational order parameters (BOOP) [33,34], defined as

$$q_l = \sqrt{\frac{4\pi}{2l+1}\sum_{m=-l}^{l}|\bar{Q}_{lm}|^2}, \tag{1}$$

where $\bar{Q}_{lm} \equiv \langle Q_{lm}(\vec{r})\rangle$ is an average of the local order parameter $Q_{lm}(\vec{r}) \equiv Y_{lm}(\theta(\vec{r}),\phi(\vec{r}))$ over all bonds connecting one particle to its nearest neighbors, with $Y_{lm}(\theta(\vec{r}),\phi(\vec{r}))$ spherical harmonics of a bond located at $\vec{r}$. Here, we choose q_6 as the order parameter because of its sensitivity to the hexagonal order. Based on the deviations of q_6 to the standard values for perfectly hexagonal, square, and line structures,

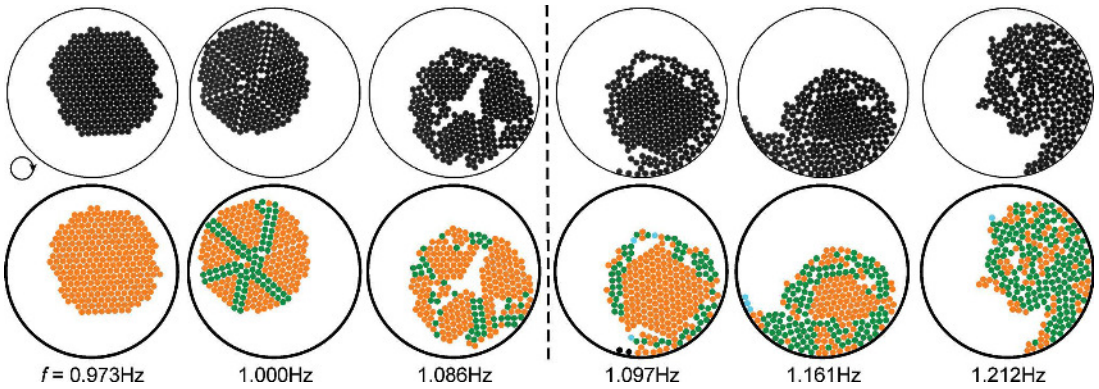

FIG. 1. (Color online) Melting process of a wet granular crystal with liquid content $W = 2.4\%$ as the swirling frequency increases, represented by the snapshots (upper panel) and local structures (lower panel). The particles in the lower panel are color coded according to their local structures: free particles with black; line, square, and hexagonal structures with cyan (light gray), green (dark gray), and orange (gray), respectively. The gray dashed line corresponds to the start of surface melting. The container swirls in the clockwise direction.

the structure that a particle is most likely belonging to is distinguished.

To achieve a homogeneous wetting condition, the sample is swirled with a relatively large initial frequency for at least one hour. As agitation starts, the initially isolated particles merge with each other into small assemblies in a rather short time scale (a few seconds), due to the cohesion arising from the formation of capillary bridges. As time evolves, those small assemblies gradually merge with each other into a single large cluster, within which the particles vigorously exchange positions with their neighbors, exhibiting a liquidlike state. To achieve an initial crystalline state, the swirling frequency is ramped down until the cluster stops reorganizing. Depending on the ramping rate, the initialized crystal may range from a perfectly hexagonal structure to a polycrystalline structure. In order to have a well-defined initial condition, we keep the ramping rate slow enough for the system to favor the former structure.

Figure 1 shows the melting process as the swirling frequency grows with a step of 6.2×10^{-4} Hz and a waiting time of 1 min between each step. A variation of either parameter by 1 order of magnitude yields the same melting threshold. At the initial frequency $f = 0.973$ Hz, the particles form a perfectly hexagonal structure. Although the crystal moves around collectively in the comoving frame, the internal structure stays stable. As the frequency increases to 1.000 Hz, the occasional impacts with the container give rise to temporally formed cracks inside the crystal. Although the cracks formed fluctuate with time in such a nonequilibrium steady state, the reduced overall packing density and the weakened internal structure persist from a statistical point of view. Note that this is different from noncohesive particles under vertical [35] or horizontal [21] agitations, where collisions with the container will tend to "heat" up the boundary layer and give rise to a granular temperature gradient as the "heat" flux propagates through. This difference could be attributed to the strong cohesion between adjacent particles, which leads to the favoring of collective motion. As the frequency increases further to 1.086 Hz, more broken bonds lead to larger voids within the cluster, along with the plastic deformation of the crystal into an amorphous state. The enhanced energy dissipation at the defects effectively increases the susceptibility for the cluster to deform under normal stress applied by the container. Meanwhile, the shear stress drives the rotation of the cluster along the swirling direction.

An abrupt change of the structure occurs between 1.086 and 1.097 Hz: all the voids inside the cluster disappear suddenly and a state with a perfectly hexagonal core surrounded by few liquidlike layers arises. We identify the new state as surface melting, since the deviations from the hexagonal structure locate only at the outer layers. At the beginning of the surface melting state, the liquidlike layer tends to "wet" the crystalline core and keeps a circular shape, suggesting a tendency to reduce its surface energy. As the frequency increases further to 1.161 Hz, melting continues inward and the molten layer tends to deform along the swirling direction. Eventually at 1.212 Hz, the sample melts completely into a comma-shaped "droplet" moving along the rim of the container in the comoving frame. The fluctuations of the surface of the molten layer, in connection with the interfacial tension of such a wet granular model system, is an interesting question to be addressed in further investigations.

To have a quantitative characterization of surface melting, we analyze the local structure of particles on the edge of a melting crystal, which is distinguished by the connectivity of particles. Based on the criteria described above, we locate all the neighbors of a particle, and recursively the neighbors of all the neighbors found, until all particles inside are found. The rescaled BOOP $\Delta\tilde{q}_6 = |q_6/q_6^{\mathrm{hex}} - 1|$ is chosen as the order parameter for surface melting, because it measures the deviation from a perfect hexagonal structure $q_6^{\mathrm{hex}} = 0.741$. Note that $\Delta\tilde{q}_6 = 0$ corresponds to the initial crystalline state. Each data point corresponds to an average of all edge particles and over all frames captured.

As shown in Fig. 2, surface melting can be clearly distinguished from the order parameter. Within data scattering,

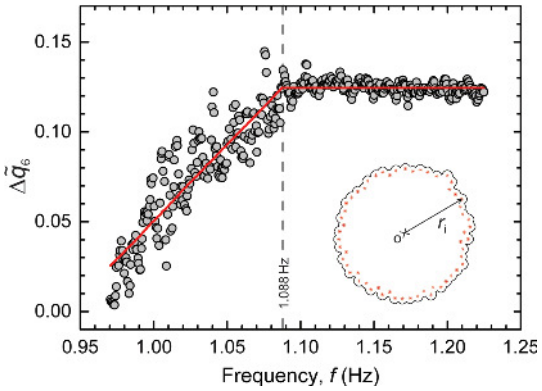

FIG. 2. (Color online) Deviation of the local structure for edge particles from a hexagonal one $\Delta\tilde{q}_6$ (see text for a definition) as frequency increases. Inset: A processed image with edge particles (stars) determined from the distance to the cluster contour line. r_i is the distance between an edge particle and the cluster center O. The gray dashed line corresponds to the melting threshold $f_{th} = 1.088 \pm 0.036$ Hz, which is determined by linear fits of the data.

$\Delta\tilde{q}_6$ initially grows with the swirling frequency. This arises from the temporarily formed cracks across the crystal, as well as the following plastic deformation into the amorphous state, because both processes lead to a weakening of the cluster at the edge. As surface melting starts, $\Delta\tilde{q}_6$ saturates at a value of roughly 0.125, since particles in a liquidlike state share a similar local structure. This behavior provides a convenient way to accurately determine f_{th}. As the solid lines in Fig. 2 demonstrate, two fits, a first followed by a zeroth order, are applied to the data, and the threshold corresponds to the intersection point that minimizes the standard error.

Figure 3(a) shows the internal structure of the crystal during the melting process, from which more features on the self-organization of particles inside the cluster can be obtained. First, it represents how the wet granular crystal evolves from crack forming to the amorphous state. In case of a crack with a constant width formed across the crystal, it will lead to a deviation of $\Delta\tilde{q}_6$ for all particles associated. The deviation is pronounced in a periodic manner along the radial direction, because the positions of particles in such a crystal are mostly fixed to a hexagonal lattice. The decay of the deviation with r arises from the average over all azimuth directions, since the relative influence from the crack decreases as the distance to the center O increases. As f grows, the enhanced crack formation leads to a larger deviation of $\Delta\tilde{q}_6$ and a continuous increase of the mean crystal size $\bar{r}_i$. At about 1.016 Hz, the deviation is strong enough to destroy the initial hexagonal lattice and allow a plastic deformation of the cluster. Consequently, large fluctuations of $\Delta\tilde{q}_6$ and of the cluster size start. Second, the change of internal structure presents the abrupt reorganization of the particles as surface melting starts. The amorphous state with large fluctuations of $\Delta\tilde{q}_6$ is suddenly replaced with a phase separation into a more compact inner core with a size of about $6d$, shielded with a molten layer of about $2d$, suggesting a first-order-like phase transition. Obvious deviations from a hexagonal packing

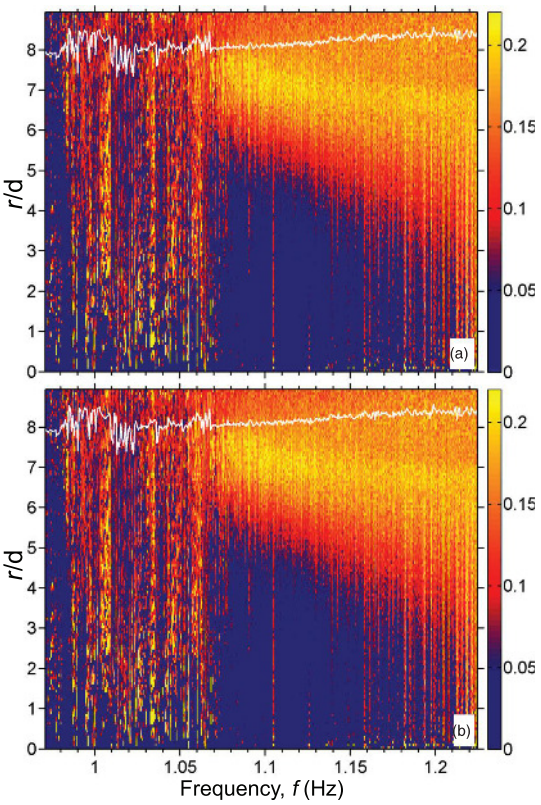

FIG. 3. (Color online) $\Delta\tilde{q}_6$ as a function of the rescaled distance r/d to the cluster center O as the driving frequency f increases (a) and decreases (b). Here $\Delta\tilde{q}_6$ corresponds to an average of the rescaled q_6 over all azimuth directions and all frames. The white curve in either plot corresponds to a measure of the cluster size $\bar{r}_i$, which is averaged over all edge particles and all frames recorded.

can be observed within the molten layer, and its thickness grows monotonically with the driving frequency, along with the dilation of the cluster. Third, it indicates that the transition into the liquidlike state is not continuous. As the thickness of the molten layer reaches roughly half of the cluster size, the inner core of the cluster loses the hexagonal structure altogether and the whole cluster reaches a liquidlike state.

Figure 3(b) shows the crystallization process as f decreases with the same rate. Its similarity to the melting process is remarkable, except for a shift of the amorphous state to a slightly lower frequency. It suggests the existence of hysteresis between the melting and the crystallization process. Further experiments with various ramping rates up to 14 runs indicate that the hysteresis, despite being comparable to the error of the threshold, is reproducible. This behavior presumably arises from the hysteresis nature between the formation and rupture of a single capillary bridge [36].

To gain further insights into the melting transition, the f_{th} is measured for various liquid content W and swirling amplitude a. As shown in Fig. 4, the threshold increases monotonically with the liquid content and saturates at $W \approx 6\%$. Assuming

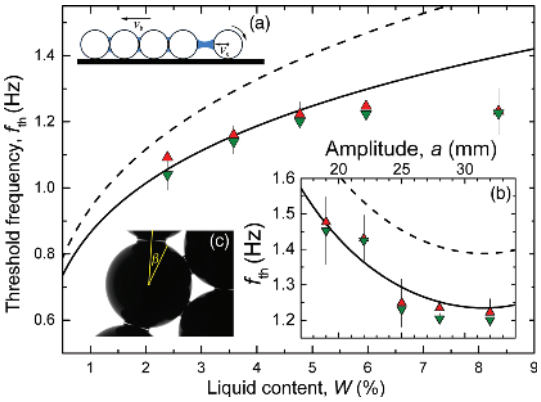

FIG. 4. (Color online) Dependency of the threshold frequency on the liquid content and the swirling amplitude (b). f_{th} is measured with the $\Delta\tilde{q}_6$ of edge particles as order parameter. The upper and lower triangles correspond to increasing and decreasing f. a and W are fixed at 31.8 mm and at $W = 4.77\%$ in the main panel and in (b), correspondingly. The dashed and solid lines are estimations from the model. (a) A sketch illustrating an edge particle rolling away from the bulk. v_s and v_b are the velocity of the edge and of the bulk particles in the laboratory frame. (c) A close view of the edge of a crystal with $W = 2.39\%$, captured with a microscope. β denotes the half-opening angle of a capillary bridge.

that surface melting represents the establishment of a new balance between the energy injection and dissipation, the dependence on W can be rationalized with the enhanced energy dissipation due to the larger rupture distance of a capillary bridge. The viscous effect can be safely ignored, because the capillary number, the ratio between the viscous and capillary forces, is less than 10^{-2}. The velocity of the swirling table $v_0 = 2\pi f a$, which plays a crucial role injecting energy into the system, provides a clue to understanding the decay of f_{th} with the increase of a shown in Fig. 4(b).

Following the above analysis, we propose a model based on a balance between the effective thermal energy injection E_i and the rupture energy of a single capillary bridge E_b. The energy injection is considered to be a two-step process: colliding with the container wall provides "macroscopic" collective motion of the cluster, followed by a transfer into the "microscopic" thermal energy through particle-particle interactions inside. As illustrated in Fig. 4(a), the particle on the edge of a cluster has more freedom to roll compared with those in the bulk, due to less restrictions from the neighbors. This difference provides the thermal energy for the edge particle $m(2\pi f a k)^2/2$, with m its mass and $k = 1 - v_s/v_b$ the relative velocity difference. The latter is 5/7 for the case that only edge particles roll, and roll without sliding and rolling frictions [37]. As the second step only occurs without interruptions from the wall, we introduce an additional factor $\alpha = (D - 2a)/(D + 2a)$, the length scale for a particle to move without disturbance from the wall over that for the swirling table to reach. Therefore the effective energy injection $E_i = \alpha m(2\pi f a k)^2/2$. On the other hand, the rupture energy of a capillary bridge can be estimated [32] to be $E_b = 3.68\cos(\theta)\sigma\sqrt{V_b d}$, with $\theta = 0.227$ the contact angle obtained from a close view of the bridges, $\sigma = 0.072$ N/m surface tension of water, and the bridge volume $V_b = \pi d^3 W/(3N_{cor})$. The coordination number $N_{cor} \approx 5.5$ is obtained from the initial crystalline state.

Consequently, the threshold frequency can be estimated with

$$f_{th} = \frac{0.60}{ka}\left(\frac{\sigma\cos(\theta)}{\rho_p d}\frac{D+2a}{D-2a}\right)^{1/2}\left(\frac{W}{N_{cor}}\right)^{1/4}, \quad (2)$$

which is shown as dashed lines in Fig. 4. The solid lines correspond to a more accurate estimation of E_b from a numerical integration of a more exact force law (Appendix of [32]), which is accurate to within 3% for W up to 6.58%. This limit corresponds to the merging of liquid bridges at $\beta = \pi/6$. A comparison with the experimental results indicates that, without any fit parameter, the model captures fairly well the dependency of f_{th} on W and A, provided that the particles are connected via capillary bridges. The saturation of f_{th} with W appears earlier than the limiting value, because the bridge volume is not always homogeneously distributed, as the snapshot shown in Fig. 4 demonstrates.

In summary, the melting of a two-dimensional wet granular crystal with 250 macroscopic "molecules" is demonstrated to be a continuous process starting from the surface. Preceding surface melting, there exists an intermediate stage where the crystal deforms plastically into an amorphous state, leading to a more fragile internal structure with large fluctuations of voids. The abrupt transition into the surface melting regime, reminiscent of a first order phase transition, can be rationalized with the balance of the energy injection and dissipation through the rupture of capillary bridges. Moreover, this experiment indicates that gravity is not a crucial factor for the surface melting of such a model system, in connection to a former numerical investigation [28] on vertically agitated wet granular matter.

In the future, further investigations on the distribution of the granular temperature, especially close to the melting transition, are necessary to address the question of the possibility to extend our current microscopic view of surface melting into systems out of thermal equilibrium. A comparison to computer simulations will shed light on such an interesting question. Moreover, the tendency for the molten layer to minimize its free surface [3,38–40] provides the opportunity to investigate the interfacial tension of fluidized cohesive granular matter.

The authors would like to thank T. Fischer, A. Fortini, D. Nelson, J. Olafson, M. Schmidt, and J. Vollmer for helpful discussions. This work is supported by the DFG through Grant No. HU1939/2-1.

[1] M. Faraday, The Athenaeum **1181**, 640 (1850).
[2] J. G. Dash, Rev. Mod. Phys. **71**, 1737 (1999).
[3] U. Tartaglino, T. Zykova-Timan, F. Ercolessi, and E. Tosatti, Phys. Rep. **411**, 291 (2005).

[4] J. G. Dash, A. W. Rempel, and J. S. Wettlaufer, Rev. Mod. Phys. **78**, 695 (2006).
[5] J. Frenkel, *Kinetic Theory of Liquids* (Clarendon, Oxford, 1946).
[6] J. W. M. Frenken and J. F. van der Veen, Phys. Rev. Lett. **54**, 134 (1985).
[7] J. W. M. Frenken, P. M. J. Marée, and J. F. van der Veen, Phys. Rev. B **34**, 7506 (1986).
[8] R. W. Cahn, Nature (London) **323**, 668 (1986).
[9] Z. H. Jin, P. Gumbsch, K. Lu, and E. Ma, Phys. Rev. Lett. **87**, 055703 (2001).
[10] R. W. Cahn, Nature (London) **413**, 582 (2001).
[11] K. Zahn and G. Maret, Phys. Rev. Lett. **85**, 3656 (2000).
[12] U. Gasser, E. R. Weeks, A. Schofield, P. N. Pusey, and D. A. Weitz, Science **292**, 258 (2001).
[13] A. M. Alsayed, M. F. Islam, J. Zhang, P. J. Collings, and A. G. Yodh, Science **309**, 1207 (2005).
[14] U. Gasser, C. Eisenmann, G. Maret, and P. Keim, Chem. Phys. Chem. **11**, 925 (2010).
[15] Z. Wang, F. Wang, Y. Peng, Z. Zheng, and Y. Han, Science **338**, 87 (2012).
[16] See, e.g., K. J. Strandburg, Rev. Mod. Phys. **60**, 161 (1988).
[17] H. Hakkinen and U. Landman, Phys. Rev. Lett. **71**, 1023 (1993).
[18] J. Duran, *Sands, Powders and Grains: An Introduction to the Physics of Granular Materials*, 1st ed. (Springer-Verlag, New York, Inc., 2000).
[19] H. M. Jaeger, S. R. Nagel, and R. P. Behringer, Rev. Mod. Phys. **68**, 1259 (1996).
[20] B. Pouligny, R. Malzbender, P. Ryan, and N. A. Clark, Phys. Rev. B **42**, 988 (1990).
[21] G. Strassburger and I. Rehberg, Phys. Rev. E **62**, 2517 (2000).
[22] J. S. Olafsen and J. S. Urbach, Phys. Rev. Lett. **95**, 098002 (2005).
[23] P. M. Reis, R. A. Ingale, and M. D. Shattuck, Phys. Rev. Lett. **96**, 258001 (2006).
[24] A. Fingerle, K. Roeller, K. Huang, and S. Herminghaus, New J. Phys. **10**, 053020 (2008).
[25] M. G. Clerc, P. Cordero, J. Dunstan, K. Huff, N. Mujica, D. Risso, and G. Varas, Nat. Phys. **4**, 249 (2008).
[26] K. Huang, K. Roeller, and S. Herminghaus, Eur. Phys. J. Special Topics **179**, 25 (2010).
[27] F. Pacheco-Vázquez, G. A. Caballero-Robledo, and J. C. Ruiz-Suárez, Phys. Rev. Lett. **102**, 170601 (2009).
[28] K. Roeller and S. Herminghaus, Europhys. Lett. **96**, 26003 (2011).
[29] G. Castillo, N. Mujica, and R. Soto, Phys. Rev. Lett. **109**, 095701 (2012).
[30] S. Aumaître, T. Schnautz, C. A. Kruelle, and I. Rehberg, Phys. Rev. Lett. **90**, 114302 (2003).
[31] C. Kimme, D. Ballard, and J. Sklansky, Communications of the ACM **18**, 120 (1975).
[32] C. D. Willett, M. J. Adams, S. A. Johnson, and J. P. K. Seville, Langmuir **16**, 9396 (2000).
[33] P. J. Steinhardt, D. R. Nelson, and M. Ronchetti, Phys. Rev. B **28**, 784 (1983).
[34] Y. Wang, S. Teitel, and C. Dellago, J. Chem. Phys. **122**, 214722 (2005).
[35] K. Huang, G. Miao, P. Zhang, Y. Yun, and R. Wei, Phys. Rev. E **73**, 041302 (2006).
[36] S. Herminghaus, Adv. Phys. **54**, 221 (2005).
[37] L. Kondic, Phys. Rev. E **60**, 751 (1999).
[38] R. Lipowsky, Phys. Rev. Lett. **57**, 2876 (1986).
[39] X. Cheng, G. Varas, D. Citron, H. M. Jaeger, and S. R. Nagel, Phys. Rev. Lett. **99**, 188001 (2007).
[40] L.-H. Luu, G. Castillo, N. Mujica, and R. Soto, Phys. Rev. E **87**, 040202 (2013).

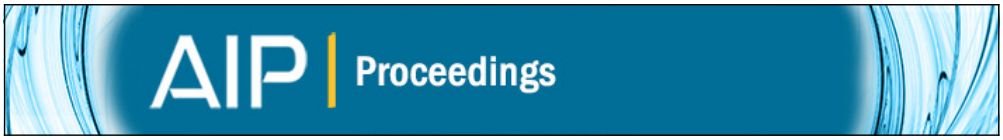

Scaling of the normal coefficient of restitution for wet impacts

Thomas Müller, Frank Gollwitzer, Christof A. Krülle, Ingo Rehberg, and Kai Huang

Citation: AIP Conference Proceedings **1542**, 787 (2013); doi: 10.1063/1.4812049
View online: http://dx.doi.org/10.1063/1.4812049
View Table of Contents: http://scitation.aip.org/content/aip/proceeding/aipcp/1542?ver=pdfcov
Published by the AIP Publishing

Scaling of the Normal Coefficient of Restitution for Wet Impacts

Thomas Müller*, Frank Gollwitzer*, Christof A. Krülle†, Ingo Rehberg* and Kai Huang*

*Experimentalphysik V, Universität Bayreuth, 95440 Bayreuth, Germany
†Maschinenbau und Mechatronik, Hochschule Karlsruhe - Technik und Wirtschaft, 76133 Karlsruhe, Germany

Abstract. A thorough understanding of the energy dissipation in the dynamics of wet granular matter is essential for a continuum description of natural phenomena such as debris flow, and the development of various industrial applications such as the granulation process. The coefficient of restitution (COR), defined as the ratio between the relative rebound and impact velocities of a binary impact, is frequently used to characterize the amount of energy dissipation associated. We measure the COR by tracing a freely falling sphere bouncing on a wet surface with the liquid film thickness monitored optically. For fixed ratio between the film thickness and the particle size, the dependence of the COR on the impact velocity and various properties of the liquid film can be characterized with the Stokes number, defined as the ratio between the inertia of the particle and the viscosity of the liquid. Moreover, the COR for infinitely large impact velocities derived from the scaling can be analyzed by a model considering the energy dissipation from the inertia of the liquid film.

Keywords: coefficient of restitution, impact, wetting, particle-laden flow, granular flow
PACS: 45.70.-n, 45.50.Tn, 47.55.Kf

INTRODUCTION

Understanding the energy dissipation associated with particle-particle interactions is crucial for describing the collective behavior of granular matter [1], i.e., large agglomerations of macroscopic particles. The coefficient of restitution (COR), firstly introduced by Newton as the ratio between relative rebound and impact velocities [2], can be used to characterize the energy dissipation at the particle level. This number provides one of the basic ingredients of computer assisted modeling, such as molecular dynamics (MD) simulation, which has been developed into a powerful tool to describe the large scale collective behavior of granular matter in the past decades [3, 4]. Besides the energy dissipation from particle-particle interactions, the dissipation arising from the interstitial air or liquid has to be considered when coping with natural phenomena such as dune migration [5] or debris flow [6], as well as with various industrial applications such as granulation process [7, 8].

The experience of building sand sculptures tells us that the rigidity of a granular material increases as a small amount of a wetting liquid is added. This is largely due to the cohesion arising from the formation of capillary bridges between adjacent particles [9]. The so-called wet granular matter behaves dramatically different from non-cohesive dry granular matter while agitated, with emerging critical behavior, such as phase transitions [10] and pattern formations [11], being traceable to the energy or force scale of a single capillary bridge. In order to gain insights into the dynamical behavior of wet granular matter, it is essential to explore the COR and the associated energy dissipation of wet impacts. A recent investigation reveals that the dependence of the COR on various particle and liquid properties can be scaled with two dimensionless numbers: the ratio between the inertia of the particle and the viscosity of the liquid (Stokes number), and that between the liquid film thickness and the size of the particle [12]. Here, further experimental results with a different density ratio between the particle and the wetting liquid are presented, in order to test the scaling of the COR with these three dimensionless numbers.

EXPERIMENTAL PROCEDURE

We measure the COR by recording a freely falling sphere with a highspeed camera (Photron, Fastcam Super 10K) at a frame rate up to 500 fps. Using a Hough transformation, the center of the sphere can be tracked in the images and the position of the sphere can be plotted against time (see Fig. 1). Fitting parabolic curves on the trajectories results in crossing points, which represent the time when the sphere hits the ground. The height of the crossing points varies slightly, owing to the various distance of the bouncing point to the camera. The slopes of the two fitted parabolae at each crossing point yield the impact velocity v_{imp} and the rebound velocity v_{reb} of the sphere, respectively. Hence the normal coefficient of restitution $e_{\mathrm{n}} = v_{\mathrm{reb}}/v_{\mathrm{imp}}$ can be determined for

Powders and Grains 2013
AIP Conf. Proc. 1542, 787-790 (2013); doi: 10.1063/1.4812049

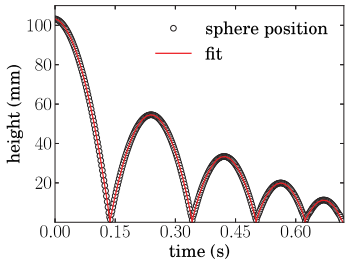

FIGURE 1. Typical trajectory of a bouncing sphere. The diagram shows a PE sphere of diameter $D = 7.9\,\mathrm{mm}$ bouncing on a glass plate covered with a $190\,\mu\mathrm{m}$ thick silicone oil (M5) film.

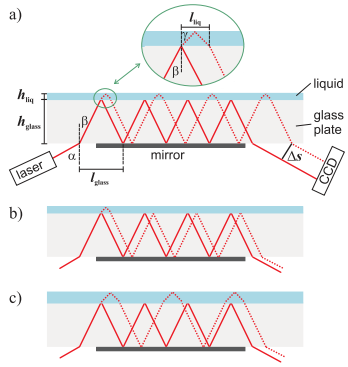

FIGURE 2. a) A sketch of the film thickness determination part of the setup. The solid lines show the beam for a dry container, the dashed lines illustrate the deviation with a liquid layer on top of the glass plate. Number of shifts by passing through the glass plate $j_{\mathrm{glass}} = 4$, number of reflections in the liquid film $j_{\mathrm{liq}} = 4$. b) $j_{\mathrm{glass}} = 4$, $j_{\mathrm{liq}} = 1$. c) $j_{\mathrm{glass}} = 3$, $j_{\mathrm{liq}} = 3$.

every impact. Polyethylene (PE) spheres with various diameter D and a density $\rho_{\mathrm{p}} = 0.94\,\mathrm{g/cm^3}$ are cleaned and pre-wetted before use. Two types of silicone oil (M5 and M50 from Carl Roth) with different dynamic viscosities $\eta = 4.6\,\mathrm{mPa\cdot s}$ for M5 and $48\,\mathrm{mPa\cdot s}$ for M50, and similar densities $\rho_{\mathrm{liq}} = 0.93\,\mathrm{g/cm^3}$ and $0.97\,\mathrm{g/cm^3}$ for M5 and M50 correspondingly are used. The bottom of the glass container, which has an inner area of $A = 100\,\mathrm{cm^2}$ is leveled within 0.03 degrees to ensure a horizontal surface and a uniform initial liquid film thickness. A sketch of the set-up and a more detailed description can be found in Ref. [12].

To investigate the influence of the liquid film on the COR, an accurate determination of its thickness is essential. Here, the thickness is measured optically by detecting the deflection of a laser beam (see Fig. 2 a) guided through the liquid film. The laser beam hits the glass plate with an incident angle of α and a refractive angle $\beta = \arcsin(n_{\mathrm{air}} \sin\alpha / n_{\mathrm{glass}})$, where n_{air} and n_{glass} are the refractive indices of air and glass, respectively. Without a liquid film, a part of the beam is reflected at the glass–air interface and then reflected at a mirror at the bottom of the glass plate. After a few reflections at the glass–air interface (here the number of reflections $j_0 = 4$, determined by the length of the mirror), the beam passes through the bottom of the glass plate again and is detected by a CCD camera.

With a liquid film of thickness h_{liq} on top of the glass plate, one reflection of the beam within the liquid film leads to a horizontal shift of the beam by a distance $l_{\mathrm{liq}} = 2h_{\mathrm{liq}} \tan\gamma$, with the refractive angle in the liquid $\gamma = \arcsin(n_{\mathrm{glass}} \sin\beta / n_{\mathrm{liq}}) = \arcsin(n_{\mathrm{air}} \sin\alpha / n_{\mathrm{liq}})$.

For the typical case that the number of reflections at the air–liquid interface j_{liq} is the same as that in the dry glass plate (Fig. 2 a), the total shift of the laser beam along the horizontal plane is $j_{\mathrm{liq}} \cdot l_{\mathrm{liq}}$ with $j_{\mathrm{liq}} = j_0$. It is also possible, as shown in Fig. 2 b, to detect reflected beams with a smaller number of passes through the liquid film ($j_{\mathrm{liq}} < j_0$), due to partial reflections at the glass–liquid interface. If the filling level is too high and consequently the shift of the beam is too big, an additional reduction of reflections in the glass plate to $j_{\mathrm{glass}} < j_0$ is also possible (Fig. 2 c). In such a case, a negative shift of $(j_0 - j_{\mathrm{glass}}) \cdot l_{\mathrm{glass}}$ has to be considered, where $l_{\mathrm{glass}} = 2h_{\mathrm{glass}} \tan\beta$ is a constant value.

Taking all the above possibilities into account, the reflected beams leave the glass with a horizontal shift which results in

$$\Delta s = \left[j_{\mathrm{liq}} \cdot l_{\mathrm{liq}} - (j_0 - j_{\mathrm{glass}}) \cdot l_{\mathrm{glass}} \right] \cos\alpha \qquad (1)$$

at the CCD. Consequently, the liquid film thickness can then be calculated by

$$h_{\mathrm{liq}} = \frac{\frac{\Delta s}{\cos\alpha} + 2(j_0 - j_{\mathrm{glass}}) h_{\mathrm{glass}} \tan\beta}{2 j_{\mathrm{liq}} \tan\gamma} \qquad (2)$$

Note that for thin films (when $j_0 - j_{\mathrm{glass}} = 0$), h_{liq} is independent on the properties of the glass plate.

Experimentally, the camera captures a series of spots with each of them corresponding to a certain combination of j_{liq} and j_{glass}. The brightest spot corresponds to the case $j_{\mathrm{liq}} = j_{\mathrm{glass}} = j_0$, therefore it is commonly used for the film thickness measurement. Figure 3 shows a comparison of the film thickness obtained from V/A, with V the volume of liquid added, and h_{liq} given by Eq. 2. With a certain V, the multiple spots detected give rise to multiple Δs. As V increases, the shift of each spot Δs follows a linear growth with various slopes and offset-

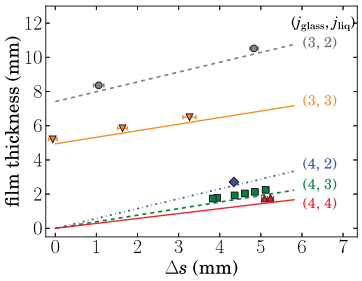

FIGURE 3. The relation between the water film thickness and the shift of the laser beam Δs at the CCD predicted from Eq. 2 (solid lines) and estimated with V/A, the toal liquid volum over the area of the container (data points).

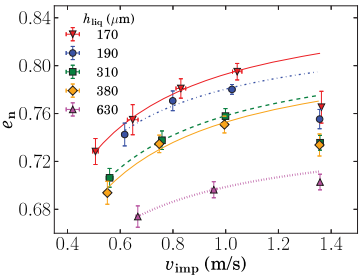

FIGURE 5. Normal coefficient of restitution e_n against the impact velocity v_{imp} for a PE sphere of fixed diameter $D = 7.9\,\text{mm}$ at different silicone oil M5 film thickness h_{liq}.

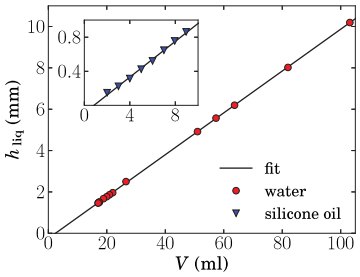

FIGURE 4. The film thickness obtained with Δs and Eq. 2 as a function of the filling volume of water and silicone oil (inset). The error bars are within the size of the symbols. Linear fits of the data with $h_{liq} = k(V - V_{men})$ yield the same $k = 0.01\,\text{cm}^{-2}$ for both liquids, and $V_{men} = (2.45 \pm 0.10)\,\text{ml}$ for water and $(0.84 \pm 0.15)\,\text{ml}$ for silicone oil.

s, which follows the prediction based on Eq. 2 with various combination of j_{liq} and j_{glass}. The systematic overestimation of the film thickness from V/A for all data sets is presumably due to the volume of the liquid captured in the meniscus of the liquid film V_{men}, since the systematic deviation from the estimation of Eq. 2 does not depend on the parameters j_{liq} and j_{glass}.

Therefore, using the variation of any spot detected by the camera, not only the brightest one, we can measure the liquid film thickness h_{liq}. This additional information from the spots with smaller intensity gives the opportunity to expand the range of h_{liq} that can be detected, provided that the free parameters j_{liq} and j_{glass} have been correctly determined from the first few data points.

Figure 4 shows that the optically obtained film thickness grows linearly with the liquid volume V, giving rise to a slope $k = 1/A$ and an estimation of the meniscus volume V_{men}. Therefore, an estimation of h_{liq} with V/A is also appropriate, provided that the meniscus volume is substracted. Nevertheless, the optical way provides a real-time monitoring of the film thickness. This will be helpful in future analysis on surface waves generated by the impact, and in monitoring the loss of liquid due to evaporation. The small deviation from the linear fit for the silicone oil film thickness data (inset of Fig. 4) indicates a correlation between V_{men} and h_{liq} for thin films, which we leave to future investigations. Figure 4 also shows the possibility to measure the film thickness up to 1 cm combining the information from various spots detected. The error of h_{liq}, on the order of $\approx 10\,\mu m$, arises mainly from the fluctuations of the spot intensity. At a larger film thickness, the spots will become too weak to be detected accurately by the camera. For thin films, silicone oil instead of water is preferable, because its low surface tension prevents the dewetting instability. Thus it is used for the following experiments.

RESULTS AND DISCUSSION

Towards a comprehensive understanding of the dependence of the COR for wet impacts on various liquid and particle properties, previous experiments with glass beads have revealed that the Stokes number and the dimensionless film thickness $\tilde{h} = h_{liq}/D$ can characterize the influence from inertia and viscous damping on the COR [12]. The Stokes number is defined as $\text{St} = \rho_p D v_{imp}/9\eta$. Here, we test the scaling with PE particles, which correspond to a density ratio $\tilde{\rho} = \rho_{liq}/\rho_p \approx 1$. Without the liquid, the COR for the PE particle on the glass plate, depending weakly on v_{imp} for the range of interest here, is measured to be 0.88 ± 0.03, averaged over 368 bouncing events.

Figure 5 shows the COR measured with an initial falling height of 9.5 cm and various film thicknesses h_{liq}.

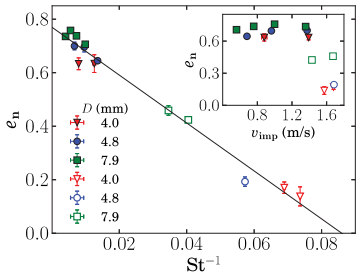

FIGURE 6. Normal coefficient of restitution e_n against the inverse Stokes number St^{-1} for a fixed $\tilde{h} \approx 0.04$. Data with closed and open symbols present measurements with silicone oil M5 and M50 correspondingly. The inset shows the same data, but plotted against v_{imp}.

The number of data points for each h_{liq} corresponds to the number of bouncings used for extrapolating the COR. The error bar arises from the statistics over 8-10 runs of the experiment. Except for the first bouncing data (the one with largest v_{imp}), the monotonic growth of the COR with v_{imp} could be fitted with $e_n = e_{inf}(1 - v_c/v_{imp})$, giving rise to a limiting COR e_{inf} at $v_{imp} \to \infty$ and a critical impact velocity v_c below which no rebound would occur. The decrease of the COR with the increase of h_{liq} clearly suggests the influence of the viscous damping, since the energy dissipated through a viscous force depends on the distance that the particle travels during the impact. Different from the case of glass beads [12], the COR for the first rebound is smaller than the fitted line for all film thicknesses. This could be attributed to the much stronger influence from the mass of liquid added to the particle during the first bouncing for the less dense PE sphere.

Besides the liquid film thickness, the COR depends also strongly on the viscosity of the wetting liquid. As shown in the inset of Fig. 6, the COR measured with silicone oil M50 as wetting liquid yields much lower values than those measured with M5. A re-plot of the COR with St^{-1} in Fig. 6 denotes a linear decay, suggesting that the dependence of the COR on h_{liq}, viscosity η and the impact velocity v_{imp} could be characterized by the Stokes number for fixed $\tilde{h}$. A linear fit with $e_n = e_{inf}(1 - St_c/St)$ yields a saturated COR $e_{inf} = 0.77 \pm 0.04$ and a critical Stokes number $St_c = 11.64 \pm 1.55$. Following a former theory [12], we could estimate $e_{inf} = e_{dry} - 3\tilde{\rho}\tilde{h}/2e_{dry} = 0.81 \pm 0.03$, which agrees with the measurement within the experimental uncertainties. This agreement suggests that the fact that e_{inf} is smaller than e_{dry} is due to the inertia of the wetting liquid, which provides the dependence on $\tilde{\rho}$ and $\tilde{h}$.

CONCLUSION

To conclude, the normal coefficient of restitution for the impact between a spherical particle and a flat surface covered with a liquid film is investigated for various impact velocities, particle and liquid properties. The technique to determine the film thickness optically and the calibration results are described in detail. Compared with the former methods [12], it provides an extended upper limit of the film thickness, and also allows the possibility to estimate the volume of the meniscus. At a certain density and size ratio, the COR is found to decay linearly with St^{-1}, which represents the scaling with the impact velocity and various particle as well as liquid properties. The parameter e_{inf} obtained from the fitting, corresponding to the saturated value of the COR, can be understood by a model considering the inertia of the liquid. A more detailed comparison to the model with various combinations of $\tilde{h}$ and $\tilde{\rho}$ will be a focus of our further investigations.

ACKNOWLEDGMENT

We thank L. Meissner for performing the dry COR measurements. We are grateful for the support from Deutsche Forschungsgemeinschaft through HU1939/2-1.

REFERENCES

1. J. Duran, *Sands, Powders and Grains*, Springer, New York, 2000.
2. I. Newton, *Mathematical Principles of Natural Philosophy*, 1687, axioms, or Laws of motion. Corollary VI.
3. C. Bizon, M. D. Shattuck, J. B. Swift, W. D. McCormick, and H. L. Swinney, *Phys. Rev. Lett.* **80**, 57–60 (1998).
4. N. Brilliantov, and T. Poeschel, *Kinetic theory of granular gases*, Oxford Univ. Press, 2004.
5. R. A. Bagnold, *The physics of blown sand and desert dunes*, Methuen, London, 1941.
6. R. M. Iverson, *Rev. Geophys.* **35**, 245 (1997).
7. S. M. Iveson, J. D. Litster, K. Hapgood, and B. J. Ennis, *Powd. Technol.* **117**, 3 (2001).
8. S. Antonyuk, S. Heinrich, N. Deen, and H. Kuipers, *Particuology* **7**, 245 (2009).
9. M. Scheel, R. Seemann, et al., *Nature Mater.* **7**, 189 (2008).
10. A. Fingerle, K. Röller, K. Huang, and S. Herminghaus, *New J. Phys.* **10**, 053020 (2008).
11. K. Huang, and I. Rehberg, *Phys. Rev. Lett.* **107**, 028001 (2011).
12. F. Gollwitzer, I. Rehberg, C. A. Kruelle, and K. Huang, *Phys. Rev. E* **86**, 011303 (2012).

Dynamics of rotating spirals in agitated wet granular matter

Kai Huang, Lorenz Butzhammer, and Ingo Rehberg

Citation: AIP Conference Proceedings **1542**, 702 (2013); doi: 10.1063/1.4812028
View online: http://dx.doi.org/10.1063/1.4812028
View Table of Contents: http://scitation.aip.org/content/aip/proceeding/aipcp/1542?ver=pdfcov
Published by the AIP Publishing

Dynamics of Rotating Spirals in Agitated Wet Granular Matter

Kai Huang, Lorenz Butzhammer and Ingo Rehberg

Experimentalphysik V, Universität Bayreuth, 95440 Bayreuth, Germany

Abstract. Pattern formation of a thin layer of vertically agitated wet granular matter is investigated experimentally. Due to the strong cohesion arising from the capillary bridges formed between adjacent particles, agitated wet granular matter exhibits a different scenario compared with cohesionless dry particles. Rotating spirals with three arms, which correspond to the kinks between regions with different colliding phases with the vibrating plate, have been found to be the dominating pattern [1]. From both top view snapshots and laser profilometry methods, the rotation frequency of the spiral arms is characterized with image processing procedures. Both methods reveal that there exists a finite rotation frequency ν_r at a threshold vibration acceleration, above which ν_r increases linearly with the peak vibration acceleration with a slope strongly dependent on the vibration frequency.

Keywords: pattern formation, granular systems
PACS: 45.70.Qj, 45.70.Mg

INTRODUCTION

From natural phenomena such as the formation of our galaxy, to the industrial processes such as coating, pattern formation is ubiquitous in the universe [2]. Explaining pattern formations, especially the accompanying length and time scales, helps us gain insight into the pattern forming systems, which are typically far from thermal equilibrium. Driven granular matter, as large agglomerations of macroscopic particles interacting with each other dissipatively, is such a non-equilibrium system [3]. Continuous energy injection is necessary in order to drive granular particles into a fluidlike state in order to process or transport them in various industries [4]. Even though a all-encompassing theory describing the dynamical behavior of granular matter, especially toward the limit of dense granular flow, is still far from established, the rich pattern forming nature of granular matter provides us the opportunity to gain insights into such a non-equilibrium system [5].

Besides the cohesionless dry granular matter, more and more attentions have been paid to the dynamics of wet granular matter recently [6]. Due to the cohesion arising from the formation of liquid bridges between adjacent particles, the static as well as dynamical behavior of wet granular matter, such as the wet sand used for sculptures, differs from its dry counterpart dramatically [7, 8]. A former investigation on the pattern formation of vertically agitated wet granular layer reveals a peculiar period tripling spiral pattern, typically composed of 3 arms that rotate continuously [1]. The preferred number of arms arise from period tripling of the agitated granular layer, which breaks the symmetry and drives the rotation of spiral arms. In the current work, the rotation frequency of the spiral arms is characterized quantitatively with two methods: One based on the horizontal motion of the arms from the top view snapshots, and the other one based on the fluctuations of the surface profile from the laser profilometry method.

EXPERIMENTAL METHODS

Figure 1(a) is a sketch of the main parts of the experimental setup. Cleaned glass beads (SiLiBeads S) with a diameter of $d = 0.78$ mm and 10% polydispersity, after proper mixing with purified water (Laborstar TWF-DI), are used as the granular sample. The amount of wetting is characterized by the liquid content $W = V_w/V_g$, where V_w is the volume of the water and V_g is that of the glass beads. It is normally kept within a few percent so that the cohesion arises mainly from the formation of capillary bridges between adjacent particles (as illustrated in the dash box). A certain amount of the sample (mass $m = 113$ g, corresponding roughly to 4–5 layers) is filled into a cylindrical polycarbonate container with an inner radius $R = 8$ cm and a height of $H = 1.06$ cm. Sinusoidal vibrations generated by an electromagnetic shaker (Tira TV50350) are used to agitate the sample against gravity. The vibration frequency f and the non-dimensional acceleration $\Gamma = 4\pi^2 f^2 A/g$, with vibration amplitude A and gravitational acceleration g, are the two control parameters. To obtain a homogeneous liquid distribution, the sample is agitated strongly into a gaslike state for a short period before each experiment. The mobility of the patterns are captured by a high speed camera (IDT

Powders and Grains 2013
AIP Conf. Proc. 1542, 702-705 (2013); doi: 10.1063/1.4812028

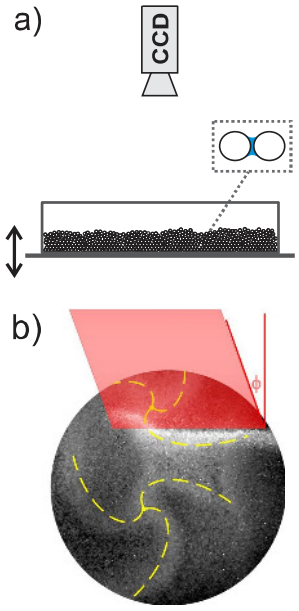

FIGURE 1. (a) A sketch of the experimental set-up. The zoom-in view shown in the dotted box illustrates a capillary bridge formed between two adjacent particles. (b) A top view image captured with a combined illumination of a laser sheet and a LED ring. $\phi = 37°$ is the angle between the laser sheet (illustrated with a half transparent parallelogram) and the horizontal plane. The dash curves highlight the spiral arms.

MotionScope M3) mounted on top of the container. The camera is synchronized with the shaker by a multi-pulse generator, in order to capture images at fixed phases of each vibration cycle. A more detailed description of the experimental setup could be found elsewhere [1].

Two methods are used to capture the mobility of the spiral arms. The first one uses the snapshots of the pattern obtained with a low angle illumination, which provides the information on the horizontal motion. The second one uses the the laser profilometry method [9], which provides information on the surface height fluctuations.

From the top view images, the rotation frequency of the spiral arms can be obtained from the gray value fluctuations $g(t)$ of regions with fixed distance to the core of the spirals, based on the fact that the spiral arms in the snapshots are brighter than the other regions, as Fig. 2(a) shows. The gray value difference is due to the fact that spiral arms correspond to kinks separating regions with different heights [1], and more light from the low angle illumination will be reflected to the camera in the kink (spiral arm) regions.

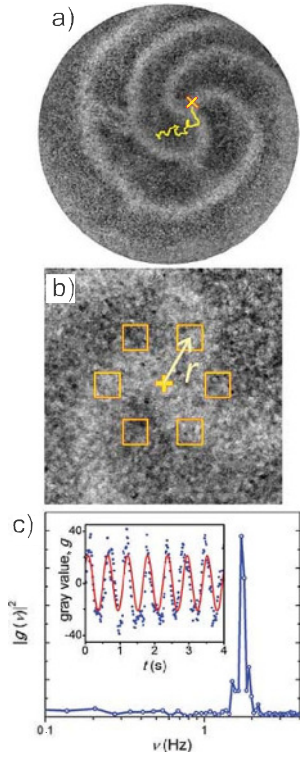

FIGURE 2. Procedure to obtain rotation frequency from top view snapshots. (a) A typical image of a three armed rotating spiral pattern (averaged over 3 consequent snapshots to enhance the contrast). The cross is the current position of the spiral core determined by the image processing procedure, and the curve corresponds to the trajectory of the spiral core in the past 12.5 seconds (1000 vibration cycles). (b) A close view of the spiral core region. The regions used to obtain gray value fluctuations marked with squares have equal distance r to the spiral core. (c) Averaged power spectrum $|g(\nu)|^2$ of the gray value fluctuations $g(t)$ obtained within 6 regions. Inset is the fluctuation with time (dot) and a fitting with a harmonic function.

The essential part of the algorithm is to choose the region of interest for the analysis of the brightness fluctuations properly. Especially the regions close to the spiral cores should be avoided, since those regions correspond to the common part of spiral arms, where the brightness fluctuations are much smaller than those further away from the core. Based on the fact that the spiral core region keeps its brightness during the rotation of spiral arms, a minimization of the gray value over continuous

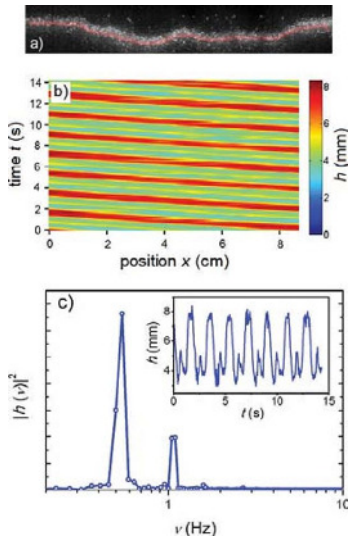

FIGURE 3. Procedure to obtain rotation frequency from laser profilometry. (a) A snapshot captured with laser sheet illumination, from which the surface profile is obtained by image processing. (b) Time-space plot of the surface profile captured with a frame rate $f/3$. h denotes the height of the profile. (c) Power spectrum of the height fluctuations $|h(\nu)|^2$, averaged over 6 positions with equal distances. The inset shows the height fluctuation with time at one position.

snapshots effectively enhances the contrast between the spiral core and the surrounding regions. The number of snapshots is chosen to cover $1/3$ of the rotation period. After proper thresholding, we are able to estimate the location of the spiral core from the weighted average of the core region.

From the trajectory of the spiral cores determined (see the superimposed curve in Fig. 2(a)), no clear relation to the rotation direction of the spiral arms could be found and the core wander around randomly. As shown in Fig. 2(b), 6 square boxes with a certain radial distance r to the spiral core, and equally distributed in the angular direction, are chosen as the regions of interest. The spatially averaged brightness within each box as a function of time is recorded individually (see the inset of Fig. 2(c) for an example). As shown in Fig. 2(c), the averaged power spectrum of the brightness over all the 6 boxes indicates clearly a periodicity of the gray value fluctuations. From the peak value $(|g(\nu_{p0})|^2$ at frequency $\nu_{p0})$ and the largest nearest neighbor value $(|g(\nu_{p1})|^2$ at frequency $\nu_{p1})$, we interpolate the rotation frequency with a weighted average $\nu_r = (|g(\nu_{p0})| \cdot \nu_{p0} + |g(\nu_{p1})| \cdot \nu_{p1})/3(|g(\nu_{p0})| + |g(\nu_{p1})|)$, where the factor 3 arises from the fact that all the three spiral arms will generate brightness fluctuations. Alternatively, the frequency of $g(t)$ is also determined directly by a sinusoidal fit of the data in the time domain (inset of Fig. 2(c)), which agrees with the ν_r from frequency domain within an error of 1%.

With the laser sheet illumination, the rotation of spiral arm is represented by the kink propagation along the illuminated line. Therefore the rotation frequency of the spiral arms corresponds to the repetition rate of the kink propagation (Fig. 3(b)). The height profile of every third vibration cycle is recorded to avoid the influence from the surface height fluctuations $(f/3)$ owing to period tripling. At a certain position, the plateau with maximal height, which represents a region bounded by two spiral arms, repeatedly appears. The inset of Fig. 3(c) shows one example of the height fluctuations with time $h(t)$. Following the above analysis on the $g(t)$, the rotation frequency is obtained from the power spectrum of the height fluctuations average over 6 equally distributed positions (see Fig. 3(c)). The smaller peak at about $2\nu_r$ arises from the height fluctuation induced by the third spiral arm.

ROTATION FREQUENCY

Utilizing both methods, we characterize the dynamics of rotating spirals. Qualitative observations reveal that the emerging spiral arms as the threshold acceleration is reached will have a finite rotation frequency. The task is to characterize the dependence of the rotation frequency on various control parameters. Here we focus only on the case of single spiral core and leave the case of multiple spirals for further investigations, because the interactions between spiral arms linked to different cores may lead to a variation of the rotation frequency.

Figure 4 shows the rotation frequency ν_r as a function of Γ for two vibration frequencies obtained from the top view snapshots taken at different time: shortly after changing control parameter Γ or with a delay of $\Delta t \approx 300$ s. For both vibration frequency f and Γ, ν_r captured at different time agree with each other within the errorbar, suggesting that the rotation speed of the arms is time independent for a constant driving condition. As Γ is beyond the threshold value Γ_{th}, the rotation frequency increases monotonically with Γ within a certain range. Beyond the upper limit, the probability to have a single spiral core is too low to obtain reliable data points.

Since the rotation speed of spiral arms is stable with time, a comparison of the results obtained with both methods described above is possible. Figure 5 shows such a comparison for $f = 80$ Hz and various Γ, obtained by collecting both $g(t)$ and $h(t)$ information consequent-

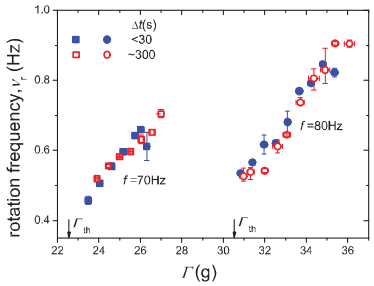

FIGURE 4. Rotation frequency of the spiral arms ν_r as a function of the peak vibration acceleration Γ for two vibration frequencies (f) with liquid content $W = 1.5\%$. The threshold for spiral pattern to emerge (Γ_{th}) is 22.5 ± 1.3 for $f = 70$ Hz and 30.5 ± 1.5 for $f = 80$ Hz. The rotation frequencies are obtained from the top view snapshots of the pattern, which are captured either shortly after varying Γ (with a delay time $\Delta t < 30$ s) or after a delay of $\Delta t \approx 300$ s.

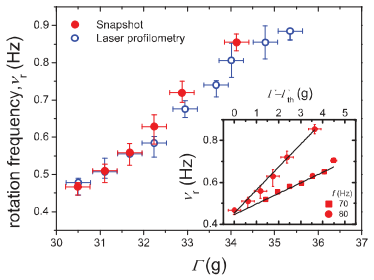

FIGURE 5. A comparison between both methods for $f = 80$ Hz. Inset shows the dependence of ν_r on the deviation of Γ from the threshold value Γ_{th} obtained from top view snapshots for both $f = 70$ Hz and 80 Hz. Solid lines are linear fits to the data.

ly for each run of experiment. The error bars correspond to the variation of ν_r for different runs of the experiment. The good agreements between the results from both methods indicate that the dependence of ν_r on Γ obtained does not rely on the method chosen, thus either method can act as a counterproof of the other. Technically speaking, the analysis of the top view snapshots, although it provides more straightforward information, will cost much more computing power compared with the analysis based on laser profilometry method, because the latter contains only one dimensional information. Therefore the laser profilometry method will be the better candidate for the future analysis on a wide range of control parameters.

In the inset of Fig. 5, the initial rotation frequency at the threshold acceleration $\nu_c(\Gamma_{th})$ and the slope of ν_r with Γ for both frequencies are compared. The dependence of ν_r on Γ obtained so far suggests a linear dependence. Linear fits of the dependence on $\Gamma - \Gamma_{th}$ yields a common threshold frequency $\nu_c = 0.45$ Hz, and a larger slope of $\Delta\nu_r/\Delta\Gamma = 0.11$ Hz for $f = 80$ Hz, compared to the slope 0.05 Hz for 70 Hz.

CONCLUSIONS

In conclusion, the rotation dynamics of spiral pattern in vertically agitated wet granular layer are characterized with two methods: one based on the horizontal motion of the spiral arms and the other one based on the vertical height fluctuation of a single illuminated line. For the case of single spiral core, both methods reveal that the rotation frequency of spiral arms grows linearly with the peak vibration acceleration and there exists a finite initial speed at the threshold acceleration where the pattern emerges.

Detailed analysis on a broader range of driving parameters, and for the case of multiple spiral cores will be a focus of further investigations. Moreover, a comparison of the rotation time scale with numerical simulations will help us to gain insight into the dynamics of fluidized wet granular matter.

ACKNOWLEDGMENTS

We are grateful for the support from Deutsche Forschungsgemeinschaft through HU1939/2-1.

REFERENCES

1. K. Huang, and I. Rehberg, *Phys. Rev. Lett.* **107**, 028001 (2011).
2. M. Cross, and H. Greenside, *Pattern Formation and Dynamics in Nonequilibrium Systems*, Cambridge University Press, 2009.
3. H. M. Jaeger, S. R. Nagel, and R. P. Behringer, *Rev. Mod. Phys.* **68**, 1259 (1996).
4. J. Duran, *Sands, Powders and Grains (An Introduction to the Physics of Granular Materials)*, Springer-Verlag, New York, Inc., 2000, 1 edn.
5. I. S. Aranson, and L. S. Tsimring, *Rev. Mod. Phys.* **78**, 641 (2006).
6. S. Herminghaus, *Adv. Phys.* **54**, 221 (2005).
7. M. Scheel, et al., *Nature Mater.* **7**, 189 (2008).
8. K. Huang, K. Röller, and S. Herminghaus, *Eur. Phys. J-Spec. Top.* **179**, 25 (2009).
9. J. Efsen, et al., *Handbook of Non-Invasive Methods and the Skin*, CRC Press Inc., Boca Raton, 1995, chap. 8, p. 97.

PHYSICAL REVIEW E **86**, 011303 (2012)

Coefficient of restitution for wet particles

Frank Gollwitzer,[1] Ingo Rehberg,[1] Christof A. Kruelle,[2] and Kai Huang[1,*]
[1]*Experimentalphysik V, Universität Bayreuth, 95440 Bayreuth, Germany*
[2]*Maschinenbau und Mechatronik, Hochschule Karlsruhe - Technik und Wirtschaft, D-76133 Karlsruhe, Germany*
(Received 8 February 2012; published 9 July 2012)

The influence of a liquid film on the coefficient of restitution (COR) is investigated experimentally by tracing freely falling particles bouncing on a wet surface. The dependence of the COR on the impact velocity and various properties of the particle and liquid is presented and discussed in terms of dimensionless numbers that characterize the interplay between inertial, viscous, and surface forces. In the Reynolds number regime where lubrication theory does not apply, the ratio of the film thickness to the particle size is found to be a crucial parameter determining the COR.

DOI: 10.1103/PhysRevE.86.011303 PACS number(s): 45.70.−n, 45.50.Tn, 47.55.Kf

I. INTRODUCTION

The coefficient of restitution (COR), first introduced by Newton [1] as the ratio between the relative rebound and impact velocities of a binary impact, has been a subject of continuous interest over centuries, along with the development of elastic [2,3], viscoelastic [4], and plastic theories [5,6]. It characterizes the energy dissipation associated with the impact, which plays a key role in understanding the collective behavior of macroscopic particles; that is, the dynamics of granular matter [7,8]. This is largely due to the fact that the dissipative nature of granular matter arises from the inelastic collisions at the particle level.

Due to its omnipresence in nature and various industries, granular matter has drawn great attention from both physical and engineering communities in the past decades [9]. Concerning the modeling of granular matter, an appropriate collision model is essential for the successful implementation of kinetic or hydrodynamic theories to granular matter [10–13]; see for example, the dynamics of Saturn's rings [14], or pattern formation under vertical agitation [15]. Despite those successful examples for dry granular matter, a continuum description for wet granular matter, which considers the cohesion arising from the wetting liquid phase, is still far from established [16,17]. Therefore, in order to provide a solid basis for a continuum modeling of wet granular flow—for example to describe natural disasters such as debris flow—a thorough understanding of the dynamics associated with wet impacts is desirable.

With the development of pharmaceutics, mining, and food industries, the COR for wet impacts has become an important issue for the engineering community in terms of decoding the underlying physics associated with the agglomeration of particles with liquid binders. The pioneering work by Rumpf [18] half a century ago included a detailed description of the capillary force of a pendular bridge and treated it as the dominating cohesive force in determining the continuum properties of wet granular matter (e.g., the tensile strength [19]). Later on, the viscous force has been found to play an important role in typical granulation processes, too [20–27]. And a dynamic liquid bridge could be an order of magnitude stronger than a quasistatic one [28,29]. Binary as well as three body impacts of particles with viscous liquid coating have been extensively investigated by experiments and models using lubrication theory [30–36].

Despite all these investigations, a well tested collision law suitable for modeling the dynamics of wet granular behavior [37–39], as well as a comprehensive knowledge of the energy dissipation associated with the impact, is still lacking. In the current work, the COR of a ball bouncing back from a flat lubricated surface is investigated as a function of the impact velocity, various particle sizes, and liquid properties. From this, the kinetic energy dissipated during the impact process is derived and discussed within the framework of existing models.

II. EXPERIMENTAL SETUP AND PROCEDURE

Figure 1 shows a sketch of the experimental setup used for the COR measurements. Spherical glass beads (SiLiBeads type P) with a diameter range from $D = 2.8$ mm to 10 mm, roughness $\approx 5\ \mu$m, and density $\rho_g = 2.58\ \mathrm{g/cm^3}$ are used in the experiments. By controlling the pressure in the vacuum nozzle, we allow an initially wet particle to fall freely onto a wet glass container (20 cm × 5 cm). The initial falling height is adjusted from 20 to 145 mm, corresponding to an initial impact velocity range from ≈ 0.3 to ≈ 1.7 m/s. Three types of liquids with various properties, as shown in Table I, are used. The bottom of the container is thick enough (2 cm) to avoid any influence on the COR [40] for the range of particle size used. It is leveled within 0.03 degrees, so that bouncing on various positions in the container explores a similar liquid layer thickness.

The layer thickness δ used in the current investigation ranges from 75 μm to 1 mm. It is measured by detecting the shift of a laser beam reflected from the surface of the liquid and the glass plate with a CCD camera (Camera 1, Lumenera Lu135). The mirror attached to the bottom of the container creates multiple reflections of the laser beam, in order to enhance the sensitivity of the device. The length of the mirror (7.8 cm) is chosen as a compromise between the sensitivity and the field of view. By fixing the container, laser, and camera on a leveled optical table, the error of the film thickness measurement could be minimized to a satisfactory level ($<10\ \mu$m).

*kai.huang@uni-bayreuth.de

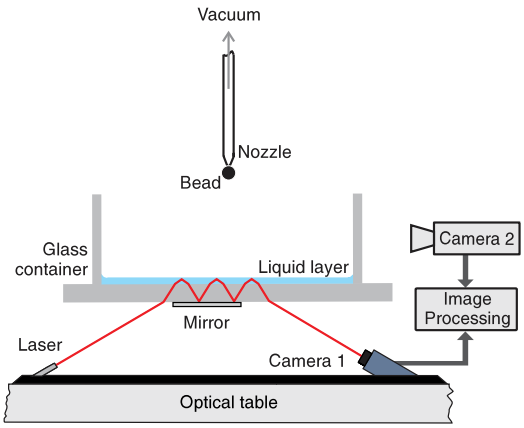

FIG. 1. (Color online) Sketch of experimental setup. The bouncing of the glass bead, initially held by the vacuum nozzle, on the glass container is recorded with a high speed camera (Camera 2). The thickness of the liquid layer is monitored by detecting the laser beam reflected from the liquid surface with Camera 1.

To obtain the impact and rebound velocities, the bouncing of the particle is recorded by a fast camera (Photron Fastcam Super 10K) and subsequently applied to an image processing procedure. A close view of the colliding event, as shown in Fig. 2, clearly demonstrates the important role that the liquid plays during the impact. As the sphere hits the liquid surface, a circular wave front occasionally accompanied with a splash will be generated. As the ball rebounds from the surface, a liquid bridge will form between the sphere and the liquid surface, which continuously deforms and elongates until it ruptures at a distance larger than the particle diameter. Associated with the rupture event, satellite droplets may form, which bounce on the liquid surface and coalesce partially into smaller droplets [41,42]. Obviously, the formation of wave fronts, deformation and rupture of liquid bridges, the viscous force, and the added mass to the sphere due to the liquid film will all contribute to the mechanical energy reduction of the impacting particle, which in turn leads to a smaller COR compared with dry impacts.

TABLE I. Material properties of liquids at 20 °C. M5 and M50 correspond to two types of silicone oil from Carl Roth.

	Density (kg/m^3)	Viscosity (mPa s)	Surface tension (mN/m)
Water	998	1.0	72.8
M5	925	4.6	19.2
M50	965	48	20.8

Figure 3 illustrates the influence of a liquid film by providing a comparison between the trajectories obtained from wet and dry impacts. The particle diameter is $D = 5.5$ mm, and the film thickness of the silicone oil M5 is $\delta = 225\ \mu$m in the wet case. To determine the location of the sphere centers, the image processing procedure employs a Hough transformation [43] (upper panel of Fig. 3). Subsequently, each bouncing trajectory is extracted and subjected to a parabolic fit [see the solid line in Fig. 3(a) as an example], in order to obtain the peak position h_{peak} and the impact velocity.

If the normal COR, also represented as e_n, is independent of the impact velocity, the velocity after the ith rebound will be related to the first impact velocity v_0 by $v_i = e_n^i v_0$. This leads to a linear decay of the peak height h_{peak} with the number of impacts i in a semilog plot, according to $\log_{10} h_{\text{peak}} = \log_{10} h_0 + 2i \log_{10} e_n$, with $h_{\text{peak}} \propto v_i^2$. The initial falling height h_0 and e_n determine the offset and slope of this line. As shown in the inset of Fig. 3(a), the logarithm of h_{peak} decreases linearly with the number of impacts for dry impacts, indicating that the normal COR stays almost constant for the number of impacts measured here. In a recent work on dry impacts [44], a more detailed analysis reveals that the dry COR decreases slightly with the increase of v_{impact}. However, this dependence is much weaker than the one for wet impacts, on which we are focusing here. In this case, the variation of the slope indicates that the COR for wet impacts decreases strongly with the number of impacts (i.e., with the impact velocity).

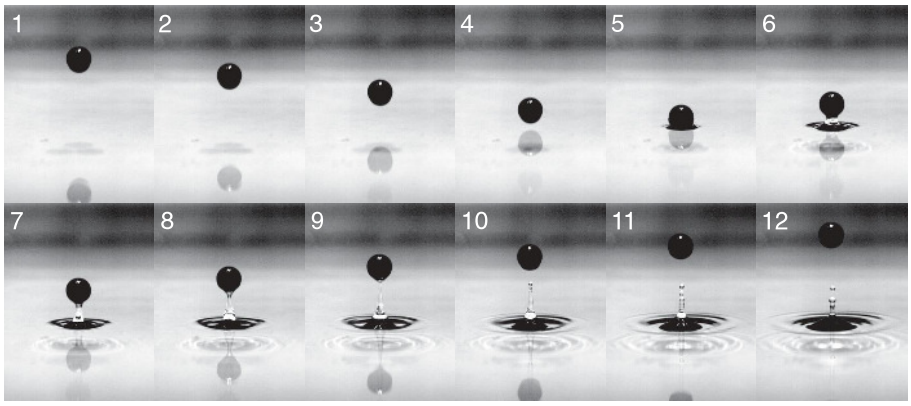

FIG. 2. A series of snapshots captured with a frame rate of 450 Hz showing a 4 mm glass bead bouncing on a glass plate covered with a 1 mm water film.

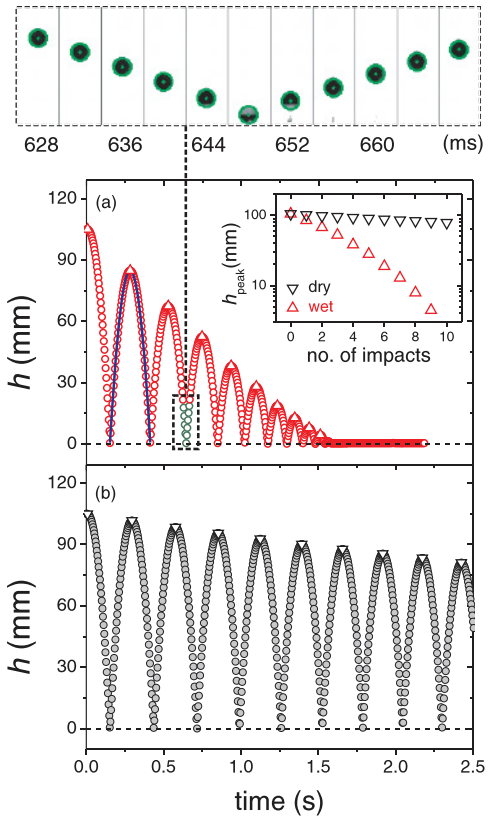

FIG. 3. (Color online) Trajectories of particle bouncing on wet (a) and dry (b) surface after image processing. The image sequence in the upper panel represents a fraction of the wet trajectory (a) with superimposed centers and boundaries of the sphere. The blue (dark gray) line in (a) corresponds to a parabolic fit to the trajectory after the first rebound. The peak positions of the trajectories h_{peak} obtained from the fits are marked with triangles in (a) and upside down triangles in (b). The inset in (a) shows h_{peak} as a function of the number of impacts.

Even though using h_{peak} gives a practical analysis of the COR, this method may suffer the influence from interstitial air. Therefore, the normal COR is obtained, based on its definition, from the ratio between the fitted rebound and impact velocities for the rest of the paper.

III. EXPERIMENTAL RESULTS

Figure 4 shows the dependence of the COR on the impact velocity v_{impact} and various particle diameters for both silicone oil (M5) and water films. Qualitatively, the same trend for the impact velocity dependence is observed: The COR grows initially with v_{impact} and saturates at a certain value, as shown by the guided lines in the upper panel. In the lower panel of Fig. 4, the rebound velocity v_{rebound} is plotted as a function of the impact velocity v_{impact}. Similar to the case without the liquid film (shown as a gray dashed line), v_{rebound} grows linearly with v_{impact} for all parameters used here. Different from the dry impacts, the fitted line has an offset with the x axis, which explains the growth of the COR with v_{impact}. Fitting the data with $v_{\text{rebound}} = e_{\text{inf}}(v_{\text{impact}} - v_{\text{c}})$ gives rise to two parameters that characterize the impact velocity dependence: A slope e_{inf} corresponding to the COR at infinite v_{impact} (i.e., the saturated value of the COR) and an offset v_{c} corresponding to a critical energy E_{c} below which no rebound would occur. $E_{\text{c}} = mv_{\text{c}}^2/2$ is obtained from the intersection v_{c} of the linear fits shown in the lower panels of Fig. 4 with the x axis, where m is the mass of the particle.

Besides the impact velocity, the COR is also found to be dependent on the size of the particles. For fixed v_{impact}, the COR decreases systematically with particle diameter for both silicone oil and water films. Since the COR is related to the fraction of kinetic energy retained after the impact, the growth of the COR with D indicates that the energy dissipation from the liquid film grows slower with D than the inertia ($\propto D^3$) of the particles.

Figure 5 shows the dependence of the parameters e_{inf} and E_{c} from the linear fits on the particle diameter for both liquids. For the dry impacts, E_{c} stays constantly at 0 within the error bar. In contrast, the critical energy for wet impacts is on the order of a few μJ. It shows a monotonic decay for the water film, and a more complicated relationship for the case of silicone oil M5 film. As shown in Fig. 5(b), e_{inf}—the upper limit of the COR—varies from 0.8 to 0.9 and is generally smaller than e_{dry}. This indicates that the ratio between the energy dissipation from the liquid, ΔE_{wet}, and the kinetic energy at impact, E_{i}, will not diminish as v_{impact} grows. For both silicone oil (M5) and water films, e_{inf} shows similar values with weak dependence on the particle sizes, although M5 silicone oil is 5 times more viscous than water. For dry impacts, the slope e_{inf} shows a weak dependence on the particle size. Linear fitting over the data from various D suggests an averaged $e_{\text{dry}} = 0.976$, as shown in Fig. 4. For wet impacts, the error bar for e_{inf} is larger as D decreases. This is presumably due to the larger influence from the liquid film, which may lead to a larger inertial effect from the liquid flow and a more complex energy dissipation scenario. Thus we keep the liquid film thickness within 1 mm for the COR dependence on the liquid properties shown below.

The influence of the liquid film thickness δ and the dynamic viscosity η on the wet impacts is presented in Fig. 6. Here, only silicone oil with various viscosities is chosen because of two reasons. First, it wets the glass surface better than water due to its low surface tension and contact angle and thus facilitates investigations on relatively thin liquid film. Second, the two types of silicone oil with various viscosities have a similar surface tension and density, which facilitates comparisons. Each data point shown here corresponds to an average of 10 runs of experiments with various initial falling heights and the error bar represents the statistical error.

Similar to the results shown in Fig. 4, the rebound velocity increases linearly with impact velocity with an offset with the x axis [as shown in Fig. 6(b)], leading to a growth of the COR with v_{impact} toward a saturated value e_{inf} smaller than $e_{\text{dry}} = 0.985$. Note that e_{dry} obtained here for the 5.5 mm particle is slightly larger than the one in Fig. 4, which presumably arises

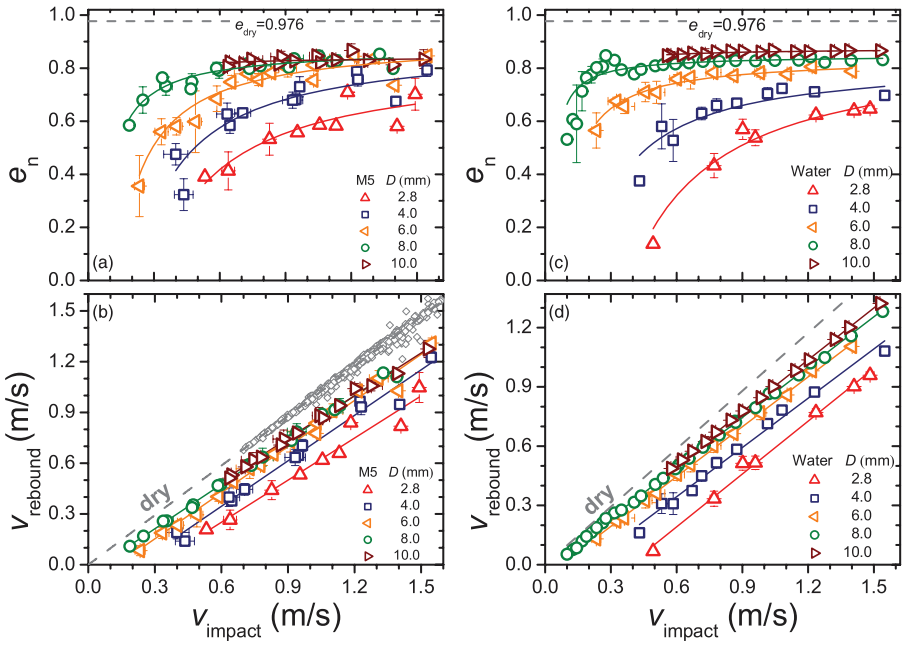

FIG. 4. (Color online) Normal restitution coefficient e_n and rebound velocity $v_{rebound}$ as a function of impact velocity v_{impact} for the impacts of particles with various diameters D on silicone oil (left column) and water (right column) films with fixed thickness $\delta = 1$ mm. The solid lines in the lower panels are linear fits to the data and their representatives are shown in the upper panels as a guide to the eyes. The dashed gray lines in the upper panels represent the normal restitution coefficient $e_{dry} = 0.976 \pm 0.001$ for dry impacts, which is obtained by a linear fit of the data for all particle sizes [gray diamonds shown in (b)]. Error bars smaller than the symbol size are not shown.

from the variation of the COR on particle diameter shown in Fig. 5(b). A comparison between both liquids shows that the v_{impact} dependence of the COR is more prominent for more viscous silicone oil M50, as the larger offset from the linear fits indicates. As the film thickness δ increases, e_n decreases systematically for both liquids, because the viscous damping force is effective over a larger distance. Further tests with increased film thickness up to 1.35 mm yield qualitatively the same v_{impact} dependence.

As shown in Fig. 6(b), the relation between $v_{rebound}$ and v_{impact} also represents the influence from the thickness and viscosity of the liquid. For wet impacts, $v_{rebound}$ decreases systematically with the liquid film thickness δ at a certain v_{impact}. As the liquid viscosity increases by an order of magnitude (from M5 to M50), this trend is more prominent, indicating the crucial role played by the viscous damping. Fitting the growth of $v_{rebound}$ with v_{impact} with a straight line again gives rise to two parameters: A slope e_{inf} that is smaller than e_{dry} and a threshold energy E_c below which no rebound would occur. As shown in Fig. 7(a), this threshold is, for M50, more than an order of magnitude larger than that for M5. This suggests the dependence of E_c on the viscosity. As shown in Fig. 7(b), the slope e_{inf} is not strongly influenced by viscosity compared with E_c. For relatively thin film, e_{inf} could be the same within the error bars. The slope e_{inf} stays constant within the range of film thickness and decays slightly for the more viscous silicone oil M50 film.

IV. SCALING WITH STOKES NUMBER

The above experimental results indicate that the COR depends strongly on the impact velocity, particle sizes, and various liquid properties. In order to explore the relation between the COR and all these parameters, it is essential to have a proper classification of the parameters in terms of dimensionless quantities that characterize the relation between inertia, viscous, and capillary effects. In the case where the viscous force dominates, lubrication theory has been applied to explain the dynamics of wet impacts [21,30,33,36]. In such a case, the Stokes number is used to characterize the dependence of the COR on various control parameters. The Stokes number $\mathrm{St} = \rho_g D v_{impact}/9\eta$ is defined as the ratio between the inertia of the particle and the viscosity of the liquid, where ρ_g is the density of the glass beads. Normally, this case is justified by the criterion $\mathrm{Re} \ll 1$ [33]. The Reynolds number Re is defined as $\rho_l \delta v_{impact}/\eta$, where ρ_l and δ are the density and the thickness of the liquid correspondingly. This implies that either the liquid is highly viscous, or the film thickness is small. Within this limit, the contribution from the liquid to the total energy dissipation is mainly due to viscous damping. Although the range of Reynolds numbers for the current investigation (up to $\approx 10^3$) suggests that the role that the viscous force plays may not always be prominent, we still use the Stokes number to rescale the dependence of the COR on various parameters as a starting point.

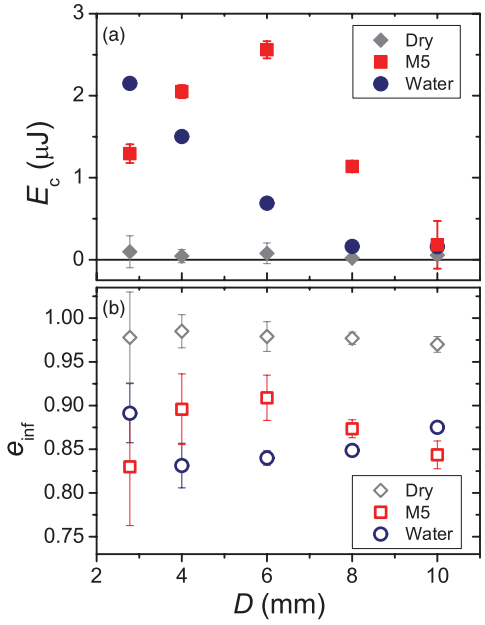

FIG. 5. (Color online) Critical energy E_c and saturated value of COR e_{inf}, obtained from linear fits in Fig. 4(b), as a function of particle diameter D. The solid line at $E_c = 0$ is a guide to the eyes.

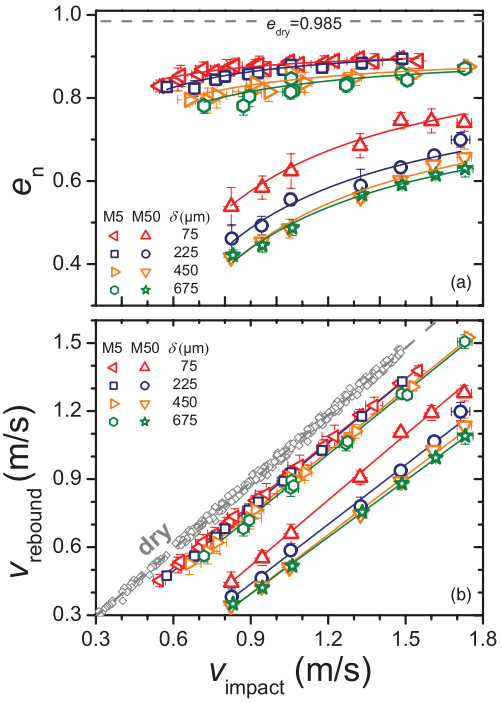

FIG. 6. (Color online) Normal restitution coefficient e_n (a) and rebound velocity $v_{rebound}$ (b) as a function of impact velocity v_{impact} for impacts of a glass bead with $D = 5.5$ mm on dry and wet surfaces covered with silicone oil M5 and M50. δ denotes the film thickness. The error bars correspond to the statistical error over 10 runs of experiments for the wet impacts. Solid lines in (b) are linear fits to the corresponding data. Their representatives are shown in (a) as a guide to the eye. For dry impacts, the restitution coefficient e_{dry} is 0.985 with an error of 0.001.

Figure 8 is a replot of the data in Figs. 4(a) and 4(c) in the e_n-St plane. For silicone oil M5, which has a kinematic viscosity 5 times that of water, the rescaling with the Stokes number yields better overlapping than that for water. This could be attributed to the lower Re range (Re = 20–360) for the case of silicone oil M5, which leads to more prominent influence from the viscosity. As shown in Fig. 8(a), data for various D show a general trend of initial growth from St $\approx$ 100 to 500, followed by a saturation to e_{inf} between 0.8 and 0.85. Concerning the case of water film (corresponding to Re = 100–1800), the scatter of the data obtained with various particle sizes [shown in Fig. 8(b)] is much more prominent than for the case of silicone oil M5 film. Although the trend of a significant growth followed by a saturated value persists, both the slope of increase and the saturated value differ as D varies.

From another point of view, Fig. 8 also reveals a relatively small difference of the COR between M5 and water films, even though the corresponding viscosity ratio is 5. This result indicates that the COR is also determined by other liquid properties. As an example, the surface tension of water is much larger than that of M5, which may lead to a larger energy dissipation from the formation of capillary waves and the break of capillary bridges upon rebound. In order to study the influence from viscosity, we focus on the results from silicone oil M5 and M50 (shown in Fig. 6), which have similar surface tension and density (see Table I), in the following part of the section.

Figure 9(a) shows the COR as a function of the St number for the data shown in Fig. 6(a). The COR grows dramatically at small St, which corresponds to the data of the more viscous silicone oil M50 case, and saturates at larger St. For various film thickness δ, this trend is qualitatively the same. This trend, as well as the data scattering at low St, is also comparable to the results with various particle diameters shown in Fig. 8(a). Quantitatively, the saturated value e_{inf} decreases as the film thickness δ grows, suggesting further dimensionless parameters associated with δ have to be considered.

This parameter is chosen as the dimensionless length scale $\tilde{\delta} = \delta/D$, because it ties the Stokes number with the Reynolds number of the liquid film. According to this definition, the ratio between the Reynolds number and the Stokes number is $\mathrm{Re/St} = 9\tilde{\delta}\tilde{\rho}$, where $\tilde{\rho} = \rho_l/\rho_g$ is the density ratio between the liquid and the particle.

In Fig. 9(b), further experiments with the restriction $\tilde{\delta} \approx 0.04$ are presented. In contrast to Fig. 9(a), the data from various film thicknesses coincide over a wide range of St if $\tilde{\delta}$ is fixed. It also gives rise to a master curve $e_n = e_{inf}(1 - \mathrm{St_c/St})$, as indicated clearly in the inset. The linear fit yields $e_{inf} = 0.908 \pm 0.002$, and a critical Stokes number $\mathrm{St_c} = 14.00 \pm 0.20$. Therefore, the usage of the Stokes number as a control parameter could be extended to the regime Re $>$ 1 and large

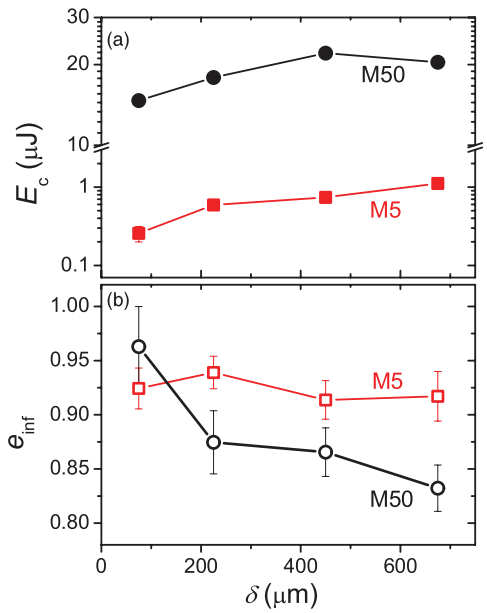

FIG. 7. (Color online) Critical energy E_c and the saturated value of the COR e_{inf} as a function of film thickness δ. E_c is obtained from the intersection v_c of the linear fits shown in the lower panel of Fig. 6 with the x axis. e_{inf} corresponds to the slope of these fits.

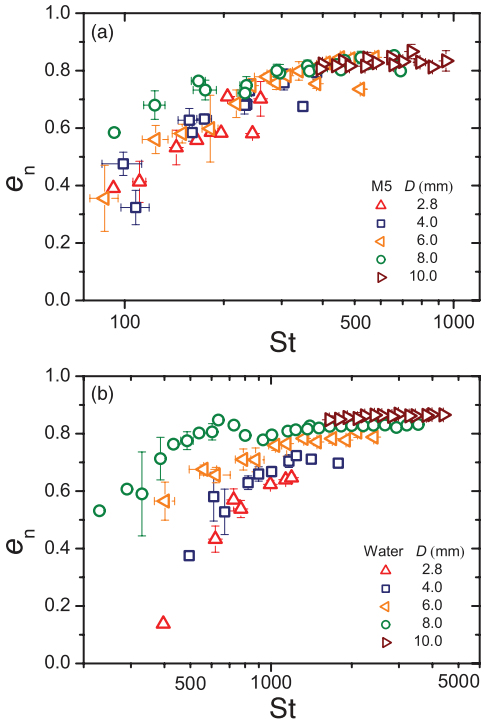

FIG. 8. (Color online) Normal restitution coefficient e_n as a function of the Stokes number St for both silicone oil (a) and water (b) films. Parameters are the same as in Fig. 4.

film thickness, provided that the dimensionless length scale $\tilde{\delta}$ is kept constant.

V. ANALYSIS OF ENERGY DISSIPATION

To understand the dependence of the COR on various particle as well as liquid properties, it is helpful to analyze the associated energy dissipation. If E_{diss} is defined as the total kinetic energy loss of the particle during the impact, the dependence of the COR on the kinetic energy at impact E_i can be written as

$$e_n = \sqrt{1 - E_{diss}/E_i}. \quad (1)$$

The dissipated energy E_{diss} can be treated as the sum of two parts: the part transferred into the solid body ΔE_{dry}, and the other part taken by the liquid phase; that is,

$$E_{diss} = \Delta E_{dry} + \Delta E_{wet}. \quad (2)$$

Provided that the two parts are independent of each other; that is. the liquid phase does not change the energy dissipation from the solid phase, ΔE_{wet} could be obtained experimentally by

$$\Delta E_{wet} = E_i\left(e_{dry}^2 - e_n^2\right). \quad (3)$$

The whole process of the colliding event can be separated into two parts: impact and rebound. During the impact, the kinetic energy of the particle will partly be transferred to the liquid. This amount of energy will finally be dissipated by the motion of the viscous liquid, including surface waves or even splashes, depending on the competition between the inertial, viscous, and surface forces. During the rebound, the rupture of the capillary bridge will lead to a certain amount of surface energy loss in addition to the damping caused by the motion of the liquid. Moreover, the mass of the liquid dragged away by the sphere might lead to a further reduction of the COR. Based on the above analysis, one can take the most prominent terms and use

$$\Delta E_{wet} \approx \Delta E_{visc} + \Delta E_b + \Delta E_{acc} \quad (4)$$

to estimate ΔE_{wet} theoretically, where ΔE_{visc} represents the energy dissipated via the viscous damping force acting on the particle, ΔE_b corresponds to the energy loss arising from the surface energy change of the fluid, and ΔE_{acc} is the kinetic energy change of the fluid before and after the colliding event.

In the limit that thin film lubrication theory applies, the viscous force acting on the particle can be estimated by $F_v = 3\pi\eta D^2 v_{impact}/(2x)$ [33], where x denotes the distance between the sphere and the plate. Following Ref. [21], one might assume the same force law for both approach and departure of the sphere, despite that the boundary condition for the latter case is dramatically different from the former one. By integrating over the distance that the viscous force applies, we obtain

$$\Delta E_{visc} = \frac{3}{2}\pi\eta D^2 v_{impact}\left(\ln\frac{\delta}{\epsilon} + \ln\frac{\delta_r}{\epsilon}\right), \quad (5)$$

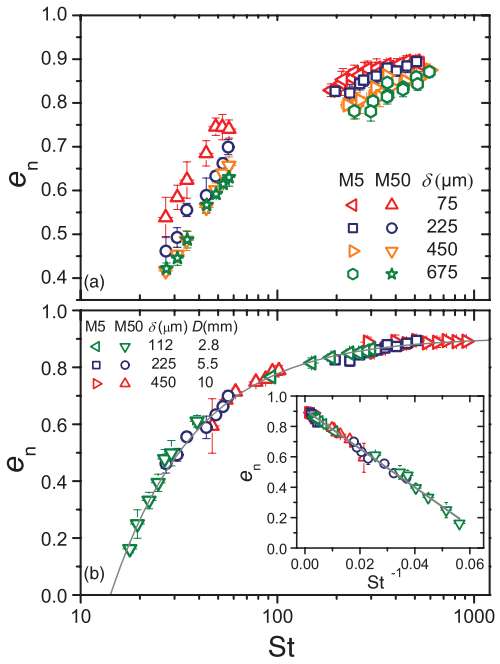

FIG. 9. (Color online) Normal restitution coefficient as a function of Stokes number St. Panel (a) corresponds to the data shown in Fig. 6. Panel (b) corresponds to the data with the dimensionless film thickness δ/D roughly constant. The other parameters are the same as in Fig. 6. The error bars correspond to the statistical error of 10 runs of experiments. The solid curve in panel (b) corresponds to the master curve $e_n = 0.908(1 - 14.00/\mathrm{St})$, which is obtained from a linear fit to all the data shown in the inset.

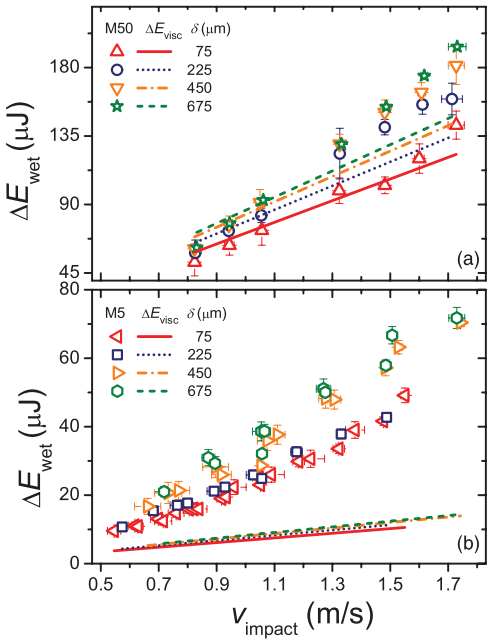

FIG. 10. (Color online) Energy dissipation ΔE_{wet} due to various liquid films as a function of impact velocity with the liquid properties the same as in Fig. 6 for both silicone oil M50 (a) and M5 (b) films. The straight lines represent the estimated values of the energy dissipation ΔE_{visc} from viscosity (see text for detailed descriptions).

where $\epsilon = 5\ \mu$m is the roughness of the sphere, and δ_{r} is the rupture distance of the liquid bridge. For a crude estimation, we take a fixed $\delta_{\mathrm{r}} = 2D$ according to the snapshots taken and assume that the velocity does not change during the impact.

In Fig. 10, ΔE_{wet} for the experimental results shown in Fig. 6 is plotted in comparison with ΔE_{visc}. Qualitatively, the monotonic growth of the energy dissipation with the impact velocity and the increase of energy dissipation with the film thickness agree with the estimation from Eq. (5). This growth with the impact velocity deviates slightly from a straight line, which is suggested by the model, indicating that the dominating energy dissipation term has a higher order dependence on the impact velocity. Quantitatively, a comparison between the estimated viscous damping term ΔE_{visc} and ΔE_{wet} reveals that a substantial amount of the latter can be attributed to the viscous damping for the case of silicone oil M50, while this term plays a much weaker role for the case of less viscous silicone oil M5. This could be understood in terms of the difference of the Reynolds number. For less viscous silicone oil M5, the range of Reynolds number is an order of magnitude larger than that for silicone oil M50. Thus the energy loss due to the inertia of the liquid film is more prominent. As a consequence, the estimated ΔE_{visc} plays a less important role in the total energy dissipation ΔE_{wet}. Since there exists a systematic deviation of ΔE_{wet} from the predicted ΔE_{visc} with the growth of the impact velocity and the decrease of the viscosity, one could estimate the threshold Reynolds number below which the viscous effect dominates. Taking $|\Delta E_{\mathrm{wet}} - \Delta E_{\mathrm{visc}}|/\Delta E_{\mathrm{wet}}$ as the order parameters and 30% deviation as the limit, one can estimate the corresponding Reynolds number to be $\mathrm{Re} \approx 10$ for the case of $\tilde{\delta} \approx 0.04$.

The second term in Eq. (4) stems from capillary forces. Upon rebound of the sphere, a liquid bridge may form between the sphere and the liquid surface. The corresponding energy dissipation due to the deformation and rupture of this liquid bridge can be estimated by an integration of the force arising from the surface tension over the length that it acts. This capillary force has two components: the surface tension acting on the perimeter of the neck ($2\pi r_{\mathrm{n}}\gamma$ with r_{n} being the neck radius and γ the surface tension), and the second part arising from the Laplace pressure p_{b} that acts on the cross section of the neck ($-\Delta p_{\mathrm{b}}\pi r_{\mathrm{n}}^2$). Based on quasistatic experimental verifications, a close form approximation of the capillary force F_c between two spheres has been given as

$$F_c = \frac{\pi D\gamma \cos(\phi)}{1 + 2.1S^* + 10S^{*2}}, \tag{6}$$

where $S^* = s\sqrt{D/(2V_{\mathrm{b}})}$ is the half separating distance s rescaled by the characteristic length scale $\sqrt{D/(2V_{\mathrm{b}})}$ with the bridge volume V_{b}, and ϕ corresponds to the contact angle [45].

Taking the rupture distance δ_c as the integration limit and assuming a contact angle of 0°, one could estimate the rupture energy of the liquid bridge to be

$$\Delta E_b \approx \pi\gamma\sqrt{2V_b D}. \tag{7}$$

A rough estimation of the bridge volume $V_b \approx D^3/16$, based on the snapshot taken, gives rise to $E_b \approx 0.7\ \mu$J for silicone oil wetting a glass bead with diameter 5.5 mm. Considering the energy dissipation obtained by the COR measurements shown in Fig. 10, E_b plays a minor role for the few mm sized particle used here. Note that E_b plays a more prominent role as D decreases, because its growth with $\sqrt{D}$ is in contrast to $E_{visc} \propto D^2$.

As demonstrated in Fig. 10, both the damping from the viscous force and the rupture of liquid bridges cannot explain the amount of energy dissipation for the case of silicone oil M5 films. Therefore, other effects, like, for example, the inertia of the liquid or surface waves, should be considered.

As a first approximation, the inertial effect could be estimated from the kinetic energy of the liquid being pushed aside by the impact [46]. The volume of the liquid can be estimated by the spherical cap immersed in the liquid film $V = \pi D^3\tilde{\delta}^2(1/2 - \tilde{\delta}/3)$. From the length scale taken as the base radius of the spherical cap $[1-(1-2\tilde{\delta})^2]^{1/2}D/2$ and the time scale δ/v_{impact} for the particle to penetrate the liquid layer, one estimates the average velocity $v_l = v_{impact}(1/\tilde{\delta} - 1)^{1/2}$. As a consequence, the kinetic energy ΔE_{acc} of the liquid being pushed aside yields

$$\Delta E_{acc} = \frac{1}{2}\rho_l V v_l^2 = 3\tilde{\rho}\left(\tilde{\delta} - \frac{5}{3}\tilde{\delta}^2 + \frac{2}{3}\tilde{\delta}^3\right)E_i, \tag{8}$$

which shows a linear dependence on the kinetic energy E_i of the impact particle. Figure 11 shows that, by taking both ΔE_{visc} and ΔE_{acc} into account, the influence from the inertia effect is more prominent for less viscous silicone oil M5. The combination of both forces leads to a better agreement with the experimental data, when compared to Fig. 10(b). However, considering both the inertial and the viscous damping parts of the energy dissipation cannot explain the experimental results for less viscous silicone oil M5 quantitatively. This indicates that further theoretical considerations (e.g., on additional energy dissipation terms, or a more careful characterization of the inertial effects) are desirable.

The fact that the ratio between ΔE_{acc} and E_i is not velocity dependent suggests that the inertia of the liquid film will not contribute to the impact velocity dependence of e_n. It does, however, explain why e_{inf} obtained from linear fits of the data is generally smaller than e_{dry}. Based on the Eqs. (3) and (4), the E_i dependent COR could be written as

$$e_n = \sqrt{e_{dry}^2 - \frac{\Delta E_{acc}}{E_i} - \frac{\Delta E_{visc}}{E_i} - \frac{\Delta E_b}{E_i}}. \tag{9}$$

In the limit of large v_{impact}, the last term $\Delta E_b/E_i$ could be safely ignored so that two independent parameters are enough to determine the impact velocity dependence of the COR. A comparison to the linear fits $e_n = e_{inf}(v_{impact} - v_c)$ employed before immediately reveals that the linear fit is a first order approximation of Eq. (9) and $e_{inf} = (e_{dry}^2 - \Delta E_{acc}/E_i)^{1/2}$. By ignoring the higher order terms of $\tilde{\delta}$ in ΔE_{acc}, one derives

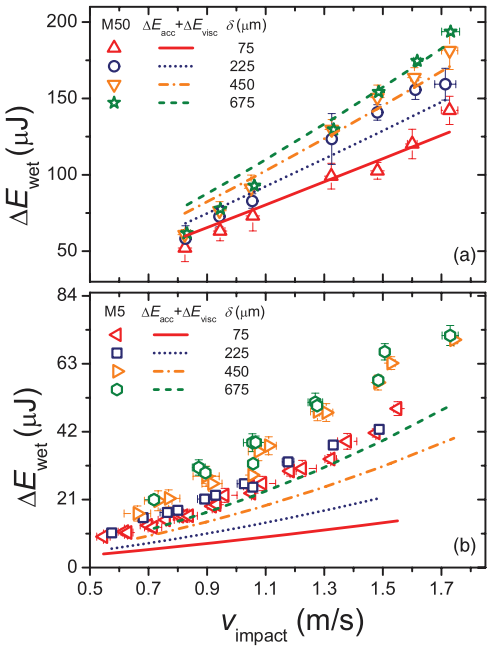

FIG. 11. (Color online) Data points are the same as shown in Fig. 10. Various curves represent the estimated values with the consideration of both viscous damping ΔE_{visc} and the energy transfer to the fluid ΔE_{acc} (see text for detailed descriptions).

a linearized form $e_{inf} = e_{dry} - 3\tilde{\rho}\tilde{\delta}/(2e_{dry})$, which suggests $e_{inf} \approx 0.92$ for typical experimental values of $\tilde{\rho} = 1/2.5$ and $\tilde{\delta} = 0.1$. In comparison to Fig. 7(b), this estimated value is close to the e_{inf} obtained from fitting. Moreover, the monotonic decrease with $\tilde{\delta}$ is captured by this formula qualitatively, except for the 75 μm thick silicone oil M5 case.

VI. CONCLUSION

In summary, the normal coefficient of restitution (COR) for a free falling sphere on a wet surface is investigated experimentally. The dependence of the COR on the impact velocity and various particle and liquid film properties is discussed in relation to the energy dissipation associated with the impact process.

(i) For dry impact, the COR corresponds to the slope of the rebound vs impact velocity. For wet impacts, the rebound velocity and the impact velocity are also found to fall onto a straight line, but with a smaller slope and an offset corresponding to a finite critical impact velocity. Even though linear fitting is only a first order approximation of e_n, it successfully characterizes the impact velocity dependence of the COR with two parameters e_{inf} and E_c. Therefore, this simplification is justified to be a good candidate for computer simulations aiming at modeling wet granular dynamics on a large scale.

(ii) The dependence of the COR on the impact velocity, dimension of the sphere and the viscosity of the liquid could be well characterized by the Stokes number, which is defined as the ratio between the inertia of the sphere and the viscosity

of the liquid, provided that the dimensionless length scale $\tilde{\delta}$ is fixed. This result supports the usage of the Stokes number for scaling the data, even beyond the low Reynolds number regime where it has originally been introduced.

(iii) Concerning the energy dissipation arising from the liquid films, the viscous damping term dominates for Reynolds number up to $\mathrm{Re} \approx 10$. Away from that limit, further effects, such as the inertia of the liquid film, have to be considered. The rupture energy of a capillary bridge during the rebound process could be safely ignored for the few mm sized particles used here.

The above conclusion suggests that further investigation on the dynamics of wet impacts is desirable for a better understanding of the COR and the energy dissipation associated. This requires an accurate determination of the particle trajectories during the impact with the liquid film experimentally, as well as a comparison with numerical simulations (see, e.g., Ref. [47]).

ACKNOWLEDGMENTS

The authors would like to acknowledge Mario Schörner for the help in the construction and calibration of the film thickness measurement part of the setup and Bryan J. Ennis and Jürgen Vollmer for helpful hints. This work is partly supported by the German Science Foundation within Forschergruppe 608 "Nichtlineare Dynamik komplexer Kontinua" through Grant No. Kr1877/3-1.

[1] I. Newton, *Mathematical Principles of Natural Philosophy* (1687) axioms, or Laws of motion. Corollary VI.
[2] H. Hertz, J. reine und angewandte Mathematik **92**, 156 (1882).
[3] A. E. H. Love, *A Treatise on the Mathematical Theory of Elasticity* (Dover, New York, 1927).
[4] R. Ramírez, T. Pöschel, N. V. Brilliantov, and T. Schwager, Phys. Rev. E **60**, 4465 (1999).
[5] D. Tabor, Proc. R. Soc. London **192**, 247 (1948).
[6] K. L. Johnson, *Contact Mechanics* (Cambridge University Press, 1985).
[7] H. M. Jaeger, S. R. Nagel, and R. P. Behringer, Rev. Mod. Phys. **68**, 1259 (1996).
[8] J. Duran, *Sands, Powders and Grains (An Introduction to the Physics of Granular Materials)*, 1st ed. (Springer-Verlag, New York, 2000).
[9] M. Nakagawa and S. Luding, eds., *Powders and Grains 2009: Proceedings of The 6th International Conference on Micromechanics of Granular Media* (American Institutite of Physics, Melville, New York, 2009).
[10] N. V. Brilliantov, F. Spahn, J.-M. Hertzsch, and T. Pöschel, Phys. Rev. E **53**, 5382 (1996).
[11] N. Brilliantov and T. Poeschel, *Kinetic Theory of Granular Gases* (Oxford University Press, 2004).
[12] J. T. Jenkins and S. B. Savage, J. Fluid Mech. **130**, 187 (1983).
[13] I. Goldhirsch, Annu. Rev. Fluid Mech. **35**, 267 (2003).
[14] F. Spahn and J. Schmidt, GAMM-Mitt. **29**, 115 (2006).
[15] C. Bizon, M. D. Shattuck, J. B. Swift, W. D. McCormick, and H. L. Swinney, Phys. Rev. Lett. **80**, 57 (1998).
[16] S. Herminghaus, Adv. Phys. **54**, 221 (2005).
[17] P. Jop, Y. Forterre, and O. Pouliquen, Nature (London) **441**, 727 (2006).
[18] H. Rumpf, *Agglomeration* (AIME, Interscience, New York, 1962).
[19] W. B. Pietsch, Nature (London) **217**, 736 (1968).
[20] B. J. Ennis, J. L. Li, G. Tardos, and R. Pfeffer, Chem. Eng. Sci. **45**, 3071 (1990).
[21] B. J. Ennis, G. Tardos, and R. Pfeffer, Powder Technol. **65**, 257 (1991).
[22] S. Iveson, J. Litster, and B. Ennis, Powder Technol. **88**, 15 (1996).
[23] S. M. Iveson and J. D. Litster, Powder Technol. **99**, 234 (1998).
[24] S. M. Iveson, J. D. Litster, K. Hapgood, and B. J. Ennis, Powder Technol. **117**, 3 (2001).
[25] J. Fu, M. J. Adams, G. K. Reynolds, A. D. Salman, and M. J. Hounslow, Powder Technol. **140**, 248 (2004).
[26] S. Antonyuk, S. Heinrich, N. Deen, and H. Kuipers, Particuology **7**, 245 (2009).
[27] P. Müller, S. Antonyuk, M. Stasiak, J. Tomas, and S. Heinrich, Granular Matter **13**, 455 (2011).
[28] D. N. Mazzone, G. I. Tardos, and R. Pfeffer, Powder Technol. **51**, 71 (1987).
[29] K. Murase, T. Mochida, and H. Sugama, Granular Matter **6**, 111 (2004).
[30] R. Davis, J.-M. Serayssol, and E. J. Hinch, J. Fluid Mech. **163**, 479 (1986).
[31] G. Barnocky and R. H. Davis, Phys. Fluids **31**, 1324 (1988).
[32] C. Thornton and Z. Ning, Powder Technol. **99**, 154 (1998).
[33] R. H. Davis, D. A. Rager, and B. T. Good, J. Fluid Mech. **468**, 107 (2002).
[34] A. A. Kantak and R. H. Davis, Powder Technol. **168**, 42 (2006).
[35] C. M. Donahue, C. M. Hrenya, and R. H. Davis, Phys. Rev. Lett. **105**, 034501 (2010).
[36] C. M. Donahue, C. M. Hrenya, R. H. Davis, K. J. Nakagawa, A. P. Zelinskaya, and G. G. Joseph, J. Fluid Mech. **650**, 479 (2010).
[37] S. Ulrich, T. Aspelmeier, A. Zippelius, K. Roeller, A. Fingerle, and S. Herminghaus, Phys. Rev. E **80**, 031306 (2009).
[38] A. Fingerle, K. Röller, K. Huang, and S. Herminghaus, New J. Phys. **10**, 053020 (2008).
[39] A. Fingerle and S. Herminghaus, arXiv:0708.2597.
[40] R. Sondergaard, K. Chaney, and C. E. Brennen, J. Appl. Mech. **57**, 694 (1990).
[41] Y. Couder, S. Protiere, E. Fort, and A. Boudaoud, Nature (London) **437**, 208 (2005).
[42] F. Blanchette and T. Bigioni, Nat. Phys. **2**, 254 (2006).
[43] C. Kimme, D. Ballard, and J. Sklansky, Commun. ACM **18** (1975).
[44] M. Montaine, M. Heckel, C. Kruelle, T. Schwager, and T. Pöschel, Phys. Rev. E **84**, 041306 (2011).
[45] C. Willett, Langmuir **16**, 9396 (2000).
[46] Jürgen Vollmer (private communication).
[47] C. Bauer, T. Bieker, and S. Dietrich, Phys. Rev. E **62**, 5324 (2000).

Soft Matter

View Online / Journal Homepage
Dynamic Article Links

Cite this: DOI: 10.1039/c2sm26074c

www.rsc.org/softmatter

PAPER

Wet granular rafts: aggregation in two dimensions under shear flow

Kai Huang,*[ab] Martin Brinkmann*[ac] and Stephan Herminghaus[a]

Received 8th May 2012, Accepted 12th September 2012
DOI: 10.1039/c2sm26074c

The aggregation and fragmentation of cohesive granular particles trapped at an air–liquid interface under shear flow are investigated by experiments and compared with numerical simulations. The cohesion owing to the formation of capillary bridges from a thin oil film covering the particles is found to dominate other particle–particle interactions. In the steady state the radius of gyration R_g of an N particle cluster follows a power law $R_g \propto N^{1/\delta}$. The fractal dimension δ of the clusters lies in the range between 1.5 and 1.6 and depends only weakly on the shear rate $\dot{\gamma}$. The probability to find a cluster of N particles or larger $P(N)$ displays an exponential tail $P(N) \propto \exp(-N/N_c)$ with a characteristic cluster size N_c. A power law $N_c \propto \dot{\gamma}^{-\beta}$ with an exponent $\beta = 0.65 \pm 0.06$ ($\beta = 0.68 \pm 0.02$) is found in our experiments (simulations). The fractal dimension of the clusters and the value of β are consistent with an estimate of the largest stable cluster based on the balance between the capillary force and the viscous drag force.

1 Introduction

Aggregation of macroscopic particles or bubbles trapped at an air–liquid interface into clusters is a common phenomenon that can be observed, *e.g.*, for cornflakes floating on milk, during a hot foam bath or in a glass of champagne.[1] The formation of these aggregates is driven by interfacial tension that is also responsible for the attraction and ordering of non-spherical objects such as tree needles or mosquito eggs floating at the water interface of a pond.[2] Applications based on the aggregation of particulate materials at interfaces are widespread and reach into industrial processes such as pharmaceutics, floatation processes in mining, and waste water treatment.[3–5] As a consequence, the structure, rheological behavior of the particle aggregates at interfaces, as well as their interactions with liquid interfaces within emulsions have attracted considerable interest over the past few decades.[6–10] Furthermore, a theory of interfacial particle aggregation and break-up can add to a better understanding of the rheology of Pickering emulsions.[11] From the perspective of fundamental research, the dynamics and self-organization of particles, emulsion droplets or bubbles at a fluid–liquid interface provide a well accessible model system to study, for example, colloidal crystals and glass transitions in two dimensions (2D).[12–18]

The spectrum of interactions between particles trapped in a fluid–liquid interface depends largely on the size of particles. For colloidal or submicron particles, the driving force behind aggregation is mainly due to van der Waals interaction and surface charges in the presence of electrolytes in the bulk liquid.[19–22] For particles with a diameter larger than tens of microns, *i.e.*, within the granular realm,[23,24] the typical interactions include monopolar forces such as the buoyancy force, dipolar forces due to the electrostatic charges at the interface, and the capillary forces mediated by deformations of the fluid–liquid interface.[1,25,26] For sub-millimeter particles focused here, the aggregation is mainly caused by the latter type of interaction.

The disintegration of dense particle clusters in the presence of shear flow has been extensively studied by Vassileva and co-workers.[27] They found that the critical shear rate required to break the aggregates depends weakly on their size, and is explained by a model considering the balance of the viscous drag and capillary interaction between particles. In a following work,[28] the breakup mechanisms, namely fragmentation and erosion, have been explored in detail.

In the present study, we focus on 2D *wet* granular clusters composed of sub-millimetric spherical glass beads trapped at an air–liquid interface. The beads are laden with a thin film of a secondary liquid immiscible with the viscous subphase. Upon contact this secondary liquid forms capillary bridges between adjacent particles, giving rise to a well-defined attractive particle–particle interaction.[29–32] This short ranged attractive force mediated by the capillary bridges is much stronger than the interactions which cause the clustering of 'dry' particles (without the secondary liquid). A quantitative comparison of the cluster size distributions in the steady state obtained from our experiment and our discrete elements method (DEM) simulations assuming frictionless soft core particles allows us to address the role of hydrodynamic interaction and interparticle friction. By considering the balance between the viscous drag force and the

[a]*Max Planck Institute for Dynamics and Self-Organization, Am Fassberg 17, 37077 Göttingen, Germany. E-mail: martin.brinkmann@ds.mpg.de*
[b]*Experimentalphysik V, Universität Bayreuth, 95440 Bayreuth, Germany. E-mail: kai.huang@uni-bayreuth.de*
[c]*Experimental Physics, Saarland University, 66123 Saarbrücken, Germany*

cohesive force of the capillary bridges we are able to relate the shear rate dependence of the cluster size distributions to the fractal dimension of the clusters.

This article is organized as follows: in the subsequent Section 2 we describe the experimental setup and the sample preparation procedure, the numerical methods used in the data analysis, and the physical model employed in the DEM simulations. In Section 3, the analyses of the structure and size distributions of the aggregates as well as a model based on the balance between the viscous drag force and the capillary force are presented.

2 Methods

2.1 Experimental setup and sample preparation

Spherical glass beads (Whitehouse scientific GP165) with diameters $D = (165 \pm 25)$ μm are cleaned subsequently with ethanol, acetone and purified water. After completely dried at 110°*C*, the spheres were etched in an oxygen plasma (Harrick Plasma) and treated with a Piranha solution, *i.e.*, a 1 : 1 volume mixture of concentrated sulfuric acid and hydrogen peroxide (35%). Subsequently, they are coated with OTS (octadecyltrichlorosilane) in a bicyclohexyl solvent (Fluka) and dried in a vacuum. After the treatment, the glass spheres are hydrophobic and exhibit a contact angle of ≈110° for an air–water interface as measured by optical microscopy.

The experimental setup to create the shear flow is illustrated in Fig. 1. The outer and inner cylinders of a Couette shear cell are driven independently by two stepper motors with angular velocities ω_o and ω_i, correspondingly. Pure glycerol with density $\rho_l = 1.26$ g cm^{-3} and dynamic viscosity $\mu = 1.2$ Pa·s is filled in the cell up to a height of 10 cm. Assuming a linear velocity profile the shear rate is constant and can be determined by $\dot{\gamma} = |\omega_i r_i - \omega_o r_o|/\Delta r$, where $r_i = 4.5$ cm and $r_o = 6.5$ cm correspond to the radius of the inner and outer cylinder, respectively, and $\Delta r \equiv r_o - r_i$. This assumption is justified because the Reynolds number of the Couette flow, $\mathrm{Re} = \rho_l \dot{\gamma} \Delta r^2/\mu$, is smaller than 10 for the range of shear rates explored in our experiments.

As shown in Fig. 2(a), the hydrophobic glass spheres initially deposited onto the air–glycerol interface will pile up occasionally. A solution of silicone oil (AK5, Wacker) in hexane with a mass concentration of 0.1% is then applied to the air–glycerol interface. After completely immersing in the solution, the particles redistribute and form a monolayer, as indicated in Fig. 2(b). Driven by the evaporation front of the hexane, the packing of the spheres becomes more and more dense. As all the hexane evaporates, a monolayer of 'wet' granular clusters is obtained, *cf.* Fig. 2(c). Owing to the compact structure we refer to these clusters as 'wet' granular rafts. To quantify the amount of the added oil phase we employ the dimensionless concentration $W = V_o/V_p$, defined as the ratio of the volume V_o of the added oil to the total volume V_p of the particles. It is kept within a few percent so as to promote the formation of capillary bridges between adjacent particles instead of large liquid clusters, see also the image in Fig. 2(c).

The sketch in Fig. 1 illustrates how the aggregates floating on the air–liquid interface are illuminated from below by means of a collimated light source in combination with an annular mirror placed at the bottom of the Couette cell. Fig. 1(f) shows a top view of the 'wet' granular rafts in a steady state captured by the high speed camera (PCO h1200s). The captured image is in turn subjected to an image processing procedure, which is capable of detecting more than 95% of the particles in the field of view and locating the cluster boundaries, as illustrated in Fig. 1(g). To achieve a steady state, the sample is initially sheared at the largest possible shear rate 48.8 s^{-1} for 10 minutes, and with a desired shear rate for a period of 30 minutes.

2.2 Numerical simulations

The dynamics of the 'wet' particles in a linear shear flow is numerically simulated applying a two-dimensional discrete element model (DEM). To account for the polydispersity of the particle size in the experiments we consider a 1 : 1 bidisperse mixture of spheres with radii $R_>$ and $R_<$, respectively, fixed by the ratio $\lambda \equiv R_>/R_< = 1.05$ of large to small radius and the mean particle diameter $D = R_< + R_>$. Each particle is assigned a mass $m_i = 4\pi\rho_p R_i^3/3$ where ρ_p is the mass density of the particles.

Particle–particle interactions are modeled employing a repulsive soft core potential and a constant attractive capillary force

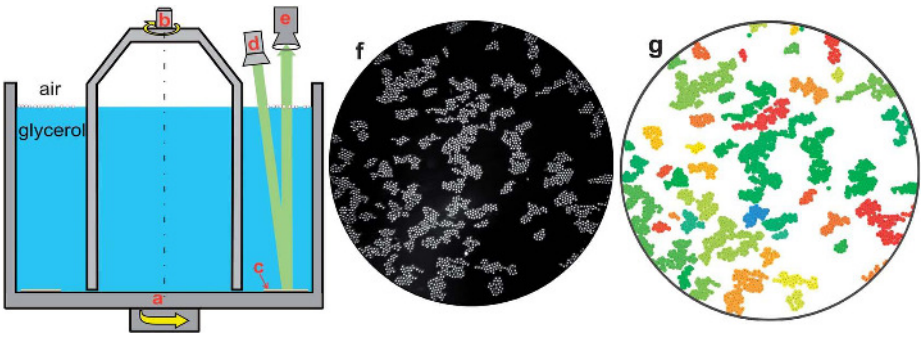

Fig. 1 Sketch of the experimental setup. The outer (a) and inner (b) cylinders of the Couette device are able to rotate independently at fixed angular velocities to create a linear shear profile in the gap. Hydrophobic glass spheres with a diameter of (165 ± 25) μm floating on glycerol are 'wet' by silicone oil. The particles are illuminated by parallel light emitted from the light source (d) and reflected by the mirror (c). Images of the aggregates are recorded in the top view (f) by a high speed camera (e) and subjected to an image processing procedure. Panel (g) shows a typical image after the image processing procedure. All particles in a cluster are displayed in the same color.

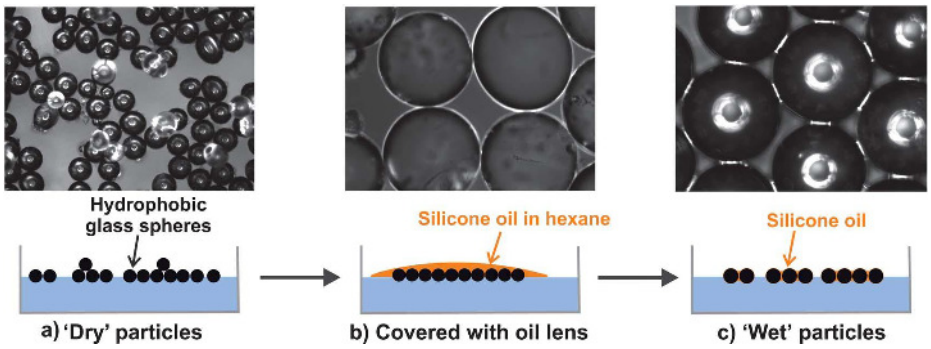

Fig. 2 Preparation of two-dimensional 'wet' granular clusters. The upper and lower rows show snapshots taken with an optical microscope and sketches to illustrate the procedure, respectively. (a) Initial state where particles are poured gently onto the air–glycerol interface; (b) particles covered by a lens composed of silicone oil solved in hexane; (c) particles bound together by capillary bridges (the white bars between adjacent particles) after evaporation of hexane.

acting below a finite separation. Tangential forces due to sliding or rolling friction, as well as dissipative normal forces are not considered, *i.e.*, two particles binding together *via* a liquid bridge can roll or slide freely relative to each other.

Following ref. 33 and 34 we chose an elastic repulsive interaction of the form

$$\boldsymbol{f}_{ij}^{(r)} = \begin{cases} -\frac{3A}{2}\sqrt{|r_{ij}-R_i-R_j|}\,\boldsymbol{e}_{ij} & \text{for} \quad r_{ij} < R_i + R_j \\ 0 & \text{else} \end{cases} \tag{1}$$

where r_{ij} is the distance from the center of particle i to the center of particle j with radii R_i and R_j, respectively, and $\boldsymbol{e}_{ij}$ is the unit vector pointing from the center of particle i to the center of particle j. The advantage of this non-linear spring force over, *e.g.*, a Hertzian contact is the diverging compressibility at zero indentation. The prefactor A in eqn (1) controls the particles' hardness.

To model the attractive capillary interaction we implemented the minimal capillary model proposed by Herminghaus in ref. 31 in our simulation code. At the same moment two particles touch, a capillary bridge is created which exerts an attractive force onto the particles. The capillary bridge is destroyed whenever the separation between the surfaces of the particles exceeds a certain threshold separation s^*.

The capillary force $\boldsymbol{f}_{ij}^{(c)}$ particle j exerts onto particle i is related to the interfacial tension of the wetting liquid and the radii of the particles by

$$\boldsymbol{f}_{ij}^{(c)} = 2\pi\sigma\sqrt{R_i R_j}\,\boldsymbol{e}_{ij} \text{ for } r_{ij} < R_i + R_j + s^*, \tag{2}$$

where $\boldsymbol{e}_{ij}$ is the unit vector pointing from the center of particle i to the center of particle j and σ is the interfacial tension of the air–liquid interface.

The spherical particles interact with the flow of the ambient liquid following Stokes' viscous drag force

$$\boldsymbol{f}_i^{(d)} = 3\pi\mu R_i(\boldsymbol{v}_i - \dot{\gamma}x\boldsymbol{e}_y) \tag{3}$$

for a sphere which is half immersed into the liquid. The dynamic viscosity of the ambient liquid is μ while $\dot{\gamma}$ denotes the shear rate.

The particle coordinate perpendicular to the direction of shear is denoted by x. We assume a linear flow profile which is not altered in the presence of the floating particles, *i.e.*, we do not account for any hydrodynamic interaction between the particles. To avoid boundary effects, and in consistency with the linear shear profile, we apply Lees Edward boundary conditions to the particles in the simulation box. For all simulation runs we set the side length of the square simulation box to $L = 80D$. To obtain the particle positions $\boldsymbol{r}_i(t)$ as a function of time t, Newton's equation of motion,

$$m_i\ddot{\boldsymbol{r}}_i = \sum_{i\neq j}^{N_p}\boldsymbol{f}_{ij}^{(r)} + \sum_{j\in\mathscr{B}(i)}\boldsymbol{f}_{ij}^{(c)} + \boldsymbol{f}_i^{(d)}, \tag{4}$$

is solved for every particle $i = 1, \ldots, N_p$ using a predictor corrector algorithm for second order ODEs. Here, the set $\mathscr{B}(i)$ is the set of particles $i \neq j$ which share a capillary bridge with particle i.

During each simulation run clusters of particles connected by capillary bridges are detected. Besides the cluster size distribution, we estimate distributions of the spatial extension of the clusters, and their elongation and orientation relative to the shear flow. For given coordinates $\boldsymbol{r}_i$ of the particles $i \in \mathscr{I}_\alpha$ in a cluster α, the latter quantities can be computed from the two-dimensional tensor

$$\tilde{\boldsymbol{M}} = \frac{1}{N_\alpha}\sum_{i\in\mathscr{I}_\alpha}\boldsymbol{r}_i\otimes\boldsymbol{r}_i - \langle\boldsymbol{r}\rangle\otimes\langle\boldsymbol{r}\rangle \text{ with } \langle\boldsymbol{r}\rangle = \frac{1}{N_\alpha}\sum_{i\in\mathscr{I}_\alpha}\boldsymbol{r}_i. \tag{5}$$

Note that the definition of this tensor is similar to the moment of inertia tensor known in classical mechanics. Here, the index set $\mathscr{I}_\alpha$ contains all indices of particles being a part of cluster α, while the number of particles in the cluster is $N_\alpha = |\mathscr{I}_\alpha|$.

A number of quantities characterizing the geometry and orientation of a cluster can be deduced from $\tilde{\boldsymbol{M}}$. The radius of gyration R_g of the particle cluster is defined as

$$R_g \equiv (\mathrm{tr}\,\tilde{\boldsymbol{M}})^{1/2}, \tag{6}$$

while the ratio $\lambda = M_>/M_< > 1$ of the larger eigenvalue $M_>$ to the smaller eigenvalue $M_<$ of $\tilde{\boldsymbol{M}}$ can be employed to define the anisotropy of the cluster.

To non-dimensionalize all physical quantities relevant in our analysis we measure lengths and distances in units of the mean

diameter of the spheres, D, forces and energies in units of $F_0 \equiv \sigma D$ and $E_0 \equiv \sigma D^2$, respectively, and time in units of $T_0 \equiv \mu D/\sigma$. From $1/T_0$, one obtains the conversion factor between experimental and simulation shear rates to be 101 s^{-1}. Using this particular rescaling, we can set the mean particle diameter D, interfacial tension σ, and the dynamics viscosity μ to unity. Consequently, the mass and mass density of the particles is measured in units of $M_0 = \mu^2 D^2/\sigma$ and $\rho_p = \mu^2/\sigma D$, respectively.

Throughout all simulation runs we set the prefactor in the non-linear spring force eqn (1) to $A = 100\sigma D^{1/2}$. This guarantees to observe only small indentations between particles at small shear rates $\dot{\gamma} < T_0^{-1}$. Moreover, we set the rupture distance of the capillary bridges to $s^* = 0.1D$ independent of the radii of the particles. According to the analysis by Willett *et al.*[35] of the volume dependence of s^* on the liquid volume, this value corresponds to a liquid saturation of $W \approx 0.7\%$ as an upper limit, assuming six bridges on a bead. The integration time step is set to $\Delta T = 10^{-3} T_0$ in all simulation runs. Before starting the shearing motion of the liquid bath in our simulations, a number of $N = 1304$ particles where sequentially placed randomly in the box without overlaps resulting in a covered area fraction of 0.16. The total duration of a simulation run was set to $T_s = 200/\dot{\gamma}$, to ensure that the distribution of particle clusters is given enough time to relax into a stationary state. During the time interval $[0.5T_s, T_s]$, the size distribution of particle clusters connected by capillary bridges and their radius of gyration are sampled in regular intervals. Besides time averages over 20 measurements in each simulation run we take a further ensemble average over 20 realizations to improve the statistics.

3 Results and discussion

In this section, we first demonstrate the enhanced cohesion of 'wet' granular rafts by comparing the aggregates formed by the same particles without ('dry' case) and with ('wet' case) oil film for the same driving in subsection 3.1. For 'wet' aggregates, we then characterize their fractal dimensions and size distributions in subsections 3.2 and 3.3 correspondingly. Finally in subsection 3.4, we rationalize the scaling factors obtained in subsections 3.3 and 3.2 with a model based on the balance between the viscous drag force and the cohesive force.

3.1 'Dry' *vs.* 'wet' aggregates

Initially without shearing, we observe for both 'dry' and 'wet' particles an accumulation in the central region of the gap, along with the evaporation front of the volatile solvent hexane. As the steady state is reached after a certain time of shearing, the behavior of 'dry' and 'wet' aggregates are dramatically different, as shown in Fig. 3(a) and (b). For the case of 'dry' particles, no large scale heterogeneities are observed and the particles follow the shear flow. The dilation of 'dry' particles compared with the initial state is mainly due to the hard core repulsion between neighboring particles.

A different behavior is observed if a certain amount of oil is added to the solvent. In our experiments, we varied the volume fraction of oil in the range between $W \approx 0.5$ and 2.5%. In any case, large, persisting clusters are formed by the 'wet' particles. These clusters rotate around their center while following the shear flow. During this motion they may also collide and merge, deform or break into several parts.

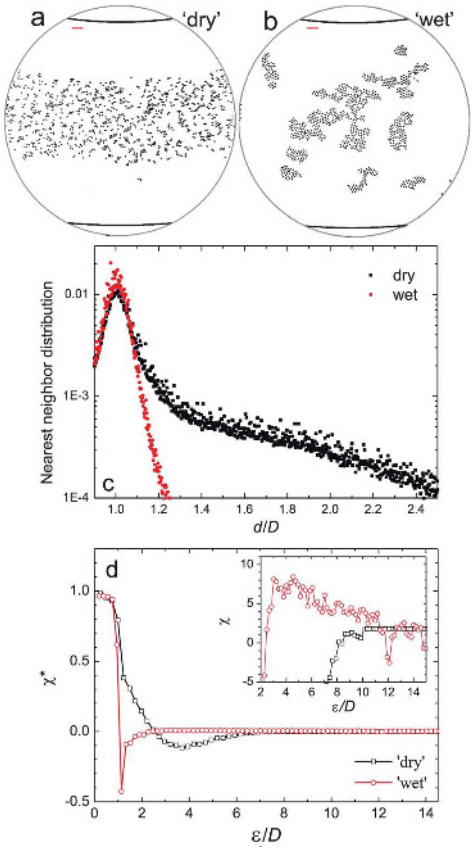

Fig. 3 Panels (a) and (b) display inverted sample images used for the morphological characterization for 'dry' and 'wet' particles, respectively, for a shear rate 7.3 s^{-1}, particle diameter $D = (165 \pm 25)$ μm, and a global area fraction of particles $\phi = 5.7\%$. Scale bar length 1 mm. (c) The nearest neighbor distribution for 'dry' and 'wet' particles as a function of the reduced distance d/D. (d) Euler characteristic χ^* for 'dry' and 'wet' particle aggregates normalized by the total number of particles as a function of the reduced disk diameter ε/D. Inset: a close view of the Euler characteristic χ (not normalized) around $\chi = 0$.

Inspection of the clusters by optical microscopy demonstrates that these clusters are formed by particles connected with each other through capillary oil bridges. The attractive forces induced by the bridges keep the particles in close contact. However, the relative positions of two merging clusters are not fixed at their first contact. Instead they could roll or slide with respect to each other until further contacts are formed that keep the newly formed structure stable. Generically, they are composed of a rigid backbone and floppy parts in their periphery. Folding or unfolding of clusters with chain-like structures under the shear flow could also be observed in some cases. As a result of the complex evolution, these 'wet' granular rafts are assemblies of dense, highly ordered domains which display a certain porosity on larger length scales.

Interactions between 'dry' particles can be explained by weak long-ranged capillary forces which are mediated by the distorted glycerol interface. These distortions are either caused by gravitational forces pushing the particles into the liquid interface or by the irregular shape of the three phase contact line which is pinned to the rough particle surface.[1,25] In the latter case, the capillary interaction depends on the relative orientation of the particles and may also be repulsive. Both interactions decay with a power law at medium separations on the scale of the particle diameter and are screened off by gravity on length scales larger than the capillary length of the glycerol–air interface. The above comparison indicates that the force owing to the formation of capillary bridges acting on adjacent particles dominates any other particle–particle interactions.

For a more quantitative characterization of the local arrangement of particles in 'wet' granular rafts we first computed the nearest neighbor distributions (NND) from our experimental data. To this end we detected the position of each particle with the image processing procedure proposed in ref. 36. This procedure is capable of locating more than 95% of the particles (on average ~850 particles in each image) in the field of view. The statistics of the NND is further improved by averaging over 1000 frames.

As shown in Fig. 3(d), the decay of the distribution above a normalized distance $d/D = 1$, *i.e.*, the mean particle diameter, is much faster for the 'wet' aggregates than for the 'dry' ones. There are almost no neighboring particles with $d/D > 1.3$, strongly suggesting that each 'wet' particle is connected to at least one neighbor *via* a capillary bridge. The broader distribution for assemblies of 'dry' particles clearly indicates that more particles are isolated as a result of the dilation driven by the shear flow. The mobility of the spheres arises from the viscous drag force which dominates the capillary interaction mediated by distortions of the liquid interface. Therefore no large clusters can be observed and the particles tend to follow the shear flow. However, it is difficult to quantify the formation of structures on length scales above the diameter of particles with the information of the NND alone.

To overcome this problem, we employ in addition the Euler characteristic of the particle distribution. The Euler characteristic, which is one of the three Minkowski measures in two dimensions, is particularly suited for this type of analysis because the Minkowski measures are well-known to capture all possible correlations within an ensemble of objects, by virtue of Hadwiger's theorem.[37] In this analysis, circular disks with diameter ε are placed at the center of each particle, and the *set union* of these disks is considered. The Euler characteristic χ of this set is defined as the number of disjoint objects minus the number of holes and is a function of the normalized disk diameter ε/D. Together with the other two Minkowski measures in two dimensions, the boundary length and the total area of the union set, it contains the same information on the particle configuration as all n-point correlation functions together.[37] We consider here only the Euler characteristic, as it contains the relevant information about the clustering of particles. As for the NND, we improve the statistics of the Euler characteristic by averaging over a large number of frames.

As shown in Fig. 3(e), the Euler characteristic χ for both 'dry' and 'wet' particles under shear flow shows a similar trend but is quantitatively very different. Here, we made use of the Euler characteristic $\chi^* \equiv \chi/N$ normalized by the particle number N for ε/D with $\chi \to 1$ as $\varepsilon/D \to 0$. While increasing the normalized disk diameter ε/D, the curves χ^* show a drop from 1 to a negative value followed by a slow increase. A drop of χ^* to a negative value indicates transition to a network-like structure. The sharp drop of χ^* for 'wet' aggregates shows that particle positions in 'wet' aggregates have a higher structural organization. The drop starts at $\varepsilon/D \approx 1$, because the merging of particles in contact reduces the number of objects and raises that of holes. Note that the slope drops much faster for the 'wet' case than for the 'dry' one, which is in accordance with the decay of NND for distances $d/D > 1$ discussed above. This sharp drop to negative values indicates that 'wet' particles have a much stronger tendency to form large and compact aggregates, since the number of holes increases substantially. The local minimum of χ^* gives rise to a characteristic value $\chi^*_{\min}$ and a corresponding characteristic disk size $\varepsilon_{\min}/D$, which are related to the local spatial structure of particles.

The parameter $\varepsilon_{\min}/D$ indicates a characteristic length above which the filling of holes starts to overwhelm the reduction of χ^* induced by the merging of clusters. We find $\varepsilon_{\min}/D \approx 1.14$ for the 'wet' particles, much smaller than the one for the 'dry' particles. This suggests that the holes in 'wet' aggregates are smaller than the ones in 'dry' aggregates. Moreover, the sudden jump of χ^* for the 'wet' case indicates that the closing of holes is much more coherent or, in other words, the holes have a much more uniform structure when compared to the 'dry' case.

The organization of the particles into extended clusters can be observed as a maximum of the Euler characteristic for large values $\varepsilon/D \gg 1$. The positive maximum of χ in the inset of Fig. 3 for 'wet' particles is a clear indication of dense aggregates while the corresponding curve for 'dry' particles does not display a maximum and approaches a constant value ≈ 1 from below. In this respect, it resembles qualitatively the form $\chi^* = (1 - \varepsilon/\ell)\exp(-\varepsilon/\ell)$ derived for uncorrelated particle positions (Poisson process) with a length scale $\ell \equiv n^{-1/2}$, where n corresponds to the area density of particles.[38]

Besides the Euler characteristic, other statistical quantities such as pair correlation functions[26] and bond orientation order parameters[39,40] are also frequently used to characterize the local particle order in clusters. A further analysis of 'wet' granular rafts with these tools will be a focus of our further investigations.

The high prevalence of a locally hexagonal packing of particles in 'wet' granular clusters revealed from the above comparisons also enables us to identify clusters conveniently by reconstructing images with a disk size $\varepsilon/D > 2/\sqrt{3}$ (as shown in Fig. 1(g)). To account for the polydispersity in the radii of the glass beads, a disk radius $\varepsilon/D = \sqrt{3}$ is chosen for the analysis below. Based on this procedure, we can perform statistics on the properties of clusters including the fractal dimensions and cumulative size distributions, based on the snapshots from both experiments and DEM simulations.

3.2 Fractal dimension

A powerful approach to quantify the internal and overall structure of particle aggregates is to compute their fractal dimensions. This method has been successfully applied in a wide

range of problems, from the formation of galaxies to the growth of urban city.[41] Here we use the fractal dimension to characterize the structure of clusters formed under the shear flow in a steady state. In such a state, no temporal evolution of the cluster size distributions could be observed, although clusters keep deforming, breaking or merging with each other under the shear flow. To achieve good statistics, more than 4×10^4 clusters from recorded images taken under various steady states are analyzed. The fractal dimension δ is obtained from double logarithmic plots of the cluster size N and the average radius of gyration R_g of the clusters as defined by eqn (5) and (6).

Both experimental and simulation results, as shown in Fig. 4, suggest a quite well defined fractal dimension δ. The averaged value δ of the exponents from experiments (1.57 ± 0.03) and simulations (1.56 ± 0.03) agrees with each other, *cf.* the solid lines in Fig. 4. This agreement again indicates that the balance between the Stokes' drag force and the capillary force due to the formation of liquid bridges determines the dynamics of 'wet' granular rafts, and it is appropriate to employ the minimal capillary model to describe the capillary force. Increasing the shear rate may lead to a slightly more fractal structure, as indicated by the subtle decrease of the fractal dimensions with increasing shear rate for the simulation results in a wider range of $\dot{\gamma}$, as shown in the inset of Fig. 4(b). This feature may be attributed to the reduced relaxation time for the clusters that are stretched under the shear flow. As the shear rate increases, the time for the floppy parts of the clusters to relax into a more stable structure *via* finding further possible bounds is limited, which presumably leads to a slightly more fractal structure.

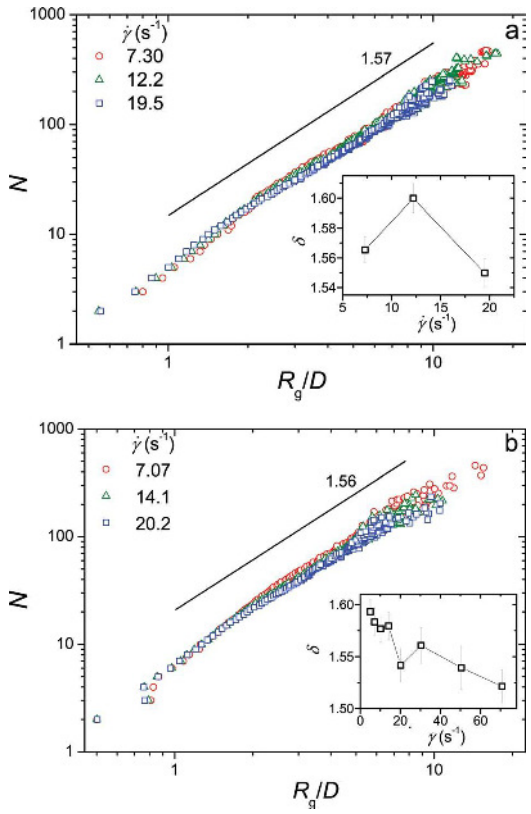

Fig. 4 The scaling between the number of particle in a cluster, N, and the gyration radius of the cluster rescaled by the averaged particle diameter, R_g/D, at various shear rates $\dot{\gamma}$ from both experiments (a) and DEM simulations (b). The liquid content for the experiments is $W = 1\%$. The solid line in both plots corresponds to the scaling averaged over all shear rates. See insets for the scaling δ at various shear rates. To have a better comparison, only three simulation results with shear rates closest to the experimental ones are shown in (b).

The fractal dimension also offers a convenient classification of aggregates in two and three dimensions and has been used frequently to characterize aggregations of colloidal particles.[42] Typical fractal structures for colloidal aggregates are the diffusion-limited aggregation (DLCA) and the reaction-limited aggregation (RLCA), with characteristic fractal dimensions of 1.44 and 1.55 correspondingly for 2D systems.[19] In our system, the fractal dimension of sheared clusters consisting of 'wet' granular particles is closer to that of RLCA than DLCA. This is not surprising, because the mobility of the particles is governed by the shear flow instead of diffusion, and the binding of particles *via* the formation of capillary bridges is selective and reversible: only those capillary bridges strong enough to sustain the viscous drag force persist. In addition, the mixture of elongational flow and rotations leads to a permanent back-folding of more distant parts of the cluster onto its main body. This will clearly lead to a more compact structure of the granular rafts and a larger fractal dimension.

Further analysis of the scaling behavior reveals two features: first, there exists a slight change of the fractal dimension at a cluster size between 10 and 20, which presumably corresponds to the length scale of the rigid components of a cluster. While taking a closer look at the structure of clusters formed (see Fig. 3(b)), the branches of large clusters typically end with relatively more compact and rigid parts with a similar length scale. We anticipate that this type of rigid component is the basic unit to form a cluster. Further analysis based on an accurate definition and determination of those rigid components will be a focus of further investigations in order to decode further the physics behind this length scale. Second, the scattering of the rescaled gyration radius, R_g/D, also grows with the cluster size. This could be attributed not only to the statistical error, but also to the deformation of clusters under the shear flow as well as interactions between clusters. For example, multiple clusters may collide with each other and form transient clusters. They may break immediately or fold into more a compact cluster and survive for a longer time, which presumably depends on the balance between the number of bonds created and the total viscous drag force acting on various rigid parts of the cluster. Therefore, the larger the cluster size, the higher the probability is for a cluster to deform into various structures, *i.e.* various R_g.

3.3 Cluster size distribution

For both experiments and DEM simulations, the cluster size distributions are obtained by counting the number of clusters with a certain size N (number of particles) for all the images captured. The distributions obtained in experiments are in a

steady state, because three distributions obtained with time intervals of 30 minutes agree with each other. Variations of the total simulation times show that 100 complete turns of the shear flow is already sufficient to reach a stationary distribution of cluster sizes. These distributions are also independent of the initial conditions: starting with $\dot{\gamma} = 0$ or 20 s^{-1} yields the same result, provided that the sample has been initialized with the desired shear rate. The global area fraction ϕ of the particles, defined as the area covered by the spheres over the total area of the interface, is also found to play a minor role, since a variation of ϕ from 10% to 25% does not lead to an apparent change of the size distribution. For the experimental results shown in Fig. 5(a), the global area fraction is around 10%, which is slightly higher at the center of the ring. In the DEM simulations, the area fraction is fixed to 16%.

Fig. 5(a) and (b) correspond to the cumulated cluster size distributions obtained from both experiments and DEM simulations. Here the cumulated probability $P(N)$ to find a cluster with N or more particles is preferred over a histogram because we mainly focus on the statistics at large N with typically low number of counts and because it facilitates comparisons owing to the normalized initial value. In the experiment, counting starts from $N = 2$ to avoid the error counting of isolated particles at the image borders. For both experimental and simulation results, $P(N)$ decays exponentially with growing N for cluster sizes greater than ≈ 8, as the semi-log plot indicates. Different from the size distribution of droplets in an emulsion[43–45] and particle aggregates in three dimensional shear flow,[46] 'wet' granular rafts display a broader size distribution. Unlike a three dimensional liquid droplet that has the tendency to evolve into a spherical shape under the influence of interfacial tension, 'wet' granular rafts consist of densely packed rigid substructures, as the snapshots in Fig. 3 indicate. The existence of an internal structure dramatically enhances the number of possible breaking processes for larger clusters, and consequently contributes to the different size distributions. More detailed analysis of the size distribution in relation to the Smoluchowski rate equation[47,48] will be a focus of further investigation.

As the shear rate increases, the cluster size distribution decays faster, because the larger viscous drag force facilitates the breaking of clusters. To quantify the shear rate dependence of the distributions, we extract the decay constant k of the exponential

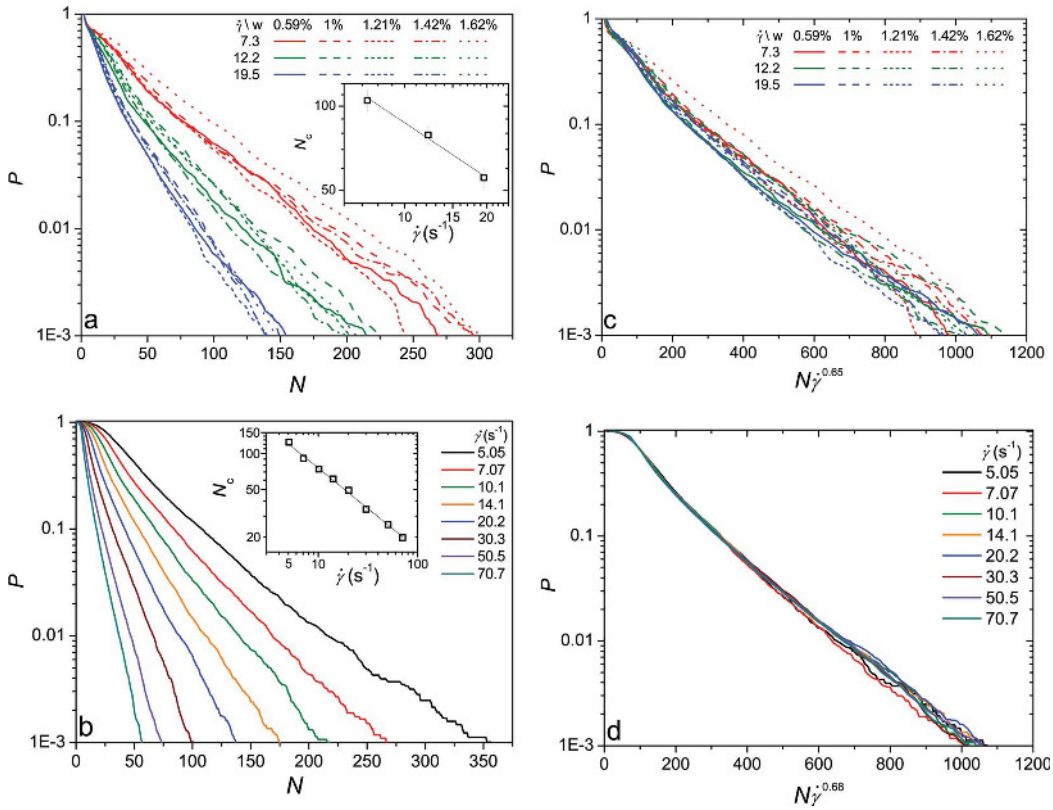

Fig. 5 Left: cumulative cluster size distribution P corresponding to the probability to find a cluster out of N or more particles. (a) Experimental results for various liquid contents W and shear rates $\dot{\gamma}$ and (b) corresponding results of DEM simulations. Insets show the scaling between the characteristic cluster size $N_c = k^{-1}$ and the shear rate $\dot{\gamma}$, where the decay rates k are obtained from linear fits of the corresponding data within the range $0.001 \leq P \leq 0.1$ in the semi-logarithmic plane. Right: corresponding P as a function of the rescaled cluster size $N\dot{\gamma}^{\beta}$. The exponent β for (c) experiment and (d) simulation corresponds to the scaling of N_c with $\dot{\gamma}$.

tails of the cumulative distributions $P(N)$ for various shear rates $\dot{\gamma}$. As shown in the insets of Fig. 5, the decay of the characteristic cluster size $N_c = k^{-1}$ with increasing shear rate $\dot{\gamma}$ follows a power law $N_c \propto \dot{\gamma}^{-\beta}$. The error bars in Fig. 5(a) correspond to the variation of the decay rate with the liquid content. The exponent $\beta = 0.65 \pm 0.06$ from our experimental data agrees with the corresponding value $\beta = 0.68 \pm 0.02$ derived from DEM simulations within the errorbar.

Different from the shear rate dependence in the experiments, varying the liquid content W will not influence the cluster size distribution dramatically as shown in Fig. 5(a). This suggests that the forces exerted onto adjacent particles by capillary bridges in our system barely depend on the bridge volume as described for pendular capillary water bridges in three-dimensional piles of spherical glass beads.[32] The higher probability for cluster sizes $N < 5$ in the experiment than that in the simulation could be attributed to the error counting of particles at the borders.

For the range of shear rates explored, the characteristic cluster size determined from the experiment is always larger than that from the simulation. This is presumably due to the reduced effective driving force arising from hydrodynamic screening. Other sources of this systematic difference may stem from the fact that the particles are not exactly half immersed into the viscous bath as assumed in our model. Another explanation for the systematic deviations may be linked to the tangential friction at the particle contacts: the additional work required to roll or slide two bounded particles could impede the formation and opening of cracks.

Utilizing the shear rate dependence obtained from the experiments, we are able to replot the cluster size distribution as a function of the rescaled cluster size $N\dot{\gamma}^{\beta}$. As shown in the right panels of Fig. 5, the collapse of the cumulative probabilities onto a master curve over the whole range of the rescaled cluster size $N\dot{\gamma}^{\beta}$ clearly demonstrates the power law dependence of the cluster size on the shear rate. A comparison between the data collapse obtained from the experiment in Fig. 5(c) and the simulation in Fig. 5(d) reveals a similar decay, which demonstrates the key role that the viscous drag force and the capillary force plays in determining the cluster size distributions.

Qualitatively, the shear rate dependence is plausible since the larger cluster experiences a larger viscous drag force which effectively increases the tensile stress in their center and tears them apart. In the following Section 3.4 we will introduce a model which is based on the balance between the viscous drag force and the capillary force. This model allows us to rationalize the power law scaling suggested by both the experiment and the simulation.

3.4 Model

The agreement between experiments and DEM simulations in the above analysis in terms of both the size distributions and structural aspects of the clusters suggests that the balance between the capillary force and the viscous drag force dominates the dynamics of 'wet' granular rafts. Following this idea, we developed a model based on the balance between the viscous drag force that deforms and eventually breaks the clusters and the attractive capillary forces that hold the particles in the cluster together. Any linear shear profile, as the one used in our experiments, can be decomposed into two parts: a hyperbolic strain flow and a rotation (*cf.* Fig. 6(a)). As sketched in Fig. 6(b), the strain flow compresses the cluster in one direction and stretches it in an orthogonal direction. Thus the cluster, which continuously rotates in the frame of reference of the strain flow, will preferentially break along the direction of elongation, provided that the viscous drag force is large enough to overcome the capillary forces.

According to the Stokes' law, the viscous drag force acting on a single particle scales as $f^{(d)} \propto \mu D v$, where μ is the dynamic viscosity of the suspending liquid, D the diameter of the particle, and v the relative velocity of the particle in the hyperbolic flow field around the particle. For a cluster shown in Fig. 6(b), we assume that the stretching part of the viscous drag forces tends to break the cluster along the y axis, since it has different sign for the region with $x > 0$ (highlighted in Fig. 6(b) by the red transparent color) and that with $x < 0$. From the sketch Fig. 6(a), we see that the strain flow velocity in the x direction grows linearly with x: $v_x = \sqrt{2}\dot{\gamma}x/2$. Here, we use for convenience a coordinate system which is rotated by 45° with respect to the direction of the shear flow.

Thus we can calculate the total viscous drag force $F^{(d)}$ exerted on the cluster along the central cutting line $x = 0$ by integrating the drag force on a single particle $F^{(d)}$ over the red transparent region of the cluster. Assuming that the effective radius R_c of the region covered by the cluster is identical to the radius of gyration R_g, we have

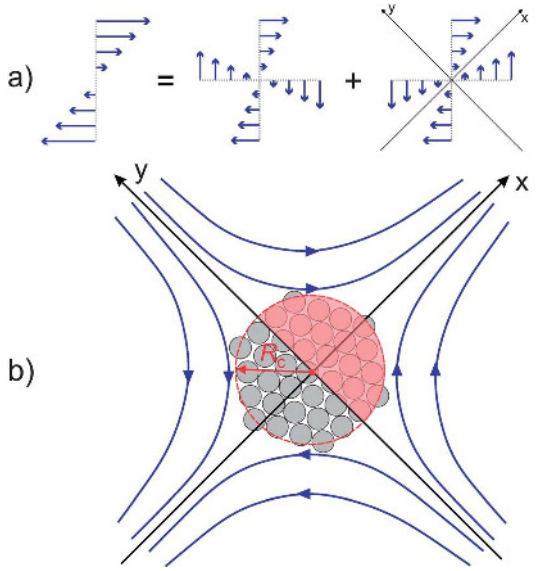

Fig. 6 (a) A sketch showing that any linear shear profile can be replaced by a superposition of a rotating and a hyperbolic straining flow field. (b) The hyperbolic stream lines of the hyperbolic flow profile will tend to compress the cluster with an effective radius R_c along the y axis and stretch it along the x axis. The center of the axes corresponds to the centroid of the cluster, and the half of the cluster located at $x > 0$ is highlighted by red color.

$$F^{(d)} = \int_{\mathscr{A}} f^{(d)} \phi \mathrm{d}A \propto \mu \phi \dot{\gamma} R_g{}^3 / D, \quad (7)$$

where $\phi \equiv ND^2/R_g{}^2 \propto N^{1-2/\delta}$ is the area fraction of particles in the cluster, and $\mathscr{A}$ is the area of a semi-circular region of the cluster with radius R_c, *cf.* also the sketch in Fig. 6.

On the other hand, the total capillary force $F^{(c)}$ acting along a cut $x = 0$ into the direction of the x axis can be estimated by[31]

$$F^{(c)} \propto n\sigma D \quad (8)$$

where σ is the interfacial tension of the wetting liquid, n is the number of capillary bridges in a cut along the line $x = 0$.

To obtain the upper limit of the number of capillary bridges which have to be destroyed during a break-up, we assume that this number is proportional to the number of particles which are cut by the line $x = 0$. Then, the number of bridges per length in the cut is proportional to the area density ϕ, and we have $n \propto \phi R_g D$. This leads to the estimate

$$F^{(c)} \propto \sigma \phi R_g D^2 \quad (9)$$

The maximum radius of gyration, R^*, of a stable particle cluster is reached when $F^{(c)} = F^{(d)}$, leading with eqn (7) and (9) to the estimate $R^* \propto \dot{\gamma}^{-1/2}$ and a maximum number of particles N^* following the scaling

$$N^* \propto \dot{\gamma}^{-\delta/2}. \quad (10)$$

A lower limit for the size of the largest mechanically stable cluster can be derived from the assumption that the number of bonds that needs to be broken is independent of the size of the cluster. This picture may apply to a system where the particle clusters are build as a hierarchy of rigid subclusters. For example, two rigid subclusters are forming a rigid cluster after creation of only three new capillary bridges. Two of these rigid clusters can now merge to form a larger, rigid cluster and so on. In each hierarchy, we will have $F^{(c)} \propto \sigma D$ independent of ϕ and R_g leading to a scaling estimate of the form

$$N^* \propto \dot{\gamma}^{-\delta/(1+\delta)}. \quad (11)$$

Both the experimental and simulation results showed that a scaling $N \propto R_g^{\delta}$ with $\delta \approx 1.6$ is valid over a wide range of N and only weakly dependent on the shear rate $\dot{\gamma}$. If we assume that the critical cluster size N^* scales linearly with the characteristic cluster size N_c we have $N_c \propto \dot{\gamma}^{-\beta}$ with an exponent in the range

$$\frac{\delta}{1+\delta} \leq \beta \leq \frac{\delta}{2}. \quad (12)$$

By explicit calculation, we indeed find that the values of β are consistent with the scaling estimates for both our experimental data and our simulation data: assuming $\delta \approx 1.6$, we obtain a lower bound $\beta_{min} \approx 0.6$ and an upper bound $\beta_{max} \approx 0.8$ for β. It is remarkable that the values of both experiments and the DEM simulations lie closer to the lower bound that corresponds to the assumption of a constant number of contacts that need to be destroyed in a cluster break-up. This agrees with the qualitative analysis based on visual inspections described in Section 3.1.

Besides the viscous drag force, inertial forces arising from the rotation of the clusters may also play a role in the break up of clusters. The internal force acting on a single particle scales as $f^{(i)} \propto \rho_p D^3 \dot{\gamma}^2 r$, with r being the distance to the cluster center. The power of the spatial dependence of the relevant component on the inertial force and that of the viscous drag force on the elongational flow is identical. Similar to the viscous forces the inertial forces acting in the x-direction on the upper half of the cluster act on the cut along the y-axis. It is immediately clear that the viscous force is dominant for small shear rates and that the inertial forces becomes prominent for shear rates $\dot{\gamma} \gtrsim \mu/\rho_p D^2 \approx 105\ s^{-1}$, only. Inertial effects can be safely neglected as the shear rate used in our experiments is much smaller.

Similar criteria have also been used to describe the breaking of aggregates trapped at an air–water interface under shear flow.[27] The attraction between particles in that case is due to the force arising from gravity-induced interfacial deformations[25] that corresponds to the 'dry' situation in our current investigation. Despite this difference, the criteria based on the force balance could explain the size of aggregates for both cases.

4 Conclusion and outlook

It has been shown that cohesive spherical particles trapped at an air–liquid interface aggregate into clusters with a characteristic size in the presence of a linear shear flow. In our experiments, the cohesive particles are prepared by introducing an immiscible second liquid that adheres to the surface of submillimetric glass beads. Capillary bridges formed by the oil phase on the surface induce a strong attractive force which dominates all other particle–particle interactions and leads to the formation of 'wet' granular rafts. In corresponding DEM simulations of particle aggregation in shear flow, the capillary force is modeled by a short ranged attractive force between adjacent particles.

The cohesion induced by the second liquid is demonstrated to dominate other particle–particle interactions, as a comparison of the snapshots to the 'dry' case reveals. The Euler characteristic shows that this strong cohesion leads to a closer packing of the particles into extended clusters. We were able to show that the size of the clusters and their gyration radius follow a power law scaling over at least one and a half order of magnitudes. Their fractal dimension δ, as revealed by both experiments and simulations, is in a range between 1.5 and 1.6, with a weak dependence on the shear rate. The values are closer to those of RLCA in 2D than for 2D DLCA. The cumulated size distribution in the steady state decays exponentially with the number of particles in the clusters. The characteristic cluster size N_c decreases with increasing shear rate. In addition, we could demonstrate that the experimentally measured cluster size distributions depend only weakly on the amount of wetting liquid in accordance with the known fact that the force between spherical bodies induced by an axially symmetric pendular bridge approaches a constant value in the limit of small volumes.

The scaling of the characteristic cluster size $N_c \propto \dot{\gamma}^{-\beta}$ with the shear rate is consistent with a model considering the balance between the viscous drag force that tends to break the cluster and the capillary force that binds particles together. This balance, together with the fractal dimension δ, provides an estimated scaling relationship between the cluster size and shear rate which agrees fairly well with the values of the exponent $\beta = 0.65 \pm 0.06$

obtained from experiments and 0.68 ± 0.02 derived from DEM simulations.

The strong cohesion forces arising from the capillary bridges and their robustness against changes in the thickness of the oil film covering the particles qualify this system as a suitable model system to study the dynamics of driven wet granular matter in two dimensions. For the particle size chosen gravity does not play an important role, and the particles are driven homogeneously by the linear shear profile. Besides the importance as a model system, this investigation also suggests to enhance the efficiency of particle aggregation by wetting films. This may be relevant for a number of applications, such as waste water treatments and ore handling.

Further characterizations of the aggregation will be focused on the anisotropy, the dynamics of the rigid components of a cluster, and the scaling with other control parameters such as viscosity and surface tension. By simulation, we would also like to check the role that hydrodynamic interactions play in such a system. At a sufficient large area fraction, the 'wet' particles under shear flow may self-organize themselves into a single large cluster. The dynamical behavior of such a cluster could help to elucidate fundamental questions about melting or jamming transitions[49,50] of cohesive and non-cohesive materials in two dimensions. In addition, it could also shed light on the stability mechanism of bicontinuous interfacially jammed emulsion gels.[7,9]

Acknowledgements

The authors thank Krishnacharya Khare for his help on OTS coating of glass spheres. Inspiring discussions with Karen Daniels, Thomas Fischer, Ingo Rehberg, Jayati Sarkar, and Matthias Schröter are gratefully acknowledged. It is also a pleasure to thank Daniel Herde, Jan Kierfeld and Julie Murison for critical reading of the manuscript and useful comments.

References

1 D. Stamou, C. Duschl and D. Johannsmann, *Phys. Rev. E: Stat. Phys., Plasmas, Fluids, Relat. Interdiscip. Top.*, 2000, **62**, 5263–5272.
2 J. C. Loudet and B. Pouligny, *Eur. Phys. J. E: Soft Matter Biol. Phys.*, 2011, **34**, 76.
3 *Colloidal Dispersions*, ed. W. B. Russel, D. A. Saville and W. R. Schowalter, Cambridge University Press, Cambridge, England, 1989.
4 G. M. Whitesides and B. Grzybowski, *Science*, 2002, **295**, 2418–2421.
5 B. A. Wills, *Mineral Processing Technology*, Butterworth-Heinemann, Oxford, UK, 6th edn, 1997.
6 H. A. Stone, *Annu. Rev. Fluid Mech.*, 1994, **26**, 65–102.
7 K. Stratford, R. Adhikari, I. Pagonabarraga, J. C. Desplat and M. E. Cates, *Science*, 2005, **309**, 2198–2201.
8 B. P. Binks and T. S. Horozov, *Colloidal Particles at Liquid Interfaces*, Cambridge University Press, 2006.
9 M. E. Cates and P. S. Clegg, *Soft Matter*, 2008, **4**, 2132.
10 G. G. Fuller and J. Vermant, *Annu. Rev. Chem. Biomol. Eng.*, 2012, **3**, 519–543.
11 E. Koos and N. Willenbacher, *Science*, 2011, **331**, 897–900.
12 P. Pieranski, *Phys. Rev. Lett.*, 1980, **45**, 569.
13 K. Zahn, R. Lenke and G. Maret, *Phys. Rev. Lett.*, 1999, **82**, 2721–2724.
14 K. Zahn and G. Maret, *Phys. Rev. Lett.*, 2000, **85**, 3656–3659.
15 M. G. Nikolaides, A. R. Bausch, M. F. Hsu, A. D. Dinsmore, M. P. Brenner, C. Gay and D. A. Weitz, *Nature*, 2002, **420**, 299.
16 P. Cicuta, E. J. Stancik and G. G. Fuller, *Phys. Rev. Lett.*, 2003, **90**, 236101.
17 C. Eisenmann, U. Gasser, P. Keim and G. Maret, *Phys. Rev. Lett.*, 2004, **93**, 105702.
18 J. J. Cerdà, T. Sintes, C. Holm, C. M. Sorensen and A. Chakrabarti, *Phys. Rev. E: Stat., Nonlinear, Soft Matter Phys.*, 2008, **78**, 031403.
19 D. J. Robinson and J. C. Earnshaw, *Phys. Rev. A*, 1992, **46**, 2045–2054.
20 P. Pieranski, *Phys. Rev. Lett.*, 1980, **45**, 569–572.
21 P. J. Lu, J. C. Conrad, H. M. Wyss, A. B. Schofield and D. A. Weitz, *Phys. Rev. Lett.*, 2006, **96**, 028306.
22 V. N. Manoharan, M. T. Elsesser and D. J. Pine, *Science*, 2003, **301**, 483.
23 *Powders and Grains*, ed. R. Garcia-Rojo, H. J. Herrmann and S. McNamara, Taylor & Francis, London, 2005.
24 J. Duran, *Sands, Powders and Grains: An Introduction to the Physics of Granular Materials*, Springer-Verlag, New York, Inc., 1st edn, 2000.
25 N. D. Vassileva, D. van den Ende, F. Mugele and J. Mellema, *Langmuir*, 2005, **21**, 11190–11200.
26 H. Hoekstra, J. Vermant, J. Mewis and G. G. Fuller, *Langmuir*, 2003, **19**, 9134.
27 N. D. Vassileva, D. van den Ende, F. Mugele and J. Mellema, *Langmuir*, 2006, **22**, 4959–4967.
28 N. D. Vassileva, D. van den Ende, F. Mugele and J. Mellema, *Langmuir*, 2007, **23**, 2352–2361.
29 C. Camoin and R. Blanc, *J. Phys., Lett.*, 1985, **46**, 67–74.
30 W. A. Goedel, *Europhys. Lett.*, 2003, **62**, 607.
31 S. Herminghaus, *Adv. Phys.*, 2005, **54**, 221–261.
32 M. Scheel, R. Seemann, M. Brinkmann, M. Di Michiel, A. Sheppard, B. Breidenbach and S. Herminghaus, *Nat. Mater.*, 2008, **7**, 189–193.
33 C. S. O'Hern, L. E. Silbert, A. J. Liu and S. R. Nagel, *Phys. Rev. E: Stat., Nonlinear, Soft Matter Phys.*, 2003, **68**, 011306.
34 S. H. E. Rahbari, J. Vollmer, S. Herminghaus and M. Brinkmann, *Phys. Rev. E: Stat., Nonlinear, Soft Matter Phys.*, 2010, **82**, 061305.
35 C. Willett, *Langmuir*, 2000, **16**, 9396–9405.
36 J. C. Crocker and D. G. Grier, *J. Colloid Interface Sci.*, 1996, **179**, 298–310.
37 K. R. Mecke, T. Buchert and H. Wagner, *Astron. Astrophys.*, 1994, **288**, 697–704.
38 K. R. Mecke and D. Stoyan, *Biom. J.*, 2005, **47**, 473–488.
39 P. J. Steinhardt, D. R. Nelson and M. Ronchetti, *Phys. Rev. B: Condens. Matter Mater. Phys.*, 1983, **28**, 784–805.
40 W. Lechner and C. Dellago, *J. Chem. Phys.*, 2008, **129**, 114707.
41 P. Meakin, *Fractals, Scaling and Growth Far from Equilibrium*, Cambridge University Press, 1998.
42 M. Lin, H. M. Lindsay, D. A. Weitz, R. C. Ball, R. Klein and P. Meakin, *Nature*, 1989, **339**, 360.
43 D. Ramkrishna, *Population Balances: Theory and Applications to Particulate Systems in Engineering*, Academic Press, San Diego, 2000.
44 P. Becher, *Emulsions: Theory and Practice*, American Chemical Society, Oxford University Press, Washington, D.C., Oxford, 2001.
45 N. B. Raikar, S. R. Bhatia, M. F. Malone, D. J. McClements and M. A. Henson, *Ind. Eng. Chem. Res.*, 2011, **50**, 6089–6100.
46 A. Tolpekin, M. H. G. Duits, D. van den Ende and J. Mellema, *Langmuir*, 2003, **20**, 2614–2627.
47 F. Family, P. Meakin and J. M. Deutch, *Phys. Rev. Lett.*, 1986, **57**, 727–730.
48 S. Kumar and D. Ramkrishna, *Chem. Eng. Sci.*, 1996, **51**, 1311–1332.
49 A. J. Liu and S. R. Nagel, *Soft Matter*, 2010, **6**, 2869.
50 D. Bi, J. Zhang, B. Chakraborty and R. P. Behringer, *Nature*, 2011, **480**, 355–358.

Period Tripling Causes Rotating Spirals in Agitated Wet Granular Layers

Kai Huang* and Ingo Rehberg
Experimentalphysik V, Universität Bayreuth, 95440 Bayreuth, Germany
(Received 30 March 2011; published 8 July 2011)

Pattern formation of a thin layer of vertically agitated wet granular matter is investigated experimentally. Rotating spirals with three arms, which correspond to the kinks between regions with different colliding phases, are the dominating pattern. This preferred number of arms corresponds to period tripling of the agitated granular layer, unlike predominantly subharmonic Faraday crispations in dry granular matter. The chirality of the spatiotemporal pattern corresponds to the rotation direction of the spirals.

DOI: 10.1103/PhysRevLett.107.028001 PACS numbers: 45.70.Qj, 45.70.Mg

From the formation of galaxies to hurricanes, from the structure of a seashell to the magnetic ordering on the atomic scale [1], spirals are ubiquitous in nature [2]. During the past decades, various spiral forming systems have been extensively investigated, e.g., Rayleigh-Bénard convection [3], the Belousov-Zhabotinsky reaction [4], and cardiac tissue [5]. Moreover, spacecraft observations of Saturn's rings—granular matter consisting of icy particles—reveal that the perturbations arising from the gravitational field of its moons propagate in the form of spiral waves [6], which have been modeled in terms of a hydrodynamical description [7]. Despite this success, a continuum description of both dense and dilute granular systems [8], including wet granular systems [9], is still far from complete.

In this Letter, we present rotating spiral kink waves formed in agitated wet granular layers. We demonstrate that the dominating three armed spiral is a manifestation of the period tripling in the system, and that the spatiotemporal chirality associated with period tripling drives the rotation of spiral arms. In contrast to those in dry granular systems [10], the arms are kinks separating regions colliding with the container at different phases. Understanding this particular spiral forming system could not only provide a step towards a continuum description of dry and wet granular matter, but also broaden our knowledge about the more general spiral forming systems mentioned above.

Figure 1 shows a sketch of the experimental setup. The granular sample is prepared by adding purified water (Laborstar TWF-DI) into glass spheres (SiLiBeads S) with a diameter $d = 0.78$ mm and 10% polydispersity. They were cleaned subsequently with ethanol, acetone and purified water, and dried in an oven before use. The liquid content $W = V_w/V_g$, where V_w is the volume of the water and V_g that of the glass beads, is kept within a few percent. A cylindrical polycarbonate container with an inner radius $R = 8$ cm and a height 1.05 cm is mounted on the electromagnetic shaker (Tira TV50350). The amount of sample (mass m) added corresponds to a height of a few particle diameters. The sinusoidal shaking frequency f and amplitude of the shaker are controlled by the function generator (Agilent FG33220). The nondimensional acceleration $\Gamma = 4\pi^2 f^2 A/g$, with vibration amplitude A and gravitational acceleration g, is obtained by an accelerometer (Dyson 3035B2).

A high speed camera (IDT MotionScope M3) mounted above the container is used to capture the patterns: the LED ring illumination provides the horizontal motion of the patterns, while the surface profile is obtained via the laser profilometry method [11]. The laser sheet illuminates a line on the sample surface with an angle $\theta = 38°$. The camera is triggered by a synchronized multipulse generator to capture images at fixed phases of each vibration cycle.

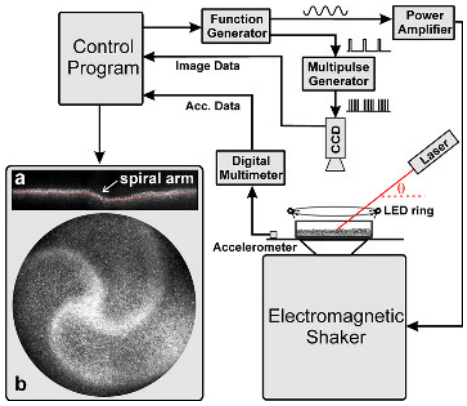

FIG. 1 (color online). The experimental setup with sample images of a spiral pattern. Vertical or horizontal information of the patterns formed is obtained by a high speed CCD camera mounted above the sample illuminated by a laser sheet or a low angle LED ring correspondingly. The camera is triggered by a multipulse generator. Snapshot (a) is captured with the laser sheet illumination. The red half transparent line is a surface profile determined by an image processing procedure. The spiral arm corresponds to a kink between regions with different heights. Snapshot (b) corresponds to the low angle illumination (averaged over three synchronized images to enhance the contrast).

Typical patterns observed are rotating spirals, which coexist with migrating fronts occasionally generated from the side wall or nucleated within the bulk (see Fig. 2). One striking feature arising from the snapshots is that both patterns show a period tripling behavior: similar patterns appear at every third vibration cycle, in contrast to the subharmonic patterns commonly seen in agitated dry granular matter [12,13]. The migrating fronts tend to merge with one of the spiral arms and vanish, because both are of the same origin: they are kinks separating regions of different phase shift within the period-3 vibration, as will be demonstrated below. The rotation period for the spiral shown in the right panel is ≈ 1.8 s, much larger than that for the driving $1/80$ s.

There is a clear threshold for the patterns to emerge, as the step change of the order parameter I_{rms} with Γ in the inset of Fig. 3 indicates. $I_{\mathrm{rms}} = \sqrt{\sum (I(x, y) - \bar{I})^2}$, with $I(x, y)$ the image intensity at the position (x, y) and $\bar{I}$ the spatial average of $I(x, y)$, is chosen as the order parameter. No clear hysteresis could be detected within the error of Γ, as step increasing (Γ_{inc}) or decreasing (Γ_{dec}) the acceleration for various waiting times Δt yields the same threshold, which is determined by the averaged steepest slope of I_{rms}. Within the range of frequencies investigated, the threshold is increasing monotonically with frequency and insensitive to the geometry of the container and the liquid content W: measurements for $f = 80$ Hz with a square shaped container (with an inner side length 10 cm) and with a varying W up to 9.4% yield qualitatively the same spiral patterns and quantitatively the same threshold. The weak dependence on the liquid content, even for the regime where large liquid clusters form, can be attributed to the insensitivity of the rigidity of the wet granular material on W [14], which is important for the kink dynamics because the granular layer will be bent and stretched. Nevertheless, wetting is a necessary condition for the present instability because no patterns could be observed without wetting liquid. Below 55 Hz, visualization of the pattern is prohibited by the particles sticking to the lid.

In the pattern forming regime, the number of rotating spirals increases with Γ. The spirals all show period tripling, and may rotate in the same or opposite directions (see the snapshot in Fig. 3). They are considered to be stable, since no decay could be observed for at least 15 minutes. Even higher Γ finally leads to a homogeneous gaslike state, where the particles occupy the whole space of the container. Decreasing Γ shows the reversed scenario: from a homogeneous gas state to the spiral patterns, until a flat featureless state appears below the threshold. In contrast to the phase diagram investigated before [15], no granular "gas bubbles" could be observed here, the reason for which is a subject of ongoing investigations.

To investigate the spiral dynamics, the surface profiles are measured with laser profilometry. Figure 4 shows the oscillations of an illuminated line close to the core of a rotating spiral arm at different time scales. The long time behavior [Fig. 4(a)] indicates the propagation of the kinks separating regions with different heights H. Observations with combined illuminations indicate that the kinks correspond to the arms of spirals. This explains why the arms look brighter: curved surface of the kink regions reflects more light from the LED ring to the camera. The birth of two counter propagating kinks corresponds to the crossing event of one spiral arm with the illuminated line. Since the spiral core is close to the illuminated line, the constant propagation speed suggests a linear relation between the radial distance to the spiral core r and time t, i.e., an

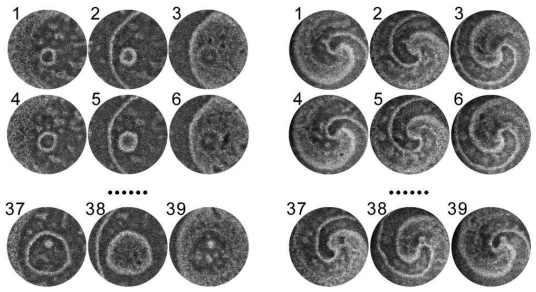

FIG. 2. Snapshots of migrating fronts (left panel) and a rotating spiral (right panel) captured at a fixed phase of continuous vibration cycles (indicated as numbers) showing the period tripling behavior. Parameters: $f = 80$ Hz, $W = 1.6\%$, $m = 96$ g and $\Gamma = 36$ (left), 37 (right).

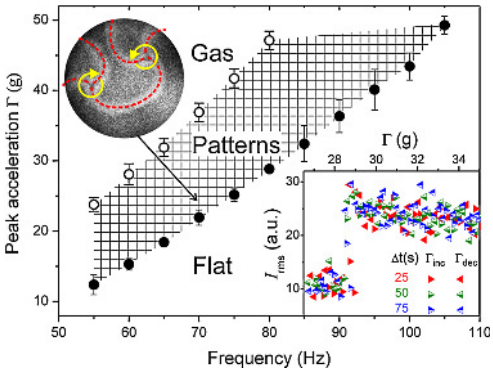

FIG. 3 (color online). Phase diagram for the patterns (shaded with squares) measured by varying Γ while keeping the vibration frequency for $m = 129$ g and $W = 1.6\%$. The region with $\Gamma > 50$ is unexplored. The snapshot (averaged over three synchronized images) shows two spirals rotating in opposite direction captured at $f = 70$ Hz and $\Gamma = 23$. The red dash curves highlight the spiral arms and yellow arrows denote the rotation directions. The inset shows the order parameter I_{rms} vs Γ at $f = 80$ Hz for various time step Δt and both directions of Γ variations.

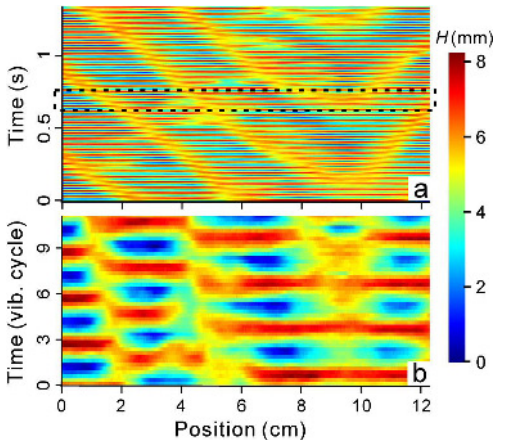

FIG. 4 (color online). Time space plots of the surface profiles obtained with laser profilometry. The long time behavior (a) presents the traveling of the kinks, i.e., spiral arms. The short time behavior (b), corresponding to the region marked with dash line in (a), shows the periodicity of the height fluctuations. Other parameters: $f = 80$ Hz, $\Gamma = 32$, frame rate 320 Hz, $H = 0$ chosen as the lowest surface height.

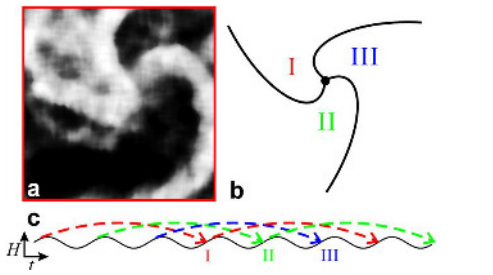

FIG. 5 (color online). (a) The covariance between two subsequent images taken as the collision with the container occurs. The brightness corresponds to the mobility of particles. Sketches (b) and (c) indicate the spatiotemporal chirality of the pattern. The black line in (c) indicates the positions of the vibrating bottom, the dash lines correspond to the center of mass in regions I, II, and III. H denotes the height.

Archimedean spiral, assuming a constant angular velocity. Once the arms are formed, they are resistant to the disturbances along the propagating arms.

At the time scale of vibration cycles, Fig. 4(b) reveals the period tripling behavior of the height fluctuations, which is in accordance with observations from Fig. 2. The fluctuation amplitude being very close to the distance between the surface of the sample at rest and the lid (≈ 7 mm) indicates that the lid plays an important role in developing the spirals. In an open container, no such patterns could be observed.

Figure 5 is meant to illustrate the rotation mechanism of the spiral arms. Figure 5(a) shows the spatially resolved covariance between two subsequent images, which is calculated by $\sum_{\Delta x,\Delta y=0}^{d} I_t(x+\Delta x, y+\Delta y) I_{t+1}(x+\Delta x, y+\Delta y)$, where t denotes time and d the particle size in pixels. The time step (2.5 ms) is short enough for the mobility of particles to be captured (bright colors corresponding to smaller covariance, i.e., higher mobility). As interpreted in Fig. 5(b) and 5(c), the higher mobility of particles (granular temperature) in region I arises from the fact that those particles have just undergone a collision with the container bottom. Region II and III will undergo this event in the consequent two vibration cycles. The bright line in Fig. 5(a) separating region II and III is due to the rotation of the spiral arm.

The qualitative idea to explain the rotation of the spirals is the assumption that regions with higher granular temperature will expand into "cold" regions. Thus we expect a maximum velocity for the spiral arm separating region I and II because region II is the "coldest" due to the longest time interval having elapsed after the last collision with the bottom. Therefore the predominating motion of the spiral arms will be the rotation towards a region that is going to collide with the container in the next vibration cycle. Reversing the time sequence among region I, II, and III—corresponding to spatiotemporal pattern with different chirality—would reverse the rotation direction of the spiral. Thus we expect rotating spirals for periodic states with multiples of the vibration period which are larger than 2. The migration fronts shown in Fig. 2 are explained by the same mechanism: the front moves towards the region lagging behind with a phase shift of 120°, corresponding to a time lapse of one vibration cycle.

To get a clue why period tripling is so dominant in our apparatus, we use a single particle bouncing model to estimate the periodicity, which is the period scaled by $1/f$. It treats the sample as one wet particle colliding inelastically with the container. In addition to the model used to describe agitated dry granular layers [13], it considers the capillary force acting on the granular layer [9] and collisions with the lid of the container. Initially the particle moves together with the container bottom until the vibrating acceleration is large enough to overcome the capillary and gravitational forces acting on the particle. After the first detachment, the particle takes a parabolic flight until the next collision occurs. After that, it may detach immediately or stay with the container, depending on the colliding phase. This process will run iteratively until the particle rests on the container bottom again, which ends the cycle and determines the periodicity. Experimentally the periodicity is determined by fitting a Gaussian profile around the peak of the surface height fluctuations in Fourier space.

Figure 6 indicates that the simplified model captures the dependence of periodicity on Γ and predicts the threshold for time dependent patterns. Periodic oscillations appear

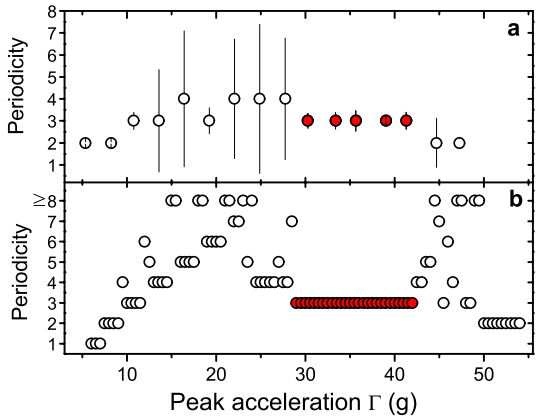

FIG. 6 (color online). Periodicity as a function of driving acceleration for $f = 80$ Hz, obtained experimentally from the surface height fluctuations (a), and estimated by a single particle bouncing model (b). Errors in (a) correspond to the variance of the Gaussian profiles fitted to the spectrum of the height fluctuations. Red solid symbols highlight period 3 regimes above the threshold. Other parameters are the same as in Fig. 3.

above a certain threshold, where the period is an integer multiple of the driving period. Increasing Γ leads to larger periods because the free flying time increases as long as the particles do not touch the lid of the container. Once they touch the lid, the periodicity starts to decay due to the additional impact from the lid. Different from the model, experimental results show high uncertainties of periodicity below $\Gamma \approx 30$, which arise from the intermittent fluctuations with small amplitude. For $\Gamma > 30$, both the experiment and the model reveal a wide range with period tripling, which corresponds to the time dependent patterns observed in the experiment. In this regime, the periodicity is robust against small surface fluctuations. Note that the wide period tripling region appears after impact with the lid, which can thus be considered as a technical trick to expand the existing range of spirals.

In conclusion, three armed rotating spirals are found to be the dominant pattern in agitated wet granular matter. The preferred period tripling could be understood by a simplified model considering complete inelastic collisions between the granular layer and the container. The spatiotemporal symmetry breaking connected with the period tripling explains the rotation of the spiral arms. A more detailed model will be needed in order to calculate the exact curvature of the spiral arms. In fact, this pattern could provide a convenient test of more elaborate theories for the dense flow of wet granular matter.

The authors thank K. Ötter for technical support, and F. Gollwitzer for help in building the setup. Inspiring discussions with I. Aranson, E. Meron, F. Rietz, K. Röller, C. Krülle, and E. Martens are gratefully acknowledged. This work is partly supported by Forschergruppe 608 "Nichtlineare Dynamik komplexer Kontinua".

*kai.huang@uni-bayreuth.de

[1] P. Ferriani *et al.*, Phys. Rev. Lett. **101**, 027201 (2008).
[2] See, e.g., http://spiralzoom.com.
[3] S. W. Morris *et al.*, Phys. Rev. Lett. **71**, 2026 (1993); B. B. Plapp *et al.*, *ibid.* **81**, 5334 (1998).
[4] A. T. Winfree, Science **175**, 634 (1972); J. J. Tyson *et al.*, Physica (Amsterdam) **32D**, 327 (1988); S. Oliver *et al.*, Nature (London) **366**, 322 (1993); V. K. Vanag *et al.*, Science **294**, 835 (2001).
[5] J. Davidenko *et al.*, Nature (London) **355**, 349 (1992); E. M. Cherry *et al.*, New J. Phys. **10**, 125016 (2008).
[6] P. A. Rosen and J. J. Lissauer, Science **241**, 690 (1988); http://photojournal.jpl.nasa.gov/catalog/PIA12545.
[7] F. Spahn and J. Schmidt, GAMM-Mitt. **29**, 115 (2006).
[8] I. Goldhirsch, Annu. Rev. Fluid Mech. **35**, 267 (2003); I. S. Aranson and L. S. Tsimring, Rev. Mod. Phys. **78**, 641 (2006); P. Jop *et al.*, Nature (London) **441**, 727 (2006); Y. Jiang and M. Liu, Phys. Rev. Lett. **99**, 105501 (2007).
[9] L. Bocquet *et al.*, C.R. Physique **3**, 207 (2002); S. Herminghaus, Adv. Phys. **54**, 221 (2005).
[10] J. R. de Bruyn, B. C. Lewis, M. D. Shattuck, and H. L. Swinney, Phys. Rev. E **63**, 041305 (2001).
[11] J. Efsen *et al.*, *Handbook of Non-Invasive Methods and The Skin* (CRC Press, Inc., Boca Raton, 1995), Chap. 8, p. 97.
[12] M. Faraday, Philos. Trans. R. Soc. London **121**, 299 (1831).
[13] F. Melo, P. B. Umbanhowar, and H. L. Swinney, Phys. Rev. Lett. **75**, 3838 (1995).
[14] M. Scheel *et al.*, Nature Mater. **7**, 189 (2008).
[15] A. Fingerle *et al.*, New J. Phys. **10**, 053020 (2008); K. Huang *et al.*, Eur. Phys. J. Special Topics **179**, 25 (2009).

ZAMM · Z. Angew. Math. Mech. **90**, No. 12, 911 – 919 (2010) / **DOI** 10.1002/zamm.201000110

Snooping in the sand

[Plenary lecture presented at the 81st Annual GAMM Conference, Karlsruhe, 26 March 2010]

Kai Huang[1,*], **Christof Krülle**[2,**], **and Ingo Rehberg**[1,***]

[1] Experimentalphysik V, Universität Bayreuth, 95440 Bayreuth, Germany
[2] Maschinenbau und Mechatronik, Hochschule Karlsruhe – Technik und Wirtschaft, 76133 Karlsruhe, Germany

Received 2 June 2010, revised and accepted 16 September 2010
Published online 16 November 2010

Key words Granular matter, phase transition, transport, segregation, pattern formation.

Because of the energy dissipation through friction and inelastic collisions between particles, agitated granular matter is generally speaking in a state far from thermal equilibrium. It can be considered as being a complex state of matter, which combines properties of the fluid and of the solid state. In order to provide data for modeling this peculiar state of matter, we investigate the dynamic behavior of granular matter under a two-dimensional vibration in two different experimental setups.

1 Introduction

Sand is a specific example for the wide class of "granular matter", which can be defined as an ensemble of solid particles interacting dissipatively when in contact. Almost all of the solid materials surrounding us in daily life, in nature, and in industrial processing of bulk solids fall into this class, and thus granular matter has attracted interest from different scientific communities over centuries.

Describing both the static and the dynamic properties of such an ensemble in terms of mathematical modeling is a great task. Although the kinetic theory has been successfully applied in modeling granular gases [1–3], the ultimate goal to model both dense and dilute granular systems is still far from reached. This is partly due to the vagueness of the definition of the term "granular matter" and its inherent complexity: no grain is like the other. A certain class of laboratory measurements have been specifically designed to facilitate such a modeling, however, and those reported here fall into this class.

Because of the dissipative interaction of granular matter, energy injection is needed in order to fluidize the material. Among the many different possibilities we concentrate here on mechanical two-dimensional vibrations, and summarize the results obtained in two specific machines. In the first apparatus – a swirling table – both vibration directions are perpendicular to the direction of gravity [4, 5], while in the second apparatus – a vibratory conveyor – one direction is parallel, and one perpendicular with respect to the plumb line [6].

In the rest part of this paper, phase transitions are discussed in Sect. 2 to provide a general framework for agitated granular matter. Within this framework, three interesting features of fluidized granular matter, namely transport, segregation and pattern formation, are introduced in Sects. 3, 4, 5 correspondingly to give further insights into this material.

2 Phase transition

2.1 Solid-fluid transition

The phase solid-fluid transition for granular matter means the transition from a solidlike phase to a fluidlike phase. In the solidlike phase, the particles rarely move; while in the fluidlike phase, they move continuously with respect to their neighbors. Although this transition is fairly obvious by visual inspection, a more objective order parameter is required in order to pinpoint this transition. As one fundamental problem distinguishing static and dynamical behaviors of granular matter, this transition has been investigated from different perspectives over decades (see for example [7, 8] and references therein). As an example, Ristow [9] used various order parameters, such as pixel change, granular temperature and pair

* E-mail: kai.huang@uni-bayreuth.de
** E-mail: christof.kruelle@hs-karlsruhe.de
*** Corresponding author E-mail: ingo.rehberg@uni-bayreuth.de, Phone: +49 921 553 344, Fax: +00 921 553 647

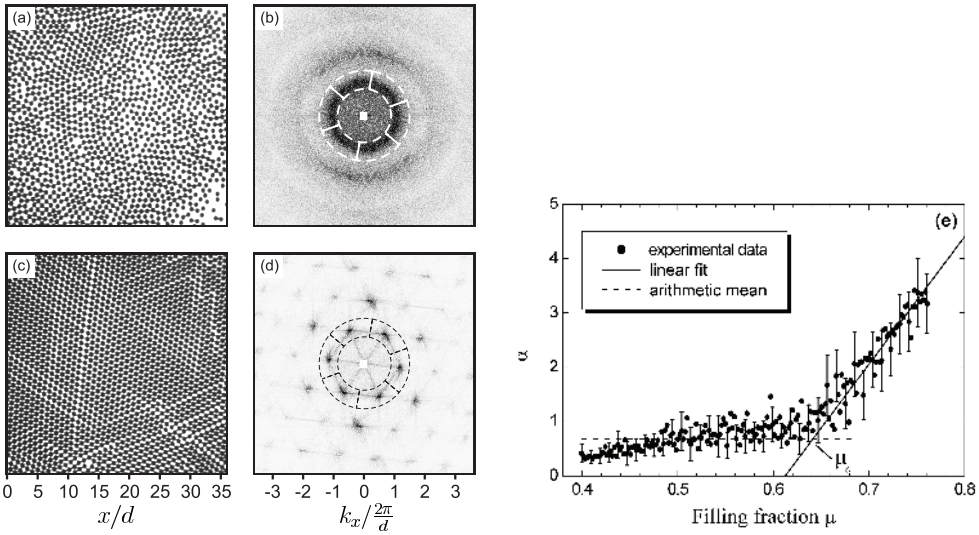

Fig. 1 (a) Image of a monolayer of 2400 small spheres (filling fraction $\mu = 0.46$) rolling on a table shaken with an amplitude $A = 1.91$ cm and a frequency $f = 1.67$ Hz. (b) Plot of the corresponding 2D power spectrum (high intensity appearing black). (c) Image of a monolayer of 4000 small spheres ($\mu = 0.76$) under the same excitation, and (d) its 2D power spectrum. The snapshots are taken in a square of size 15 cm at the center of the cell. The intensity change of the overlays in the 2D power spectra indicates the transition from a fluidlike to a solidlike phase. (e) Evolution of the order parameter α (normalized intensity variation in azimuth direction) with the filling fraction indicates that the transition is a critical phenomenon. After Aumaître et al., 2003 [4].

distribution function, to determine the transition quantitatively. The variation of all those order parameters with the strength of driving reveals that this transition is a critical phenomenon. Moreover, it has also been found that the critical point scales with the driving as $A_0 f^2$, where A_0 is the driving amplitude and f is the frequency. This is reminiscent to the case of vertical vibrations [10–12], where fluidization starts as the normalized peak vibration acceleration $\Gamma = 4\pi^2 f^2 A/g$ is of the order of 1.

By combining two horizontal vibrations that are perpendicular with each other, one could generate a swirling motion to drive the granular matter. With this type of driving, all the points of the swirling container perform the same type of orbit motion and the energy injection through collisions between particles and the container wall is the same at different phases. Utilizing the swirling apparatus, Scherer et al. investigated the dependance of granular dynamics on the number of particles [13]. As the number density increases, particles become less mobile due to the more frequent collisions. As the number density goes beyond a certain value, a solidlike cluster will form (as shown in Fig. 1(c) [4]). This transition can be reproduced by molecular dynamics simulations based on a nonlinear repulsive force model and the solidlike cluster dynamics can be captured by a 'Pancake' model [13]. In a later study [4], this transition was also characterized by the Fourier space representative of the snapshots. As shown in Fig. 1(b)(d) (see [4]), crystallization of the particles is clearly indicated by intensity peaks in the k space. Choosing the peak value of the normalized intensity variation α as an order parameter, a critical solid-fluid transition point could also be extrapolated. Moreover, this investigation indicated that this transition acts as a precondition for segregation.

2.2 Rotation-reptation transition

Associated with the solid-fluid transition, the dynamical behavior of granular matter under swirling motion may also change dramatically. Scherer et al. [14] found that the sense of rotation of a swirling granular cluster will change with the packing density. At lower packing densities, the cluster rotates in the same sense as the swirling container (rotation mode). At higher packing densities, the rotation changes its direction and the diffusivity of particles within the cluster is dramatically reduced (reptation mode).

Recently, Feltrup et al. [5] reconsidered the rotation of swirling granular clusters under a broken rotational symmetry of the container. This study reveals that, except for the rotation and reptation motion, granular particles might rotate in a 'snake mode' at relatively low packing density. As shown in Fig. 2, particles tend to form a chain like cluster that travels

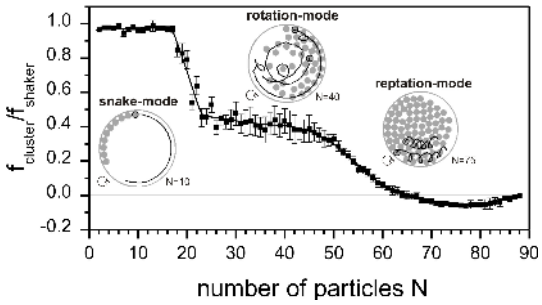

Fig. 2 Depending on the filling fraction, there exist three different modes of two dimensional granular matter under swirling motion: a snake mode, a rotation mode, and a reptation mode. Solid lines correspond to tracer particle trajectories. Particles surrounded by circles correspond to the ends of the tracks. The solid line in the plot serves as guide to the eyes. After Feltrup et al., 2010 [5].

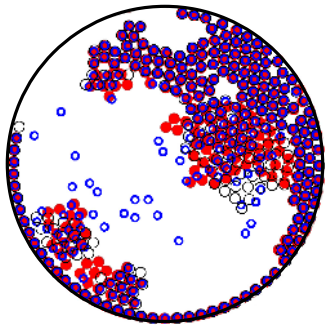

Fig. 3 (online colour at: www.zamm-journal.org) Stack plot of swirling wet particles before (red particles, lower stack), during (thick blue circles) and after (thin black circles, highest stack) an intermittently occurring rearrangement process, in which sublimation plays a crucial role. Particle diameter $d = 4\,\text{mm}$, liquid content $W = 1\%$, swirling frequency $f = 1.67\,\text{Hz}$, and swirling amplitude $A = 1.59\,\text{cm}$.

along the container wall with the same frequency and direction as the driving. When the particle number is higher than a certain value, the beads start to pile up in the radial direction, entering a so-called rotation mode. The cluster still rotates counterclockwise but with a lower frequency than the driving. As the particle trajectories indicate, the motion of particles within the cluster is more random. Further increase of the particle number slows down this rotation, until, at a critical particle number N_c, the rotation stops. Beyond this particle number, the cluster starts to rotate in the opposite direction, performing a motion called 'reptation'. A detailed description of the second and third motion can be found in [14].

Molecular dynamics simulations based on the Hertzian contact model [15] have been used to study the rotation-reptation transition [14]. It suggests that the change of dynamical structure of the cluster, which depends on the packing density, might play a role in the rotation-reptation transition. Simulation results show that at low packing density, the diffusion coefficient stays constant at a high value. As the packing density increases to the value that the granular cluster reptates, it starts to decrease linearly with the number of filled particles. The reduced mobility of particles indicates that the rotation-reptation transition is related to the transition from a fluidlike phase to a solidlike phase.

In order to understand the essence of rotation-reptation transition, the dimensionality of the apparatus was reduced to a quasi-one-dimensional annulus [16]. The swirling annulus experiment indicated that the physics of one dimensional collisions is sufficient to explain the effect, namely by proposing a 'free path restriction' mechanism. At low packing densities, single trajectories of the spheres are not disturbed by frequent collisions with neighbors, so that the travel distance in the driving direction is greater than that in the other direction. This results in a continuous forward drift with some fluctuations. If the particle number is increased, the variance of the drift applied to the particles at different locations within the cluster becomes more significant. Therefore collisions between adjacent particles are more frequent and more energy is dissipated while swirling. The rotation speed of the cluster reduces until, at a certain point, the forward motion is completely restricted and reptation motion dominates. The competition between forward and backward movements also leads to the fluctuation of the single particle trajectories and longitudinal density waves.

The rotation-reptation transition is a robust phenomenon. This was demonstrated by breaking the symmetry of the swirling table with some fixed obstacles. In this situation, the rotation-reptation transition still exists, however it occurs at a lower packing density [5]. As the obstacle is fixed close to the border of the container, the rotation of the cluster gets more inhibited and the rotation-reptation transition tends to occur at lower number densities. It's trivial to see that as the distance between the obstacle and the container wall doesn't allow one particle to pass through, the 'snake mode' is completely suppressed. Surprisingly, it was found that placing the obstacle at the center of the container can actually accelerate the rotation frequency over a large range of number densities. This feature has been found to be related to the driving mechanism of the cluster. Under swirling motion, the cluster collides regularly with the container wall and obtains energy there. Thus one can speculate that the number of particles at the layer closest to the container wall determines the rotation speed of the cluster. From experimental data, Feltrup et al. (2009) compared the cluster rotation frequency and the number fraction of particles at the container wall and found an interesting correlation. Thus the speed-up of the rotation with an obstacle can be understood, because the obstacle acts as an additional motor for the cluster rotation.

2.3 Sublimation of swirling wet granular matter

In nature, the flow of granular matter, such as propagation of sand dunes, landslides etc., is always influenced by humidity to some extent. In chemical or pharmaceutical industry it is of tremendous importance to the efficiency of the production line to control or prevent agglomeration of granular materials due to humidity. This topic has drawn special attention from scientists over decades [17–19]. More recently, with the advance of our knowledge on wetting and de-wetting, there is a growing interest in understanding the dynamical behavior of wet granular matter in terms of particle-particle attraction arising from the formation of capillary bridges [20–22]. Depending on the amount of wetting liquid, the wetting of particles can be characterized into three different regimes. In the first regime, the film thickness of the wetting liquid is within the roughness of particles: only small capillary bridges forming between asperities of neighboring particles dominate the cohesion. In the second regime, the covering liquid film is thick enough to form one capillary bridge for each contact and the curvature of the particle instead of the asperities dominates the capillary force. In the third regime, the amount of wetting liquid is sufficient to connect various capillary bridges into liquid clusters. The cohesive force in wet granular matter is much stronger than the gravity of the particles with an averaged size no more than few millimeters, so that the angle of repose doesn't exist for a pile of wet sand [23]. Besides applications in industry, wet granular matter may also act as a model system to study systems far from equilibrium, because of the strong energy dissipation due to the rupture of liquid bridges and inelastic collisions between particles [24].

Due to cohesion, the dynamics of wet granular matter under swirling motion is dramatically different from that of dry particles described above. Instead of following the orbit motion of the container as dry particles, wet spheres tend to form rigid clusters that stick to the border of the container (spheres painted red in Fig. 3). This rigid cluster will rearrange itself via intermittent sublimation processes towards a final state (black spheres in Fig. 3). The mechanism that triggers the failure of the rigid cluster and the phase transition from a solidlike to a gaslike state is a focus of current investigations.

2.4 Sublimation driven by vertical vibrations

Coexistence of different phases is known to accompany the fluidization of granular material. For example, submitting a two-dimensional vertical packing of beads to vertical or horizontal vibrations fluidizes the upper layers, while the lower lying material still maintains a crystalline structure [9, 25–27].

Now we focus on granular phase transitions driven by the circularly vibratory conveyor [6]. Through the construction of a ring-shaped vibrating channel, the long-time dynamics of a closed, mass conserving system devoid of disturbances from the influx and outpouring of grains can be studied. The main piece of the vibratory conveyor is a torus-shaped vibrating channel of light-weight construction (carbon fiber strengthened epoxy) with an average diameter of 450 mm and a channel width of 50 mm. Firmly connected to the channel are four symmetrically arranged rotating vibrators. The complete oscillation system, the channel and drivers, are suspended with elastic bands in a highly adjustable frame.

The driving of the vibratory conveyor is done by an electric motor with integrated frequency inverter. The above is connected via compensation clutches to the vibrators. The excitation results from the simultaneous counter rotation of unbalanced masses, which are coupled with a gear (see the inset of Fig. 5). If two synchronously acting linear vibrators are oriented perpendicularly, then - through appropriate choice of the phase shift between the two - the shape of the vibration can be chosen and numerous Lissajous figures (linear, circular, elliptical) can be produced. The phase can be adjusted through the choice of angle at which the unbalanced masses are mounted (for example 90 degrees for circular vibration). One great advantage of the annular vibratory conveyor is the possibility to make the solid phase rotate to demonstrate that the coexistence of solid and fluid regions is not caused by small potential inhomogeneities in the forcing, particle container interactions or a tilt of the apparatus.

For the experiments [6] a densely packed monolayer of 21 500 spherical basalt glass beads (density $\rho = 3.0\,\mathrm{g/cm^3}$) with diameter $d = 1.18 \pm 0.03\,\mathrm{mm}$ was prepared on the channel floor. The granular system was observed from the top via a conical mirror placed in the center of the ring, similar to [28]. Thus a side view of the whole channel was captured with a single high-speed digital camera 2 (resolution: 1280×1024 pixels at rates up to 500 images per second). Digital image processing delivers 360° panoramic side views of the granular profile in the channel as presented in Fig. 4.

To provide deeper insights into the mechanism, experiments were modeled using a three-dimensional molecular dynamics simulation applying an event-driven algorithm described in [29]. The entire channel moved both vertically and horizontally with the same values of frequency and shaker amplitude as in the experiment. The parameters characterizing changes in relative surface velocity for both particle-particle and particle-wall collisions were the coefficient of sliding friction $\mu = 0.5$ and the maximum rotational coefficient of restitution $\beta_0 = 0.35$. These values were chosen because they successfully reproduced surface wave patterns observed in vertically vibrated granular media [29]. To match the minimum layer depth required for surface wave formation in experiment the coefficient of normal restitution for interactions between particles, e, was set to 0.97. The coefficient of restitution with the walls was the only fit parameter and a value of 0.93 was found to quantitatively reproduce the experimental results. To prevent inelastic collapse the coefficient of

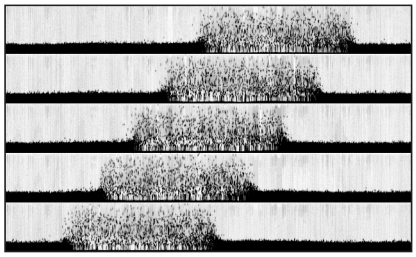

Fig. 4 Snapshots through the inner side wall of a ring shaped channel driven by the vibratory conveyor covering 360 degrees during the downwards motion of the container. Time increases from top to bottom by 1.72 s (20 cycles) between consecutive snapshots. For clarity all images are stretched in the vertical direction by a factor of 4. ($f = 11.6$ Hz, $\Gamma = 1.23$.) After Götzendorfer et al., 2005 [6].

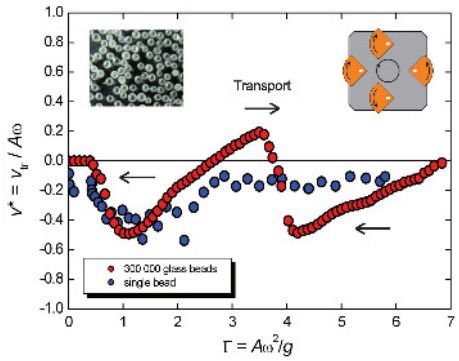

Fig. 5 (online colour at: www.zamm-journal.org) Normalized transport velocity v^* of a granular flow ($\approx$ 300 000 glass beads with 1 mm diameter, see inset) on the vibratory conveyor with circular vibration, compared with the mean velocity of one single glass bead.

normal restitution for both types of collisions approaches unity as the normal velocity v_n approaches zero according to $\max(e, 1-(1-e)(v_\mathrm{n}/\sqrt{gd})^{3/4})$ [29].

3 Transport

The combined action of vertical and horizontal vibration of the support has been utilized already for a long time for the controlled transport of bulk cargoes in a whole variety of industrial processes [30–32]. So-called "vibratory conveyors" are well established in routine industrial production for controlled transport of bulk solids. The transported goods can thereby be moved through three different mechanisms in the desired direction: (a) sliding of the particles by asymmetric horizontal vibration ("gliding principle"), (b) ballistic trajectories of the particles caused by inclined linear oscillation ("throw principle"), and (c) horizontal transport through vertical vibration of a support with an asymmetric saw tooth profile of the base ("ratchet principle").

For the transport experiments the channel was loaded with 450 g of carefully sieved glass beads with mean diameter 1.1 mm. The layer thickness of the grains was about five particle diameters. The average transport speed was determined from the time of circulation of a colored tracer particle that the bulk carried along. This occurs automatically through a PC supported image processing system that detects the signal changes from the passing of the tracer through a row of the image and records the associated transit time.

Surprisingly, the mean transport direction depends, for circular agitation, on the amplitude A and frequency f in a characteristic manner (see Fig. 5). Below a critical value $\Gamma = 0.44$, the transport is impeded through static friction. Above this threshold, the bulk velocity initially increases before reaching its first maximum at $\Gamma = 1.1$, with half the circulation speed of the circular motion. Increasing the excitation further leads to a deceleration of the granular flow, actually reversing its direction of motion in the range $2.70 < \Gamma < 4.01$. This alternating behavior repeats itself at still higher Γ.

For industrial applications, this observed reversal effect is relevant as the direction of a granular flow can be selected through the frequency of the excitation alone. One can employ such two-way conveyors for example in larger cascading transport systems as control elements to convey the material to different processes as needed.

4 Segregation

Particles of various size or density might segregate while moving [11]. The so called Brazil nut effect is one example: big brazils are always seen on top of other nuts after shaking a mixture [33]. Granular flow on an inclined surface, reminiscent to the case of landslide or avalanches, will also lead to segregation and formation of strip patterns [34]. Utilizing the Brazil-nut effect, avalanche balloons are developed in order to reduce the possibility for skiers to be buried by avalanches (see for example [35]). Not only in nature and our daily lives, segregation of particles is also of great importance to the processing of powders in industries [36]. In the past two decades, there has been an upsurging number of laboratory experiments to unveil the mechanism of the segregation driven by vertical vibrations or rotation [37–43]. Counterintuitively, it has been

found that large light particles might sink under vertical vibrations while in the meanwhile equally sized heavy particle rises [44–46]. By testing a number of different combinations of particle size and density, Breu et al. studied the dependance of the transition from Brazil-nut effect to its reverse on the particle size and density ratio [45]. The switch between different effects was found to be also sensitive to the external excitations, which suggests the possibility to control the demixing direction by tuning the driving parameters.

Here we focus on the segregation of particles agitated horizontally, where gravity driven flow doesn't play an important role in the segregation process. Aumaître et al. investigated the segregation of a binary mixture and monolayer of small spheres and larger disks driven by swirling motion [47]. After a certain time interval, the initially hexagonally located large disks are found to collapse into clusters that tend to stay at the center of container. This phenomenon can be understood by the idea of *excluded volume depletion* as in colloid systems [48]: As larger disks organize themselves into clusters, the excluded volume for small spheres around larger disks is reduced, which means more possible configuration states, or an entropy gain of the system. From the decay of nearest-neighbor distance with time, a mean collapse velocity could be obtained. The mean collapse velocity of the disks is found to increase exponentially with the driving frequency. By fixing large disks at their initial configuration, they measured the pressure density distribution within the container. It was shown that the granular gas pressure, defined as $P(\mathbf{r}) = n(\mathbf{r})mv_{rms}^2(\mathbf{r})/2$, where $n(\mathbf{r})$ denotes the local particle density, is smaller between the disks than outside the array. The fact that small spheres don't follow the pressure gradient and create higher particle density within the array indicates that there should exist a net force acting on the larger cylinders pushing them to the center of the container. Based on kinetic gas theory, they derived an effective collision frequency which gives a characteristic time scale for the collapsing process. Using this time scale, the growing of the average number of contacts at various driving frequencies collapses on a single curve.

In a following investigation [4], Aumaître et al. studied the demixing of bidisperse spheres under swirling motion. For various driving amplitude and frequency, a critical filling fraction above which segregation occurs was observed. Moreover, the threshold for segregation was found to be associated with the fluid-solid like phase transition of the spheres. Using the normalized intensity of the power spectrum of the snapshots of small spheres as order parameter (similar to the case shown in Fig. 1), they measured the fluidlike to solidlike phase transition and found that the critical filling fraction for phase transition is slightly lower than that for segregation, leading to the conclusion that granular phase transition is a precondition for segregation. During the solidification process, small spheres try to lock larger spheres in the solidlike phase so as to minimize the energy input, because larger spheres will pick up more energy while colliding with the container wall. It was concluded that the main mechanism for size segregation is the compression force exerted by the lateral boundary and mediated by the developing lattice of the smaller spheres.

Within the concept for depletion force, the segregation of bidisperse particles could be explained. Turning to the case of one intruder particle, Schnautz et al. studied the Brazil-nut effect and its reverse in a swirled setup [49]. The intruder was observed to migrate either to the center or to the border of the container, provided that a critical filling fraction was reached (as shown in Fig. 6). By quantitative characterization of the temporal evolution of the intruder position, they found that heavier particles tend to be pushed to the center while lighter ones move to the opposite direction. The critical ratio determining the Brazil-nut effect or its reverse measured by experiments was found also in numerical simulations. Based on the comparison between experiments and theory, it was concluded that neither gravity, nor interstitial air, nor surface properties of the spheres are relevant for the migration process. The key to understand the Brazil-nut effect in this horizontal driven system is the density gradient along the radial direction (high density in the center and low density near the boundary).

5 Pattern formation

Pattern formation of vibrofluidized granular matter has been a topic of interest since the 18th century [50, 51] and has intrigued a growing interest in the past decades (see for example [11, 29, 52–54]). Some of the patterns are reminiscent to those observed in normal Newtonian fluid, while others, such as the two dimensional localized excitations (so called 'oscillons') [53], are dramatically different.

Driven by the circularly vibratory conveyor, localized waves have been observed in an annular channel within a certain range of granular layer thickness [55]. The panoramic view of the wave patterns delivered by a conic shaped mirror (as shown in Fig. 7) reveals the subharmonic feature of the wave packets. Moreover, depending on the height of the granular layer, the wave packet may travel along the channel with different direction and velocity. A one dimensional Navier-Stokes like model was used to capture the dependance of the length and traveling velocity of the wave packets with the layer thickness.

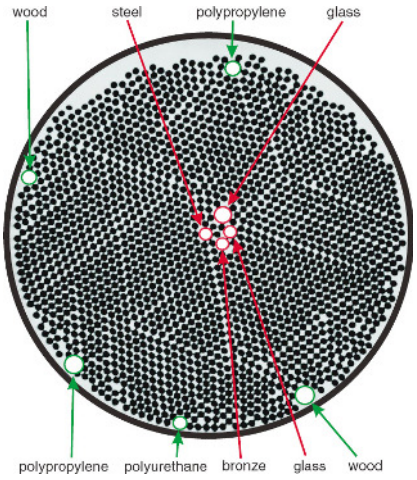

Fig. 6 (online colour at: www.zamm-journal.org) Horizontal Brazil-nut effect and its reverse. Snapshot of 1600 glass spheres (diameter $d = 6$ mm, filling fraction $\mu = 0.68$) in a swirling dish of diameter $D = 29$ cm. After several minutes of horizontal swirling agitation, nine selected intruder particles made of various materials with different sizes are driven either to the center of the container or to its boundary. Shaker amplitude $A = 1.91$ cm and frequency $f = 1.67$ Hz. After Schnautz et al., 2005 [49].

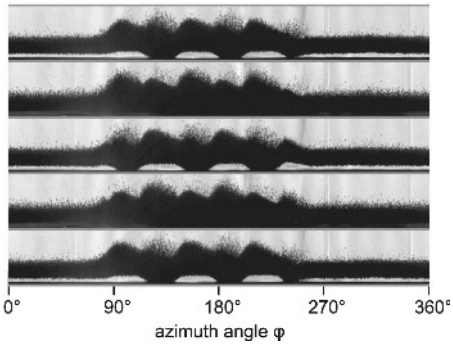

Fig. 7 Localized subharmonic pattern in a circularly vibrated granular bed. Panoramic snapshots through the inner sidewall of the channel. Time increases from top to bottom in steps of half a forcing period. For clarity, the images are stretched vertically by a factor of 3.5. Layer of particles $H_0 = 12$. After Götzendorfer et al., 2006 [55].

6 Summary

To summarize, we reported on recent advances in understanding the dynamics of granular matter by focusing on two special experimental setups: a horizontal swirling table and a circularly vibrating conveyor. It has been demonstrated that transitions among solidlike, fluidlike, and gaslike states of granular matter are critical phenomena. Furthermore, these transitions are suggested to be closely related to many interesting features of granular matter such as rotation-reptation transition of granular cluster, change of transport direction, density or size segregation, localized pattern formation, and so on, which are often of great importance in various industrial processes. Although the origin of granular phase transitions is still a mystery and a complete modeling of granular matter is far from complete, phase transitions can be treated as the clue towards understanding other interesting and often counterintuitive dynamics of granular matter.

References

[1] I. Goldhirsch, Rapid granular flows, Annu. Rev. Fluid Mech. **35**, 267 (2003).
[2] J. T. Jenkins and S. B. Savage, A theory for the rapid flow of identical, smooth, nearly elastic, spherical particles, J. Fluid Mech. **130**, 187 (1983).
[3] T. Pöschel and N. Brilliantov, Granular Gas Dynamics (Springer, Berline, Heidelberg, New York, 2003).
[4] S. Aumaître, T. Schnautz, C. A. Kruelle, and I. Rehberg, Granular phase transition as a precondition for segregation, Phys. Rev. Lett. **90**(11), 114302 (2003).
[5] A. Feltrup, K. Huang, C. A. Kruelle, and I. Rehberg, The rotation-reptation transition under broken rotational symmetry, Eur. Phys. J., Special Topics **179**, 19 (2009).
[6] A. Götzendorfer, J. Kreft, C. A. Kruelle, and I. Rehberg, Sublimation of a vibrated granular monolayer: Coexistence of gas and solid, Phys. Rev. Lett. **95**(13), 135704 (2005).
[7] S. Luding, Towards dense, realistic granular media in 2d, Nonlinearity **22**(12), R101 (2009).
[8] Z. Zhang, N. Xu, D. T. N. Chen, P. Yunker, A. M. Alsayed, K. B. Aptowicz, P. Habdas, A. J. Liu, S. R. Nagel, and A. G. Yodh, Thermal vestige of the zero-temperature jamming transition, Nature **459**, 230 (2009).
[9] G. H. Ristow, G. Straßburger, and I. Rehberg, Phase diagram and scaling of granular materials under horizontal vibrations, Phys. Rev. Lett. **79**(5), 833–836 (1997).

[10] J. Duran, Sands, Powders and Grains (An Introduction to the Physics of Granular Materials), 1st edition (Springer-Verlag, New York, 2000).
[11] H. M. Jaeger, S. R. Nagel, and R. P. Behringer, Granular solids, liquids, and gases, Rev. Mod. Phys. **68**(4), 1259–1273 (1996).
[12] K. Huang, K. Roeller, and S. Herminghaus, Universal and non-universal aspects of wet granular matter under vertical vibrations, Eur. Phys. J., Special Topics **179**, 25 (2009).
[13] M. A. Scherer, K. Kötter, M. Markus, E. Goles, and I. Rehberg, Swirling granular solidlike clusters, Phys. Rev. E **61**(4), 4069–4077 (2000).
[14] M. A. Scherer, V. Buchholtz, T. Pöschel, and I. Rehberg, Swirling granular matter: From rotation to reptation, Phys. Rev. E **54**(5), R4560–R4563 (1996).
[15] K. L. Johnson, Contact Mechanics (Cambridge University Press, Cambridge, 1985).
[16] M. A. Scherer, T. Mahr, A. Engel, and I. Rehberg, Granular dynamics in a swirled annulus, Phys. Rev. E **58**(5), 6061–6072 (1998).
[17] H. Rumpf, Agglomeration (AIME, Interscience, New York, 1962).
[18] W. B. Pietsch, Tensile strength of granular materials, Nature **217**, 736 (1968).
[19] S. M. Iveson, J. D. Litster, K. Hapgood, and B. J. Ennis, Nucleation, growth and breakage phenomena in agitated wet granulation processes: a review, Powder Technol. **117**, 3 (2001).
[20] S. Herminghaus, Dynamics of wet granular matter, Adv. Phys. **54**, 221–261 (2005).
[21] S. Nowak, A. Samadani, and A. Kudrolli, Maximum angle of stability of a wet granular pile, Nature Physics **1**, 50–52 (2005).
[22] M. Scheel, R. Seemann, M. Brinkmann, M. Di Michiel, A. Sheppard, B. Breidenbach, and S. Herminghaus, Morphological clues to wet granular pile stability, Nature Materials **7**(3), 189–193 (2008).
[23] D. J. Hornbaker, R. Albert, I. Albert, A. L. Barabasi, and P. Schiffer, What keeps sandcastles standing?, Nature **387**, 765 (1997).
[24] A. Fingerle, K. Roeller, K. Huang, and S. Herminghaus, Phase transitions far from equilibrium in wet granular matter, New J. Phys. **10**(5), 053020 (2008).
[25] E. Clément and J. Rajchenbach, Fluidization of a bidimensional powder, Europhys. Lett. **16**, 133 (1991).
[26] J. Gallas, H. Herrmann, and S. Sokołowski, Molecular-dynamics simulation of powder fluidization in 2 dimensions, Physica A **189**, 437 (1992).
[27] A. Götzendorfer, C. H. Tai, C. A. Kruelle, I. Rehberg, and S. S. Hsiau, Fluidization of a vertically vibrated two-dimensional hard sphere packing: A granular meltdown, Phys. Rev. E **74**(1), 011304 (2006).
[28] E. van Doorn and R. Behringer, Wavy Instability in Shaken Sand, in: Powders & Grains, edited by R. Behringer and J. Jenkins (Balkema, Rotterdam, 1997), p. 397.
[29] C. Bizon, M. D. Shattuck, J. B. Swift, W. D. McCormick, and H. L. Swinney, Patterns in 3d vertically oscillated granular layers: Simulation and experiment, Phys. Rev. Lett. **80**(1), 57–60 (1998).
[30] G. Pajer, H. Kuhnt, and F. Kuhnt, Fördertechnik – Stetigförderer (VEB Verlag Technik, Leipzig, 1988).
[31] F. Rademacher and L. T. Borg, On the theoretical and experimental conveying speed of granular bulk solids on vibratory conveyors, Eng. Res. **60**, 261 (1994).
[32] E. Sloot and N. Kruyt, Theoretical and experimental study of the transport of granular materials by inclined vibratory conveyors, Powder Technol. **87**, 203 (1996).
[33] A. Rosato, K. J. Strandburg, F. Prinz, and R. H. Swendsen, Why the brazil nuts are on top: Size segregation of particulate matter by shaking, Phys. Rev. Lett. **58**(10), 1038–1040 (1987).
[34] O. Pouliquen, J. Delour, and S. B. Savage, Fingering in granular flows, Nature **386**, 816 (1997).
[35] See for example: http://www.abs-lawinenairbag.de.
[36] M. H. Cooke, D. J. Stephens, and J. Bridgewater, Fundamental powder mixing mechanisms, Powder Technol. **15**, 215 (1976).
[37] R. Jullien and P. Meakin, A mechanism for particle size segregation in three dimensions, Nature **344**, 425 (1990).
[38] D. A. Huerta and J. C. Ruiz-Suárez, Vibration-induced granular segregation: A phenomenon driven by three mechanisms, Phys. Rev. Lett. **92**(11), 114301 (2004).
[39] M. Schröter, S. Ulrich, J. Kreft, J. B. Swift, and H. L. Swinney, Mechanisms in the size segregation of a binary granular mixture, Phys. Rev. E **74**(1), 011307 (2006).
[40] Z. S. Khan and S. W. Morris, Subdiffusive axial transport of granular materials in a long drum mixer, Phys. Rev. Lett. **94**(4), 048002 (2005).
[41] X. Yan, Q. Shi, M. Hou, K. Lu, and C. K. Chan, Effects of air on the segregation of particles in a shaken granular bed, Phys. Rev. Lett. **91**(1), 014302 (2003).
[42] M. E. Möbius, B. E. Lauderdale, S. R. Nagel, and H. M. Jaeger, Brazil-nut effect: Size separation of granular particles, Nature **414**, 270 (2001).
[43] N. Burtally, P. J. King, and M. R. Swift, Spontaneous air-driven separation in vertically vibrated fine granular mixtures, Science **295**(5561), 1877–1879 (2002).
[44] T. Shinbrot and F. J. Muzzio, Reverse buoyancy in shaken granular beds, Phys. Rev. Lett. **81**(20), 4365–4368 (1998).
[45] A. P. J. Breu, H. M. Ensner, C. A. Kruelle, and I. Rehberg, Reversing the brazil-nut effect: Competition between percolation and condensation, Phys. Rev. Lett. **90**(1), 014302 (2003).
[46] T. Shinbrot, Granular materials: The brazil nut effect in reverse, Nature **429**, 352 (2004).
[47] S. Aumaître, C. A. Kruelle, and I. Rehberg, Segregation in granular matter under horizontal swirling excitation, Phys. Rev. E **64**(4), 041305 (2001).
[48] A. D. Dinsmore, A. G. Yodh, and D. J. Pine, Phase diagrams of nearly-hard-sphere binary colloids, Phys. Rev. E **52**(4), 4045–4057 (1995).

[49] T. Schnautz, R. Brito, C. A. Kruelle, and I. Rehberg, A horizontal brazil-nut effect and its reverse, Phys. Rev. Lett. **95**(2), 028001 (2005).
[50] E. F. F. Chladni, Entdeckungen ueber die Theorie des Klanges (Weizmanns Erben und Reih, Leipzig, 1787).
[51] M. Faraday, On a peculiar class of acoustical figures; and on certain forms assumed by groups of particles upon vibrating elastic surfaces (abstract), Philos. Trans. R. Soc. Lond. A **3**, 49–51 (1830).
[52] J. P. Gollub and J. S. Langer, Pattern formation in nonequilibrium physics, Rev. Mod. Phys. **71**(2), S396–S403 (1999).
[53] P. B. Umbanhowar, F. Melo, and H. L. Swinney, Localized excitations in a vertically vibrated granular layer, Nature **382**, 793–796 (1996).
[54] I. S. Aranson and L. S. Tsimring, Patterns and collective behavior in granular media: Theoretical concepts, Rev. Mod. Phys. **78**(2), 641 (2006).
[55] A. Götzendorfer, C. A. Kruelle, I. Rehberg, and D. Svenšek, Localized subharmonic waves in a circularly vibrated granular bed, Phys. Rev. Lett. **97**(19), 198001 (2006).

PHYSICAL REVIEW E **79**, 010301(R) (2009)

Fluidization of granular media wetted by liquid ^{4}He

K. Huang,* M. Sohaili, M. Schröter, and S. Herminghaus†
Max Planck Institute for Dynamics and Self-Organization, Bunsenstrasse 10, 37073 Göttingen, Germany
(Received 17 October 2008; published 27 January 2009)

We explore experimentally the fluidization of vertically agitated polymethylmethacrylate spheres wetted by liquid ^{4}He. By controlling the temperature around the λ point, we change the properties of the wetting liquid from a normal fluid (helium I) to a superfluid (helium II). For wetting by helium I, the critical acceleration for fluidization (Γ_c) shows a steep increase close to the saturation of the vapor pressure in the sample cell. For helium II wetting, Γ_c starts to increase at about 75% saturation, indicating that capillary bridges are enhanced by the superflow of the unsaturated helium film. Above saturation, Γ_c enters a plateau regime where the capillary force between particles is independent of the bridge volume. The plateau value is found to vary with temperature and shows a peak at 2.1 K, which we attribute to the influence of the specific heat of liquid helium.

DOI: 10.1103/PhysRevE.79.010301 PACS number(s): 45.70.−n, 68.08.Bc, 67.25.dm

It is a well-known experience that the addition of a certain amount of wetting liquid to a pile of sand increases its mechanical stability dramatically [1–5], leading to a material stiff enough for sculpting sand castles. The increased mechanical stability of wet granulates is due to the formation of liquid bridges between adjacent grains, which exert attractive forces by virtue of their surface tension [6–10]. As has recently been shown, the presence of liquid changes the acoustic properties of the granulate as well [11]. Wet granular media exist in many chemical, pharmaceutical, or food production processes, where the question how to handle them appropriately is of great economic significance [12–14]. Moreover, wet granular media are also model systems to study phase transitions far from equilibrium [15]. A detailed understanding of the interaction between the liquid and the grains is therefore of major importance.

In both basic research and many industrial processes, vertical vibration is a widely used fluidization scheme [16]. For wet granulates, an extra force must be exerted in wet grains to overcome the cohesive capillary forces, in contrast to the fluidization of a dry granular pile [17–20]. These forces increase the critical shaking acceleration Γ_c needed for fluidization, which makes Γ_c a good parameter to study the influence of a wetting liquid [21–23].

Here we measure Γ_c for polymethylmethacrylate spheres wetted by liquid helium. Helium wets most substrates perfectly [24–26] so that a zero contact angle can be assumed. When its temperature is below the λ point (2.17 K for bulk helium), liquid helium will undergo a phase transition into a superfluid (helium II) where many interesting phenomena such as the "fountain effect" arise, owing to its two-fluid properties [27–32]. In this paper we study how the difference between a superfluid and a normal fluid changes the mechanical properties of a granular medium wetted by this liquid.

A sketch of the experimental setup is shown in Fig. 1. The granular sample consists of 0.6 g polymethylmethacrylate spheres (Bangs Labs) with an average diameter of $d \approx 10\ \mu$m and 15% width of the size distribution. This prevents the formation of a crystalline packing which would result in unwanted side effects. The sample is fluidized by sinusoidal vertical vibrations with a driving frequency $f = 110$ Hz and a nondimensional acceleration $\Gamma = 4\pi^2 f^2 A/g$, where g is the gravitational acceleration and A is the shaking amplitude. The sample is contained in a cylindrical cell made of 99.95% oxygen-free copper, which ensures good thermal contact with the surrounding helium bath. The temperature in the cryostat is controlled by adjusting the pressure above the liquid helium.

The amount of helium in the sample cell is controlled by adding room temperature helium gas, which was passed through a cold trap for purification. A well-defined amount of helium gas was admitted to the cell using a gauged cylinder volume. All measurements are taken after the pressure in the cell becomes stable.

The sample was illuminated with laser pulses with 532 nm wavelength and a repetition rate of 22 Hz, phase locked to the vibration of the sample. The speckle pattern from the back-scattered light is captured with a charge coupled device camera (Hamamatsu C9300) with a quantum efficiency 58% at this wavelength. A polarizer in front of the camera suppresses directly reflected light. The camera and laser are synchronized so that the images are taken at a fixed phase of every fifth vibration cycle. The power injected by the laser pulses is on the order of 10^{-6} W. This is at least one order of magnitude less than the energy injected by vibrations, which we estimate to be $\approx 2.6 \times 10^{-5}$ W from the inelastic collisions between the sample and the bottom plate at $\Gamma = 2$.

To create a reproducible initial packing, we first fully fluidize the sample by shaking it for a few seconds with a Γ of 6 ± 1. Then we ramp Γ down to below 1 during approximately 1 min. The critical acceleration for fluidization Γ_c is then measured by slowly increasing and decreasing Γ. Γ_c differs by maximally 15% for fluidization and solidification [23]; the values reported here are averages between both values. The transition between solid and fluid states of the sample is determined by visual inspection of the variation of the speckle pattern in real time. As soon as the sample fluidizes, the speckle pattern no longer stays stable and starts to

*kai.huang@ds.mpg.de
†stephan.herminghaus@ds.mpg.de

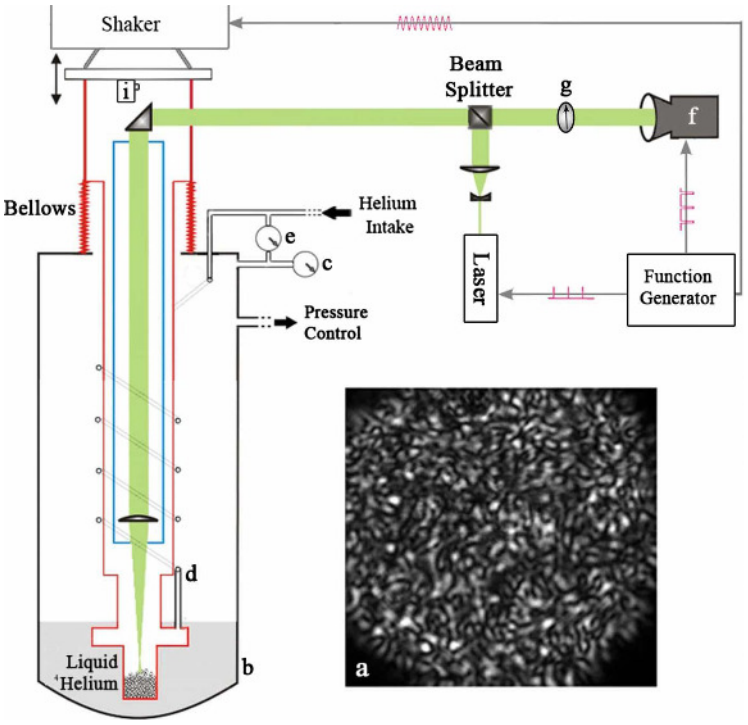

FIG. 1. (Color online) Sketch of the experimental setup. (a) is a typical top view of the sample. The temperature in the cryostat (b) is adjusted by controlling the pressure [measured by pressure gauge (c)] above the liquid helium. Helium gas is added into the sample chamber through a capillary (d). Gauge (e) measures the pressure difference between cell and cryostat. The sample is illuminated by laser pulses, and images are taken by a charge-coupled device camera (f) with a polarizer (g) in front. The sample cell can be vibrated vertically by an electrodynamic shaker (LDS V555) which is mounted upside down above the cryostat. The strength of vibration is measured by an accelerometer (PCB Piezotronics 353B33) (i).

vary with time. This method was found to agree with measurements based on the correlation of subsequent images.

Figure 2 shows the dependence of the critical acceleration for fluidization on the amount of helium gas added at different temperatures around the λ point. For clearer display we use a scaled critical acceleration for fluidization $\Gamma^* = (\Gamma_c - \Gamma_{dry})/\Gamma_{dry}$. Γ_{dry}, the fluidization acceleration for a dry sample, is an average of Γ_c before it increases due to wetting.

Moreover, we scale the amount of helium added, n, by the amount of helium gas needed for the pressure in the cell to reach saturation, n_{sat}, by defining $n^* = n/n_{sat}$. For $n^* < 1$, n^* can be treated as the fractional saturation of helium, P_c/P_0, in the cell, where P_c is the pressure in the cell and P_0 the saturated vapor pressure, because most of the helium added stays in the vapor phase. For $n^* > 1$, $n^* - 1$ grows linearly with liquid content W, by which we denote the ratio of the volume of the wetting liquid and the total volume occupied by the sample. The data with largest n^* shown below correspond to a liquid content varying from 10% to 38% at different temperature.

Figure 2 shows that the behavior of Γ^* can be divided into three distinct regimes. In regime 1 the sample behaves the same as a dry granular medium; the scaled critical acceleration stays around zero. Adding helium gas in this regime leads to the increase of pressure in the cell and the formation of the first atomic layer of helium on the particles. This layer is, however, not mobile enough to form liquid bridges [27].

Regime 2 corresponds to the asperity wetting regime, where Γ^* increases monotonically with the amount of added helium. In this regime the helium film condensed on the particle surface is thick enough to form small liquid bridges between the asperities of adjacent particles. With the increase of helium adsorbed, the number of small capillary bridges at the asperity level increases, which leads to a higher cohesive force between adjacent particles.

In regime 3, the amount of adsorbed helium is enough to fill the roughness on the grains, such that they appear as completely wet, perfect spheres to all further added liquid. Γ^* shown in Fig. 2, within experimental scattering, stays constant, in agreement with earlier experiments with other liquids at room temperature [21]. This independence from n^* comes from the fact that the capillary force is dominated by the curvature of the spheres instead of the volume of the liquid bridges. With the increase of n^*, capillary bridges will coalesce and form bigger liquid clusters, but Γ^* will not change due to the constant Laplace pressure imposed by the packing geometry [22].

It is regime 2 where the difference between superfluid and normal fluid wetting is significant. For superfluid wetting the sample enters regime 2 already at a fractional saturation of about 0.75, which is far below the 0.95 observed for normal fluid wetting. We interpret the increase of Γ^* to be due to the formation of bridges between asperities of neighboring spheres by the condensed unsaturated helium film. The amount of helium adsorbed can be described by the Frenkel-Hasley-Hill equation [33,34]; it is proportional to $[-\ln(P_c/P_0)]^{-1/3}$ and therefore as shown above to $[-\ln(n^*)]^{-1/3}$.

Figure 3(a) shows that Γ^* increases linearly in regime 2 with the unsaturated helium film thickness, both above and below the λ point. This can be understood in the following

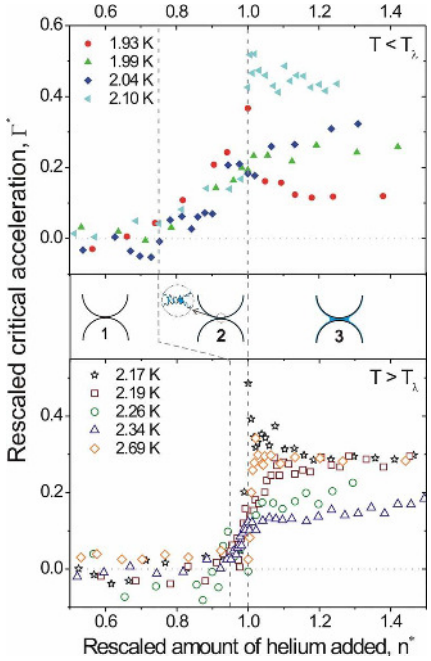

FIG. 2. (Color online) Scaled critical acceleration for fluidization, Γ^*, as a function of the amount of helium added, n^*, for superfluid (top) and normal fluid (bottom) wetting. $\Gamma^*=0$ corresponds to the behavior of dry grains, and $n^*=1$ to the transition from an unsaturated to a saturated helium film. Three different regimes can be distinguished: dry (1), asperity (roughness) (2), and complete wetting (3). Sketches of the three regimes on the grain size scale are shown in the middle. The dashed lines separating the regimes are guides to the eye. Each data point is an average of three measurements; the standard error is within 0.05.

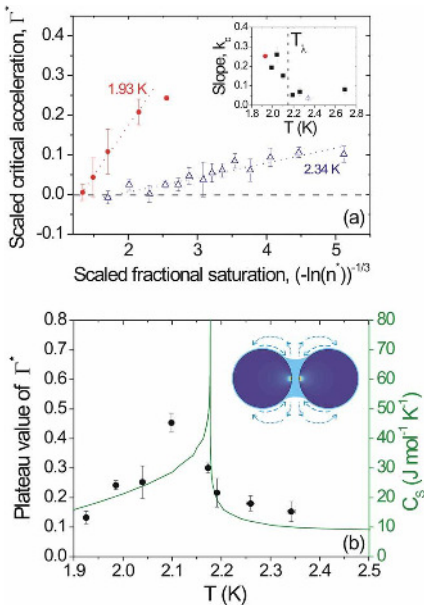

FIG. 3. (Color online) (a) In regime 2 Γ^* varies linearly with the scaled saturation $[-\ln(n^*)]^{-1/3}$. Dotted lines are fits with Eq. (3). The inset of (a) shows the temperature dependence of the fit parameter k_c. (b) The temperature dependence of the plateau value of Γ^* in regime 3 (black dots). The dark green line is the specific heat C_s of bulk helium taken from [38]. The inset of (b) shows a sketch of two completely wetted particles. The color code illustrates the temperature gradients generated by energy dissipation. Blue dashed arrows indicate the flow of superfluid in the helium film driven by the fountain effect, and blue dotted arrows depict evaporation of helium from the surface of the meniscus.

way. To fluidize wet granular media, the driving force has to overcome the capillary forces between the grains or between container walls and the particles. The gravitational force can be neglected here because it is two orders of magnitude smaller than the capillary force. In the asperity regime 2, the capillary force f_b is given by [6]

$$f_b = \frac{R^2}{2\pi\delta^2}\tilde{V}F_b, \tag{1}$$

where

$$F_b = 2\pi R\gamma\cos(\theta) \tag{2}$$

is the capillary force in the complete wetting regime, R is the radius of the particle, $\tilde{V}$ is the bridge volume, which depends linearly on the amount of helium adsorbed, δ is the amplitude of the roughness of the particles, and θ is the contact angle. The linear growth of the cohesive force with the bridge volume in this regime explains the linear dependence of Γ^* on the amount of helium adsorbed [Eq. (1)]. Therefore we fit in Fig. 3(a) the values of Γ^* with

$$\Gamma^* = k_c[-\ln(n^*)]^{-1/3} + \beta, \tag{3}$$

with the slope coefficient k_c and β as fitting parameters.

The temperature dependence of k_c shown in the inset of Fig. 3(a) depicts the enhancement of the cohesive force by adsorbed superfluid film below the λ point. This is readily explained from the strongly different transport mechanisms in the superfluid state. First, the superflow enables the forming capillary bridge to acquire more liquid from its surroundings during bridge formation. Second, the impact of the spheres radiates quantum excitations into the superfluid at the point of contact, dragging extra superfluid toward the contact region by osmosis ("fountain effect") [28,29]. This is in contrast to normal fluid wetting, where only liquid very close to the contact point is sucked into the bridge by the negative Laplace pressure.

As is clearly seen in Fig. 2, the critical acceleration shows a plateau in regime 3 both above and below T_λ, as is observed as well with standard liquids [6,21,23]. The constancy of Γ^* reflects the weak dependence of the capillary force upon liquid volume for fully developed capillary bridges [6,22]. However, since the surface tension depends only weakly on temperature close to T_λ, we would expect to ob-

serve roughly the same plateau value for all temperatures, which is clearly not the case.

Figure 3(b) shows the temperature dependence of the plateau value of Γ^* in regime 3. It shows a peak at about 2.1 K, close to the superfluid transition. This can be qualitatively understood as a combination of two effects. In the normal fluid regime, capillary bridges will acquire their full volume only close to T_λ, where the specific heat of the liquid (shown for comparison) is large and prevents strong heating of the bridge from dissipated energy. Farther away from T_λ, the bridges heat up and evaporate back into the asperity regime. In the superfluid regime, temperature is effectively equalized by the superflow. The heat intake due to bridge rupture and grain impact thus gives rise to a strong superflow toward the contact points. However, it is well known that the presence of a superflow in an adsorbed liquid film leads to a strongly increased contact angle θ [35]. This is due to the Kontorovich pressure term [36] adding to the disjoining pressure, and leads to dynamical incomplete wetting in liquid helium, as observed experimentally [37]. This effect is weak close to T_λ, but increases further into the superfluid regime. As a consequence, the capillary force (and thus the plateau value of Γ^*) is reduced according to Eq. (2).

We need to mention that no clear signature of a viscous effect can be found. This can be understood by calculating the ratio between the energy dissipation by viscosity and by rupture of capillary bridges [6]. At the temperature 2.1 K, it yields 0.0046, indicating that the system is still in the capillary region where viscosity can be ignored.

To conclude, we demonstrate with liquid helium, a liquid that has a surface tension only 1/200 that of pure water, that the increase of mechanical stability of granular materials by wetting is prominent. Beyond that, our main findings can still be explained on the basis of a simple capillary model [6] by taking superfluid properties of liquid helium, such as the "fountain effect", into account.

Inspiring discussions with Mario Scheel, Axel Fingerle, Martin Brinkmann, Jürgen Vollmer, and Isaac Goldhirsch are gratefully acknowledged. We thank Udo Krafft and Günter von Roden for their indispensable technical support.

[1] J. Duran, *Sands, Powders, and Grains* (Springer, New York, 2000).
[2] S. R. Nagel, Rev. Mod. Phys. **64**, 321 (1992).
[3] D. J. Hornbaker, R. Albert, I. Albert, A.-L. Barabasi, and P. Schiffer, Nature (London) **387**, 765 (1997).
[4] P. Schiffer, Nat. Phys. **1**, 21 (2005).
[5] S. Nowak, A. Samadani, and A. Kudrolli, Nat. Phys. **1**, 50 (2005).
[6] S. Herminghaus, Adv. Phys. **54**, 221 (2005), and references therein.
[7] L. Bocquet, E. Charlaix, S. Ciliberto, and J. Crassous, Nature (London) **396**, 735 (1998).
[8] L. Bocquet, É. Charlaix, and F. Restagno, C. R. Phys. **3**, 207 (2002).
[9] T. C. Halsey and A. J. Levine, Phys. Rev. Lett. **80**, 3141 (1998).
[10] W. B. Pietsch, Nature (London) **217**, 736 (1968).
[11] Th. Brunet, X. Jia, and P. Mills, Phys. Rev. Lett. **101**, 138001 (2008).
[12] H. Rumpf, *Agglomeration* (AIME Interscience, New York, 1962).
[13] S. M. Iveson, J. D. Litster, K. Hapgood, and B. J. Ennis, Powder Technol. **117**, 3 (2001).
[14] T. Gröger, U. Tüzün, and D. M. Heyes, Powder Technol. **133**, 203 (2003).
[15] A. Fingerle, K. Roeller, K. Huang, and S. Herminghaus, New J. Phys. **10**, 053020 (2008).
[16] I. Gutman, *Industrial Uses of Mechanical Vibrations* (Business Books, London, 1968).
[17] A. Alexeev, V. Royzen, V. Dudko, A. Goldshtein, and M. Shapiro, Phys. Rev. E **59**, 3231 (1999).
[18] A. Götzendorfer, C.-H. Tai, C. A. Kruelle, I. Rehberg, and S.-S. Hsiau, Phys. Rev. E **74**, 011304 (2006).
[19] N. Mujica and F. Melo, Phys. Rev. Lett. **80**, 5121 (1998).
[20] J. S. Olafsen and J. S. Urbach, Phys. Rev. Lett. **95**, 098002 (2005).
[21] M. Scheel, D. Geromichalos, and S. Herminghaus, J. Phys.: Condens. Matter **16**, S4213 (2004).
[22] M. Scheel, R. Seemann, M. Brinkmann, M. Di Michiel, A. Sheppard, B. Breidenbach, and S. Herminghaus, Nature Mater. **7**, 189 (2008).
[23] Z. Fournier *et al.*, J. Phys.: Condens. Matter **17**, S477 (2005).
[24] E. Cheng, M. W. Cole, W. F. Saam, and J. Treiner, Phys. Rev. Lett. **67**, 1007 (1991).
[25] J. Klier, P. Stefanyi, and A. F. G. Wyatt, Phys. Rev. Lett. **75**, 3709 (1995).
[26] N. Bigelow, P. J. Nacher, and J. Dupont-Roc, J. Low Temp. Phys. **89**, 135 (1992).
[27] J. Wilks, *The Properties of Liquid and Solid Helium* (Clarendon Press, Oxford, 1967).
[28] J. F. Allen and H. Jones, Nature (London) **141**, 243 (1938).
[29] H. London, Proc. R. Soc. London, Ser. A **171**, 484 (1939).
[30] E. Long and L. Meyer, Phys. Rev. **85**, 1030 (1952).
[31] L. Meyer, J. Low Temp. Phys. **3**, 199 (1970).
[32] K. R. Atkins, B. Rosenbaum, and H. Seki, Phys. Rev. **113**, 751 (1959).
[33] R. Bowers, Philos. Mag. **44**, 485 (1953).
[34] J. Israelachvili, *Intermolecular and Surface Forces* (Academic, San Diego, 1992).
[35] S. Herminghaus, Europhys. Lett. **42**, 443 (1998).
[36] V. M. Kontorovich, Sov. Phys. JETP **3**, 770 (1956).
[37] M. Poujade, C. Guthmann, and E. Rolley, Europhys. Lett. **58**, 837 (2002).
[38] R. J. Donnelly and C. F. Barenghi, J. Phys. Chem. Ref. Data **27**, 1217 (1998).

Eur. Phys. J. Special Topics **179**, 25–32 (2009)

DOI: 10.1140/epjst/e2010-01191-5

THE EUROPEAN PHYSICAL JOURNAL SPECIAL TOPICS

Regular Article

Universal and non-universal aspects of wet granular matter under vertical vibrations

K. Huang[1,2,a], K. Röller[1,b], and S. Herminghaus[1,c]

[1] Max-Planck-Institute for Dynamics and Self-Organization, Bunsenstr. 10, 37073 Göttingen, Germany
[2] Experimentalphysik V, Universität Bayreuth, 95440 Bayreuth, Germany

Abstract. The phase diagram of vertically vibrated wet granular matter is investigated by both experiments and molecular dynamics type simulations, with a focus on the coexistence regime of the fluid and gas phases. Phase diagrams measured at various parameters including the rupture energy of liquid bridges, are presented. While for elastic grains, the transition from the fluid to the fluid-gas coexistence phase is found to be determined only by the rupture energy of liquid bridges [Fingerle et al. New J. Phys. **10**, 053020 (2008)], inelasticity is found to introduce non-universal features into the phase diagram, which are also affected by the grain size.

1 Introduction

Many of the peculiar features of granular matter can be traced down to the dissipative nature of its grain scale dynamics. This gives rise to a wide variety of complex collective phenomena, and identifies granular matter as an interesting candidate for the investigation of physics far from thermal equilibrium. It has been proved useful to describe the collective behaviour of a large number of grains with notions borrowed from the physics of equilibrium phase transitions. For instance, granular matter can behave like a solid, a liquid, or a gas [1,2], depending on the balance between energy injection and dissipation. As a particularly well controlled way of injecting energy, vertical vibration has been widely employed and explored in detail [3–12]. While 'classical' research on granular systems tried to avoid any side effects due to cohesion, the dynamical behavior of *wet* granular matter has been attracting more and more interest from physicists more recently [13–15]. The energy dissipation mechanism in wet granular matter is dramatically different from that of dry granular matter. In wet granular matter, the formation of capillary bridges between adjacent particles [16,17] gives rise to a well defined energy scale in the system, which is absent in dry granulates [14].

Since the interest of physicists has only recently turned to wet granular matter, its dynamical behavior is still much less well understood than that of its dry counterpart [14,15]. In a previous study [18], we investigated phase transitions of vertically vibrated wet granular matter by both experiments and molecular dynamics type simulations. Aside from a solid-fluid transition which is well known from dry granular systems, a second transition was found which leads to the formation of a gas phase. While the solid-fluid transition was determined by the force acting on the sample as in the dry systems, the fluid-gas transition was found to be driven by the injected energy. In the present study, we explore the scaling for the various transition lines with system parameters and try to distinguish what properties can be seen as 'universal' (depending

[a] e-mail: kai.huang@uni-bayreuth.de
[b] e-mail: klaus.roeller@ds.mpg.de
[c] e-mail: stephan.herminghaus@ds.mpg.de

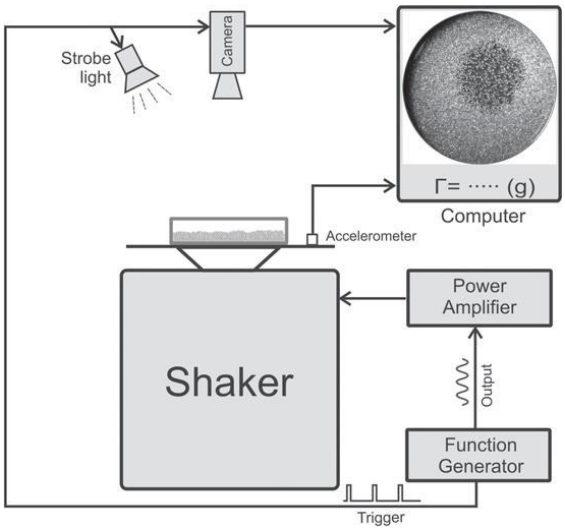

Fig. 1. Sketch of the experimental setup. Function generator, strobe light source and the high speed camera are synchronized with each other so that the images are captured at a certain phase of each vibration cycle. An example of a top view of the sample is shown in the inset photograph on the top right.

only on intrinsic parameters), and which have to be considered as non-universal (i.e., dependent on extrinsic parameters, like the volume of the container). In particular, we will address the question how the system properties are affected by inelastic effects in the impact between grains.

2 Experimental setup

Figure 1 shows a sketch of the experimental setup. Glass spheres with diameters 1.06 mm, 1.22 mm and 1.5 mm (Whitehouse scientific, GP1060, GP1220, GP1500) are used as the granular sample. The width of the size distribution was about 10%, which was sufficient to suppress crystallization. The glass beads were cleaned subsequently with ethanol, acetone, and Millipore water, and dried in an oven before use. The glass beads were placed into a flat cylindrical glass container, which was closed with a glass lid mounted on a separate stand. The latter fits well enough into the container to prevent glass beads from exiting, but enables free exchange of air, such that the gas pressure inside the cell was kept at atmospheric pressure. The height of the glass bead fill, h, was well below the total height of the cell, H, which could be adjusted by vertically moving the glass lid. A certain amount of wetting liquid was mixed into the sample before the experiment. Water, which has a surface tension of $\gamma \approx 72\,\mathrm{mN/m}$, was mostly used to wet the sample. Silicone oil (AK 5, Wacker; $\gamma \approx 21\,\mathrm{mN/m}$), was also used for comparison. Both liquids wet the glass surface well, with a contact angle below 10 degrees. The liquid content, W, is defined as the ratio between the volume of the added wetting liquid and the total volume the sample occupies (i.e., the area of the sample cell times the height of the granular pile, h). The container, which has a diameter of 145 mm, was mounted on an electromagnetic shaker (Tira TV5880/LS). A sinusoidal signal from a function generator is used to drive the shaker. The strength of the vibration is measured by an accelerometer (Kistler 8702B100M1). The sample is illuminated with a strobe light (Helio Strobe Beta A2) and viewed from top by a high speed camera (PCO 1200s). The camera is externally triggered by the function generator so that the image is captured at the same phase of each vibration cycle. All measurements are taken after

the wetting liquid is distributed homogeneously within the sample by shaking the sample at a low frequency $f < 20Hz$ and high acceleration $\Gamma \approx 10$ for a few minutes.

3 Results and discussions

3.1 Observations

As the frequency and amplitude of the drive are varied, a number of characteristic changes in the appearance of the sample are observed. At low acceleration, the glass beads just follow the harmonic vertical motion of the container, but no site exchange processes take place. This can be assessed most conveniently by the strobe light illumination, which reveals a completely static sample in this case. As the acceleration is increased, however, relative movements of the beads are observed, or even the appearance of a 'bubble' of a particularly 'hot' granular gas, surrounded by a 'fluid' (i.e., dense but mobile) phase [18]. We will explore in the present article the phase diagram of this system, both experimentally and by simulation, and try to distinguish its universal from non-universal features.

The phase diagrams are measured by keeping the driving frequency f at a certain value and varying the peak vibration acceleration $\Gamma = 4\pi^2 f^2 A/g$, where g is the gravitational acceleration and A is the vibration amplitude. The transition from the solid (S) to the fluid (F) phase is determined experimentally by first completely fluidizing the sample, followed by slowly decreasing Γ until the particles stop moving. This criterion turned out to be better defined than just increasing Γ and detecting the onset of particle motion: We assume this to be due to the difficulty to initialize the system with reproducible packing geometry. The transition from the fluid phase to the to the fluid-gas coexistence (C) occurs at an acceleration where a 'gas bubble' nucleates (see the top view image embedded in Fig. 1). After nucleation, the (circular) granular 'gas bubble' grows spontaneously to a certain size. As Γ is decreased again, the size of the gas bubble decreases continuously to zero, which indicates that there is a significant hysteresis for this transition. Within the hysteresis regime, the 'gas bubble' is unstable and fluctuates strongly in size. These fluctuations make a precise determination of the point of vanishing bubble size very difficult. We therefore rather define the F-C transition as the acceleration at which nucleation is observed. It is clear that the fluctuations of the gas bubbles close to the phase boundary are worthy of further investigations, which are currently under way. The transition from the fluid-gas coexistence (C) to the gas (G) phase again takes place at a well defined value of Γ, and leads to a completely homogeneous gaseous state of the sample. The abbreviations S, F, C and G are henceforth used as abbreviations for solid, fluid, fluid-gas coexistence, and gas phases.

3.2 Phase diagram: Experiments vs. simulations

Figure 2 shows the experimentally determined phase diagram in both Γ-f and Γ-v planes, where $v = 2\pi Af$ is the maximum vibration velocity of the container bottom. The S-F boundary is located at $\Gamma \approx 1.9$, independent of the driving frequency f. It therefore lies higher than the corresponding transition for dry granular matter ($\Gamma \approx 1.2$ [2]). This increase represents the enhanced mechanical stability of the granulate due to the network of capillary bridges forming between the grains. The independence of the critical acceleration upon the frequency of the driving underscores its physical significance. In fact, since the acceleration is directly related to a force, this transition has been identified as 'force driven' [18]. In the fluid-gas coexistence regime (C) (cf. photograph in Fig. 1), the size of the 'gas bubble' grows with the driving amplitude, while keeping its circular shape. During this growth, the surrounding fluid phase is pushed aside, and the height of the granular fluid increases until it reaches the top of the container. If the drive is increased further, the size of the 'gas bubble' saturates, and the density difference between gas and fluid phases decreases until the sample finally enters a homogeneous gas phase. This corresponds to reaching the boundary between the coexistence regime (C) and the gaseous phase (G).

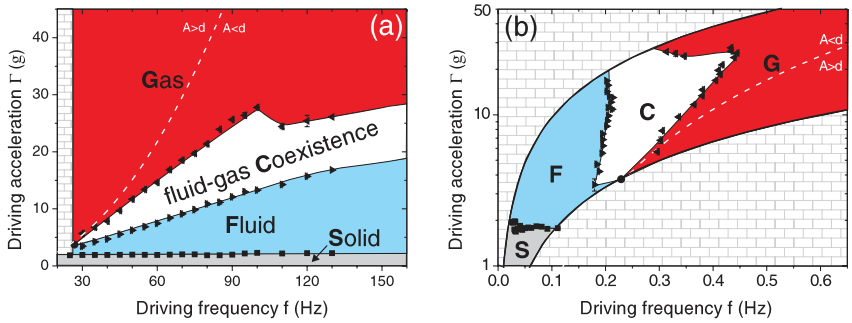

Fig. 2. Phase diagram of water-wet glass spheres with diameter $d = 1.5\,\mathrm{mm}$, at a liquid content of $W = 1\%$ in Γ f plane (a) and Γ v plane (b). Filling height of the sample is 55% of the container height $H = 6.6\,\mathrm{mm}$. Regions color coded by gray, blue, white and red correspond to solid (S), fluid (F), fluid-gas coexistence (C) and gas (G) phases. The regions covered with brick patterns in the current and following plots are unexplored due to the limitation of the apparatus. The solid black dot corresponds to the converging point of the F-C and C-G transition lines. The dashed line indicates $A = d = 1.5\,\mathrm{mm}$ (A is the vibration amplitude).

As shown in Fig. 2(b), the F-C transition occurs at a certain driving velocity (i.e., maximum velocity of the oscillating wall). This strongly suggests that this transition is linked to a certain characteristic velocity, or kinetic energy per particle. In fact, it has been successfully argued that the (F)-(C) transition is determined by the balance between the energy required to break the capillary bridges between adjacent grains and the average kinetic energy of their center-of-mass motion [18]. As a simple mean-field model predicts, the (C)-(G) boundary should be just parallel to the (F)-(C) boundary, at somewhat higher energy [18]. This is clearly not the case: the observed structure of the phase boundary is much more complex. Particularly prominent is the sharp backward bend which occurs at $\Gamma \approx 25\mathrm{g} =: \Gamma_b$. We will com back to this feature further below.

A glance back at Fig. 2(a) shows that the F-C and C-G transition lines in the phase diagram approach each other as the driving frequency decreases (Fig. 2(a)). They seem to intersect at $f_c \approx 27\,\mathrm{Hz}$ and $\Gamma_c \approx 3.6$. This point can be accurately detected by varying both the driving frequency and acceleration. We decrease f continuously while keeping the size of the gas bubble maximal by varying Γ, until the gas bubble vanishes. The data points shown in Fig. 2 are averages of four measurements each, and the error bar is within the size of the data points. In an attempt to rationalize this finding, we just note that f_c compares quite favorably with a natural time scale t_g of the system, which can be derived from the attractive capillary force and the bead mass, m. Setting $t_g := \sqrt{m/\gamma}$, we have $f_g = 1/(2\pi t_g) \approx 45\mathrm{Hz}$, which is not far from f_c. This must clearly be investigated in further detail.

In a previous study [18], molecular dynamics type simulations based on two different models have been employed to study the phase diagram of elastically colliding particles. One of the models assumes that the attractive interaction between two particles which are connected by a liquid bridge is independent of the distance of the particles up to a certain distance at which the liquid bridge ruptures. This model has been termed the minimal capillary model. In contrast, the so-called thin-thread model has been used as well, which assumes the attractive force to be described by a delta-function located at the rupture distance. Both models consider the rupturing of liquid bridges as the only source of energy dissipation in the granular sample. In that case, the F-C transition should occur near $E^* = 1$, where E^* is the kinetic energy injected by one collision with the wall normalized by the rupture energy $E_b \propto R^2\gamma\sqrt{W}$ [18]. The most significant result was that the phase diagrams obtained with these two quite different force models were in almost perfect quantitative agreement. This can be seen as a justification to work with the thin-thread model, since this allows event-driven simulations which are much less time consuming than full integrations of an equation of motion with finite forces. In the present

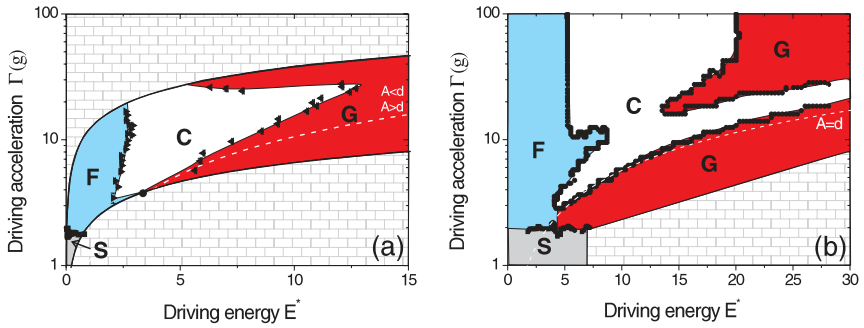

Fig. 3. Comparison of phase diagram between experiment (a) and simulation (b) in the Γ-E^* plane, where E^* is the energy injection rescaled by rupture energy of a liquid bridge. Restitution coefficient between particles $\epsilon_{pp} = 0.8$, and between particle and container $\epsilon_{pw} = 1$. The simulated system contains 1200 two-dimensional particles.

work, we therefore performed simulations using the thin thread model as in [18], but implement at the same time *inelasticity* in the particle collisions, in order to match the real experimental conditions more closely. We use a constant coefficient of restitution, ϵ, which is defined as $\epsilon := p_f/p_i$, where p_i and p_f are the momenta before and after the collision, respectively.

In the experimental phase diagram shown in Fig. 3(a), we see that the fluid-coexistence (F-C) transition occurs at $E^* \approx 2.5$, which is significantly larger than unity, and hence larger than obtained before in elastic simulations. We interpret this shift as being due to the influence of inelasticity in the collisions, frictional forces, and dimensionality [18] (simulation were in two dimensions). To support this view, we present in Fig. 3(b) simulations with inelastic impact dynamics ($\epsilon < 1$). Clearly, the F-C transition line is shifted to values of the normalized energy well above unity, which is in qualitative agreement with the experimental findings. Furthermore, the position of horizontal S-F transition line agrees quantitatively with experiment. An additional feature revealed by the simulation is that the fluid-gas coexistence region basically consists of two regimes. One elongated region appears at lower Γ and approximately follows the line at which the vibration amplitude equals the particle diameter $A \approx d$. This seems to be a geometry-driven effect which is intimately connected to inelasticity, since in former simulation results with elastic particles [18] it was entirely absent. The other region, which is mainly bounded by two vertical lines corresponding to two well-defined driving energies, is located at higher Γ and corresponds to the coexistence region as predicted by both earlier (elastic) simulations and mean-field theory [18]. In the intermediate Γ region, both fluid-coexistence (F-C) and coexistence-gas (C-G) transitions are distorted, suggesting a superposition of both mechanisms.

3.3 Scaling of the F-C transition

Let us now investigate the variation of the positions of the transition lines as different system parameters are varied, in order to check the ideas put forward above. Fig. 4 shows phase diagrams for different liquid content W and particle diameter. As the liquid content and particle diameter change, the rupture energy of liquid bridges, $E_b \propto R^2\gamma\sqrt{W}$, varies. We see that by choosing the rescaled driving energy, E^*, as the abscissa, the data for the F-C transition collapse on a single line within experimental scattering. This indicates that this transition is indeed dominated by the rupture energy alone.

We also investigated the influence of system dimensions on the observed phase transitions by varying the sample height (h) and the container height (H), as shown in Fig. 5. While the C-G transition line shifts substantially to the right as H is increased while h is kept constant, the F-C transition transition line remains almost unchanged. In contrast, changing the sample height, h,

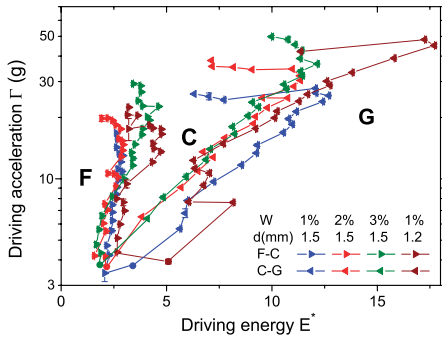

Fig. 4. Phase diagrams for water-wet glass spheres at different liquid content W and particle diameters d in the Γ-E^* plane, where E^* is the driving energy rescaled by the rupture energy of liquid bridges. Heights of the granular sample and the container are $h = 3.6\,\mathrm{mm}$ and $H = 6.6\,\mathrm{mm}$ correspondingly.

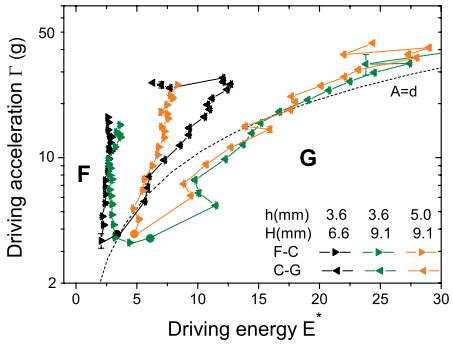

Fig. 5. Phase diagram for different sample height h and container height H for 1.5 mm glass spheres. The samples are wetted by water with liquid content $W = 1\%$.

at constant H mainly affects the F-C transition, but not the C-G transition. We conclude that while the C-G transition is determined by container size and should therefore be considered 'non-universal', the F-C transition is mainly governed by the sample itself. Furthermore, we may rationalize qualitatively how the dependence of the F-C transition upon the height of the sample comes about. As is illustrated in Fig. 6, the shift of the F-C transition line may be due to the increased number of collisions involved in the injected energy's travelling from the container bottom (where it is injected) upwards through the sample. If the average number of collisions required for the energy to reach the top layer is n, the effective energy which reaches the top layer is $E_{top} = E_{\mathrm{inj}}\epsilon^{2n}$, where ϵ is the restitution coefficient of the collision between particles, and E_{inj} is the energy injected through collisions between bottom layers of the sample and the container. If the energy of the top layer exceeds the capillary bridge energy, $E_{top} > E_b$, particles on top layers will be driven into a gaseous phase. For larger sample heights, h, the dissipation of energy within the sample increases and therefore more energy injection is needed to meet the criterion $E_{top} > E_b$. This may explain the shift of the fluid-coexistence (F-C) transition line to a higher value at increased h.

3.4 Scaling of the C-G transition

The behaviour of the C-G transitions is more complex. This line consists of a lower branch which tends to follow the curve where the vibration amplitude equals the particle diameter, but there

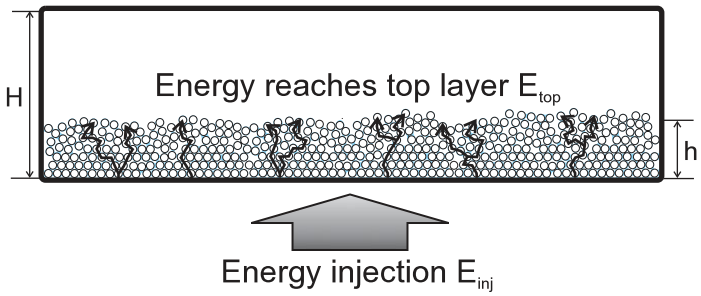

Fig. 6. A sketch showing how energy injection is transmitted upwards through collisions between neighboring particles. h and H are height of the sample and the container correspondingly.

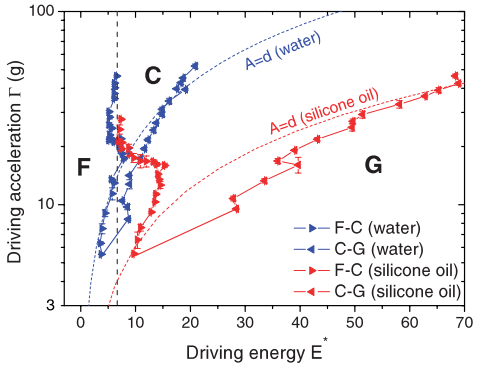

Fig. 7. Phase diagram of 1 mm glass spheres wetted by water and silicone oil in Γ-E^* plane. The surface tension of water is more than three times that of silicone oil. Other parameters are: liquid content $W = 1\%$, $h = 3$ mm and $H = 9.1$ mm. Dashed lines correspond to $A = d$, the gray dashed line serves as a guide to the eye.

is as well a strong dependence on the height of the container, as already mentioned. This may be termed 'non-universal' behaviour, and we have already seen that inelasticity plays a vital role as well in shaping this transition line. Turning back to Fig. 4, we see that the horizontal upper branch shifts considerably to larger acceleration, Γ_b, as the liquid content is increased. This is in line with earlier simulations [18] which suggested that the sharp backward bend in the C-G transition line occurs when the vibration amplitude equals the rupture distance of the capillary bridges. The latter is increased as the liquid content increases, which would be consistent with an upshift of the horizontal upper boundary of the coexistence region. This aspect needs further investigation.

Finally, we have varied the surface tension of the wetting liquid to check the concepts put forward above. As shown in Fig. 7, phase diagrams for different wetting liquid are investigated for $d = 1$ mm particles. Again, we observe approximate data collapse for the F-C transition above the curve defined by $A = d$. This confirms that the scaling with rupture energy of liquid bridges in this region is appropriate. Again, the transition line between the C and G phases seems to be dominated by geometric effects, such as the equality of A and d.

4 Conclusions

To summarize, we have confirmed by experimental studies as well as by simulations taking inelasticity into account that the phase diagram of mechanically agitated wet granular

matter shows two universal phase transitions which depend only on few general intensive system parameters. One is the solid-fluid (S-F) transition which is driven by the applied force scale, represented here by the applied acceleration. The position of this transition line is directly given by the adhesive force acting between adjacent grains. The second is the transition between a fluid (F) phase and fluid-gas coexistence (C), and is driven by the injected kinetic energy. Its position is given by the energy which propagates from the bottom of the pile (where agitation occurs) to the upper surface of the sample, where evaporation and thereby the transition to coexistence is taking place. The relevant energy scale is the energy which is needed to break a liquid bridge between two adjacent grains. Aside from these two transitions, which in the plane spanned by the acceleration and agitation velocity are represented by a horizontal and a vertical straight line, respectively, there are as well a number of non-universal features, which mainly show up in the transition from fluid-gas coexistence to the gas phase. These depend notably on geometric relations like the size of the container, and are furthermore strongly dependent on the inelasticity of the grains.

References

1. H.M. Jaeger, S.R. Nagel, R.P. Behringer, Rev. Mod. Phys. **68**, 1259 (1996)
2. J. Duran, *Sands, Powders and Grains* (*An Introduction to the Physics of Granular Materials*) 1st edn. (Springer-Verlag, New York, Inc., 2000)
3. F. Melo, Phys. Rev. Lett. **75**, 3838 (1995)
4. W. Losert, D.G.W. Cooper, J.P. Gollub, Phys. Rev. E **59**, 5855 (1999)
5. P.B. Umbanhowar, F. Melo, H.L. Swinney, Nature **382**, 793 (1996)
6. A. Goetzendorfer, J. Kreft, C.A. Kruelle, I. Rehberg, D. Svensek, Phys. Rev. Lett. **95**, 135704 (2005)
7. A. Goetzendorfer, C.A. Kruelle, I. Rehberg, D. Svensek, Phys. Rev. Lett. **97**, 198001 (2005)
8. I.S. Aranson, L.S. Tsimring, Rev. Mod. Phys. **78**, 641 (2006)
9. K. Huang, G.Q. Miao, P. Zhang, R.J. Wei, Phys. Rev. E **73**, 041302 (2006)
10. P.M. Reis, R.A. Ingale, M.D. Shattuck, Phys. Rev. Lett. **96**, 258001 (2006)
11. A. Prevost, P. Melby, D.A. Egolf, J.S. Urbach, Phys. Rev. E **70**, 050301 (2004)
12. R.D. Wildman, D.J. Parker, Phys. Rev. Lett. **88**, 064301 (2002)
13. L. Bocquet, E. Charlaix, F. Restagno, C. R. Physique **3**, 207 (2002)
14. S. Herminghaus, S., Adv. Phys. **54**, 221 (2005)
15. N. Mitarai, F. Nori, Adv. Phys. **55**, 1 (2006)
16. M. Scheel, D. Geromichalos, S. Herminghaus, J. Phys. Condens. Matter **16**, S4213 (2004)
17. M. Scheel, R. Seemann, M. Brinkmann, M. Di Michiel, A. Sheppard, B. Breidenbach, S. Herminghaus, Nat. Mat. **7**, 189 (2008)
18. A. Fingerle, K. Roeller, K. Huang, S. Herminghaus, New J. Phys. **10**, 053020 (2008)

Eur. Phys. J. Special Topics **179**, 19–24 (2009)

DOI: 10.1140/epjst/e2010-01190-6

THE EUROPEAN PHYSICAL JOURNAL SPECIAL TOPICS

Regular Article

The rotation-reptation transition under broken rotational symmetry

A. Feltrup[1], K. Huang[1], C.A. Krülle[2], and I. Rehberg[1]

[1] Experimentalphysik V, Universität Bayreuth, 95440 Bayreuth, Germany
[2] Maschinenbau und Mechatronik, Hochschule Karlsruhe – Technik und Wirtschaft, 76133 Karlsruhe, Germany

Abstract. In a swirled circular container, granular particles can change their sense of rotation when the packing density is increased, exhibiting a transition from rotational to reptational motion. In addition, here we report a 'snake mode' that arises at a lower packing density, where particles form a chain like cluster that rotates with the same frequency as the container. We investigate experimentally transitions between these three modes under the influence of geometrical distortions which break the rotational symmetry of the container. The driving mechanism for the rotational motion of the clusters is also discussed.

Due to its ubiquity in nature, industry and our daily lives, granular matter has attracted interest from both engineering and scientific communities over centuries [1–3]. Because of the energy dissipation through internal friction and inelastic collisions between particles, agitated granular matter is generally speaking in a non-equilibrium state. Therefore it acts also as a model system to study systems far from equilibrium. In the past decades, many interesting phenomena of granular matter under the driving of vertical or horizontal vibrations have been discovered, for instance pattern formation [4,5], localized excitation [6,7], and size or density segregation [8–10]. For granular matter, we are now able to determine the movements of particles with the aid of high speed photography, which enables us to explore this non-equilibrium system at both 'microscopic' and 'macroscopic' levels [11,12]. In addition, computer simulations could be employed to explain various phenomena including pattern formation, cluster formation, and inelastic collapse [4,13–15].

Here we focus on a quasi two-dimensional system driven by horizontal swirling. A motion not only frequently used to stir up the bouquet of a glass of wine, but also to agitate the particles in vibrational mills [16,17]. Moreover this motion proved to be able to enhance the efficiency of pneumatic conveying [18], which is widely applied in many chemical engineering and industrial processes. Such a quasi two-dimensional system is conceptionally simple since gravitation plays no role. As a technical advantage, here one is able to trace all particles with the help of image processing procedures.

Former studies on such a system reveal that the sense of rotation of the granular materials changes with the packing density [19]. At lower packing densities, the cluster rotates with the same direction as the swirling container (rotation mode). At higher packing densities, the rotation changes its direction and the diffusivity of particles within the cluster is dramatically reduced (reptation mode). This is a robust phenomenon and frequently observed in various industrial processes, for example in the vibrational mills for grinding feed materials [16,17]. Further studies indicate that this transition occurs also in a one dimensional swirling annulus [20]. In a follow-up study [21], the particles are found to be embedded into a solid-like cluster in the reptation mode. This is discovered by recording the trajectory of a tracing particle and

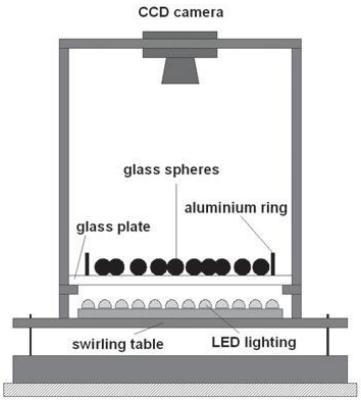

Fig. 1. Sketch of the experimental setup.

compare the density and temperature in different modes. Later on, similar image processing techniques are employed to study horizontal particle segregation, the Brazil-Nut effect and its inverse [22–24].

To understand the transitions between different modes of the cluster rotation, it is necessary to know the driving mechanism for the clusters. For the swirling table, one might speculate that the rotational symmetry of the driving wall is essential for the rotational motion of the clusters. Based on this speculation, we raise the question how stable those modes are under a broken rotational symmetry. In order to answer this question, we introduce one or two obstacle particles into the container in a systematic way and measure the rotational velocity of clusters.

A device similar to the one used in Ref. [19] is used for the experiments, as sketched in Fig. 1. The container consists of an aluminium ring with an inner diameter of 10.5 cm mounted on a glass plate. It is vibrated horizontally, performing a so called *swirling* motion. It means that every point of the container is moving along a circular path described by $x = Acos(2\pi f_d t)$ and $y = Asin(2\pi f_d t)$, where A is the amplitude and f_d the driving frequency. In our experiment the amplitude of the motion is set to 1.59 cm and the driving frequency to 1.67 Hz in a counterclockwise direction (viewed from above). The dish is filled with glass beads with a diameter $D = 10.0 \pm 0.02$ mm and a density of 2.5 g/cm^3. The maximum number of spheres which can fit into a monolayer is 88. To disturb the rotational symmetry obstacles made out of aluminium spheres with a diameter of 10 mm are fixed to the glass plate. The granular sample is illuminated from below by a LED array. A charge coupled device (CCD) camera is mounted on top of the swirling table to take pictures in the comoving frame. The images captured by the camera are then subjected to an image processing procedure to locate and trace all the particles in the container. The particle tracking is based on the Hough transformation adapted to detect circular objects [25]. After this procedure, we are able to obtain both the position and the velocities of all the particles at all time for different measurements.

Without any fixed obstacles, we observe three different kinds of motion of clusters depending on the number of particles inside the dish. Visualization of cluster motions in different modes are shown as insets in Fig. 2(a). The trajectories of randomly selected beads are superimposed on the snapshots taken by the camera. At low particle numbers all beads travel to the border after a short time, forming a snake-like cluster which travels along the container wall with the same frequency and direction as the driving. The formation of this so called snake mode, first observed by M. Raithel, depends on the size of the dish and couldn't be observed in larger dishes [26]. The dependency of dish radius and driving parameters on the formation of this mode is still under investigation. When the particle number is higher than a certain value, the beads start to pile up in the radial direction, entering a so-called rotation mode. The cluster still rotates counterclockwise but with a lower frequency than the driving. As the particle trajectories indicate, the motion of particles within the cluster is more randomized. Further

increase of the particle number slows down this rotation, until at a critical particle number N_c the rotation stops. Beyond this particle number, the cluster starts to rotate in the opposite direction, performing a motion called reptation. From the hypocycloidal trajectories, one could assume that the granular matter is in a solid-like state [21]. A description of the second and third motion was already presented in Ref. [19].

To get a quantitative expression of this behavior, we look at the cluster rotation frequency f around its center of mass, which is calculated as:

$$f = \frac{1}{2\pi N} \sum_{i=1}^{N} \left\langle \frac{\mathbf{r}_i^* \times \mathbf{v}_i^*}{|\mathbf{r}_i^*|^2} \right\rangle_t \tag{1}$$

with $\mathbf{r}_i^*$ and $\mathbf{v}_i^*$ the positions and velocities of the particles relative to the center of mass and $\langle\rangle_t$ the time average for each particle.

$$\mathbf{r}_i^* = \mathbf{r}_i - \frac{1}{N} \sum_{j=1}^{N} \mathbf{r}_j \tag{2}$$

$$\mathbf{v}_i^* = \mathbf{v}_i - \frac{1}{N} \sum_{j=1}^{N} \mathbf{v}_j \,. \tag{3}$$

This rotation frequency is then rescaled by the driving frequency f_d to get the normalized cluster rotation frequency f_c

$$f_c = \frac{f}{f_d}. \tag{4}$$

Figure 2(a) shows the normalized cluster rotation frequency as function of the particle number without any fixed obstacles. The transition from snake to rotation mode happens at $N = 17$. Further increase of the particle number leads to a drop of the rotation frequency to around 0.4 of the driving and in this mode particles no longer move in a collective manner. For the particle number range between 23 and 46, a plateau regime is observed, where the cluster rotation is insensitive to the number of particles in the container. When the number of particles is increased further, the cluster slows down until at $N_c = 66$ the rotation changes its direction and the cluster enters a reptation mode.

The effect of breaking the rotational symmetry by inserting fixed obstacles into the system can be seen in Fig. 2(b). If the obstacle is fixed at the center of the dish, the cluster rotation is almost undisturbed. One interesting feature is that in the rotation or reptation mode, the cluster rotation frequency is slightly higher than without any obstacles and the rotation-reptation transition increases to $N_c = 69$. This reveals that the system is more favorable to the rotational mode in this case. If the obstacle is placed at a distance of $3.65\,D$ from the center of the container, leaving a gap of 1.1 particle diameters between the obstacle and the aluminium ring, the rotation-reptation transition reduces to $N_c = 63$ and the snake mode ends at $N = 15$. If we move the obstacle further to the border, a slight shift of the rotation-reptation transition to lower particle numbers can be observed as the critical value of $N_c = 61$ indicates. The snake mode is suppressed completely, which can be understood as the traveling path of the snake is blocked by the obstacle. By inserting a second obstacle at the opposite side of the container wall, not only the snake mode but also the rotation mode is nearly suppressed too, the critical particle number for the rotation-reptation transition is found at $N_c = 18$ for this configuration. This indicates that the reptation mode becomes more favorable.

To understand the different rotation frequencies below the critical particle number N_c, we look at the driving mechanism of the system. One driving source comes from collisions of the beads with the border of the dish, the other comes from the bottom of the container. In Fig. 2(c) we plot the ratio between the number of particles at the border and the overall number of particles in the container as function of the particle number for all configurations shown in Fig. 2(b). Without obstacle or with one obstacle at container center, the ratios show a constant

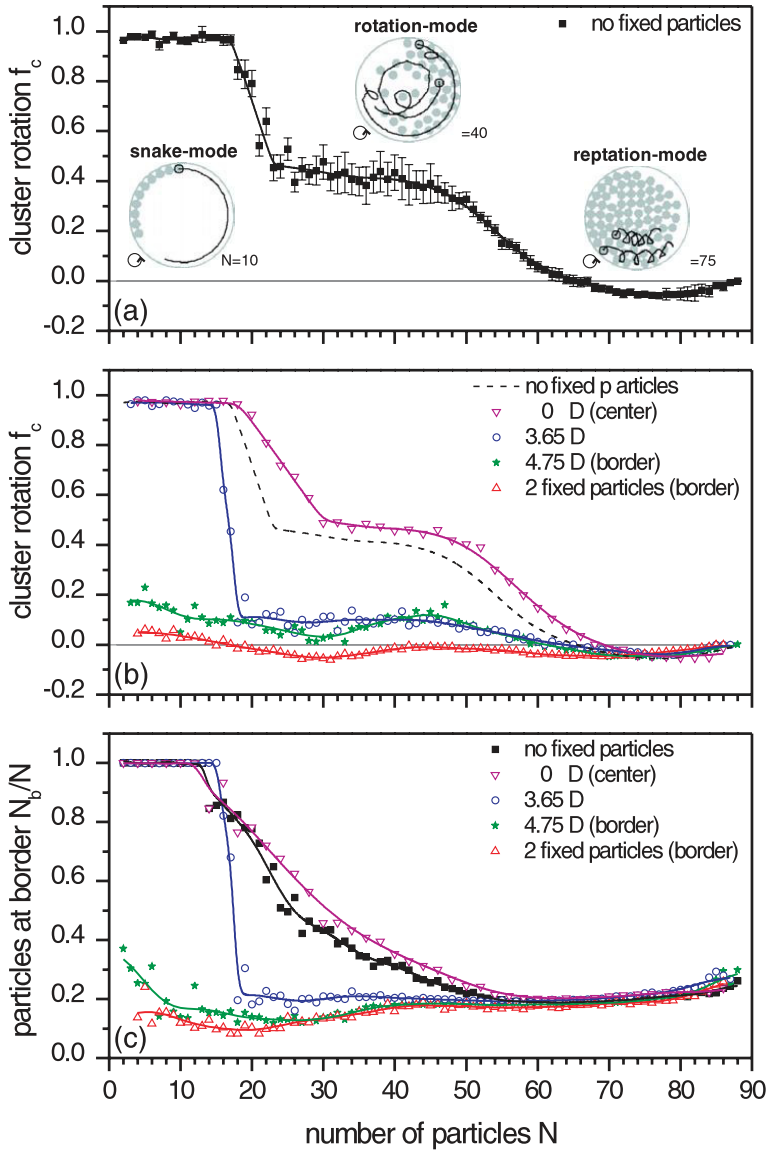

Fig. 2. (a) Rotation frequency of the cluster as a function of the number of particles N without fixed obstacles. Snapshots of images captured at different modes are shown as insets. Solid lines correspond to particle trajectories shown as examples. Particles surrounded by circles indicate the ends of the tracks. (b) Cluster rotation frequency as function of N with fixed obstacles. Different symbols correspond to different gap width between the obstacle and the container boundary in units of particle diameter D. With two fixed particles both are fixed at the boundary at opposing sides of the dish. The dashed line is a replot of (a) for comparison. (c) Ratio between particles at the border and the total number of particles as a function of N for the same configurations as above. The lines in all the plots are guide to the eyes.

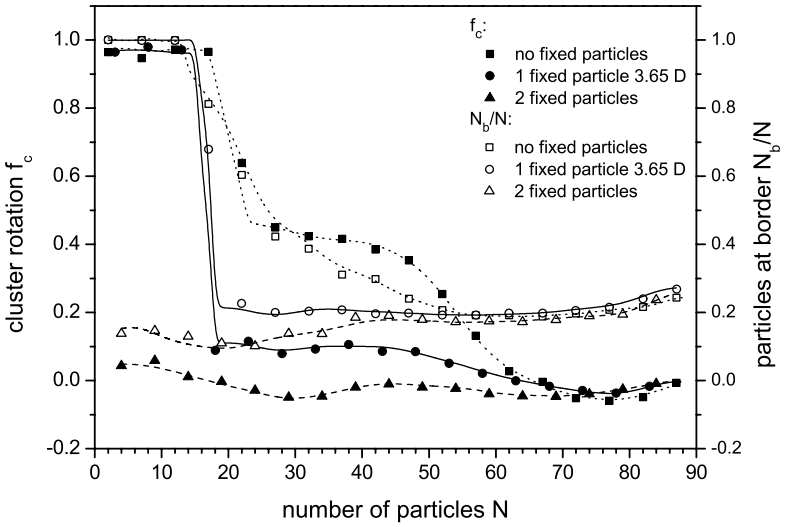

Fig. 3. Comparison between the cluster rotation and the fraction of particles at the border for three different configurations. The lines are guide to the eyes.

value of 1 for low particle numbers and thereafter a slow decay with the increase of particle number until they reach a fairly constant value of 0.2 at particle numbers of about $N = 60$. For the configuration with a gap that allows only one particle to pass through (corresponding distance from the center of the container $3.65\,D$), a sharp drop of the ratio is observed at the transition to the rotational mode happens. For the configurations with obstacles at the border we always have a fairly constant particle ratio of about $20 \pm 10\,\%$ at the border. For all configurations shown here, similarities between the rotation frequency and the fraction of particles at the border suggest that the driving of rotation mainly stems from the interaction from particles at the border with the container wall.

One might notice that for the configurations without any obstacles or with one obstacle at the center, the drop in the particle fraction at the border begins while the system is still in the snake mode according to the rotation frequency. This can be understood by the fact that at $N \geq 13$ particles can be found in the second row adjacent to the snake travelling with the same frequency as the snake itself. This results in a drop in the particle fraction while leaving the rotation frequency unchanged. In the case that the gap between obstacle and the container wall only allows one particle to pass through, this effect is suppressed so that the drop happens at the same particle number.

To have a direct comparison between the normalized cluster rotation frequency and the fraction of particles at the border, we replot both of them for 3 different configurations in Fig. 3. The correlation between the two curves for each configuration indicates that the main driving force for the rotation of the cluster comes from the border of the container, while the bottom of the container plays a minor role.

To summarize, we study the rotation of swirling quasi two-dimensional granular clusters under a distorted geometry. Depending on the packing density, granular particles might rotate in a snake mode, rotation mode or reptation mode. The rotation frequency of clusters in the snake mode and the rotation mode depends sensitively on the distance between the obstacle and the container wall. When the obstacle is close to the center of the container, it indeed speeds up the rotating motion. This observation might have potential applications in industry to improve the efficiency of transport or mixing processes. In contrast, if the obstacle is fixed closer to the container border, the reptation mode is favored. Once the gap between the obstacle and container border is smaller than a particle diameter, the 'snake mode' vanishes and the rotation

frequency is dramatically reduced. The dependance of the rotation frequency of clusters on the particle number at the container border reveals that the rotation motion of clusters is mainly driven by the container wall.

We thank Sonia Utermann-May for her comments on the manuscript. This work is partly supported by Forschergruppe 608 'Nichtlineare Dynamik komplexer Kontinua'.

References

1. J. Duran, *Sands, Powders and Grains: Introduction to the Physics of Granular Materials* (Springer-Verlag, New York, 1999)
2. H.M. Jaeger, S.R. Nagel, R.P. Behringer, Rev. Mod. Phys. **68**, 1259 (1996)
3. R. García-Rojo, H.J. Herrmann, S. McNamara, eds., *Powders and Grains* (A.A.Balkema, Rotterdam, 2005)
4. F. Melo, P.B. Umbanhowar, H.L. Swinney, Phys. Rev. Lett. **75**, 3838 (1995)
5. E. Clément, L. Vanel, J. Rajchenbach, J. Duran, Phys. Rev. E **53**, 2972 (1996)
6. P.B. Umbanhowar, F. Melo, H.L. Swinney, Nature **382**, 793 (1996)
7. L.S. Tsimring, I.S. Aranson, Phys. Rev. Lett. **79**, 213 (1997)
8. N. Burtally, P.J. King, M.R. Swift, Science **295**, 1877 (2002)
9. P.M. Reis, T. Mullin, Phys. Rev. Lett. **89**, 244301 (2002)
10. A.P.J. Breu, H.M. Ensner, C.A. Kruelle, I. Rehberg, Phys. Rev. Lett. **90**, 014302 (2003)
11. S. Warr, J.M. Huntley, G.T.H. Jacques, Phys. Rev. E **52**, 5583 (1995)
12. J.C. Crocker, D.G. Grier, J. Coll. Interf. Sci. **179**, 298 (1996), ISSN 0021-9797
13. I.S. Aranson, L.S. Tsimring, Rev. Mod. Phys. **78**, 641 (2006)
14. I. Goldhirsch, G. Zanetti, Phys. Rev. Lett. **70**, 1619 (1993)
15. T. Pöschel, N. Brilliantov, *Granular Gas Dynamics* (Springer, 2003)
16. T. Yokoyama, H. Tamura, H. Usui, G. Jimbo, in *Proceedings of the Eighth European Symposium on Comminution*, edited by E. Forssberg (1994), p. 413
17. T. Inoue, K. Okaya, in *Proceedings of the Eighth European Symposium on Comminution*, edited by E. Forssberg (1994), p. 425
18. H. Li, Y. Tomita, Powder Technol. **107**, 144 (2000)
19. M.A. Scherer, V. Buchholtz, T. Pöschel, I. Rehberg, Phys. Rev. E **54**, R4560 (1996)
20. M.A. Scherer, T. Mahr, A. Engel, I. Rehberg, Phys. Rev. E **58**, 6061 (1998)
21. M.A. Scherer, K. Kötter, M. Markus, E. Goles, I. Rehberg, Phys. Rev. E **61**, 4069 (2000)
22. S. Aumaître, C.A. Kruelle, I. Rehberg, Phys. Rev. E **64**, 041305 (2001)
23. T. Schnautz, R. Brito, C.A. Kruelle, I. Rehberg, Phys. Rev. Lett. **95**, 028001 (2005)
24. D.C. Hong, P.V. Quinn, S. Luding, Phys. Rev. Lett. **86**, 3423 (2001)
25. C. Kimme, D. Ballard, J. Sklansky, Commun. ACM **18**, 120 (1975), ISSN 0001-0782
26. M. Raithel, Diploma thesis, Universität Bayreuth (2009)

Phase transitions far from equilibrium in wet granular matter

2008 New J. Phys. 10 053020

(http://iopscience.iop.org/1367-2630/10/5/053020)

New Journal of Physics
The open-access journal for physics

Phase transitions far from equilibrium in wet granular matter

A Fingerle, K Roeller, K Huang and S Herminghaus[1]
Max Planck Institute for Dynamics and Self-Organization, Bunsenstrasse 10, 37073 Göttingen, Germany
E-mail: axel.fingerle@ds.mpg.de, klaus.roeller@ds.mpg.de, kai.huang@ds.mpg.de and stephan.herminghaus@ds.mpg.de

New Journal of Physics **10** (2008) 053020 (10pp)
Received 28 January 2008
Published 15 May 2008
Online at http://www.njp.org/
doi:10.1088/1367-2630/10/5/053020

Abstract. The phase diagram of vertically agitated wet granular matter is presented, both experimentally and by simulation. We observe two phase transitions, one of which is driven by the applied force (acceleration), the other by injected energy (velocity of container walls). All observed features can be traced down to the hysteretic nature of capillary bridge formation and rupture. Other details of the interaction are remarkably irrelevant, suggesting a certain universality for the investigated phenomena.

Phase transitions in condensed matter under thermally equilibrated conditions are by far the best understood examples of collective behavior. The astonishing fact that a solid melts at a precisely defined temperature, although the thermal energy is broadly distributed among the many degrees of freedom, can be completely apprehended from the principle of free energy minimization. Furthermore, the role of thermal fluctuations, which lead to the striking universality near critical points, was cast into a closed theory by means of the renormalization group [1]. Hence, the physics of phase transitions at thermal equilibrium has matured into solid textbook knowledge (see, for instance [2]).

Phase transitions far from equilibrium, on the contrary, are still far from being understood on such a general basis, despite their ubiquity and striking similarity. Well-known examples that are currently of great interest range from collective pattern formation in systems of molecular [3] and micron scale [4, 5] to transitions in social behavior [6]–[8]. In particular, dynamic transitions in granular matter, such as soil liquefaction due to earthquakes, fluidization by vibration, or phase separation ([9]–[18]; [19] and references therein) are examples in systems of great practical interest. As the strength of the external drive is varied, sudden changes in the

[1] Author to whom any correspondence should be addressed.

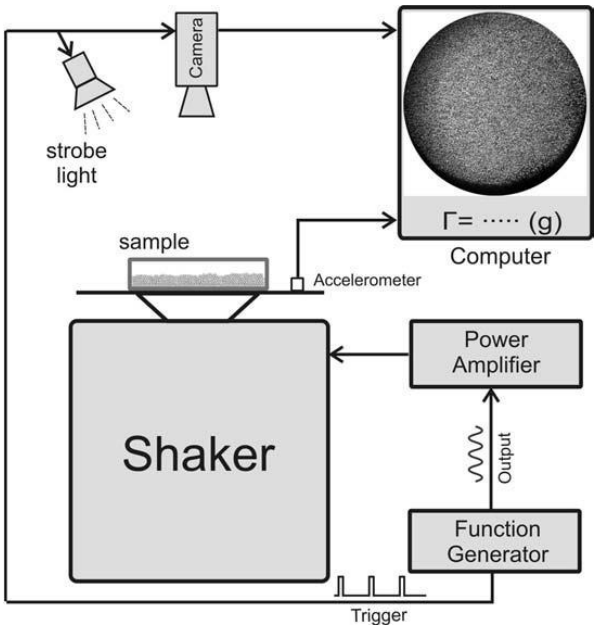

Figure 1. Sketch of the experimental set-up. Strobe light illumination enables accurate assessment of the phase boundary between the solid and the liquid phase. Image acquisition with a well-defined time lapse is necessary as well for a reliable determination of the (spatially varying) granular temperature.

dynamical behavior of the granulate can be observed. Furthermore, it has become apparent that *wet* granular matter provides a particularly well-suited model system for the study of such phenomena [19]–[21]. The main difference between dry and wet granular systems is that in the latter, liquid capillary bridges forming between adjacent grains provide a well-defined energy scale determined by the surface tension of the liquid [19, 22]. In the present paper, we analyze the dynamics of wet granular matter under vertical agitation in a closed container. We present the phase diagram and demonstrate that many of its features are quantitatively independent of the details of the 'microscopic' interaction mediated by the capillary bridges. This may be viewed as some kind of universality in its own right.

As a well-defined granular system, we chose spherical glass beads (density of the glass $\approx 2.5\,\mathrm{g\,cm^{-3}}$), which can be purchased in large quantities and with reasonable quality. They are widely used as model granulates and thus provide good comparability with other studies. The average diameters of the spheres ranged from 0.5 to 1.5 mm. The width of the size distribution was about 10% of the average diameter in each sample. As the liquid, we used water in most experiments, and sometimes *n*-nonane for comparison. Both liquids wet the glass surface well, with a contact angle below 10°. The main difference is the surface tension, γ, which is $72\,\mathrm{mN\,m^{-1}}$ for water and $24\,\mathrm{mN\,m^{-1}}$ for nonane. This allows for comparing strongly different rupture energies of the capillary bridges. A wide cylindrical container (14 cm diameter petri dish with lid, cf figure 1) was used in order to eliminate side wall effects, which had been reported to dominate fluidization in narrow containers [21]. The petri dish was filled to about two-thirds of its height with granulate, mounted on an electromagnetic vertical shaker, the lid closed and set in

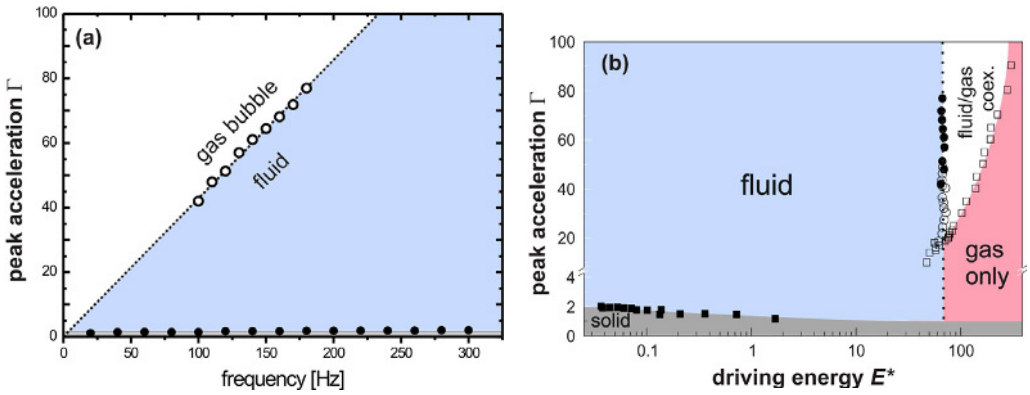

Figure 2. (a) Experimental phase diagram of wet granular matter under vertical agitation ($R = 850\,\mu$m, $w = 0.41\%$; water as the liquid). (b) Same as (a), but presented in the plane spanned by the parameters Γ and E^*. The data for water (closed) and n-nonane (open) collapse in this plot. Note that the vertical scale has been split for proper presentation of the solid/fluid phase boundary.

oscillatory motion, $z(t) = A\cos(2\pi\nu t)$. The dimensionless peak acceleration, $\Gamma = 4\pi^2 A\nu^2/g$ (where g is the acceleration due to gravity) serves as a control parameter. Typical frequencies are a few hundred Hertz. For Γ below and around one, the gravitational force on the granular pile, as viewed in the rest frame of the petri dish, is always pointing downwards, although sinusoidally varying in magnitude. As a consequence, the grains are never lifted from their support, and the position of each grain within the sample remains fixed [9]. This represents a solid condensed state. It should be noted that the capillary bridges are much smaller than the glass beads, and thus small as compared to the capillary length of the liquids used, which is around 2 mm.[2] Gravity effects on the distribution of the liquid can thus be safely neglected.

As Γ is increased above unity by increasing A, the pile periodically experiences a lifting force. For a dry granulate, this leads to fluidization at a certain threshold, $\Gamma_c \approx 1.2 =: \Gamma_{dry}$ [9]. It manifests itself by the onset of a mild movement of the grains, as revealed by direct visual inspection. As liquid is added to the granulate, Γ_c increases strongly. This corresponds to the dramatic difference in mechanical strength observed between a dry granulate, which flows almost like a liquid, and the visco-plastic texture of a wet granulate [19]. It was shown before that the increase in Γ_c can be well understood from the attractive interaction due to the liquid capillary bridges forming between adjacent spheres [19, 21]. In particular, the excess $\Gamma - \Gamma_{dry}$ must be just large enough to overcome the forces exerted by these bridges by virtue of the surface tension of the liquid. Confirming earlier measurements [21], we found Γ_c to be largely independent of frequency. This can be clearly seen in figure 2(a), where the closed circles indicate the transition between the solid (below, gray) and the fluidized (above, blue) state.

At sufficiently high Γ, we could observe an additional transition, which is indicated by the open circles in figure 2(a). Above this line, a dense fluidized phase coexists with a dilute gas-like phase. The latter shows up as a 'gas bubble', an example of which can be seen in

[2] The capillary length is given by $\sqrt{\gamma/\rho g}$, where ρ is the density of the liquid. It is 2.7 mm for water and 1.7 mm for n-nonane.

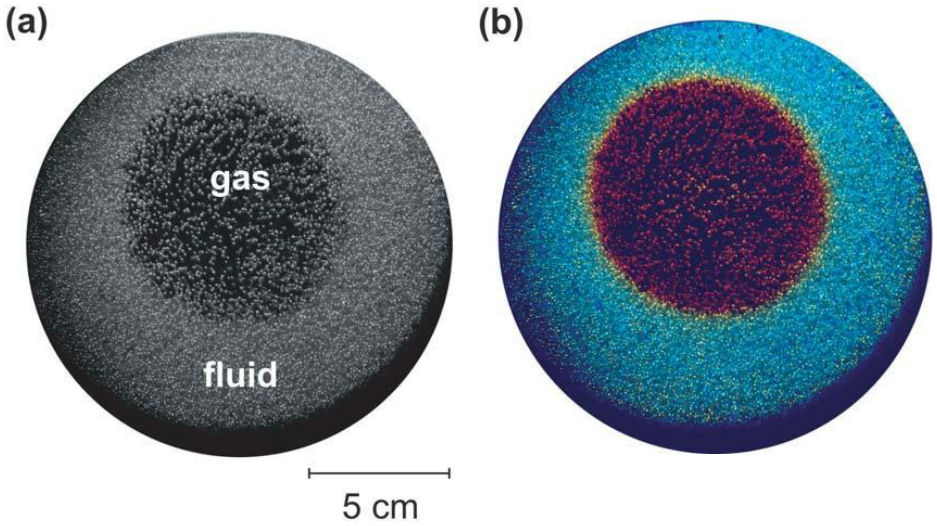

Figure 3. Fluid-gas coexistence. (a): top view of the experimental set-up at high excitation. The petri dish is illuminated from above and observed in reflection. The glass spheres appear as bright dots. In the middle of the sample, a large gas bubble is clearly visible, while the outer part is filled with a condensed fluidized phase (a video is available online[3]). (b): same snapshot as in (a) but colored according to temporal autocorrelation. The color scale extends from blue (slow movement) to red (fast movement).

figure 3. The bubble is found to sometimes wander around in the container, which shows that its presence is not linked to a lateral inhomogeneity in the excitation amplitude, but is intrinsic to the system under study.

In order to assess the granular temperature in either phase, i.e. the average kinetic energy of the glass beads, we determined their velocity qualitatively by means of a simple autocorrelation procedure. Images were taken with a fast video camera at two consecutive periods of the agitation. They were subtracted from each other, and the square of the result was taken, in order to obtain a measure for the temporal changes in brightness. This was averaged over areas small enough to contain not more than one bead at a time (5×5 pixels). The result, which qualitatively captures the horizontal component of the velocity, was encoded in color, with blue corresponding to little movement and red corresponding to strong movement. The color scale extends to about $3\,\mathrm{cm\,s^{-1}}$ at dark red. Clearly, a large difference in the granular temperature is found between the gas phase and the fluid phase. This is in sharp contrast to two-phase coexistence as commonly known from equilibrium systems, where temperature is uniform in the steady state.

An obvious feature of figure 2(a) is that the data suggest the phase boundary between the fluid-state and the fluid-gas coexistence to be a straight line meeting the origin of the diagram (dotted line). The quantity Γ/ν, which is proportional to the peak velocity of the container walls, is constant along this line. This is interesting in view of earlier experiments using a different

[3] See stacks.iop.org/NJP/10/053020/mmedia 'Experiment'. The frame rate in the movie is equal to the shaking frequency ($50\,\mathrm{s^{-1}}$). The particles are 1.09 mm diameter glass beads, wetted by water.

agitation scheme [14], where a pronounced transition, reminiscent of condensation from a gas into a viscous fluid, occurred when the peak velocity of the container walls came below a critical value, v_c. This value was found to correspond to the kinetic energy a bead must have in order to rupture the liquid bridge binding it to a neighboring bead. It is given by $\frac{m}{2}v_c^2 = E_{cb}$, where m is the mass of the glass bead and $E_{cb} \propto R^2\gamma\sqrt{w}$ is the energy needed to rupture a capillary bridge [19], [23]–[26]. R is the radius of the beads and w denotes the liquid content of the sample, defined as the volume of the added liquid divided by the total volume of all glass spheres. Following this view, it is convenient to introduce the characteristic dimensionless 'driving energy', $E^* := \frac{m}{2}v^2/E_{cb}$, where $v = 2\pi Av$ is the peak velocity of the container walls (bottom and lid in our experiment). E^* corresponds to the typical energy of a bead close to the container wall in a dense granulate, where the motion of the walls largely determines the velocity of the glass beads close to it. E^* will henceforth be considered as an alternative control parameter. By varying A and ν, the two parameters Γ and E^* can be controlled independently.

It is enlightening to plot the loci of the observed transitions in the plane spanned by Γ and E^*. The result is shown in figure 2(b). The transition from the solid (gray) to the fluid phase (blue) is represented by a more or less horizontal line, indicating that this transition is independent of energy, but driven by acceleration (Γ). In contrast, the fluid phase is separated from the fluid/gas coexistence region (white) by a vertical line, indicating a transition driven by injected energy (E^*), but independent of force. The perfect matching of the data obtained for water (closed) and *n*-nonane (open), the surface tension of which is a factor of 3 smaller than that of water, strongly suggests that our scaling of the driving energy with respect to the bridge rupture energy, E_{cb}, is physically appropriate. As the amplitude was further increased, the container was finally filled homogeneously with a hot gas phase. This is represented as the red shaded area in the figure.

In order to demonstrate the essential role of the capillary bridges, we performed molecular dynamics type simulations in two-dimensions (2D) with ideally circular, frictionless discs mimicking the glass beads. The attractive pairwise *hysteretic* interaction potential [19, 21] illustrated in the inset of figure 4 models the capillary bridges (dotted: approach and solid: retract). The repulsion between particles is modeled by a Hertz-potential ($\propto (-s)^{5/2}$), which is turned on for negative s only. The bridge is thus assumed to exert a constant force upon retraction, and to rupture at a distance s_c. A gravitational force acting in the vertical direction is included in the simulations as well. The liquid content per grain is assumed to be the same everywhere. This is justified from the experimental observation that the liquid distributes rapidly in the sample, and quite evenly on each sphere after impact [27]. At the top of figure 4, a snapshot of a 2D stationary state is shown, as obtained by 2D simulation (one lateral and one vertical coordinate). It is clearly seen that the simulation produces a dense plug as well as a gaseous region, which are in coexistence with each other.

In the main panel of figure 4, the density as well as the granular temperature, $T = \langle E_{kin}\rangle$, in units of the rupture energy, E_{cb}, are plotted as a function of the lateral coordinate, on the same scale as the simulation box above. The granular temperature is found to vary over two orders of magnitude. This clearly demonstrates, in accordance with the experiment, that the observed phenomenon is by no means akin to coexistence between thermodynamic phases, but is an intrinsically non-equilibrium state. The appearance of a cold dense phase in coexistence with a dilute hot phase complies qualitatively with earlier results obtained with *magnetically* cohesive granular beads [15]. Although that system does not exhibit a defined energy loss scale, as opposed to the system we study here, the essential feature is similar: in the dense phase,

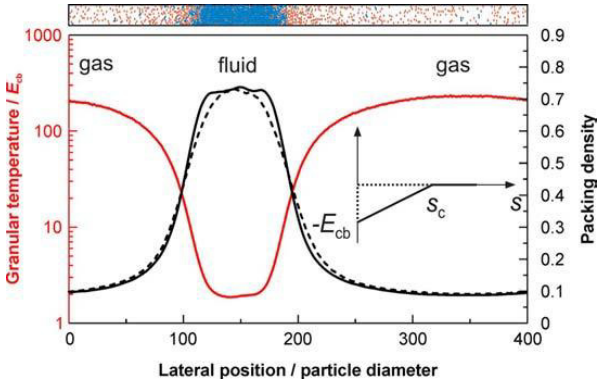

Figure 4. Box on top: snapshot of molecular dynamics type simulation of 1200 particles at parameters where fluid/gas coexistence occurs (a video is available online[4]). Blue grains have at least one liquid bridge, red grains have none. Main panel: plot of the granular temperature (red curve) and the number density (solid black curve) on the same scale as the simulation box above. The temperature varies laterally over two orders of magnitude, being high in the gas, but very low within the fluid plug. The density is also shown for event-driven simulations (dashed black curve, square well potential).

where the mean free path is small, the collision frequency is high. This gives rise to strong dissipation, and hence to very effective cooling.

Figure 5(a) shows the phase diagram as obtained from the simulations, in the same plane as figure 2(b), but on log/linear scale to better reveal the details. We clearly see the horizontal line separating the solid (gray) from the fluid phase (blue) or, at higher E^*, form a solid/gas coexistence (white). As found in the experiments, the fluid phase is separated from the fluid/gas coexistence by a vertical line. The fluid/gas coexistence region is bounded by a second line located at larger driving energy, which indicates the transition to a homogeneous gas-like state (red). In this transition line, a bulge is observed where the excitation amplitude A equals the rupture length s_c of the capillary bridges. Unfortunately, scaling the simulation parameters according to the experimental conditions (note that the simulation is 2D) reveals that this bulge is just out of the range accessible to our experimental set-up.

In figure 5(b), we replotted the coexistence region in the plane spanned by the driving energy, $\frac{m}{2}v^2$, and the capillary bridge energy, E_{cb}. We rescaled them as $\tilde{E}_{kin} := mv^2/2F_g s_c = v^2/2gs_c$ and $\tilde{E}_{cb} := E_{cb}/F_g s_c$, respectively. Obviously, $\tilde{E}_{kin} \propto E_{cb}$ for both transition lines, supporting that this transition is exclusively governed by the bridge rupture energy. The gravitational energy scale naturally separates out, in contrast to dry granulates [16]. The only marked difference between the simulation (figure 5(a)) and the experiment (figure 2(b)) is the value of E^* at which the fluid phase region ends.

This discrepancy can be removed by considering the impact of the inelasticity of the glass beads used in the experiments. Their restitution coefficient, ε, as determined experimentally for particle–wall collisions, was found to be $\varepsilon \approx 0.90 \pm 0.01$. Including this inelasticity in our simulations, we observed that the critical line shifted towards higher driving velocities by a

[4] See stacks.iop.org/NJP/10/053020/mmedia 'Simulation 2D'.

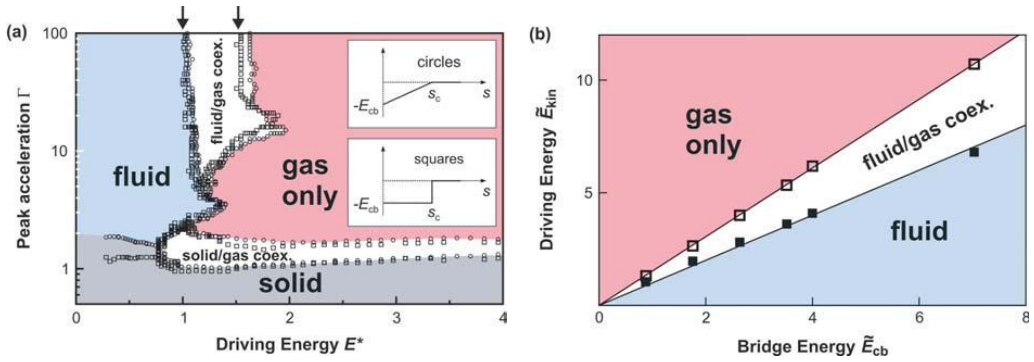

Figure 5. (a) Phase diagram from simulations with 1200 particles in 2D. The horizontal boundary of the solid phase is clearly obtained, as well as the vertical fluid/gas boundaries which are also seen in the experiment. The arrows at the top indicate the slopes of the lines in the inset of (a). The insets show the hysteretic interaction potentials chosen (dotted: approach and solid: retract). (b) Variation of the transition points with the surface tension, as obtained from our simulations. The transition energies scale precisely with E_{cb}. The slopes yield the critical (scaled) driving energies E^* as 1.00 ± 0.09 and 1.52 ± 0.02, respectively (arrows in (a)).

factor of 7.3 in 2D, and by a factor of 31 in 3D. Qualitatively, the phase diagram remained unchanged. Note that the characteristic Y shape of the phase boundaries, which is qualitatively observed in the experiment as well (figure 2(b)), entails the existence of a tricritical point at the lower tip of the coexistence region. It is of great interest how this compares to similar phenomena known from equilibrium physics [28, 29]. This will be the focus of a forthcoming study.

In order to investigate whether the observed behavior is of appreciable universality, we varied the interaction potential used in the simulations. In figure 5(a), the circles represent simulations assuming a constant capillary force upon retraction (triangular potential well, upper inset), while the squares were obtained assuming a square-well retraction potential, representing the limiting case of a delta-function force located at the rupture distance (square well, lower inset). As the figure clearly shows, even these extreme cases give almost identical results. The only significant difference is the position of the solid/fluid transition at small driving velocities, which is expected due to the vanishing contact force for the square-well potential. The other details found in the phase transition lines do not seem to depend crucially on the interaction characteristics. The only relevant ingredient of the latter is their being dissipative in the proposed hysteretic sense.

A particular significance of the square-well potential is that it leads to vanishing forces, except for a set of zero measure on the time axis. This enables event-driven simulations, which are much more economic in computational power than the full integration of the equation of motion. For the square-well potential, we can thus perform simulations with very many particles, and in 3D. For these simulations, we used hard-core repulsion between the particles. A 3D simulation at parameters corresponding to fluid/gas coexistence is shown in figure 6(a). The similarity with the experimental results displayed in figure 3 is obvious. As

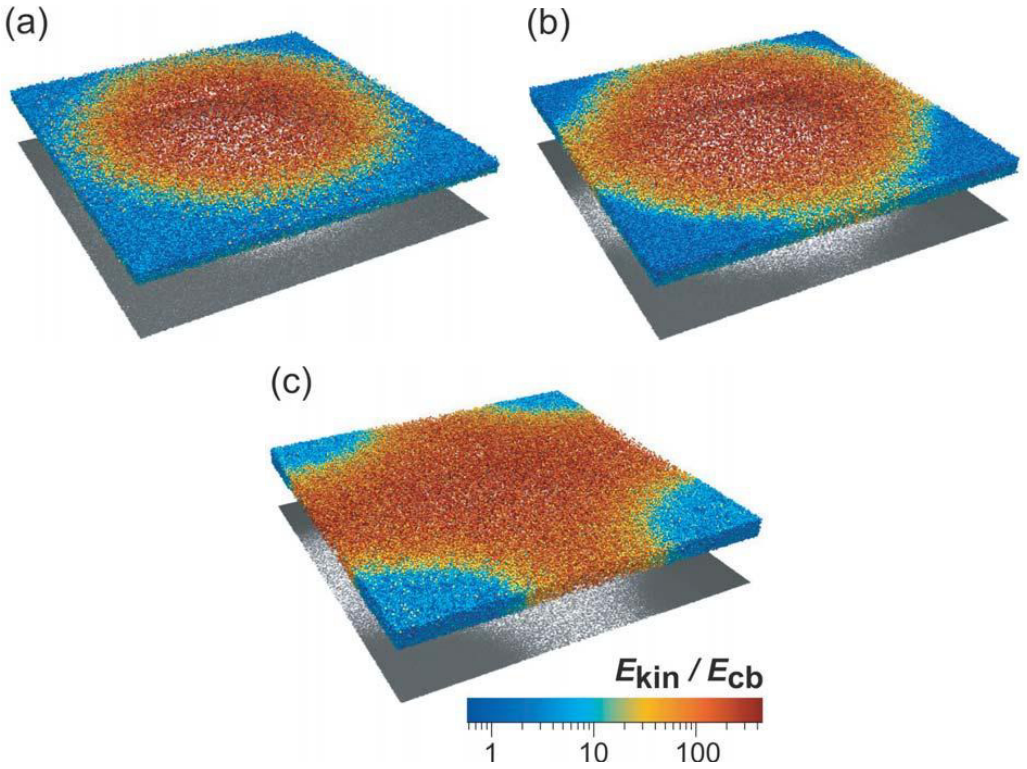

Figure 6. Snapshots of event-driven 3D simulations at early (a), intermediate (b), and late (c) stage (a video is available online[5]). The color indicates the kinetic energy of the grains, similar to figure 3(b). The 'shadow' is computed such as to imitate illumination from above, in order to account for the areal density of the particles (dark regions correspond to high density).

we let the bubble expand to system size, it finally reaches the boundaries of the box. Due to the periodic boundary conditions, this corresponds to a diamond-shaped condensed region centered at the corner between four adjacent replicas of the simulation boxes (figure 6(b)). Figure 6(c) shows the situation somewhat later. Clearly, the diamond shaped condensate region has rounded to a circular spot, strongly suggesting the presence of an interfacial tension. It appears prospectively interesting to investigate this in detail, since interfacial tensions are usually defined as equilibrium free energies, which certainly does not apply here. We note in this context that the force law has some noticeable influence on the interfacial density profile, as shown in figure 4 by the solid (triangular well, full integration) and dashed (square well, event driven) black curve.

Let us try to understand our findings in a more general framework. From the 'traditional' conditions invoked for the description of equilibrium phase transitions, only the homogeneity of the lateral pressure carries over to driven steady states, due to the required force balance at the phase boundaries. In contrast, the familiar uniformity of temperature breaks down. In what

[5] See stacks.iop.org/NJP/10/053020/mmedia 'Simulation 3D'.

IOP Institute of Physics DEUTSCHE PHYSIKALISCHE GESELLSCHAFT

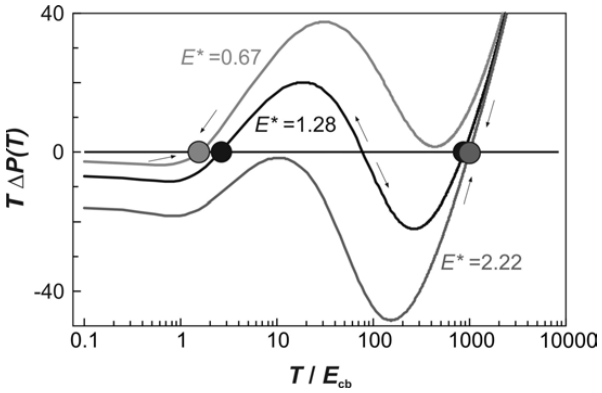

Figure 7. The net power, $\Delta P = P_{\mathrm{diss}} - P_{\mathrm{inj}}$, as a function of the granular temperature. ΔP is multiplied by the granular temperature here in order to achieve a clear presentation of data in a single graph. Depending on the driving energy E^*, we obtain either one (gray) or two (black) stable zeros, corresponding to a single phase or two-phase coexistence, respectively. The arrows denote the response of the system to small fluctuations.

follows, we ask for the mechanism by which the symmetry in the formerly homogenous system is broken, and how the system finds its steady state within the broken symmetry.

The power injected into the system from the oscillating walls, P_{inj}, must be balanced at each lateral position within the sample by dissipation, P_{diss}. Assuming a certain[4] velocity distribution for the grains, both quantities can be evaluated in a straightforward way, such that the net power $\Delta P(T) = P_{\mathrm{diss}} - P_{\mathrm{inj}}$ can be obtained as a function of temperature [20]. Clearly, in a dissipative system like the one under study, the velocity distribution will in general deviate from the 'usual' Gaussian [30, 31], exhibiting non-Gaussian 'tails'. However, these affect only a small fraction of the particles [31, 32] and are of minor impact on the average collision frequency, which in turn determines the dissipation rate. In order to compute the abovementioned quantities, it thus appears sufficient to use a Gaussian velocity distribution for the sake of simplicity.

Figure 7 shows the obtained result, displayed for three values of the driving energy, E^*. For $E^* < 0.67$, we obtain just one stable (i.e. positive slope) zero, which is at low temperature. It corresponds to a moderately dense state, which has just enough free volume for the critical separation s_c to be exceeded frequently enough to balance the injected power, P_{inj}. On the other hand, for $E^* > 2.22$, we have again only one stable zero, but this corresponds to a high temperature. It represents a dilute phase, the temperature of which is determined mainly by the balance of the energy uptake from the motion of the boundaries with the dissipation due to the 'wet' impacts with them.

At intermediate velocities (black curve in figure 7), two stable zeros (black circles) are obtained, one for low and one for high temperature. This is to be identified with the fluid/gas coexistence observed in the simulations as well as in the experiments for intermediate velocities. Since this continuum theory does not take gravity into account, it is intrinsically independent of the parameter Γ used in figure 5, and thus corresponds to the vertical lines in the phase diagram. The mean field model predicts the coexistence in the stripe $0.67 < E^* < 2.22$ of the

phase diagram, which compares quite favorably with figure 5(b) for $\Gamma \gg 1$ (where gravity is irrelevant) given the crudeness of the involved assumptions.

We thus have shown by experiments, simulation and analytical theory that the phase diagram of wet granular matter under vertical agitation can be quite well understood on the basis of a very simple model, which only takes the hysteretic formation and rupture of capillary bridges into account. The weak dependence of the phase diagram on details of this interaction is remarkable, and indicates significant universality of the obtained results.

Acknowledgment

Inspiring discussions with Stephan Ulrich, Annette Zippelius and Mario Liu are gratefully acknowledged.

References

[1] Wilson K G and Kogut J 1974 *Phys. Rep.* **12** 75
[2] Yeomans J M 1992 *Statistical Mechanics of Phase Transitions* (Oxford: Oxford University Press)
[3] Ertl G and Imbihl R 1995 *Chem. Rev.* **95** 697
[4] Fox J J, Gilmour R F Jr and Bodenschatz E 2002 *Phys. Rev. Lett.* **89** 198101
[5] Chakrabarti J, Dzubiella J and Löwen H 2004 *Phys. Rev.* E **70** 012401
[6] Farkas I, Helbing D and Vicsek T 2002 *Nature* **419** 131
[7] Vollmer J, Vegh A G, Lange Ch and Eckhardt B 2006 *Phys. Rev.* E **73** 061924
[8] Sumpter D J T 2006 *Phil. Trans. R. Soc.* B **361** 5
[9] Duran J 2000 *Sands, Powders, and Grains* (New York: Springer)
[10] Nagel S R 1992 *Rev. Mod. Phys.* **64** 321
[11] van der Weele K, van der Meer D, Versluis M and Lohse D 2001 *Europhys. Lett.* **53** 328
[12] Iveson S M, Litster J D, Hapgood K and Ennis B J 2001 *Powder Technol.* **117** 3
[13] Samadani A and Kudrolli A 2000 *Phys. Rev. Lett.* **85** 5102
[14] Geromichalos D, Kohonen M, Mugele F and Herminghaus S 2003 *Phys. Rev. Lett.* **90** 168702
[15] Blair D L and Kudrolli A 2003 *Phys. Rev.* E **67** 021302
[16] Götzendorfer A, Kreft J, Kruelle C A and Rehberg I 2005 *Phys. Rev. Lett.* **95** 135704
[17] Fingerle A and Herminghaus S 2006 *Phys. Rev. Lett.* **97** 078001
[18] Götzendorfer A, Kruelle Ch A, Rehberg I and Svensek D 2006 *Phys. Rev. Lett.* **97** 198001
[19] Herminghaus S 2005 *Adv. Phys.* **54** 221
[20] Fingerle A and Herminghaus S 2008 *Phys. Rev.* E **77** 011306
[21] Scheel M, Geromichalos D and Herminghaus S 2004 *J. Phys.: Condens. Matter* **16** S4213
[22] Mitarai N and Nori F 2006 *Adv. Phys.* **55** 1
[23] Willett Ch D, Adams M J, Johnson S A and Seville J P K 2000 *Langmuir* **16** 9396
[24] Lian G, Thornton C and Adams M J 1998 *Chem. Eng. Sci.* **53** 3381
[25] Mikami T, Kamiya H and Horio M 1998 *Chem. Eng. Sci.* **53** 1927
[26] Simons S J R and Fairbrother R J 2000 *Powder Technol.* **110** 44
[27] Fingerle A and Herminghaus S 2007 Mechanisms of dissipation in wet granular matter *Preprint* arXiv:0708.2597
[28] Leiderer P and Bosch W 1980 *Phys. Rev. Lett.* **45** 727
[29] Petrova A E, Krasnorusskii V N, Sarrao J and Stishov S M 2006 *J. Exp. Theor. Phys.* **102** 636
[30] Losert W *et al* 1999 *Chaos* **9** 682
[31] Rouyer F and Menon N 2000 *Phys. Rev. Lett.* **85** 3676
[32] Fingerle A, Scheel M and Herminghaus S Determining granular velocity distributions by Mössbauer spectroscopy, in preparation